THE EFFECT OF TEMPLATED GRAPHITIZATION ON ELECTROMECHANICAL PROPERTIES OF CARBON NANOFIBER

A Dissertation

by

JIZHE CAI

Submitted to the Office of Graduate and Professional Studies of
Texas A&M University
in partial fulfillment of the requirements for the degree of

DOCTOR OF PHILOSOPHY

Chair of Committee,	Mohammad Naraghi
Committee Members,	Dimitris C. Lagoudas
	James G. Boyd
	Lin Shao
Head of Department,	Rodney Bowersox

May 2018

Major Subject: Aerospace Engineering

Copyright 2018 Jizhe Cai

ABSTRACT

Theory predicts that carbon nanofibers (CNFs), processed via carbonizing polymeric nanofibers, as down-sized version of carbon fibers (CFs) should be significantly stronger than CFs, due to size-dependent defects in CFs such as skin-core radial inhomogeneity. To close the gap between the predictions and experimentally achieved strength of CNFs, the processing-microstructure-properties relationship in CNFs was studied. The CNFs in my study were fabricated by thermal stabilization and carbonization of electrospun polyacrylonitrile (PAN) nanofibers which contain CNTs inclusions. In this research the formation of graphite-like structures (turbostratic domains) within CNFs was promoted by adding CNTs to the precursor in a process known as templated graphitization, in which the presence of CNTs can facilitate the arrangement of carbon atoms, obtained as a result of the carbonization of PAN, into a graphite-like structure (sp^2 carbon bonds) similar to what exists in CNTs. It is further demonstrated that the templating effect of CNTs is more pronounced when PAN chains are aligned with each other and with CNTs, as was achieved in this research by hot-drawing the precursors. The existence of CNTs effectively promotes the formation of highly ordered polymer interphase.

The study on the microstructure and mechanical properties of CNFs confirms that the modification of the precursor microstructure, such as enhanced chain alignment, can be maintained during carbonization, and indeed leads to enhanced graphitic alignment. Based on the MEMS-based nano-mechanical tension tests on CNFs, the combined effect of precursor hot-drawing and graphitic templating effect resulted in CNFs with tensile

strength and modulus of 6.9 GPa and 250 GPa, respectively, which are the largest values reported up to date for this type of material. Moreover, the multifunctional properties of electrospun CNFs, including piezoresisitivty and electrical conductivity, were restudied both experimentally and via continuum models, demonstrating the strong correlation between microstructure modification and properties improvement.

In summary, a clear strategy for developing low-cost high performance CNF/CNTs hybrid nanofibers was obtained based on new understanding of the load bearing mechanism within CNF. These nanofibers can be used as the multifunctional building blocks for a host of applications, including aerospace and automotive industry.

DEDICATION

This work is dedicated to my father, Jun Cai, for making me who I am.

ACKNOWLEDGEMENTS

I would like to sincerely express my thanks and gratitude to my advisor, Dr. Mohammad Naraghi for his expertise, encouragement, understanding and support during my Ph.D. study period in Texas A&M University, which makes it to be an invaluable experience in my life. I would also like to thank my committee members, Dr. Dimitris C. Lagoudas, Dr. James G. Boyd and Dr. Lin Shao for their kindly support and valuable feedbacks.

The use of the TAMU Materials Characterization Facility is also acknowledged. I would like to thank Dr. Yordanos Bisrat, Dr. Amanda Henkes and Dr. Winson Kuo for their technical support for various characterization instruments. I would also like to thank Dr. Hansoo Kim and Mr. Tom Stephens from TAMU Microscopy and Imaging Center for their help in TEM and SEM experiments. I am grateful to Dr. Frank Gardea, Dr. Sneha Chawla, Seokjin Hong, Yijun Chen and all other members from our group for their helps during my graduate study, research and dissertation writing.

Lastly, my deepest appreciation belongs to my father and mother, Jun Cai and Zhihong Chen for their continued patience, understanding and support. One of the important motivations that supports me to finish this challenging Ph.D. study is to make my parents proud and I hope I have accomplished that with this achievement. To my wife, Quanjing Chen, and son, Tianhang Cai, I won't be this strong without your accompany during my whole Ph.D. study. I love you all so much!

CONTRIBUTORS AND FUNDING SOURCES

This work was supervised by a dissertation committee consisting of Professor Mohammad Naraghi (advisor) and Professors Dimitris C. Lagoudas and James G. Boyd of the Department of Aerospace Engineering and Professor Lin Shao of the Department of Nuclear Engineering.

All work for the dissertation was completed independently by the student.

The authors acknowledge the support from Air Force Office of Scientific Research, under the award number FA9550-15-1-0170, and Qatar National Science Funds, under the award number 8-2048-2-804. The FE-SEM acquisition was supported by the NSF grant DBI-0116835, the VP for Research Office, and the TX Eng. Exp. Station.

NOMENCLATURE

f_c	Alignment of crystallite domains
σ	Angle between fiber axis and backbone direction
α	Angle between nitrile group and backbone direction
f	Alignment of polymer chain
f_{SWNTs}	Alignment of SWNTs in hybrid nanofiber
I_{HH}	Raman intensity in HH configuration
I_{VV}	Raman intensity in VV configuration
T_g	Glass transition temperature
λ	Hot-drawing ratio
d_i	Initial fiber diameter
d_f	Final fiber diameter
I_{HH}	Raman intensity in HH configuration
I_{VV}	Raman intensity in VV configuration
V_f	Volume fraction
E	Modulus
L_a	Crystallite size
λ_L	Laser wavelength in Raman spectroscopy
I_D	Raman intensity from D-peak
I_G	Raman intensity from G-peak
f_{002}	Herman's orientation factor of graphitic crystallite

ρ	Electrical resistivity
ε	Strain
υ	Poisson's ratio
m	Mass of electron
φ	Electrical potential
I	Electrical current
J_0	Current density
P	Power input
CFs	Carbon fibers
PAN	Polyacrylonitrile
DC	Direct current
CNFs	Carbon nanofibers
PS	Polystyrene
MEMS	Microelectromechanical system
NFES	Near-field electrospinning
PEO	Polyethylene oxide
PCL	Polycaprolactone
PVDF	Polyvinylidene difluoride
PPTA	Poly (p-phenylene terephalamide)
CNTs	Carbon nanotubes
CQDs	Carbon quantum dots
MWNTs	Multi walled carbon nanotubes

PE	Polyethylene
PP	Polypropylene
HOG	Highly ordered graphitic
PPy	Polypyrrole
EMI	Eectromagnetic interference
SE	Shielding efficiency
SWNTs	Single walled carbon nanotubes
DMF	Dimethylformamide
DSC	Differential scanning calorimeter
XRD	X-ray diffraction
FWHM	Full-width at half maximum
FT-IR	Fourier-transform infrared spectroscopy
WAXD	Wide angle X-ray diffraction
DIC	Digital image correlation
SAED	Selected area electron diffraction
SEM	Scanning electron microscopy
TEM	Transmission electron microscopy
FIB	Focused ion beam
PAN-co-MAA	Polyacrylonitrile-co-Methacrylic Acid
GNP	Graphite nano-platelets
TRGO	Thermally reduced graphene oxide
f-SWNTs	Functionalized single walled carbon nanotubes

HO	Hghly ordered
EELS	Electron energy loss spectroscopy
GF	Gage factor
R	Electrical resistance

TABLE OF CONTENTS

Page

Page

Page

LIST OF FIGURES

LIST OF TABLES

1. INTRODUCTION*

Developing carbon filament through carbonizing cotton threads or bamboo slivers for light bulb dates back to late 19th century. However, carbon fibers (CFs) as promising materials for mechanical reinforcements in composites and structural light-weighting were introduced as late as 1963 by researchers in England [1-2]. One of the first commercialized CFs with unprecedented mechanical strength at the time was developed by carbonizing polyacrylonitrile (PAN) by Toray Industries, Inc. in Japan in 1971, branded as T300, with tensile strength of 2.5 GPa, which was further improved to 3.5 GPa through modifications in material systems and fabrication process[3]. Since then and in the past 50 years of development, the mechanical strength of CF has evidently improved from 2.5 GPa to 7.0 GPa for T1100G from Toray [4].

The development of high strength PAN based CF opened up the opportunity of utilizing CF and its composites as the next-generation of structural materials in aerospace industry to substitute traditional metal based materials. The most important advantage of CF reinforced composite materials over traditional materials is its high specific mechanical properties, mainly strength and modulus, which can be utilized to reduce the weight of load bearing components, as a means to improve performance metrics such as fuel efficiency in aerospace and automotive industry, and maneuverability in aviation.

* Part of this section is reprinted with permission from "High-performance structural fibers for advanced polymer matrix composites", by National Research Council, 2005, The National Academies Press, Washington, DC.

Driven by the benefits of CFs for structural light-weighting, increasing the strength of CFs and their composite materials has been the focus of research in both academia and industry for several decades [5-8]. However, as shown in Fig.1.1 [9], restricted by the precursor development and fabrication processes, the mechanical strength of CF seems to have reached a plateau [10-11].

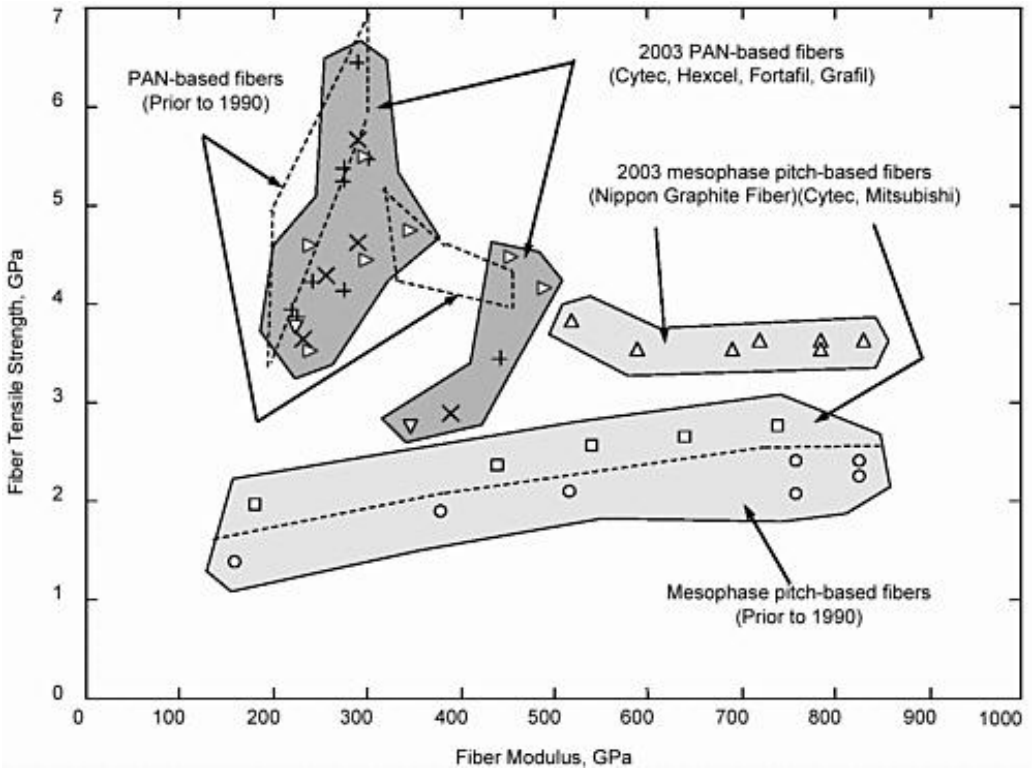

Figure 1.1. Improvement of the mechanical properties of commercial PAN-based and mesophase pitch-based carbon fibers from the period prior to 1990 to 2003.[9] Reprinted from [9] with permission.

1.1 Fabrication of carbon fiber and its mechanical property size effect*

The carbon fibers with diameters of 5-10 μm are fabricated via thermal stabilization and carbonization of polymers, such as lignin [12], PAN homopolymer or copolymers and petroleum pitch [2]. The CFs with highest strength are all based on PAN copolymers precursors. Compared to PAN homopolymer, PAN copolymers allow for higher chain alignment and crystallinity in the precursor fiber due to reduced polarity of non-PAN co-monomers, which translates into higher graphitic alignment and improved mechanical performance of CFs. The lowered stabilization temperature of PAN copolymer will also facilitate the mechanical performance improvement in CFs by reducing the possibility of thermal degradation during processing. Therefore, PAN copolymers are the most abundantly used precursors for high strength CFs [13-14].

Despite the high strength of PAN-based carbon fibers with tensile strength values of as high as 7 GPa for Toray T1100G, studies on CFs point to strong anisotropic strength size effects, in which the strength of CFs is much more sensitive to diameter than length [14-17]. This anisotropic size effect can partly be explained in terms of a size-dependent radial inhomogeneity in PAN-based CFs, which can severely compromise their strength [11, 17-19]. The radial inhomogeneity, also known as skin-core inhomogeneity, refers to the specific morphology of PAN-based CFs in which the skin is distinctly more graphitic than the core [17]. This size (diameter)-dependent phenomena occurs as a result of low oxygen diffusion

* Part of this section is reprinted with permission from "Carbon nanotube reinforced small diameter polyacrylonitrile based carbon fiber." by H.G. Chae, Y.H. Choi, M. L. Minus, S. Kumar. Composites science and technology. 2009;69(3-4):406-413.

during stabilization to the core of the fiber [11, 15]. Therefore, decreasing the average diameter of the PAN precursor fiber could effectively lower the extent of the structural inhomogeneity in CF, which should in principle improve the mechanical strength of CF [11, 20].

To develop high performance CFs, the gel-spinning method was developed to fabricate precursor polymer fiber [21], in which spinneret is used to squeeze diluted high molecular weight polymer solution to gel-like filament. This is followed by drawn the precursor fibers to align the polymer chain with the drawing direction. Drawing is a crucial step to achieve high mechanical performance fibers as it aligns the polymer chain and increasing crystallinity of the drawn fiber. Along with fiber microstructure evolution, there is an evident fiber thinning during the drawing process. While drawing the precursor is required to align polymer chains, excessive drawing can induce defects (such as chain scissor) in the fiber or even break them during the drawing process. This fact limits the minimum achievable precursor fiber diameter which can be achieved by drawing the precursor. Therefore, in traditional precursor fabrication methods such as gel-spinning, there exists a lower limit for the diameter of CF, which is about 3-5 μm. Even in some novel approaches developed by Dr. Kumar's group, known as island-in-sea bi-component gel-spinning method, the minimum achievable CF diameter is still about 1 μm [20]. For the CF with diameter ranging from 1 μm to 11 μm, strong mechanical size effect has been experimental observed, Fig.1.2 [20]. Hence, to achieve high strength of CF through decreasing its diameter, new precursor fabrication method needs to be introduced.

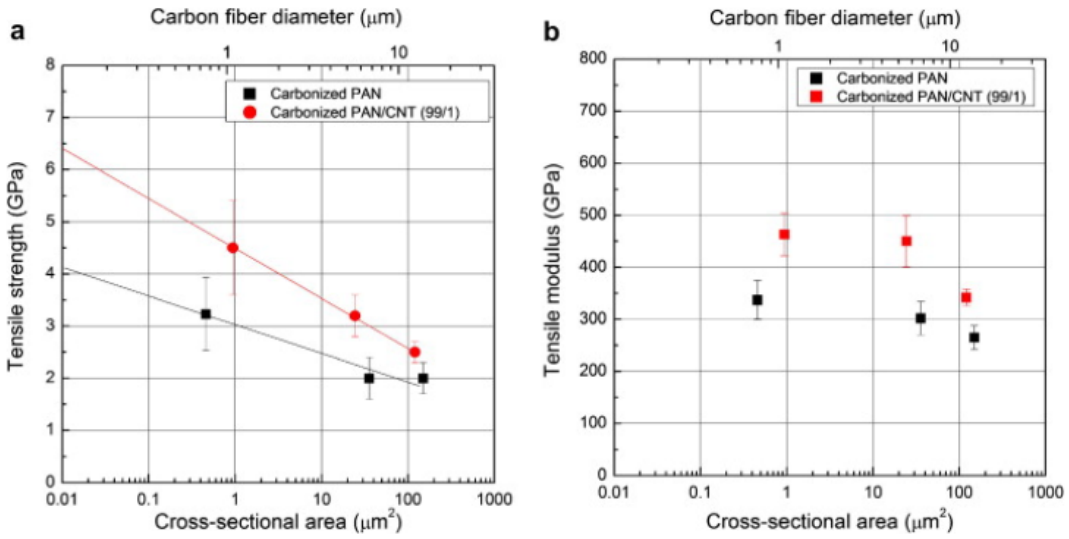

Figure 1.2. Effect of CFs and CF/CNTs diameter on its mechanical properties.[20] Reprinted from [20] with permission.

To address the above limitations, carbon nanofibers (CNFs) with their submicron diameter (100-300 nm) have increasingly attracted attention from researchers in different areas especially in the past decade [22-24], for their higher structural homogeneity, multifunctional properties, high surface to volume ratio and low defect density [18, 22]. CNFs have been fabricated through different methods, such as carbonization of electrospun PAN precursor nanofibers [18] and vapor grown fabrication [25-26]. Among these methods, electrospinning is an effective method for manufacturing polymer fibers with diameter in nanometer scale and provides an effective platform to modify molecular structure of polymers [27], required to improve mechanical strength [28], electrical [29] and thermal conductivity [30] of nanofibers. Electrospun CNFs are fabricated through three stages: Stage

I: electrospinning to fabricate precursor PAN nanofibers; Stage II: stabilization of PAN nanofibers and Stage III: carbonization of PAN nanofibers [31-32]. More details of the processing steps of CNFs is shown in Fig.1.3.

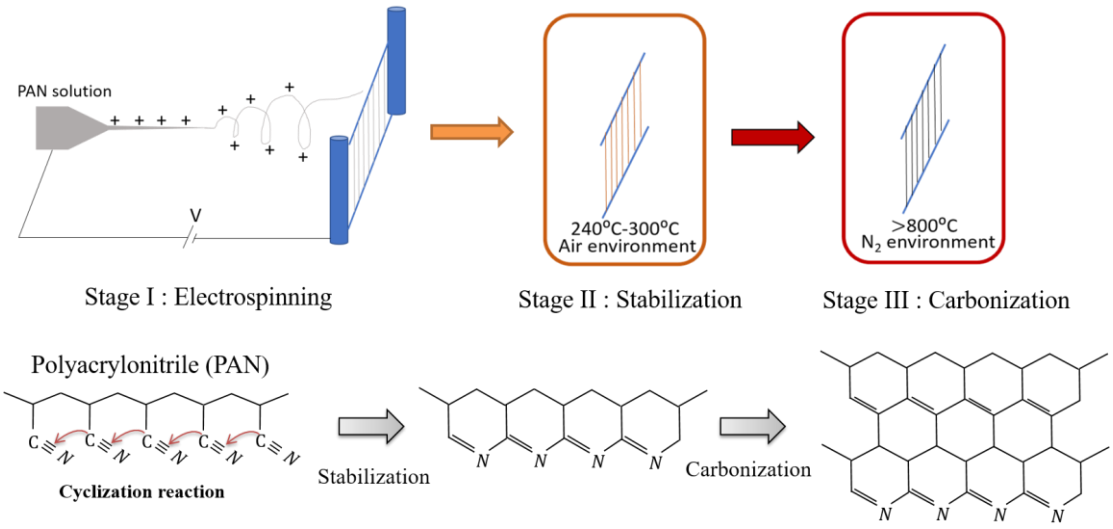

Figure 1.3. Fabrication process of CNFs with electrospun PAN precursor nanofibers.

After obtaining PAN precursor nanofibers in stage I, stabilization process is applied to transfer the PAN precursor from linear atomic structure to thermally stable ladder structure (stage II). Stabilization is typically performed at the temperature range of 240-300 ºC in air. During this process, complicated chemical reactions happens, such as oxidation, dehydration and cyclization, which requires diffusion of oxygen from environment into core of fiber to participate into the reaction and release of the generated heat to the environment. Therefore, care needs to be taken to prevent the local overheating

or incomplete stabilization limited by oxygen diffusion of the PAN precursor fibers, which will adversely affect the mechanical properties of the obtained CFs [14, 33-34].

The stabilized PAN fibers are then carbonized at temperature ranges from 900 ºC to 1600 ºC under inert atmosphere in stage III. During this process, the non-carbon atoms within the fiber are eliminated and the cyclized PAN chains will be cross-linked to form turbostratic carbon, which is a kind of imperfect graphitic structure. In turbostratic structure, the adjacent atomic planes are shifted with respect to each other, therefore the inlayer distance increases from 0.335 nm for perfect graphite to > 0.345 nm. Typically, after carbonization process, the carbon content in CNF exceeds 90%.

Classified based on the trajectory of the jet, the electrospinning process can be divided into two major categories, regular electrospinning [35] and near-field electrospinning [36], as discussed in the subsequent sections.

1.2 Regular electrospinning process*

Although electrospinning was first discovered by Rayleigh in 1897, it has become more attractive for researchers in recent decades due to its capability in fabricating nanomaterials, especially in generating ultrafine polymer nanofiber with diameters down to several tens of nanometers [35, 37]. As shown in Fig.1.4 in electrospinning a high DC voltage applied between a polymer solution source and a grounded target generates

* Part of this section is reprinted with permission from "Electrospinning of nanofibers: reinventing the wheel?" by D. Li, Y. Xia. Advanced Materials. 2004;16 (14):1151-1170 and "Molecular orientation and mechanical property size effects in electrospun polyacrylonitrile nanofibers" by M. Naraghi, S.N. Arshad, I. Chasiotis. Polymer. 2011;52 (7):1612-1618.

electrostatic forces on the charged solution, leading to the formation of a solution jet, jet stretching and thinning, hence, polymer fiber with submicron diameters form on the collecting target. During the electrospinning process, as the high voltage (10s kV) is applied to the syringe needle, the surface of the polymer solution droplet held by its own surface tension gets electrostatically charged at the needle tip [38]. Then, electrostatic forces, including mutual electrostatic repulsion between electric charges on surface of the jet and Coulombic force applied to the induced charges of the jet by the applied electric field, act on the solution droplet to stretch it to form a conical shape, known as Taylor cone. By increasing the electric field to a critical value, the electrostatic force will overcome the

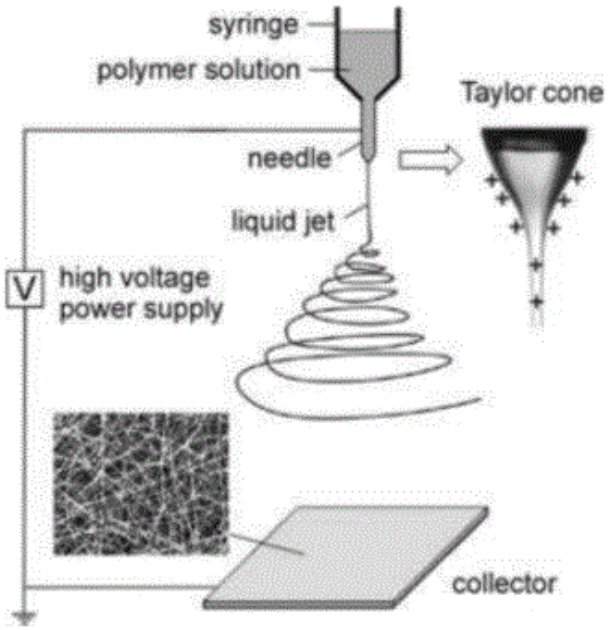

Figure 1.4. Schematic diagram of electrospinning experimental setup.[37] Reprinted from [37] with permission.

surface tension of polymer solution and form solution jet ejected towards the collector surface. During the travel of solution jet, the electrostatic forced induce solution jet stretching, and solvent evaporates, leading to the formation of polymer nanofiber on the target.

The microstructure and morphology of polymer precursor nanofibers can be modified to some extent by tuning the electrospinning parameters [39-42]. Typically, the electrospinning parameters are separated as two categories, which are solution parameters and processing parameters. Molecular weight of polymer, concentration, viscosity, surface tension and electrical conductivity of polymer solution are all in the first category, and they all play important roles in controlling the morphology of the electrospun nanofibers. The applied voltage, flow rate, collector, distance between syringe tip and collector and environment are among the processing parameters which also control the microstructure and morphology of nanofibers.

To modify the microstructure of electrospun polymer nanofiber, M. Naraghi, *et al.* [27] demonstrated an evident improvement in PAN nanofiber Young's modulus through applying longer electrospinning distance. This was attributed to lower solvent content of as-electrospun fibers which had travelled longer distances, as shown in Fig.1.5, allowing them to maintain higher chain alignment. Therefore, the properties of CNF fabricated from the electrospun PAN nanofiber is highly dependent on the electrospinning parameters and polymer solution properties [11, 43]. Apart from polymer chain alignment, crystallinity of as-electrospun polymer nanofiber can be tailored from 0 % (amorphous fiber) to 50% (semi-

crystalline fiber) through controlling the applied voltage, feed rate and different collector systems [44].

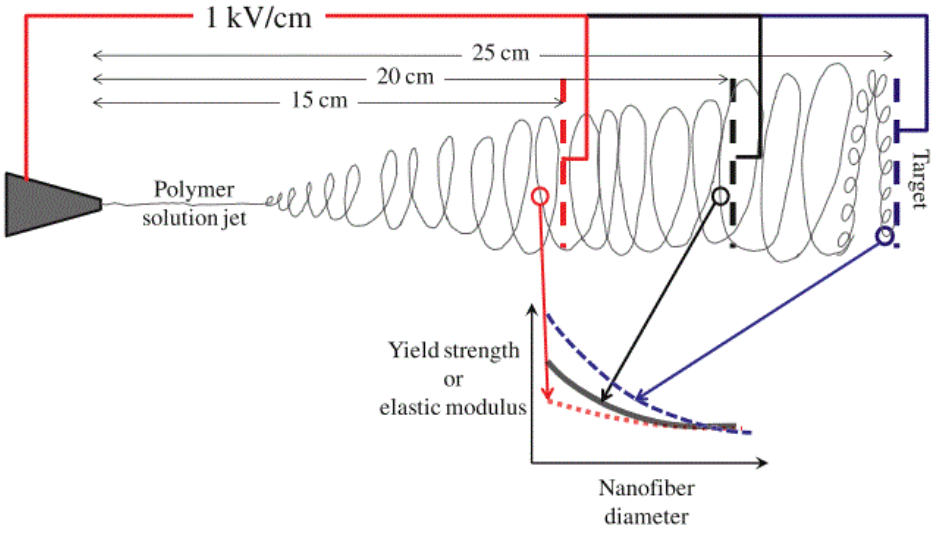

Figure 1.5. Relationship between mechanical property size effects and electrospinning parameters.[27] Reprinted from [27] with permission.

Apart from the effect on microstructure of electrospun polymer nanofiber, electrospinning parameters also play an important role in determining the morphology of the obtained nanofiber. For example, through changing the surface tension and viscoelastic properties of the polymer solution, there is transition from smooth fiber to beaded fibers for the as-electrospun nanofibers [45]. By controlling the humidity of the environment, Casper, et al, demonstrated that the surface morphologies of polystyrene (PS) fibers could be modified to exhibit porous surface [46]. Therefore, regular

electrospinning has been demonstrated to be a versatile approach to fabricate polymer nanofibers with various microstructures and morphologies, which makes it to be a promising method for developing nanomaterials in various fields.

1.3 Near-field electrospinning process*

In the most common form of electrospinning, the polymer solution jet undergoes a whipping motion, often referred to as bending instability [47] . This instability, caused by repulsion between induced electrostatic charges on the jet, is considered to be one of the most critical mechanisms in drawing and thinning the polymer solution jet, to generate nanofibers and align the polymer chains within nanofibers [27, 48] . However, the whipping motion is stochastic in its nature, as it is driven by the distribution of induced charges along the jet. Thus, it often introduces some randomness with a rather wide distribution in the process output parameters, such as chain alignment within nanofibers, diameter distribution, physical properties of nanofibers, nanofiber alignment and position along a target [27, 49-50]. The poor controllability over the output parameters, inherent to conventional electrospinning, is a roadblock to the application of electrospun nanofibers for some applications such as microdevices [51] and carbon-based MEMS [52] which require precise positioning of electrospun nanofibers [53-54].

* Part of this section is reprinted with permission from "Continuous near-field electrospinning for large rea deposition of orderly nanofiber patterns" by C. Chang, K. Limkrailassiri, L. Lin. Applied physics letters. 2008;93:123111.

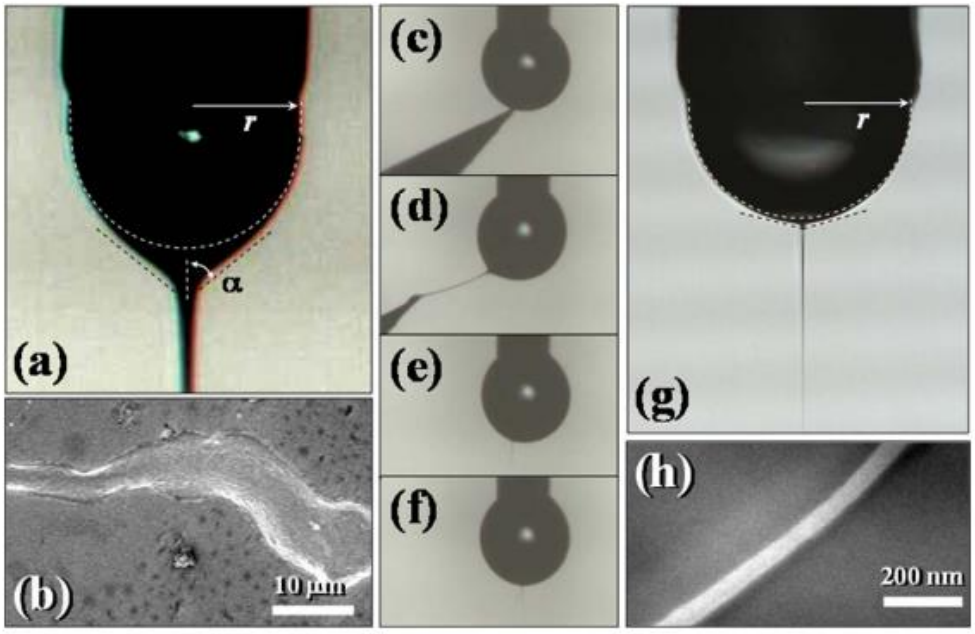

Figure 1.6. Comparison between regular electrospinning and continuous near-field electrospinning polymer solution jet.[55] Reprinted from [55] with permission.

To overcome these limitations, near-field electrospinning (NFES) process was developed which allows for precision positioning of nanofibers by capturing the electrospinning jet before the bending instability has initiated [36, 53-55]. NFES method has been applied to fabricate nanofibers from different polymers, such as polyethylene oxide (PEO) [56], polycaprolactone (PCL) [57], polyvinylidene difluoride (PVDF) [58], with diameters ranging from 30 nm – 10 μm. While in conventional electrospinning, major thinning of the jet occurs during the bending instability, the formation of nanofibers in NFES often relies on smaller initial polymer solution jet and employing lower solution concentrations with considerably lower viscosities and thus increases drawability [55], as shown in Fig.1.6. To further promote the application of near-field electrospinning in fabricating nanofiber

in large scale, various approaches had been developed, such as continuous [55] and multi-nozzle NFES [54]. In the continuous NFES, a sharp tungsten probe is controlled by manipulator to stretch a thin strip of polymer solution from the droplet to form a local high electric charge intensity to initiate the electrospinning process under relatively low electric field [55-56]. The nanofibers fabricated via NFES have been used in a variety of applications [36], as conductive electrode [59], energy harvester devices [51] and flexible wearable devices [60].

1.4 Post-processing of as-electrospun nanofiber*

Although electrospinning method is an effective method to fabricate PAN precursor nanofiber, the method offers relatively limited opportunities in controlling the microstructure of polymeric precursors, comparing to traditional spinning method. For instance, the polymer chain alignment and crystallinity in as-electrospun PAN nanofiber is much lower than the traditional PAN precursor fiber from gel-spinning method [43], which evidently lowers the mechanical performance of the polymer nanofiber. Upon carbonization, the lower polymer chain alignment and crystallinity lowers the alignment of graphitic domain along the fiber axis with larger size in obtained CNFs, therefore compromising CNF's tensile strength. Comparing with traditional CFs from gel-spun PAN precursor fibers with tensile strength and modulus of 4.7 GPa and 299 GPa [34], the highest averaged tensile strength and modulus of CNFs obtained by carbonizing as-electrospun PAN precursor nanofibers are only 3.5 GPa and 172 GPa, respectively [18].

* Part of this section is reprinted with permission from "Characterization of the adhesion of single-walled carbon nanotubes in poly(p-phenylene terephthalamide) composite fibers" by L. Deng, R.J. Young, S. Zwaag, S. Picken. Polymer. 2010;51(9):2033-2039.

Therefore, engineering the microstructure of as-electrospun precursor nanofibers, especially aligning polymer chain, is a key requirement to further improve the strength and modulus of electrospun CNFs [11].

There has been some efforts to enhance chain alignment in as-electrospun nanofibers by controlling the electrospinning parameters. For instance, through increasing the electrospinning distance, the alignment of polymer chain in as-electrospun PAN nanofiber has been effectively improved due to reduced residual solvent for nanofiber with longer electrospinning distance [27]. Moreover, Dr. Dzenis and co-works [61] found that reduction of electrospun fiber diameter from 2.8 μm to 100 nm results in an evident increase in modulus and toughness, due to the increased chain alignment and lowered crystallinity within the fibers. Despite all the efforts made, the alignment of as-electrospun nanofiber is still much lower than the polymer fiber fabricated by regular spinning process with post-drawing treatment. For instance, the Herman's orientation factor and crystallinity of as-electrospun PAN nanofiber are 0.5 and 16.8% [27], which are much lower than 0.89 and 50% for gel-spun PAN fibers [62]. Therefore, post-electrospinning treatments, such as mechanical drawing of the nanofibers, should be implemented to further improve the polymer chain alignment and therefore increasing its mechanical properties. In polymer nanofibers, the post-electrospinning drawing needs to be applied under relatively high temperatures, typically higher than the glass transition temperature of the polymer, to enhance the mobility of the polymer chains and facilitate chain alignment via drawing. Hence, it may be referred to as hot-drawing.

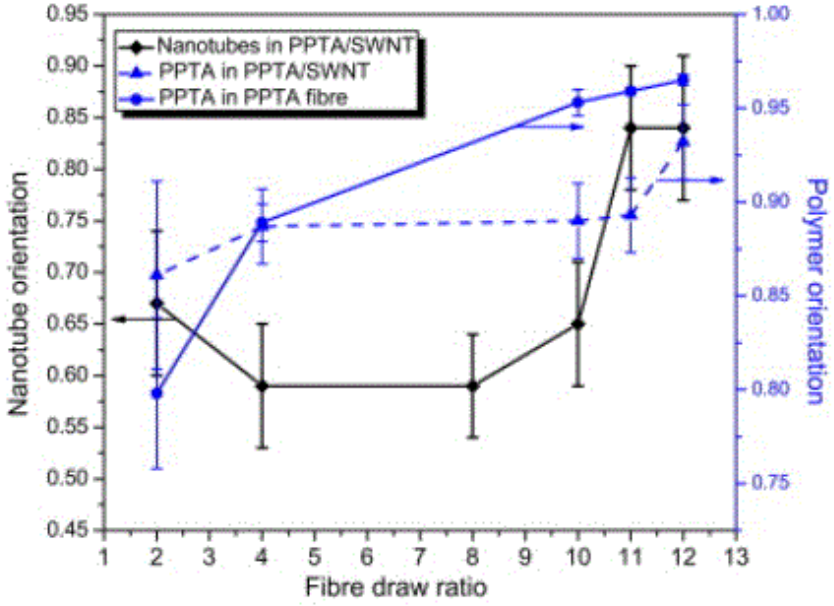

Figure 1.7. Effect of hot-drawing ratio on polymer chain alignment.[64] Reprinted from [64] with permission.

Hot-drawing of electrospun nanofibers can be used to align the polymer chains and nano-particles inclusions embedded in the polymer [63-66]. For instance, as shown in Fig.1.7, by increasing the hot-drawing ratio (final length/initial length of fiber), there is a continuous increase in the chain alignment of poly (p-phenylene terephalamide) (PPTA) fibers [64]. Moreover, aligning the chains enhances the chain packing, thus, it facilitates the crystallization of the polymer fiber. Therefore, it often leads to enhanced degree of crystallinity, crystal size and crystalline phase alignment [67-68]. Apart from the chain alignment, hot-drawing can also reduce the structural defects inside the fiber [69] and fiber surface defects [63] through smoothing nanofiber surface, evaporating residual solvent and reducing voids during the reorientation of polymer chains.

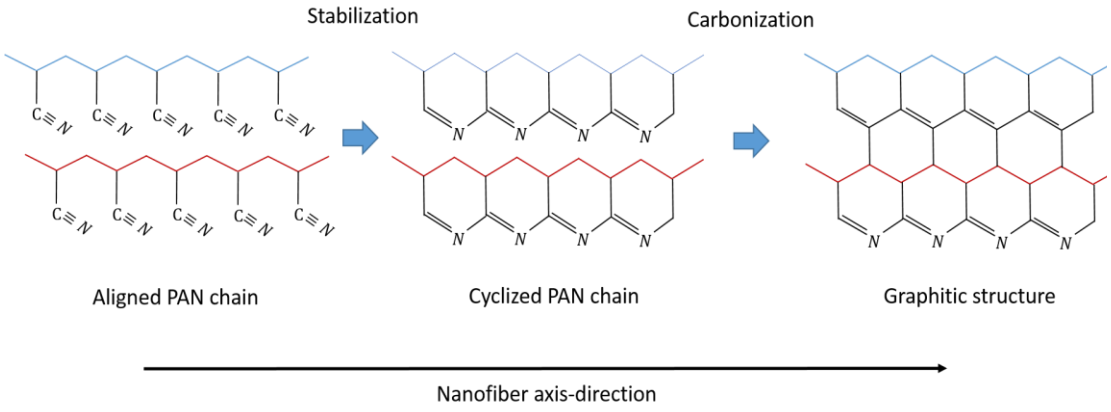

Figure 1.8. Schematic description of structural evolution of CNF fabricated by hot-drawn electrospun PAN precursor nanofibers.

State-of-the-art as-electrospun CNFs often suffer from poor graphitic alignment due to the lack of polymer chain alignment of the precursor nanofiber. That is because a prerequisite for graphitic alignment in CNFs is the alignment of polymeric chains in the PAN nanofiber precursor [7, 70], while as mentioned earlier, as electrospun nanofibers often have low degree of chain alignment, mainly due to fast solvent evaporations during electrospinning, which suppresses chain mobility [27]. Thus, the high in-plane strength of sp^2 C-C bonds provides ample opportunities to enhance the strength of CNFs by aligning the graphitic domains with the fiber axis [8], as shown in Fig.1.8. Hence, hot-drawing can be applied to as-electrospun PAN nanofibers as a post-processing treatment to enhance the performance of the fabricated CNFs [21, 68, 71].

Previous efforts have been made in our group to enhance chain alignment in PAN nanofibers as precursors for CNFs [43]. In this regard, hot-drawing has been successfully applied to the as-electrospun PAN nanofiber ribbons, which effectively enhances polymer chain alignment and crystallinity. The microstructure evolution within the precursor nanofiber has been preserved to some extent during the following stabilization and carbonization process, therefore evident graphitic structure alignment improvement has been achieved in hot-drawn CNFs. Based on the nano-mechanical testing of individual CNF, aligned graphitic structures provide 71% and 111% improvement in modulus and strength respectively. Despite the fact the previous work clearly demonstrates the contribution of hot-drawing of precursor to mechanical properties of CNFs, the details of hot-drawing in the prior work need to be revisited as excessive hot-drawing led to structural damage in CNFs, partly canceling out the enhancements in CNF strength caused by precursor hot-drawing. Moreover, the prior work primarily include carbonization at rather low temperatures (~1100°C), where the turbostratic domains are at their early stages of growth.

1.5 Templating graphitization of CNTs in CF*

In recent decades, the carbon nanomaterials, such as fullerene, graphene, carbon nanotubes (CNTs) and carbon quantum dots (CQDs) have received increasingly attention

* Part of this section is reprinted with permission from "Novel fluorescent carbonic nanomaterials for sensing and imaging" by A. P. Demchenko, M.O. Dekaliuk. Methods and applications in fluorescence. 2013;1:042001 and "High resolution transmission electron microscopy study on polyacrylonitrile/carbon nanotube based carbon fibers and the effect of structure development on the thermal and electrical confuctivities" by B. A. Newcomb, L.A. Giannuzzi, et al. Carbon. 2015;93:502-514.

due to their superior chemical, physical, mechanical and thermal properties [72], as shown in Fig.1.9. Carbon nanotubes (CNTs) are special allotropes of carbon with a cylindrical nanostructure. Based on the numbers of the rolled layers of graphene, CNTs are typically divided into two types: single-walled carbon nanotubes, and multi-walled carbon nanotubes. The CNTs were produced by Iijima in 1991 through applying arc-discharge evaporation method [73]. Since then, the outstanding physical properties of CNTs had been successfully demonstrated by researchers, such as outstanding mechanical properties, electrical conductivity and thermal conductivities, which makes CNTs to be a promising materials in various fields, For instance, the modulus and fracture strength of individual MWCNTs was experimentally measured to be about 1 TPa and >100 GPa [74], respectively.

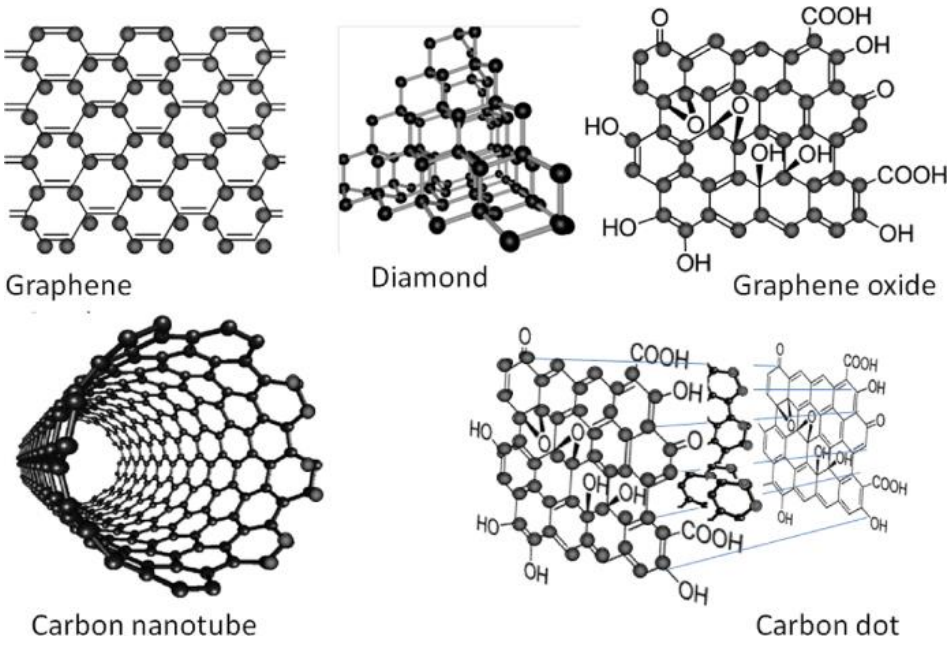

Figure 1.9. Schematic diagram of various carbon nanomaterials.[72] Reprinted from [72] with permission.

The electrical resistivity of carbon-arc method fabricated MWCNTs is in the range from 6×10^{-2} Ω m to 5×10^{-8} Ω m, from semi-conducting to metallic [75]. The thermal conductivity of individual MWCNTs is 300 ± 20 W/mK [76]. To benefit from the outstanding physical properties of CNTs in larger scales, different CNTs based nanocomposite materials had been developed by researchers in different fields.

Apart from directly utilizing the excellent physical properties of CNTs themselves, the existence of nanofillers in hot-drawing process, such carbon nanotubes [68], reduced graphene oxide [66], carbon nanochip [67], is shown to have an evident influence on the microstructure of the polymer fiber, such as the crystallinity, polymer chain alignment, and therefore its properties [64, 66]. Several approaches have been devised and successfully implemented to develop polymer-based CNT-reinforced nanocomposites, including electrospinning [77], gel spinning [71], and melt spinning [78]. In this regard, electrospinning provides a platform to add nanoparticles, such as CNFs to enhance the morphology of polymeric nanofibers. In addition to the direct reinforcement effect, CNTs are found to drastically alter the morphology of polymers especially the semicrystalline ones [79], such as Nylon 66 [80], polyethylene (PE) [81], polypropylene (PP) [82], or polyacrylonitrile (PAN) [83]. For instance, CNTs, can nucleate crystallization of polymers from a polymer solution, and lead to formation of extended polymer chains in a shear flow [71, 84-85]. Zhang et al [86], showed existence of CNTs will perform as heterogeneous nucleating agents for the formation of polypropylene (PP) transcrystals perpendicular the nanotube fiber axis, which brings an effective mechanical properties improvement. This effect is likely due to epitaxial interactions between CNTs and polymer backbone [16, 68], and the comparable length of C-

C bond in polymer backbones [71 84]. The high surface to volume ratio of CNTs significantly enhances the efficiency of this method [84]. By controlling solution properties and shear flow, thickness of the extended chain layer on CNTs can be as large as ~10 nm [87]. For instance, the addition of CNTs to PAN micro and nanofibers, via respective gel spinning or electrospinning, and shear and elongational flows in these processes, led to considerable chain alignment [16, 71, 87]. Stacking of extended chains, facilitated by epitaxial interactions, can also reduce void formation [87].

Recent studies on polyacrylonitrile (PAN) fibers with CNT inclusions suggests that the presence of CNTs in PAN precursor will assist in graphitization during the carbonization [88-89]. For example, Guo et al [90], had demonstrated the strong interaction between matrix PAN and CNTs in the PAN/CNTs hybrid composite film, moreover, the existence of CNTs effective increases the crystallinity of PAN matrix. The enhanced graphitization is partly caused by the suppression of chain relaxation due to reinforcing effect of CNTs, which enhances PAN cyclization during thermal stabilization process [16, 91]. Moreover, CNTs act as templates to guide graphitization [70, 87, 91]. As shown in Fig.1.10, the existence of CNTs in CF will facilitate the formation of highly ordered graphitic structure (HOG) with outstanding mechanical and electrical properties, therefore bringing an increase in the overall mechanical and electrical properties of CF/CNTs hybrid fiber [70, 89]. Hence, carbonization of PAN in molecular vicinity of CNTs/graphene increases graphitic order and the mechanical reinforcing effect of CNTs [11, 16, 92-93].

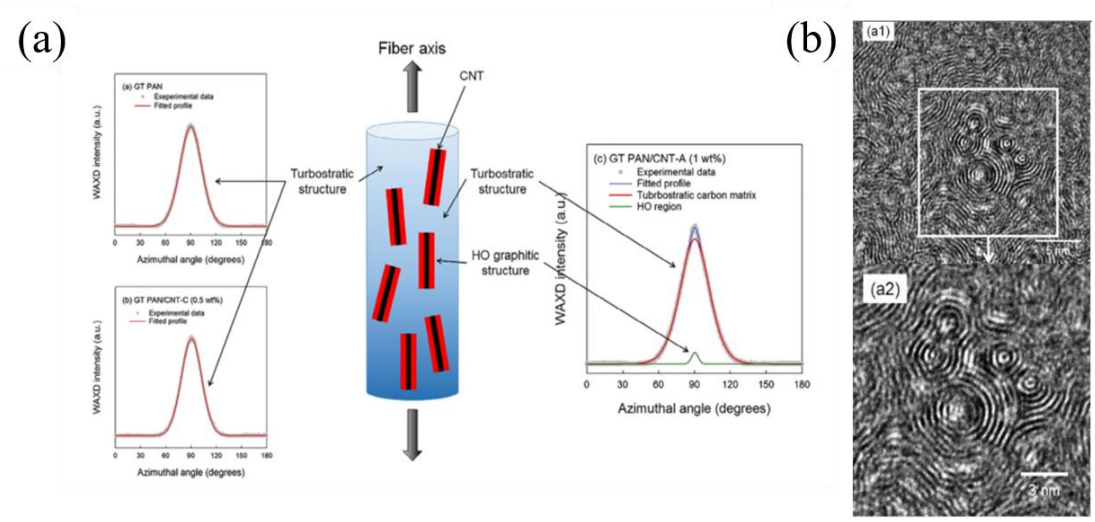

Figure 1.10. (a) Schematic description of carbon fibers with turbostratic carbon matrix, templated graphitic structure and CNTs and **(b)** TEM image of HOG structure.[88] Reprinted from [88] with permission.

Similarly, inclusions of graphene nanoparticles in PAN precursors enhance graphitization via templating effect, as observed in reactive force field molecular dynamic simulations of carbonizing PAN [91]. Hence, carbonization of PAN in presence of CNTs/graphene increases graphitic order, while it will reduce the density of microscale defects (voids), and together with mechanical reinforcing effect of CNTs [16, 92-93], will enhance the mechanical properties of hybrid structures [11]. Moreover, the carbonization temperature is also an important parameter influencing the graphitic structure concentration, therefore mechanical performance [18], electrical conductivity [94] and piezoresistive effect [95] of CNF.

1.6 Multifunctional applications of CNF

Apart from the high potential mechanical properties of electrospun CNF, other physical properties of them have also been studied, such as electrical conductivity, thermal conductivity. For example, the electrical conductivity of individual carbon nanofiber is measured to be 2 S/cm for 973 K carbonization and will be increased to 7 S/cm for 1873 K carbonization [96]. The thermal conductivity of CNFs is measured to be 160 W/mK based on T-type individual nanofiber thermal conductivity measurement [97]. These properties and the coupling between the fields allows for the application of CNFs not just as structural elements but also as multifunctional components.

1.6.1 Energy storage

The application of CNFs and its composite in energy storage area has been widely investigated. Due to its outstanding electrical conductivity, large surface areas and structural stability, CNFs is thought to be a promising electrode materials to substitute the traditional graphite based electrode. Bonino, et al [98] fabricated the composite carbon-tin oxide nanofibers to be used as the anodes in lithium-ion battery, which exhibits higher discharge capacities than pure CNF and theoretical capacity of graphite. To further increase the surface area of the electrode, Ji, et al [99] developed porous CNF through resolving the SiO_2 nanoparticles embedded in the electrospun CNF/SiO_2 hybrid nanofibers with acid. The porous structure of the CNF provides an effective increase of the surface area of the electrode, therefore makes it to be a promising material for anodes in lithium-ion battery. Apart from the porous CNFs, hollow CNFs were also developed to

be applied as freestanding electrodes with better mechanical performance with large surface areas [100].

1.6.2 Sensing

The external stimuli induced property change of CNFs, especially electrical conductivity change, has been exploited to develop CNFs base sensors. The CNFs based electrical conductive elastomer nanocomposite was developed by Zhu, et al [101], which exhibits about 2-3 orders of magnitude in reversible resistivity at 120% strain. Moreover, CNFs surface-derivatized with various polymer brushes had also been developed as flexible gas sensor based on the electrical conductivity change due to the existence of the vapor [102]. Irritant gases, such as NH_3 or HCl can also be detected by CNF coated with thin layer of polypyrrole (PPy), due to reaction between PPy and the irritant gas induced composite electrical conductivity change.

1.6.3 Electromagnetic interference shielding

Due to the ability to absorb and reflect electromagnetic radiation, application of carbon nanofiber in electromagnetic interference (EMI) shielding has been developed by researchers in recent years. Hong, et al [103] successfully developed vapor grown CNF mats for EMI shielding, which exhibit effectiveness (shielding efficiency (SE), 52-81 dB, 1.5 GHz) and high SE/density (370-470 dB cm^3/g). Apart from pure CNF mats, introducing dielectric, magnetic or electrical conductive particles, such as titanium dioxide (TiO_2) and magnetite (Fe_3O_4) into the nanofiber will effectively improve the performance of the hybrid nanofiber mats [104]. The incorporation of magnetite nanofiller (Fe_3O_4) in electrically

conducting CNFs effectively increase both magnetic and dielectric losses, therefore, the EMI shielding performance of hybrid nanofiber mat. The EMI shielding performance of CNTs/CNF hybrid nanofiber has also been investigated, which shows thin CNFs sheets have a significant SE of >15 dB in the range of 300 MHz to 3 GHz [105].

1.7 Research objectives and outlines

Despite considerable studies on the processing-microstructure relationships in CNFs which are obtained by carbonization of as-electrospun PAN/CNTs composite nanofibers, the relationship between microstructure and properties of CNFs fabricated under the templating effect of graphitic nanoparticles such as CNTs is highly unexplored. That is partly rooted in experimental limitations in measuring the mechanical properties of nanostructures. Moreover, the processing-microstructure-property relationships in CNFs with CNTs inclusions needs to be revisited such that issues of chain alignment and CNTs alignment are addressed. In this regard, one of the lingering issues is how to align polymer chains effectively without inducing defects in the precursor via hot-drawing. Addressing these issues is the primary focus of this thesis, and it can set a foundation for the development of the next generation high strength nanoscale reinforcements for structural light-weighting. Hence, the overarching goal of this work is to unravel the processing-microstructure-property relationships in carbon nanofibers (CNFs) in which the formation of graphite-like structures (graphitization) is promoted under the templating effect of CNTs. The CNF properties of interest include mechanical properties and electromechanical couplings. To address the goal, we have identified three objectives:

Objective 1: Develop post-processing techniques to induce molecular chain alignment in PAN/CNTs electrospun hybrid nanofibers and investigate the effect of post-processing on microstructure and mechanical properties of nanofiber ribbons.

Objective 2: Research the effect of CNTs inclusions on microstructure, mechanical properties of hybrid CNFs in response on thermomechanical treatments on precursors.

Objective 3: Explore the relationship between microstructure and functional properties, such as electrical conductivity and piezoresistivity of CNFs for developing their multifunctional applications.

In chapter 2, the templating effect of CNTs on microstructure evolution and mechanical properties of the electrospun hybrid PAN/CNTs precursor nanofiber with different post-processing conditions was studied. To further broaden the application fields of PAN nanofiber and CNFs, the near-field electrospinning process was studied in chapter 3. From the experimental results in chapter 2 and 3, the basic processing-microstructure relationship in fabricating hybrid PAN/CNTs precursor nanofiber was obtained for ***Objective 1***. Then, in chapter 4, through applying the most promising precursor fabrication parameters, CNF and CNF/CNTs were obtained by carbonizing the precursor nanofibers from ***Objective 1***. In this chapter, based on the analysis of CNF microstructure evolution induced mechanical properties improvement, a clear path for fabricating high strength CNFs was developed. Moreover, the research on the effect of CNTs templating effect on microstructure and mechanical properties of CNF/CNTs hybrid nanofibers demonstrates the significant contribution of thermo-mechanical post-processing (hot-drawing) on

exerting templated graphitization effect of CNTs in CNF, which is for ***Objective 2.*** The experimental piezoresistivity testing of individual CNF in chapter 5 and multi-resolution continuum model developed in chapter 6, were applied to shed light on microstructure-functional properties relationship in CNFs, for exploring their multifunctional applied fields in ***Objective 3***. Therefore, together with recent developments in scalable electrospinning methods, this research brings about a clear processing-microstructure-electromechanical performance relationship, which can set the foundation for the development of low-cost high performance multifunctional nanoscale reinforcements.

2. FABRICATION OF PAN/CNTs PRECURSOR AND ITS MICROSTRUCTURE EVOLUTION[*]

Mechanical properties of carbonized micro and nanofibers is highly influenced by the microstructure of their precursor in relation to the precursor processing parameters. Therefore, major efforts have been devoted to engineering the microstructure of precursors. These efforts often are intended to enhance the chain alignment in precursors, which is a prerequisite for higher graphitic alignment in carbonized structures. The most abundantly used precursor of CNFs is polyacrylonitrile (PAN) which is fabricated via solution electrospinning. Moreover, electrospinning can provide a platform to add graphitic nanoparticles such as CNTs to the PAN precursor to influence the microstructure of the obtained electrospun nanofiber, through factors such as templating effect of CNTs for the PAN chains and changes in the solution properties. A down side of electrospinning in generating CNF precursors however is that the polymer chain alignment within the as-electrospun nanofiber is much lower than the gel- or wet-spun PAN precursors used to fabricate CF in industry. The lower chain alignment in as-electrospun PAN precursors is an inherent feature of electrospinning process, which is caused by factors such as fast solvent evaporation that suppresses chain mobility.

[*] Part of this chapter is reprinted with permission from "Microstructural evolution and mechanics of hot-drawn CNT-reinforced polymeric nanofibers" by J. Cai, S. Chawla, M. Naraghi. Carbon. 2016;109:813-822.

In this chapter, microstructural changes in electrospun PAN/SWNT nanofibers induced due to a combined effect of SWNT inclusions and hot-drawing has been studied for the first time. The latter was mainly intended to enhance chain alignment in the presence of CNTs. The microstructural evolution of various PAN/SWNTs hybrid nanofibers with increasing hot-drawing ratio were analyzed by exploring polymer crystal structures, polymer chain alignment and SWNTs orientation. Through these analysis, a clear understanding of the effect of SWNTs concentration and draw ratio on microstructure of SWNTs reinforced semicrystalline polymer precursor was obtained. Combined with mechanical tests on PAN/SWNT ribbons, a structural and reinforcement mechanism of hybrid nanofiber is proposed. The thorough analysis of precursor microstructure evolution provides a solid foundation for improving mechanical properties of electrospun CNF through controlling its microstructure.

2.1 Experimental

2.1.1 Fabrication of ribbons of PAN/SWNT composite nanofibers

Ribbons of PAN/SWNT composite nanofibers were fabricated by electrospinning, Fig.2.1(a). Different contents of single walled carbon nanofibers (SWNTs) obtained from OCSIAL LLC (diameter: 1.8 ± 0.4, length: ≥ 5um) corresponding to 0.1-0.5 wt.% of SWNTs relative to PAN were dispersed in dimethylformamide (DMF) (Sigma–Aldrich) via 24 hrs ultrasonication. After a visually homogeneous SWNTs/DMF solution was obtained, polyacrylonitrile (PAN) powder from Sigma–Aldrich with molecular weight of 150,000 g/mol was dissolved into SWNTs/DMF to obtain a 10 wt.% solution (PAN in DMF). The SWNT content significantly influenced the electrospinning process by altering

the solution viscosity and electrical conductivity. Hence, the feeding rates of the polymer solution during electrospinning was adjusted within 0.6 ml/h to 2.0 ml/h for solutions with different SWNT contents with the goal of obtaining stable electrospinning jet. As shown in Fig.2.1(b), highly aligned polymer nanofibers ribbon were obtained by using a rotating disk collector with a peak-up velocity of ~5.7 m/s at electrospinning voltage and distance of 25 kV and 20 cm, respectively.

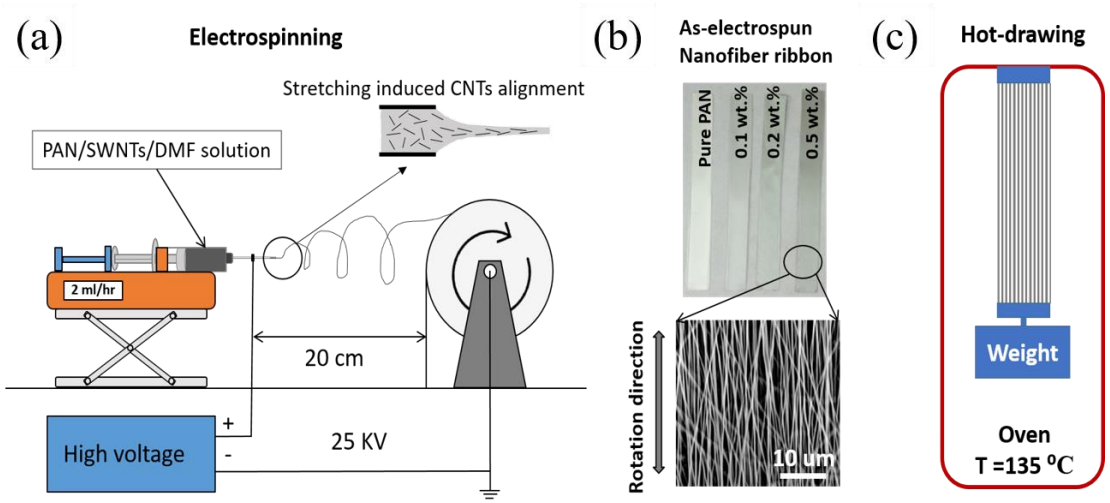

Figure 2.1. (a) Electrospinning experimental set-up and **(b)** obtained aligned PAN/SWNTs nanofiber ribbons and **(c)** hot-drawing setup of nanofiber ribbon.

2.1.2 Hot-drawing of PAN/SWNT nanofiber ribbons

The electrospun PAN/SWNT nanofiber ribbons were subjected to hot drawing, as shown in Fig.2.1(c). To this end, the as-spun PAN/SWNTs nanofiber ribbon were stretched by applying hanging weights equivalent to 19 MPa engineering stress at 135 °C

environment in an oven. When the draw ratio reached a desired value (λ = 2 and 4, λ is the hot-drawing ratio, which equals to the final length of ribbon divided by initial length), the stretched ribbon were cooled down to room temperature in the oven. The diameters of PAN/SWNTs nanofiber were measured by using FEI Quanta 600 FE-SEM with at least 50 measurements.

2.1.3 Material characterization of PAN/SWNT nanofibers

Glass transition temperature of PAN/SWNTs nanofiber was obtained by using a differential scanning calorimeter (DSC) TA Q20 with 10 °C/min heating rate, from room temperature to 150 °C. The X-ray diffraction spectrum of PAN/SWNT ribbons (XRD) (CuKα, wavelength of 0.154 nm) were obtained using GADDS BRUKER-AXS MWPC 3-thircle X-ray Diffractometer. Diffraction patterns were analyzed by using Origin 9.0. The crystallinity was calculated based on the relative areas under the deconvoluted amorphous and crystalline peaks [71]. The PAN crystal size is also calculated by using Scherrer's equation (K = 0.9). The orientation of the PAN chains in the crystalline phase was determined based on the azimuthal scans of the diffraction peak at $2\theta \approx 17°$ [106]. The alignment of crystals was quantified for comparison purposes between different fabrication conditions as $f_C = \frac{180-FWHM}{180}$, where FWHM corresponds to the full-width at half maximum value of the crystalline peak [66]. Polymer chain molecular orientation was measured by using polarized FT-IR (Thermo Nicolet 380, wave length range 300-3000 cm^{-1}) method [27]. In this method, polarized IR beam was irradiated on the aligned PAN/SWNTs nanofiber ribbons, and the transmission spectrums were acquired for two

polarization conditions in which the plane of polarization of the incident light was parallel and perpendicular to the fiber direction. The orientation factor of polymer chains, f, was calculated as [27]:

$$f = \frac{3}{2} < cos^2\sigma > -\frac{1}{2} = \frac{(D-1)(D_0+2)}{(D_0-1)(D+2)} \text{ with } D = \frac{A_{\parallel}}{A_{\perp}} \; and \; D_0 = 2cot^2\alpha \qquad (2.1)$$

where σ is the average angle between fiber axis and backbone direction of PAN molecule, and α is the angle between nitrile group in PAN and its backbone direction, approximated as 70°. Therefore, the orientation factor, *f*, qualitatively representing the orientation of PAN molecular backbone, lies between 0 and 1, corresponding to totally random and fully aligned polymer chains with respect to the fiber axis. The obtained orientation factor of polymer chain was the averaged value of three measurements.

2.1.4 Characterizing SWNT alignment in PAN/SWNT nanofibers

Orientation factor of SWNTs in PAN/SWNTs was obtained through polarized Raman spectroscopy by using Horiba Jobin-Yvon LabRam Raman Confocal Microscope with a He-Ne laser. For materials containing SWNTs, polarized Raman spectroscopy is an effective method to qualitatively characterize the orientation of SWNTs [64, 66]. The intensity of the Raman peak is a sum of contributions from all SWNTs within the composite. In this work, a simple and rather qualitative parameter, $f_{SWNTs} = 1 - \frac{I_{HH}}{I_{VV}}$, was used to compare alignment of SWNTs between different fabrication conditions, in which I_{HH} and I_{VV} corresponds to Raman intensities of HH and VV configurations, where the incident and scattered laser are both perpendicular and parallel to the fiber axis,

respectively. The obtained orientation factor of SWNTs is the averaged value of three measurements in each fabrication condition.

2.1.5 Mechanical characterization of ribbons

The mechanical properties of PAN/SWNT ribbons were measured in tension by using Gatan MT10365 tensile testing device. The gage length was 5 mm and crosshead speed of loading was 0.2 mm/min. For each fabrication condition, a minimum of three experiments were tested and the average values of the properties were reported. The stress applied on the sample was calculated by dividing the force by the true fiber area, which was estimated as the ratio of the linear density of the ribbon and the density of solid PAN [107]. Considering the high alignment of nanofibers in the ribbon, the obtained mechanical properties of ribbons are a measure of the average properties of individual polymer nanofibers.

2.2 Results and discussion

Aligned PAN/SWNTs nanofiber ribbons were electrospun on a rotating metal target. As shown in Fig.2.1(a), the as-fabricated nanofibers are well aligned with the rotating direction of the target, which sets the foundation for polymer chain alignment characterizations in our study. Addition of SWNTs in general led to thicker nanofibers. For instance, as shown in Fig.2.2, the diameter of the pure PAN nanofibers was 314±58 nm, comparable to 0.1 wt.% PAN/SWNTs nanofibers diameter of 312 ± 64 nm, shown in Fig.2.3, and 0.2 wt.% PAN/SWNTs nanofibers diameter of 436 ± 92 nm, shown in Fig.2.4,

while 0.5 wt.% PAN/SWNTs nanofibers are considerably thicker (diameter of 538 ± 86 nm) (Fig.2.5).

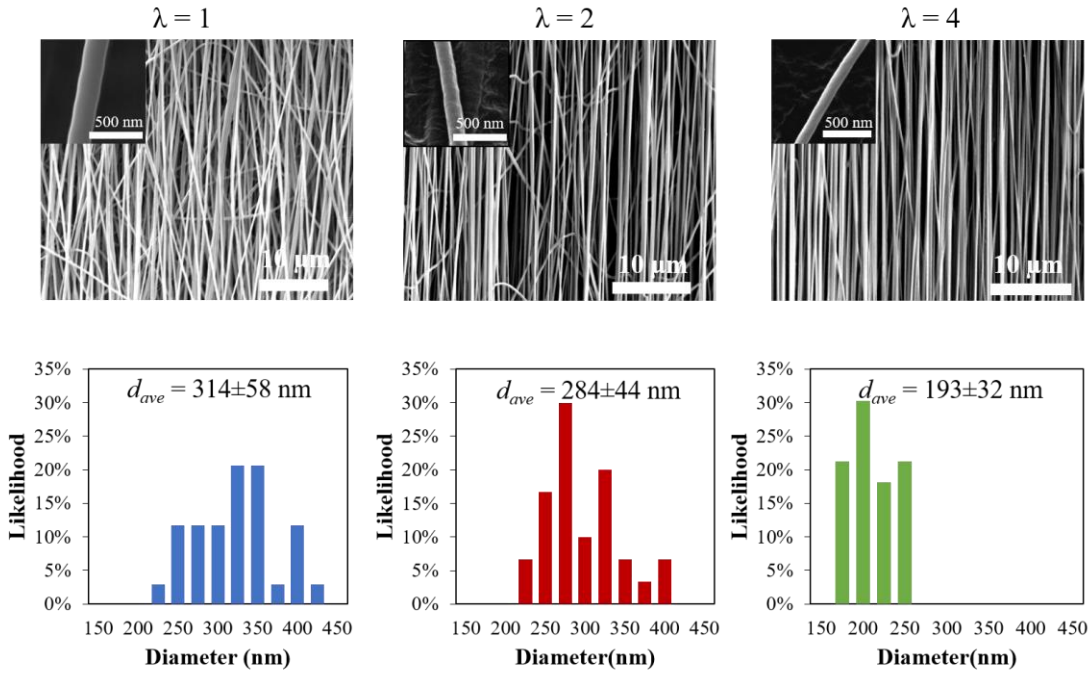

Figure 2.2. Pure PAN ribbon SEM images and nanofiber diameter distribution with different hot-drawing ratios.

The formation of the thicker nanofibers at higher SWNT concentrations can be partly attributed to the increase in the viscosity of the electrospinning solution with the addition of SWNTs (Fig.2.3-2.5). Further insight, however, was obtained by considering the variations of the diameters of nanofibers with different SWNT contents as a result of hot-drawing. To this end, ribbons of aligned nanofibers were subjected to hot-drawing above the T_g of PAN. We studied three stretch ratios of λ = 1 (as-fabricated), λ = 2 and λ = 4. The stretch ratio was defined as the final length of the ribbon to its initial length.

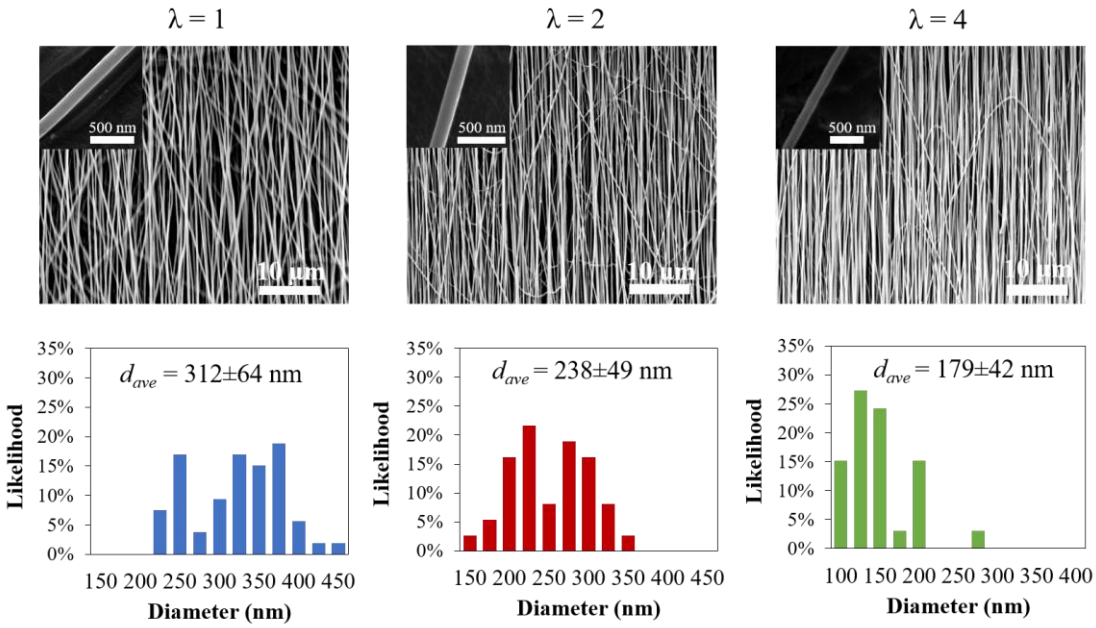

Figure 2.3. 0.1 wt.% PAN/SWNTs ribbon SEM images and nanofiber diameter distribution with different hot-drawing ratios.

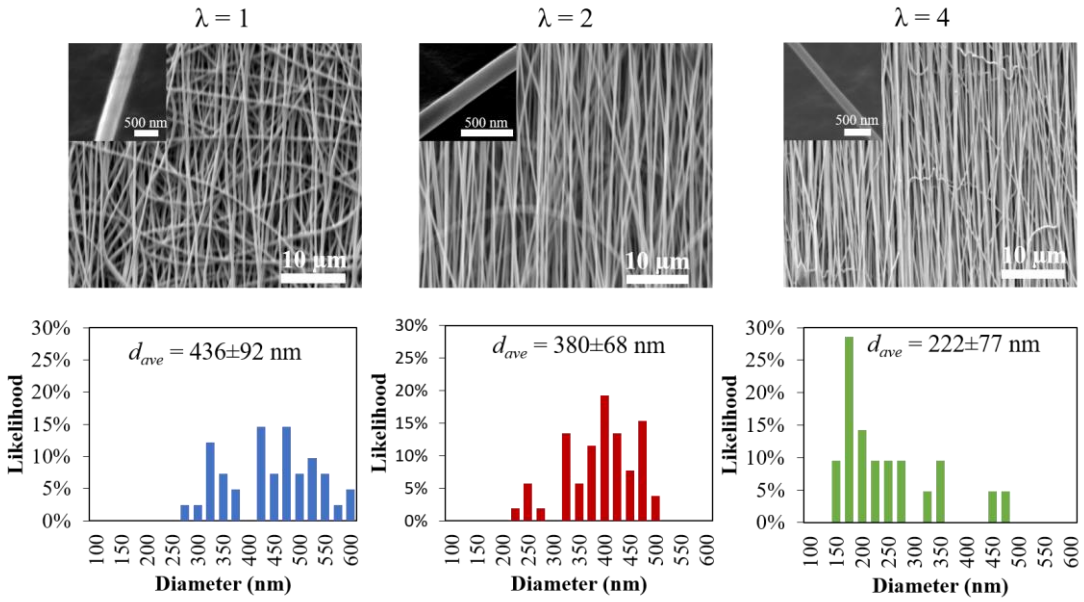

Figure 2.4. 0.2 wt.% PAN/SWNTs ribbon SEM images and nanofiber diameter distribution with different hot-drawing ratios.

An SEM image of the as electrospun ribbon of pure PAN nanofibers is shown in Fig.2.2, demonstrating the high degree of alignment of pure PAN nanofibers, achieved via electromechanical forces during electrospinning. As increasing the concentration of the SWNTs in polymer solution, there is an increase in the polymer solution charge density. Therefore, during the electrospinning process, the repulsive force between solidified nanofibers on target which still has some residual electrical charges and the polymer solution jet makes the obtained polymer nanofiber to be less aligned, shown in Fig.2.5. As increasing the hot-drawing ratios, the aligned polymer nanofibers are obtained.

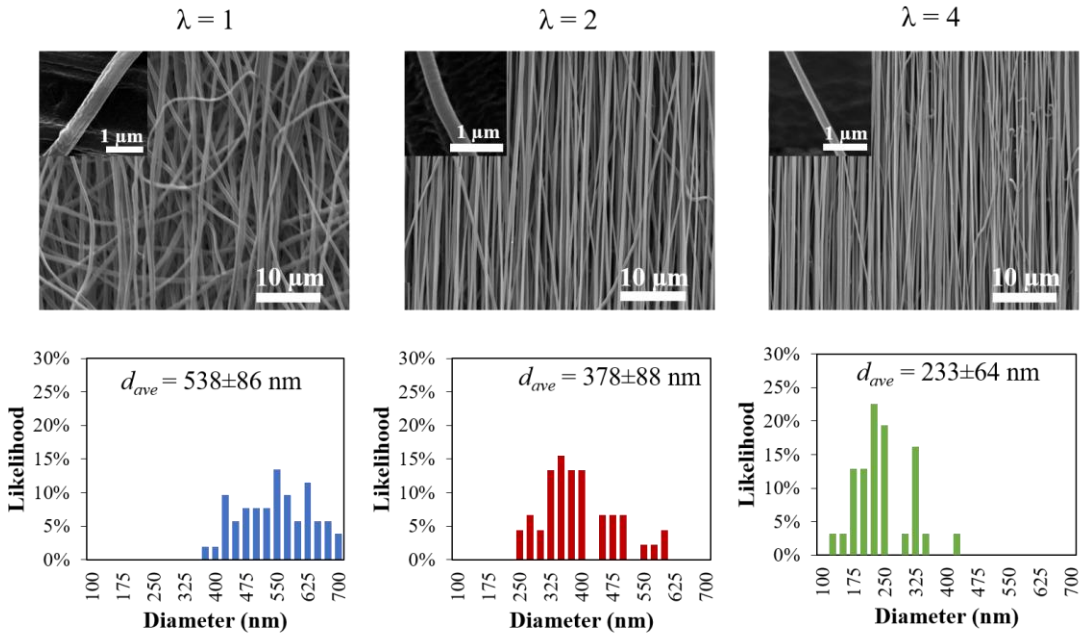

Figure 2.5. 0.5 wt.% PAN/SWNTs ribbon SEM images and nanofiber diameter distribution with different hot-drawing ratios.

The ratio of the volume of the nanofibers before and after hot-drawing can be calculated as $\lambda(d_f/d_i)^2$, where d_i and d_f are the average diameter of the nanofibers before and after drawing, respectively. According to this analysis, the deformation of the nanofibers during hot-drawing is *not entirely* volume-preserving, and can lead to both volume dilatation and shrinkage, depending on the concentration of the SWNTs. For instance, the average diameter of as-electrospun 0.1 wt.% PAN/SWNTs nanofiber decreases from 312±64 nm to 179±42 nm by hot-drawing to stretch ratio of λ=4, respectively, shown in Fig.2.6. This is despite the fact that a perfectly volume preserving drawing would require a reduction of average fiber diameter from 312 nm in the as-electrospun ones to 156 nm. These theoretical predictions of the diameter based on volume preserved deformations are slightly lower than the measured corresponding value, suggesting void formation and volume dilatation (by ~31%) during hot drawing. Similar void formations at stretch ratios above 2 have also been observed in cold-drawn PAN nanofibers [108]. On the other hand, the ratio of the volume of as-electrospun nanofibers with 0.5 wt.% SWNTs (after to before hot-drawing) is 0.75, indicating a marked reduction in volume, by as much as 25%. This considerable reduction in diameter of the nanofibers with 0.5 wt.% SWNTs can only be possible if we assume that the chains in the as-electrospun nanofibers were highly unpacked, with nanoscale porosities between chains. In other words, at such high concentrations of SWNTs, the fillers (and even potentially the agglomerates of the fillers) can act as spacers between polymer chains. With this analysis, the thicker diameter of the as-electrospun nanofibers with SWNT concentrations of ~0.5 wt.% is attributed to the low packing density of polymer chains, where further

packing is prevented by the presence of stiff SWNTs. More evidence in support of the unpacked structure of PAN chains can be found by considering the glass transition in composite nanofibers, as discussed in the following section.

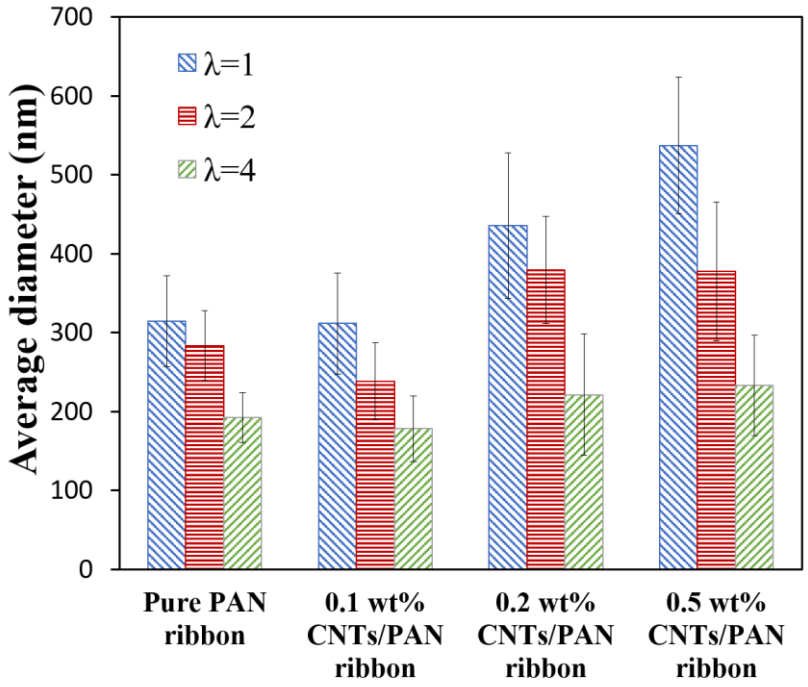

Figure 2.6. Average diameters of PAN/SWNTs with different SWNTs concentrations and hot-drawing ratios.

2.2.1 Effect of SWNT inclusions on glass transition temperature of PAN nanofibers

As shown in Fig.2.7, DSC measurements point to a ~2.5°C increase in the T_g of PAN nanofiber with the addition of 0.1 wt.% SWNTs from 105.6°C to 108.9 °C, likely

due to SWNT confinement effects on PAN chains and the consequent restricted mobility of the chains [106]. However, further increase in the SWNT content from 0.1 wt.% to 0.2 wt.% and 0.5 wt.% seems to slightly lower the T_g of the composite nanofibers, although all the composite fibers tested had a T_g higher than the neat polymers.

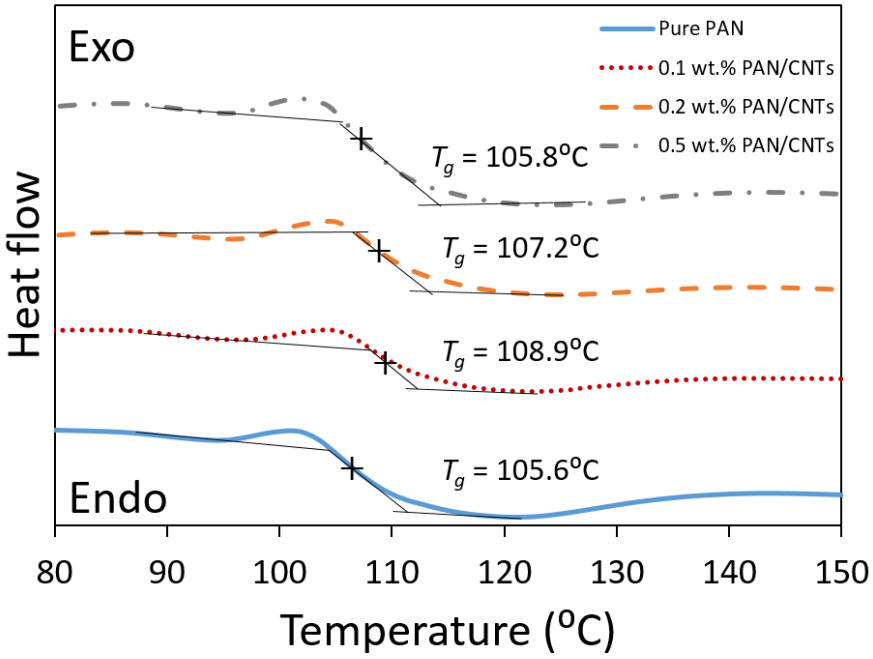

Figure 2.7. DSC results of PAN/SWNTs ribbons with different SWNTs concentrations.

The reduction in T_g of PAN/SWNT fibers by increasing the SWNT content beyond 0.1 wt.% indicates lower interactions between SWNTs and polymer chains (lowered SWNT confinement effect) despite the apparent increase in SWNT content. This is partly an indirect indication of poor SWNT dispersion or SWNT agglomeration [109]. The

reduction in the T_g of composites with the addition of SWNTs due to SWNT agglomeration has also been observed in macroscale polystyrene/SWNT nanocomposites [110]. However, due to minute dimensions of the sample, sample preparation for TEM imaging, as a means to directly detect agglomerations was not pursued. The reduction in T_g of composite nanofibers can also be partly attributed to the low packing of polymer chains, as a result of which the interaction between PAN chains is lowered.

2.2.2 Effect of hot-drawing on microstructure of PAN/SWNT nanofibers

In addition to diameter changes, post-fabrication drawing can drastically alter the alignment of polymer chain and SWNTs. The alignment of polymer chains was measured in this work by using polarized FT-IR and was expressed in terms of the Herman orientation factor, *f*, as discussed in the Experimental section. As shown in Fig.2.8, the orientation factor of the as-electrospun nanofibers, regardless of SWNT content, is rather low in the range of 0.30-0.54. This chain alignment is induced by electrostatic and mechanical forces applied on polymer solution during electrospinning. Moreover, among as-electrospun PAN/SWNT nanofibers, the orientation factor of polymer chains in 0.1 wt.% PAN/SWNTs nanofibers is slightly lower than the pure PAN nanofiber. That is potentially caused by the reduced mobility of the chains due to the obstructive effect of SWNTs during the electrospinning process. The reduced chain mobility due to the presence of 0.1 wt.% SWNTs in PAN nanofibers also corroborates with the increased T_g of the 0.1 wt.% PAN/SWNTs nanofibers observed in section 2.2.1. It is also interesting to note that further addition of SWNTs leads to a higher chain alignment, such that the orientation factor increases from 0.30 for 0.1 wt.% PAN/SWNTs nanofibers to 0.54 for

0.5 wt.% PAN/SWNTs nanofibers, respectively. This considerable increase in chain alignment by increasing SWNT content from 0.1 wt.% to 0.5 wt.% can be explained based on the charge density of the SWNT containing polymer solution. In other words, the higher SWNT content facilitates the flow of charges within the jet due to high electrical conductivity of SWNTs. As a result, charge induction will be enhanced at higher SWNT contents, leading to increased electrostatic drawing by the electric field of electrospinning. Therefore, the as-electrospun nanofibers formed with higher SWNT contents showed higher chain alignment.

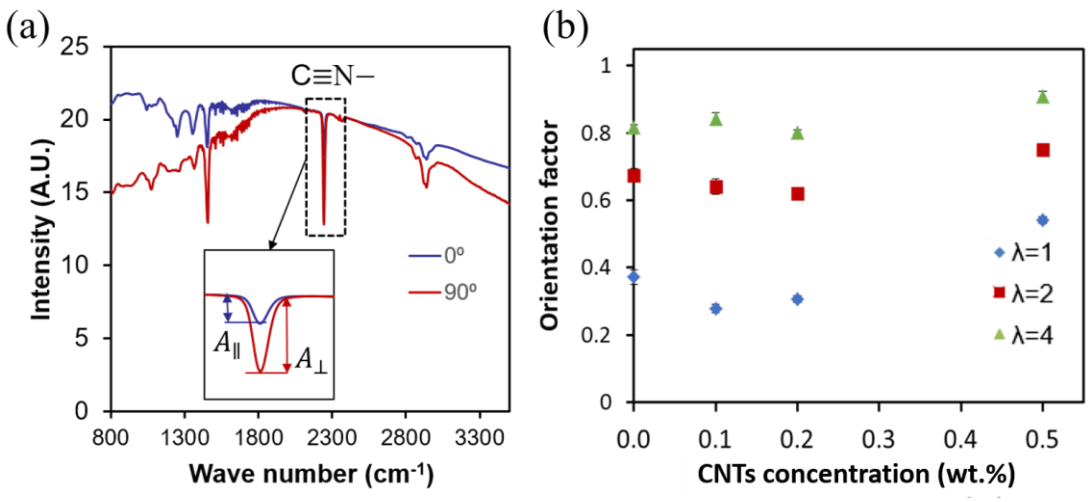

Figure 2.8. (a) Polarized FT-IR results of nanofiber ribbon and **(b)** orientation factors of polymer chain in polymer nanofiber with different SWNTs concentration and hot-drawing ratios.

Despite the rather low orientation factor of the as-electrospun nanofibers, hot-drawing can drastically improve the chain alignment for all SWNTs concentrations studied, Fig.2.8. For example, the orientation factor of PAN chains in pure PAN nanofibers increased from 0.37 to 0.82 as a result of hot-drawing to a draw ratio of 4. It is also interesting to note that the orientation factor of polymer chains in as-electrospun fibers shows a strong dependency on SWNT content, varying in a range of 0.28-0.54 with a relative change of as high as 90% (compare the case of 0.1 to 0.5 wt.% SWNT content). However, at a draw ratio of 2, the variation range of orientation factor is narrowed down and the relative change in orientation factor among samples with different SWNT contents

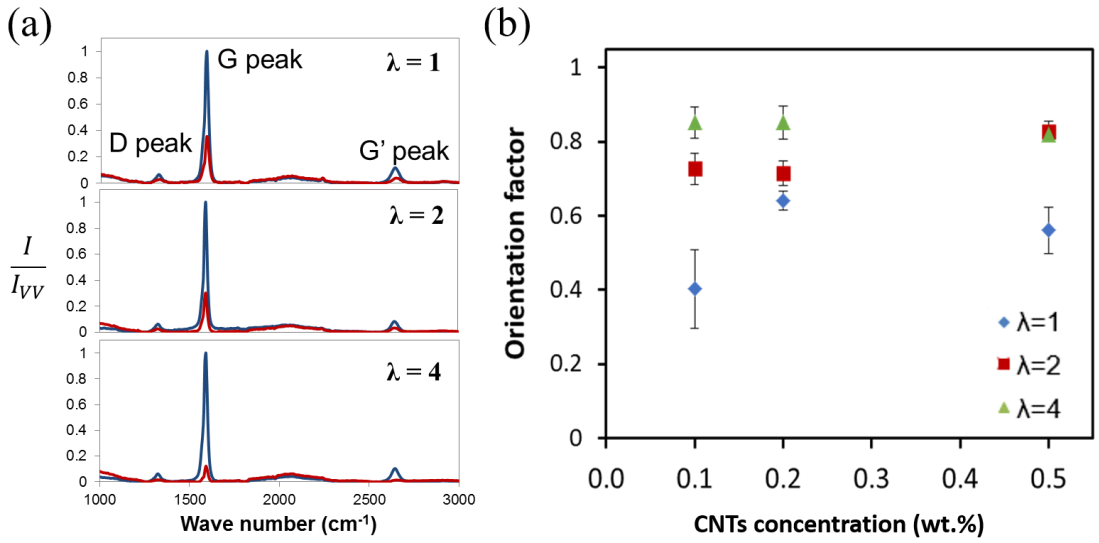

Figure 2.9. (a) Polarized Raman spectrum results of nanofiber and **(b)** orientation factor of SWNTs in polymer nanofiber with different SWNTs concentration and hot-drawing ratios.

drops to ~20%. Further drawing the fibers to a draw ratio of 4 drops the relative change to ~12%. Hence, the chain alignment in hot-drawn electrospun nanofibers is less dependent on the initial state of chains and more controlled by the post fabrication drawing.

Apart from the polymer chain alignment, alignment of SWNTs within the polymer nanofiber is also influenced by the electromechanical and thermomechanical loads applied on fibers during electrospinning and subsequent hot-drawing. In other words, the flow of the polymer solution during electrospinning and the elongational and shear strains applied to the fibers during drawing has the tendency to align the SWNTs with the fiber axis. As discussed previous section, the alignment of SWNTs within the aligned bundle of nanofibers was measured via polarized Raman spectroscopy and was expressed as $f_{SWNTs} = 1 - \frac{I_{HH}}{I_{VV}}$, in which I_{HH} and I_{VV} corresponds to Raman intensities of HH and VV configurations. As shown in Fig.2.9(b), the as-fabricated 0.1 wt.% PAN/SWNTs nanofibers has the lowest SWNTs orientation factor. This result is expected from the reduced polymer chain mobility which was inferred from the increased T_g of 0.1 wt.% PAN/SWNTs nanofibers. In other words, chain mobility which facilitates chain and SWNT reorientation during electrospinning is considerably lost with the addition of well-dispersed 0.1 wt.% SWNTs.

However, among hot-drawn samples which contain SWNTs, the SWNT alignment is slightly higher than the rest in nanofibers which contain 0.1 wt.% SWNT compared to nanofibers with 0.2 and 0.5 wt.% SWNTs. In other words, hot-drawing is more effective in aligning SWNTs in low SWNTs concentration nanofiber. Hence, there

is an increased resistance to reorientation of SWNTs in samples with 0.2 and 0.5 wt.% SWNT content potentially due to direct interactions between SWNTs within SWNT agglomerates in these samples. It is to be pointed out that the highest Raman intensity ratio ($\frac{I_{VV}}{I_{HH}}$) achieved is about 6.7, significantly smaller than the conventional gel spun fiber of about 38, with drawing ratio ≈ 51 [71].

The alignment of polymer chains, during electrospinning and subsequent hot-drawing, facilitates the formation of the crystalline structure of PAN nanofiber. The crystalline phase in PAN nanofibers not only may contribute to high mechanical performance [71], but also facilitated the formation of turbostratic domains in PAN during pyrolysis [89]. Therefore, understanding the crystalline structure in PAN/SWNTs hybrid nanofiber is crucial in the development of nanofibers with high mechanical properties. The crystallinity in PAN nanofibers was studied via X-ray diffraction as a function of SWNTs content and drawing. As is shown in Fig.2.10 (a), no sharp peak which would be reminiscent of crystallinity, is observed in the as-electrospun PAN nanofibers. Hence, the degree of crystallinity in the as-fabricated fibers is considered to be negligible. Thus, it is concluded that the chain alignment which was achieved during electrospinning (see for instance Fig.2.8) was not sufficient to trigger crystallization within the as-electrospun PAN nanofibers. While the electromechanical forces of electrospinning tend to align the chains by inducing elongational flows, massive solvent loss during the formation of solid fibers can suppress chain mobility and prevent the formation of the crystals, which evident limits the mechanical properties of the as-electrospun PAN nanofibers. In contrast to as-

electrospun nanofibers, after applying hot-drawing, the hot-drawn nanofibers show a sharp crystalline peak at $2\theta \sim 17°$, corresponding to the (100) plane in PAN polymer chain hexagonal packing.

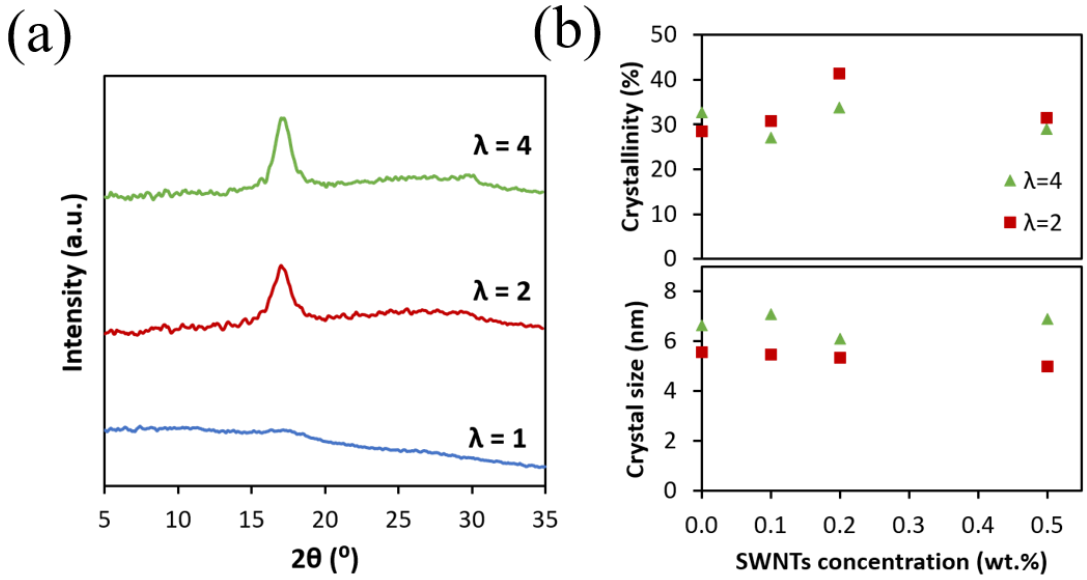

Figure 2.10. (a) WAXD curves obtained for 0.1 wt.% PAN/SWNTs ribbon and **(b)** calculated crystallinity and crystal size for different SWNTs concentrations and hot-drawing ratios.

The degree of crystallinity and the crystal size of polymer nanofiber with different SWNTs concentrations, corresponding to the diffraction angle of $2\theta \sim 17°$ in the x-ray pattern were also calculated as discussed in section 2.1.3. As shown in Fig. 2.10(a) & (b), the degree of crystallinity and the size of crystals significantly increases with drawing, and

to a lower degree it is also a function of SWNT content. By drawing the samples to λ = 2 and λ = 4, the degree of crystallinity in all samples increases to ~30-40%. The highest crystallinity is observed at a SWNT content of ~0.1-0.2 wt.%, which can be attributed to epitaxial growth of crystalline domains of PAN around SWNTs [83]. On the other hand, further increase in SWNT content to 0.5 wt.% lowers the crystallinity due to lowered interface area between SWNTs and polymer chains, therefore lowering the epitaxial growth of crystalline domains.

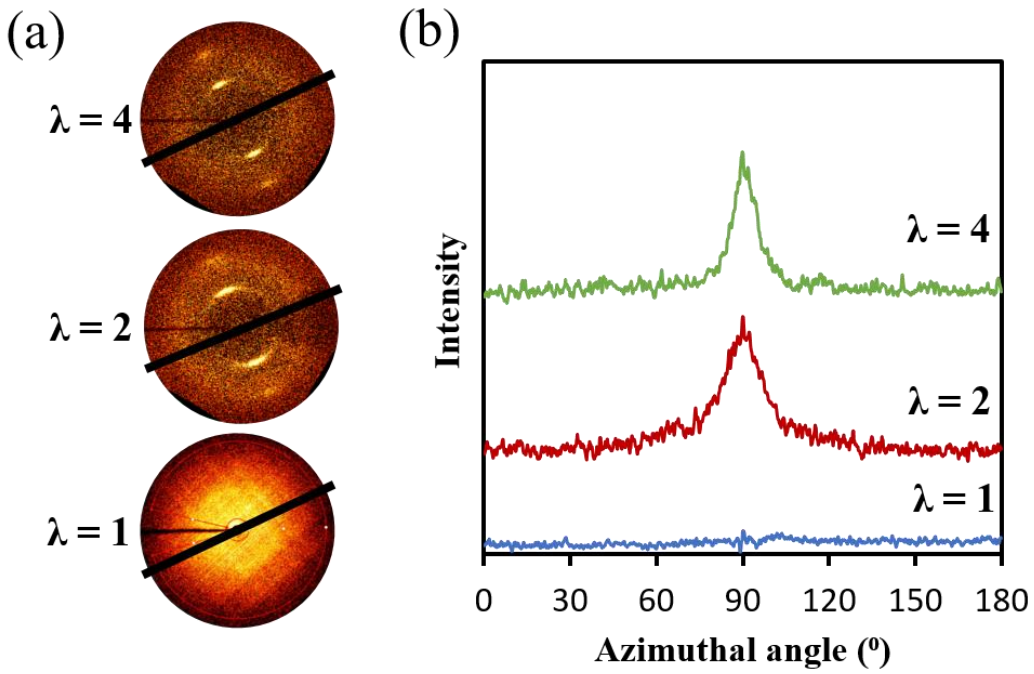

Figure 2.11. (a) 2D diffraction pattern from WAXD with a black line showing fiber direction and **(b)** azimuthal intensity scan of 0.1 wt.% PAN/SWNTs nanofibers with different SWNTs concentration and hot-drawing ratios.

It is also interesting to note that the size of the crystals in samples drawn to λ = 4 is systematically, although slightly, larger than those of λ = 2. Moreover, as shown in the 2D diffraction pattern of PAN/SWNT obtained via WAXD, such as the one shown in Fig.2.11(a), the crystalline peaks are observed at azimuthal angles of ±90° with respect to fiber axis. Thus, the polymer chain backbones in the crystalline phase is laid parallel to the fiber axis. Hence, the formation of this crystalline phase can be attributed to the drawing-induced alignment of polymer chains, which facilitates the packing of polymer chain along the fiber direction.

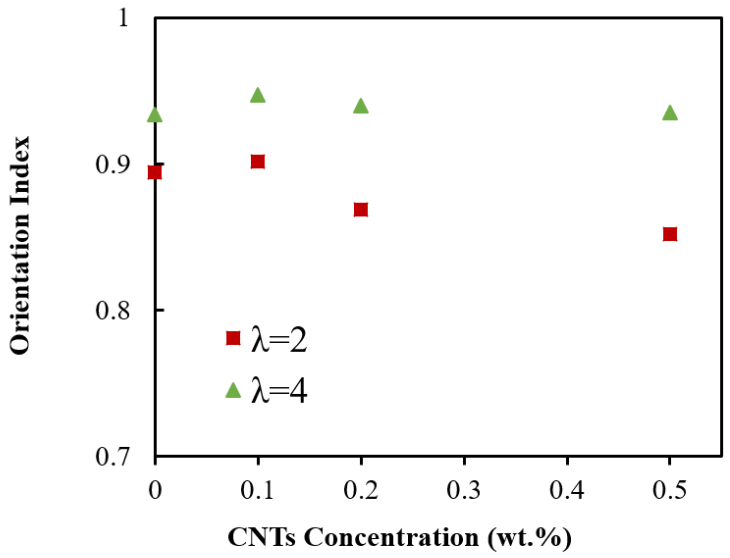

Figure 2.12. Crystalline phase orientation factor with different SWNTs concentration and hot-drawing ratios.

While the degree of crystallinity seems to reach a plateau at a draw ratio of 2 with no further increase by drawing to a draw ratio of 4, Fig.2.12, the orientation of crystalline domains in PAN/SWNTs nanofiber monotonically increases with the draw ratio in all nanofibers with different SWNTs contents. Hence, it is concluded that the formation of the crystalline domains as a result of hot-drawing reaches a limit near or before $\lambda = 2$, controlled for instance by the loss of segmental chain mobility in the transitional regions in between crystalline domains. In samples which were drawn to $\lambda = 4$, further drawing results in higher alignment of the already formed crystals with the drawing direction.

2.2.3 Mechanical performance of PAN/SWNT ribbons

Mechanical properties of PAN/SWNTs ribbons with various SWNT contents and different hot-drawing ratios were measured in tension using the setup discussed in section 2.1.5. Typical stress-strain curve for 0.1 wt.% PAN/SWNTs ribbons are shown in Fig.2.13(a). The elastic modulus, strength and energy to failure of ribbons were measured from the stress-strain curves as respectively the slope of the curve at strains below 2%, the maximum stress the sample has experienced during loading, and the energy to failure per unit mass of the ribbon. Given the viscoelastic behavior of polymer nanofibers [108], these properties are expected to slightly depend on strain rate, and as such their relative values among samples with different processing parameters is emphasized here. The as-electrospun samples demonstrate a nearly elastic-perfectly plastic behavior to engineering strains as high as 50%. However, upon hot drawing to draw ratios of 2 and 4, the samples become stiffer and stronger, while their ductility drops to as low as ~10-15%.

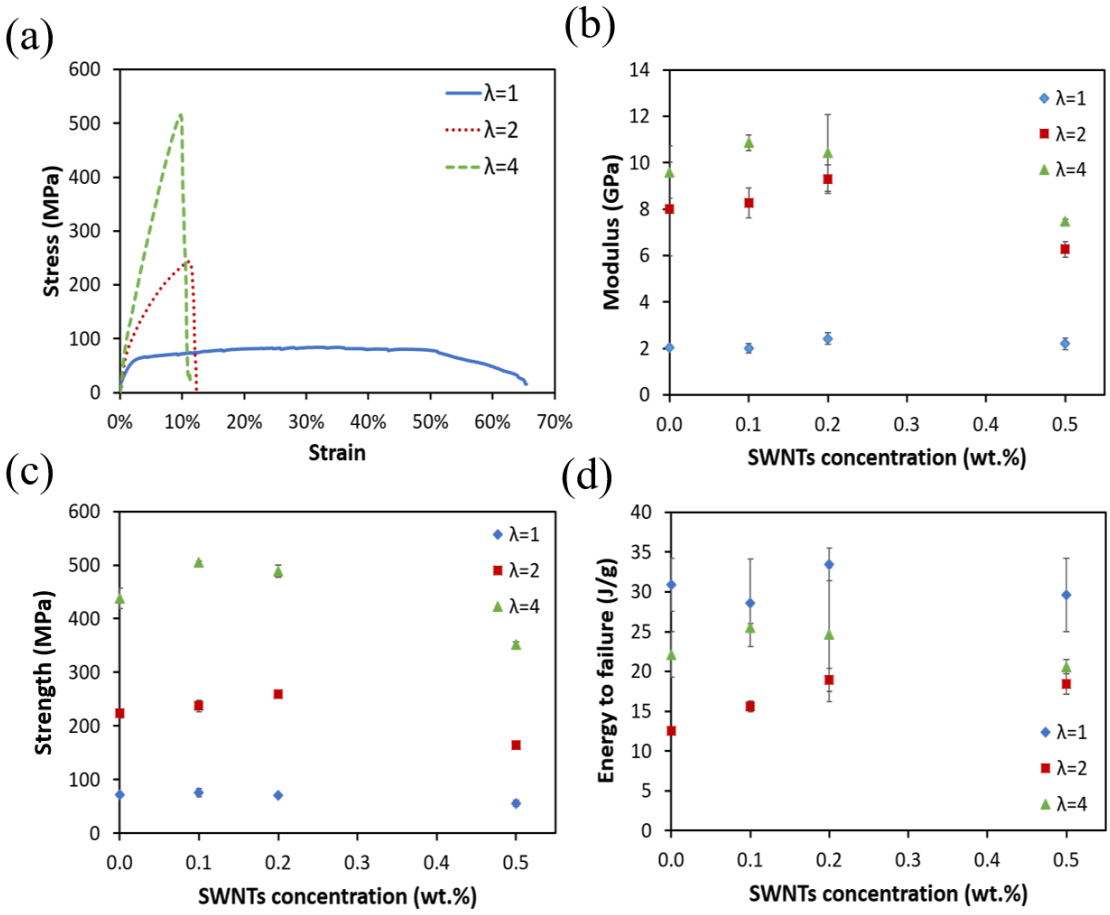

Figure 2.13. (a) Typical stress-strain curve for 0.1 wt.% PAN/SWNTs nanofibers, **(b)** modulus **(c)** strength and **(d)** energy to failure(J/g) for PAN/SWNTs nanofibers ribbons with different SWNTs concentrations and hot-drawing ratios.

The monotonic increase in strength and modulus with draw ratio can all be attributed to enhanced alignment of polymer chains and degree of crystallinity which also scales with draw ratio as evident from polarized FT-IR and XRD studies. Moreover, there is an evident correlation between the chain alignment and degree of crystallinity with sample ductility [66]. That is, the as-fabricated samples with low degree of crystallinity and

chain alignment show ductility of as high as 50%, while both types of hot drawn samples (draw ratio of 2 and 4) have higher degrees of crystallinity (~30-40%) and lower ductility (10-15%). Hence, the loss in ductility in hot-drawn samples is likely caused by the alignment polymer chain and the formation of the crystalline structures. In other words, as the crystals form, the chains get anchored in the crystalline domains, and their mobility is lost. The loss in ductility, caused by limited chain mobility, lowers the energy to failure in hot-drawn samples especially at $\lambda = 2$. However, part of the loss in energy to failure is recovered by further hot-drawing the samples to $\lambda = 4$, mainly due to higher chain alignment which also leads to higher strength.

It is also worth noticing the dependence of mechanical properties on SWNT contents. In the as-fabricated nanofibers, no clear dependence of mechanical properties on SWNT is found. That is likely due to the low alignment of SWNTs within nanofibers (Fig. 2.9), which lowers the contribution of SWNTs to overall load bearing in the fibers. However, in the hot-drawn samples, the SWNTs are considerably more aligned (Fig.2.9), hence, they carry load more effectively in the matrix. For instance, as shown in Fig.2.13(b), the addition of 0.1 wt.% SWNTs to pure PAN increases the modulus of hot-drawn nanofibers ($\lambda = 4$) from 9.6 GPa to 10.9 GPa. The comparison between the two moduli, a result of the addition of 0.1 wt.% SWNT with high degree of SWNT alignment along the fiber axis, allows us to calculate an "effective elastic modulus of SWNTs", also known as the modulus reinforcement efficiency. This factor is defined as the relative change in the modulus of the composite material per unit volume of the SWNTs (dY_c/dV_f) [109]. Accordingly, the efficiency factor of modulus of fillers in the case of the samples

with 0.1 wt.% SWNTs is calculated to be about 2.1 TPa, shown in Fig.2.14(a). This value, among the highest values reported in SWNT reinforced nanocomposites [109], is much larger than the theoretical modulus of SWNTs (~ 1TPa), indicates the formation of polymeric interphases around SWNTs with enhanced microstructure, such as crystallinity, and crystalline domain alignment. The interphase is likely the result of templating effects of SWNTs facilitated by strong SWNT-polymer chain interactions, as a result of which polymer sheath layers can form around SWNTs. An example of the polymeric sheath forming around SWNTs is shown in TEM image of a protruded SWNTs (Fig.2.14(b)), in which the sheath is ~5 times thicker than the diameter of individual SWNTs of ~2 nm [109, 111].

Despite the high efficiency of modulus reinforcing effect at 0.1 wt.% SWNT content, the dY_c/dV_f of 0.2wt.% and 0.5 wt.% are 0.71 and -0.71 GPa, respectively, suggesting a loss in reinforcement effect of SWNTs at higher than 0.1 wt.% SWNT content, potentially due to the agglomeration of SWNTs which lowers polymer interphase area. The highest measured value of dY_c/dV_f of SWNT in this work is even higher than the corresponding value of microfiber with 1 wt.% SWNTs (1.1 TPa) [71], demonstrating the effectiveness of the combination of electrospinning and hot-drawing in developing high reinforcement effect of SWNT in polymer nanofibers.

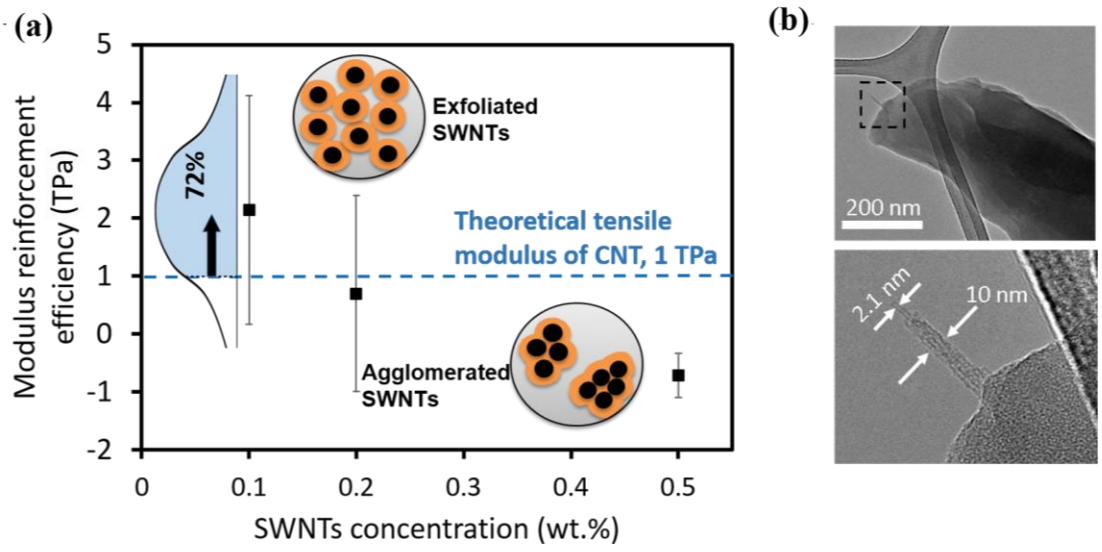

Figure 2.14. (a) Calculated modulus reinforcement efficiency of SWNTs for PAN/SWNTs with λ=4 and schematic description of effect of SWNT dispersion on interphase area, in which black circles represent SWNTs, gray regions represent bulk PAN nanofiber matrix, and orange regions represent highly ordered interphase regions, **(b)** TEM image of a protruded SWNT with polymer sheath around it, pointing to the strong interactions between SWNTs and the polymer. The region shown in a dotted box in the top figure is shown in higher magnification in the bottom image.

The highly ordered polymer interphase is originated from the strong interactions between the nitrile group on PAN and surface of CNTs, which have been demonstrated both by molecular dynamic simulation [112] and experimental observation [50]. Mobility of polymer chain around CNTs surface is strongly restricted, which increases the mechanical properties of polymer along the fiber axis direction and facilitates the formation of highly ordered polymer interphase. Moreover, the improved polymer chain alignment along fiber

axis direction obtained from hot-drawing also promotes the formation of this interphase. The modulus of the polymer interphase could be interpreted by applying a three-phase rule of mixture equations for composite fiber, as follows,

$$E_{hybrid} = E_{CNTs}V_{f,CNTs} + E_{Interphase}V_{f,Interphase} + E_{Matrix}V_{f,Matrix} \quad (2.2)$$

where E_{hybrid} is the modulus of the whole hybrid PAN/CNTs nanofiber, E_{CNTs}, $E_{Interphase}$ and E_{matrix} are modulus from CNTs, polymer interphase and polymer matrix and $V_{f,CNTs}$, $V_{f,Interpahse}$ and $V_{f,Matrix}$ are the volume fraction of these phases to the whole hybrid nanofiber. The volume fraction of CNTs is calculated from its concentration. The modulus of hybrid nanofiber with 0.1 wt.% CNTs is obtained from experiment, which is 10.9±0.3 GPa, and modulus of matrix is the same as the pure PAN nanofiber with $\lambda = 4$, which is 9.6±1.1 GPa. Modulus of CNTs is set as its theoretical modulus, 1 TPa. Thus, the polymer interphase modulus required to satisfy the above equation as a function of the interphase thickness is shown in Fig.2.15. The thickness of this highly ordered polymer chain layer was found to be ~10 nm [87] for certain hybrid PAN/CNTs fiber, which is also comparable to the thickness of the interphase measured in our studies from TEM results. Assuming that the interphase thickness in 0.1 wt.% electrospun PAN/CNTs hybrid nanofiber is also ~10 nm, the calculated modulus of polymer interphase is 17.5 GPa, which is ~1.8 times larger than the polymer matrix modulus (~9.6±1.1). This high modulus value of PAN is comparable to the modulus of the oriented crystalline phase of PAN.

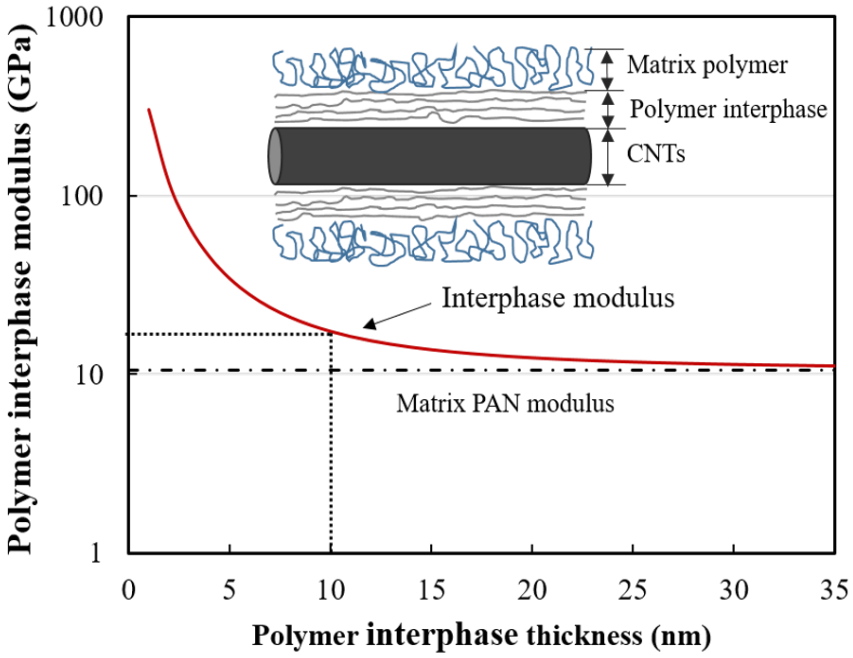

Figure 2.15. Calculated polymer interphase modulus with increasing thickness.

2.2.4 Description of microstructure evolution

Base on the microstructural and mechanical characterizations of PAN-SWNT ribbons, presented in previous sections, the microstructural evolution of electrospun PAN/SWNTs nanofibers under hot-drawing is described as shown in Fig.2.16. The as-fabricated electrospun PAN/SWNTs nanofibers are mainly composed of amorphous polymer region without any crystalline phases. The as-fabricated ribbons have relatively low degrees of polymer chain and SWNT alignment, potentially due to rapid solvent loss during electrospinning, which suppresses chain mobility required for flow induced reorientation of polymer chains and SWNTs. The addition of SWNTs slightly enhances

the alignment of both SWNTs and polymer chains, due to higher charge mobility in the composite jet (with SWNT fillers) which increases the pulling electrostatic force on the jet. However, the major improvement in polymer chain and SWNT alignment is achieved as a result of hot-drawing at ~135°C, considerably above T_g of PAN. In the hot-drawing process, the mobility of polymer chains was increased thermally, thus, the applied stress aligned the polymer chain and SWNTs during the process. As a result of the thermomechanical treatment, the degree of crystallinity in nanofibers was drastically

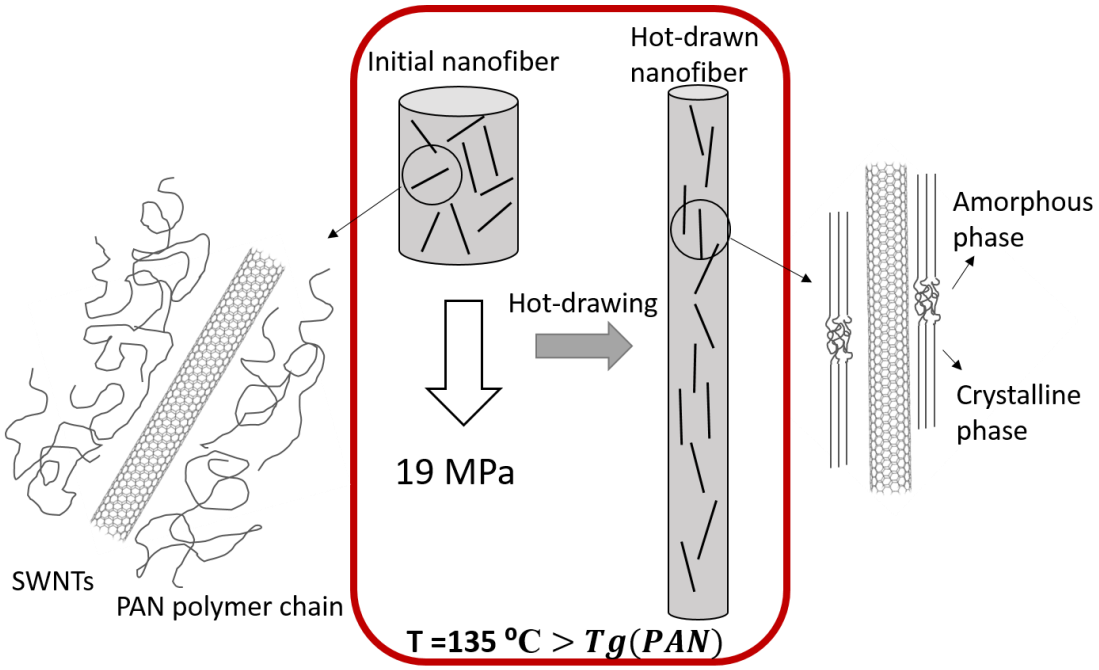

Figure 2.16. Schematic diagram of structural evolution for electrospun PAN/SWNTs nanofibers with hot-drawing.

enhanced. Among the hot-drawn samples with different SWNT concentrations, 0.1 wt.% PAN/SWNTs nanofibers exhibit highest mechanical properties, degree of crystallinity, and quality of interphase. Interestingly, the modulus of the 0.1 wt.% PAN/SWNTs nanofibers exceeds the rule of mixture predictions, suggesting morphological changes in the polymer phase in that sample, such as the formation of the highly ordered polymer interphase around SWNTs. In other words, during the thermomechanical treatment, the crystalline structure of the PAN/SWNTs is also modified due to the templating crystallization effect of SWNTs in PAN nanofiber. The crystalline phase generated on the surface of SWNTs can in principle increase the interfacial stress transfer between SWNTs and matrix, therefore accounting for the improvements in the mechanical properties observed in 0.1 wt.% PAN/SWNTs. The structural changes in 0.1 wt.% PAN/SWNTs as a result of hot-drawing is schematically shown in Fig.2.16. However, adding more SWNTs to nanofibers adversely affects mechanical properties, likely due to the formation of SWNT agglomerates, which lower the effective interface between SWNTs and matrix.

2.3 Conclusion

To unravel the reinforcement effect of SWNTs in electrospun nanofibers, PAN/SWNTs nanofibers with different SWNTs concentrations were fabricated by using electrospinning. Hot-drawing was then applied to the obtained nanofibers to further modify its microstructures, enhance the alignment of the PAN chains and SWNTs. The SWNT content was varied between 0.1 wt.% to 0.5wt.% relative to the PAN content. At 0.1 wt.% SWNTs, the as-electrospun samples demonstrated a marked increase in T_g and lowest chain alignment which was all attributed to high quality of dispersion of SWNTs

at such low SWNT loading and the confinement effects of well-dispersed SWNTs on polymer chains, which lowered their mobility. The hot-drawing led to major enhancements in chain alignment and led to major orientation-induced crystallization for all SWNT contents. By comparing the crystalline structure of the samples which were hot-drawn to different draw ratios, we concluded that the formation of the crystalline domains reaches a limit near or before a draw ratio of 2, and after that it is controlled by the loss of segmental chain mobility in the transitional regions in between crystalline domains. Further drawing however can further reorient the crystals such that their backbone is more aligned with the fiber axis (the same as the drawing directions). Moreover, in hot-drawn samples with 0.1 wt.% SWNT content we measured a modulus reinforcement efficiency of ~2.1 TPa, among the highest measured in the literature. That is likely due to the high SWNT-matrix interactions which leads to the formation of low-defect density polymeric interphases around the SWNTs. At higher SWNT contents, the agglomeration lowered the modulus efficiency factor, such that at 0.5 wt.%, negative efficiency factors were also detected.

3. NEAR-FIELD ELECTROSPINNING FOR FABRICATING PAN NANOFIBERS ON SPOOL

Polyacrylonitrile (PAN) nanofibers have long been the subject of studies as precursor for high performance materials such as carbon nanofibers. However, the inherent disadvantage of regular electrospinning, such as the solution jet whipping induced relatively large fiber diameter distribution has restricted its further development as the precursor for high performance carbon nanofiber. In this chapter, we report for the first time the successful application of low-voltage near-field electrospinning method to fabricate continuous polyacrylonitrile (PAN) nanofibers directly on a spool (rotating target).

By analyzing the effect of different NFES parameters on morphology of as-electrospun PAN nanofiber, we demonstrate the high controllability on the shape of the electrospun fiber cross sections in a wide range, from oval shapes to circular. Moreover, compared with regular electrospinning, NFES with higher solution jet stability shows an evident improvement in narrowing the nanofiber diameter distribution. In addition, we studied the mechanical properties of individual nanofibers via microdevices, as a means to gain more insight into their microstructure. The nano-mechanical tests reveal a two-zone mechanical size effect. We attributed this abnormal size effect to solvent residues in as-electrospun nanofibers, which can play a significant role in dissipating the chain alignment achieved via electrostatic forces during electrospinning. The residual solvent content depends on the duration of electrospinning and thus the electrospinning distance.

The thorough study of the effects of NFES parameter on morphology and mechanical properties of PAN nanofiber provides a solid foundation to develop nanofibers with narrow diameter and property distributions to further broaden the application areas of nanofibers.

3.1 Experimental

3.1.1 Fabrication of PAN nanofibers

As shown in Fig.3.1(a) and (b), 27 gauge (200 µm I.D.) stainless steel needle is connected to the syringe pump to dispense the polyacrylonitrile solution at rate of ~200µL/hr. A 6-12 wt. % solution of polyacrylonitrile with molecular weight of 150,000 g/mol in dimethylformamide (DMF), both obtained from Sigma–Aldrich, was utilized as the electrospinning polymer solution. Custom-made rotating aluminum cylindrical target with controllable rotating speed was used to collect the electrospun polymer nanofiber. The distance between the polymer droplet and the target surface was maintained at 400 to 600 µm. A 300V to 1000 V voltage difference was supplied between the needle and the target, by using a 0-1 kV dc power supply from Acopian. The linear speed of rotating target was 86.5 mm/s, which is the largest allowable value in our current experimental setup. After a polymer droplet was formed at the tip of the needle, a T-4-22 tungsten probe from GGB industries was used to initiate the localized instability on the polymer droplet, by bringing the probe tip to the proximity of the droplet surface under an optical microscope. The probe position was controlled via a linear positioning stage. In addition to the rotary motion, the target was also displaced in the direction perpendicular to the jet to collect nanofibers continuously next to each other, instead of on top of each

other, as shown in Fig.3.1(d). The whole NFES process was performed under the optical microscope. The recorded video of the NFES is in supplemental materials.

3.1.2 Mechanical tests on individual nanofiber

Tension tests on individual nanofibers were performed via bulk micromachined devices specifically designed for this purpose. Each device consisted of platforms to mount an individual nanofiber, and compliant polysilicon beams to serve as load sensor. One side of the nanofiber was attached to the load sensor, while the other side was griped on the device and displaced relative to the load sensor via a piezoelectric actuator. The tests were performed under an optical microscope and the elongation of the fiber and load on the fiber was measured by correlating digital images of the tests via digital image correlation (DIC). The diameter of the nanofibers were measured via SEM imaging on an unloaded section of the nanofiber, left outside of the gage length.

3.2 Results and discussion

PAN nanofibers were electrospun from a solution of PAN in DMF by using the NFES setup explained in the section 3.1, and shown in Fig.3.1(a). We studied the formation of electrospun fibers at various solution concentrations (6 wt.% - 12 wt.%), electrospinning voltages (250 - 600 V) and distances (250 - 700 μm). As shown in previous studies, the aforementioned electrospinning parameters, voltage, distance and solution concentration, play an important role in determining the shape of the cross section and diameters of the electrospun fiber on target [53, 55]. In all cases, the target tip velocity was 86.5 mm/s, which is comparable to the take-up velocities employed in previous studies [50].

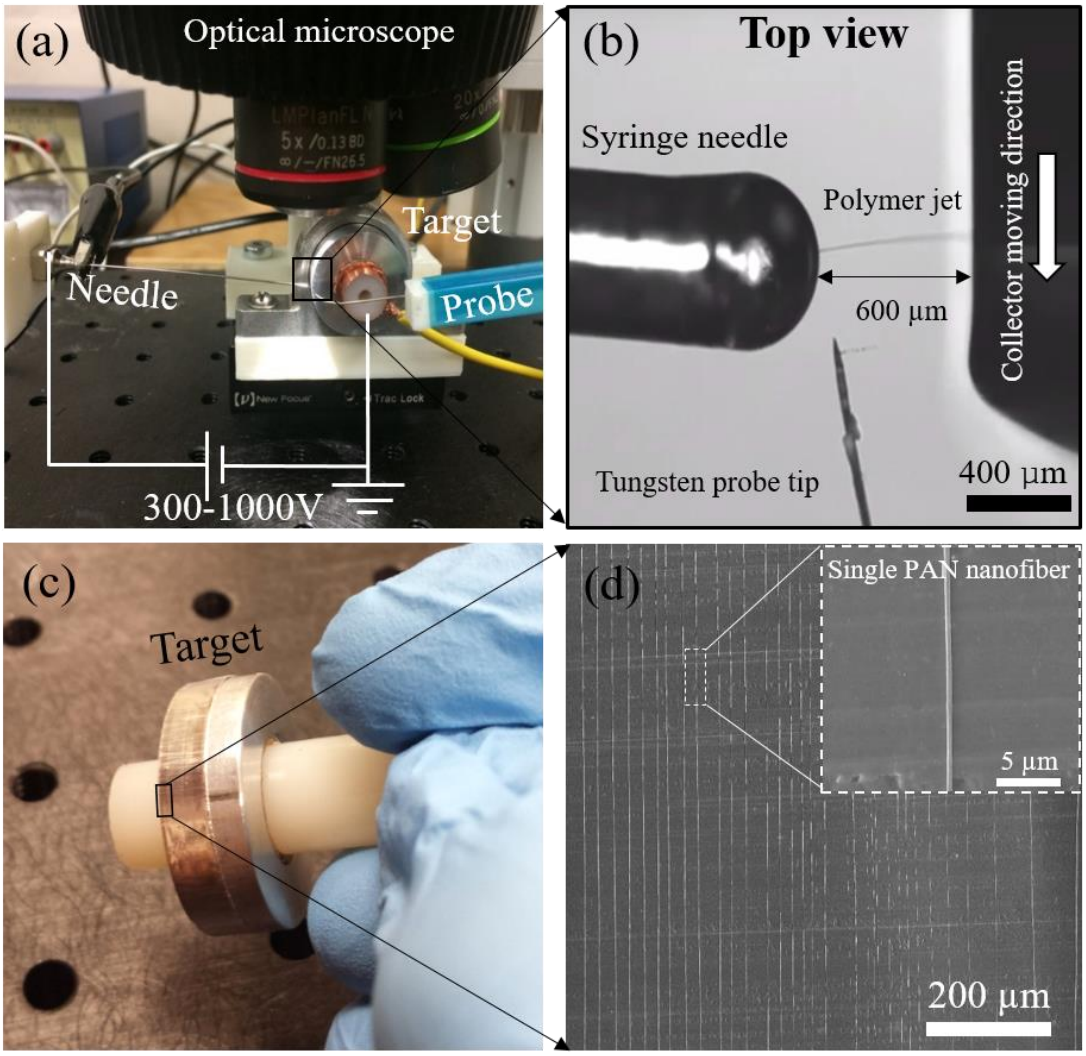

Figure 3.1. (a) NFES electrospinning experimental setup, **(b)** optical microscope image shows the NFES solution jet, **(c)** NFES target with nanofiber on surface and **(d)** SEM image shows the parallel aligned single PAN nanofiber with homogeneous morphology.

The setup was placed under an optical microscope to monitor the process, as shown in Fig.3.1(b). We used a horizontal NFES setup in which the average electrostatic field is nearly horizontal, and normal to gravity. In each case, a droplet was initially formed at the

tip of the needle by pumping liquid via a syringe pump. The electrospinning voltage was then applied. Next, the tip of a sharp tungsten probe was brought to the proximity of the droplet surface (~50μm) by manipulating the probe via a manual positioning stage, Fig.3.1(b). The tip of the tungsten is believed to assist with the localization of induced electrostatic charges on the droplet, enhancing local electrostatic forces applied on the jet, thus, facilitating the jet initiation.

To understand the effect of electrospinning parameters on PAN fiber spinning process and geometry, we first investigated the stability of the electrospinning process and fiber diameters obtained at various solution concentration, ranging from 6 wt.% to 12 wt.%. The electrospinning voltage and distance in this case are 400 V and 500 μm, respectively. In case of solution concentrations of 10 wt.% and 12 wt.%, the droplet was found to easily dry up and clog the syringe needle, thereby the electrospinning process was interrupted. In these cases, the rather high viscosity of the solution was also a major obstacle to continuous electrospinning. By decreasing the solution concentration to 8 wt.%, the electrospinning process initiated by bringing the tungsten probe near the droplet and would continue stably, leading to the formation of the smooth electrospun nanofiber/fiber on the rotating target, as shown in Fig.3.1(b-d).

We also studied lower solution concentrations of 6 wt.%, but the electrospinning was not continuous in these cases. This is likely due to low chain entanglement in the solution, manifested in the low viscosity of the solution, which leads to jet breakup due to surface tension [113]. Hence, similar to conventional electrospinning, the solution

concentration in NFES should be within an allowable range for successful fiber spinning. Solution concentrations below this range will interefer with continuous fiber production in both methods due to insufficient chain entanglements, while concentrations above the range will poorly flow due to high viscosity. However, the upper range of allowable solution concentration appears to be lower in NFES. That is mainly because of the slower flow rates employed in the NFES and the larger residence time of the droplet on the tip of the needle, during which the solvent can evaporate, and the solution concentration can increase locally beyond the electrospinable range.

With a solution concentration of 8 wt.%, we managed to orderly collect PAN nanofibers on the rotating spool, shown in Fig.3.1(d). As shown in this figure, each revolution of the spun PAN nanofiber nicely deposited on the target parallel to each other. The SEM image of individual nanofiber shows that the electrospun nanofibers have a smooth surface. No breakage of the nanofibers were observed on the spool, which literally means a single long PAN nanofiber was fabricated on the surface of the target with a length of over ~1.5 m (~17s electrospinning) and a diameter of 313±26 nm (aspect ratio of over $5x10^6$).

3.2.1 Effect of electrospinning parameters on fiber diameter and morphology

More insight into the effect of NFES parameters on fiber diameter and morphology was obtained by varying the electrospinning voltage and distance at a constant solution concentration of 8 wt.%. At first, different voltages ranging from 250 V to 600 V were applied to perform NFES with the electrospinning distance fixed at 500 μm. As shown in

Fig.3.2, at an applied voltage of 250 V, the electrostatic force between polymer droplet and target is not strong enough to overcome the surface tension and initiate the electrospinning. Thus, electrospinning was not successful and no fibers were formed in this condition (Shown with a red × in Fig.3.2). By increasing the voltage to 400 V, the electrospinning was initiated and stably continued. As a result, PAN nanofibers with a circular cross section, diameter of 507 ± 155 nm and smooth surfaces were formed. Interestingly, further increasing the electrospinning voltage by ~25 % to 500 V, changed the cross section of the fibers from nearly circular to an oval, thus ribbons formed in this case. The width of the ribbon (the longer diameter of the oval) was parallel to the target

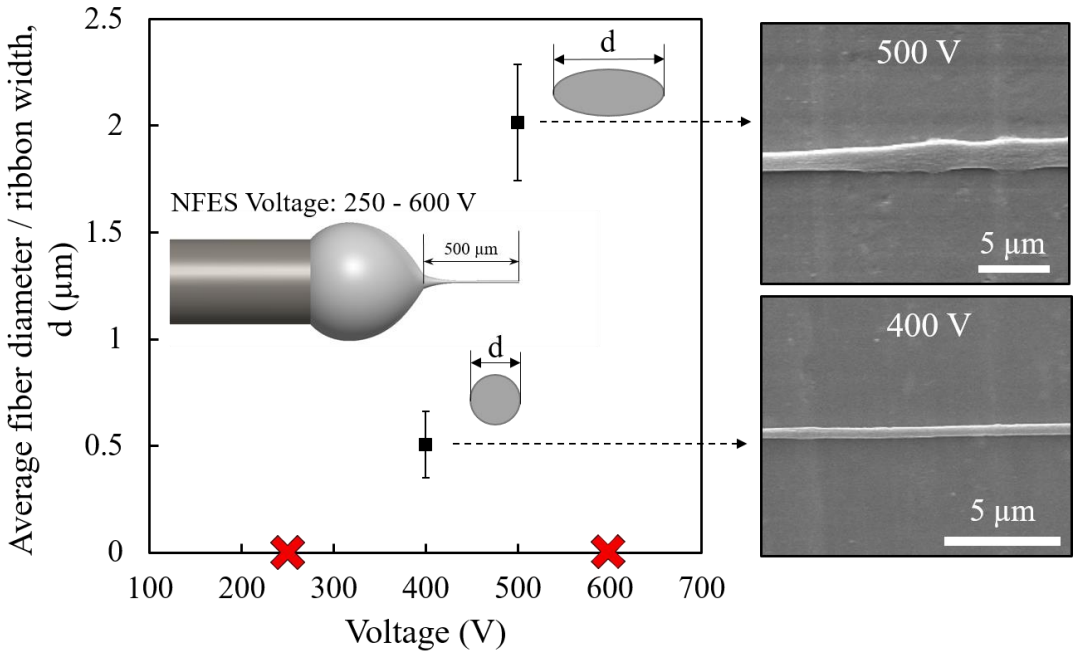

Figure 3.2. Effect of NFES voltage on fiber diameter and morphology (Red Cross sign indicates unsuccessful experiment case).

surface, and it was measured in SEM to be 2.02±0.27 µm. The out of plane dimension of the ribbons (the smaller diameter of their oval cross section) is estimated to be ~400 nm in SEM. Moreover, the ribbons were no longer smooth as compared to the 400 V case (SEM images in Fig.3.2).

The formation of wide ribbons at 500 V is an indication of the higher flow rates achieved by increasing the electrostatic forces applied on the droplet. It is to be noted that since the electrostatic field will both induce charges on the droplet and pull on the induced charges, one may expect the electrostatic forces on the droplet to increase with the square

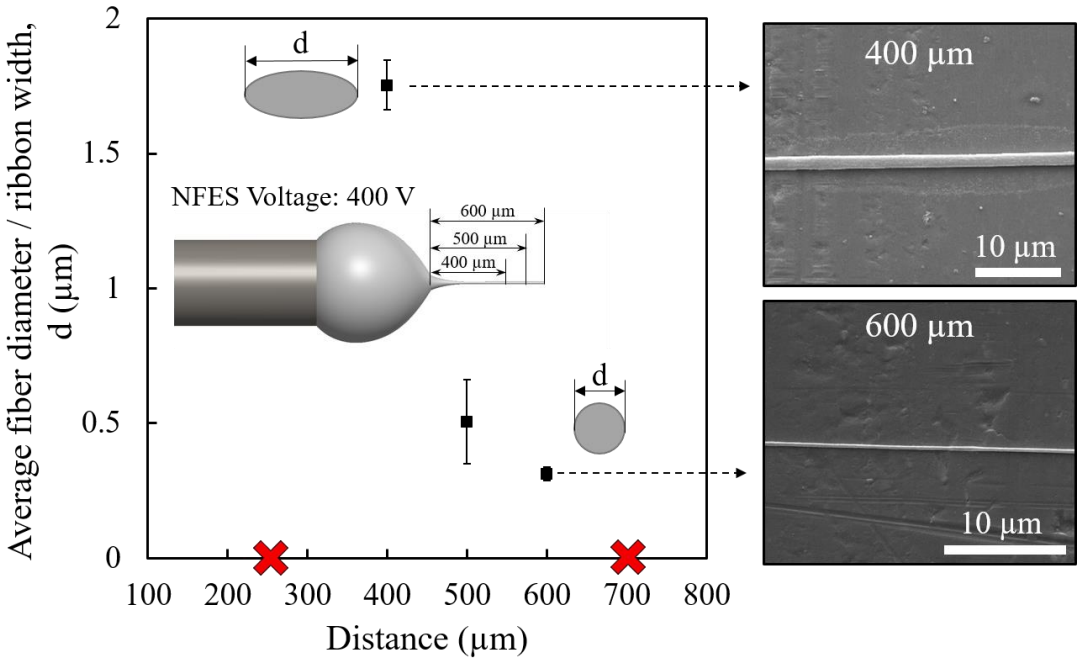

Figure 3.3. Effect of NFES distance on fiber diameter and morphology (Red Cross sign indicates unsuccessful experiment case).

of the voltage. Hence, increasing the voltage from 400 V to 500 V should in principle increase the electrostatic forces by more than 50%. Apart from that, the formation of less smooth fibers at higher voltages with an oval cross section is likely an indication of the deformation of the jet as it hits the target. To elaborate, one must consider the fact that the rate of solvent loss during electrospinning is a function of the surface area of the jet and forming fibers. Thus, the rate of solvent evaporation is expected to be significantly lower at 500 V (in which wide ribbons form) compared to 400 V. Hence, when the jet hits the target at higher voltage, it is still not fully solidified and can get deformed and flatten out due to the impact of hitting the target. This phenomenon has been also observed in regular electrospinning [114]. The nonuniform flattening of the jet on the target may simply reflect the slight variations of the solvent residue of the jet as it reaches the target.

To further reduce the average diameter of PAN nanofiber and achieve nanofibers with smooth surfaces, we studied the effect of distance at a fixed voltage on electrospinning, shown in Fig.3.3. At the fixed voltage of 400 V used here, the lowest allowable distance to initiate stable electrospinning is 400 μm, which generated PAN ribbon on target with width about 1.75±0.09 μm and thickness of 400±41 nm. When the electrospinning distance was reduced below 400 μm, a short circuit happened between the metal needle and grounded target, and electrospinning could not be initiated. The formation of PAN ribbons with a relatively large width at 400 μm is likely due to the fact the jet in these cases contains a considerable amount of residual solvent when it reaches the target, and thus, it is rather soft and can deform upon impacting the target, shown in Fig.3.4. This mechanism of flattening the ribbons on the target is similar to that presented

earlier in this document to explain the formation of ribbons at 500 V and 500 µm. By increasing the electrospinning distance, PAN nanofibers with near circular cross sections were obtained on the surface of the rotating target. The largest available electrospinning distance is 600 µm, which generates PAN nanofiber with diameter 313±26 nm. Larger distances did not allow for successful electrospinning due to insufficient electrostatic forces on the droplet which could not overcome the surface tension.

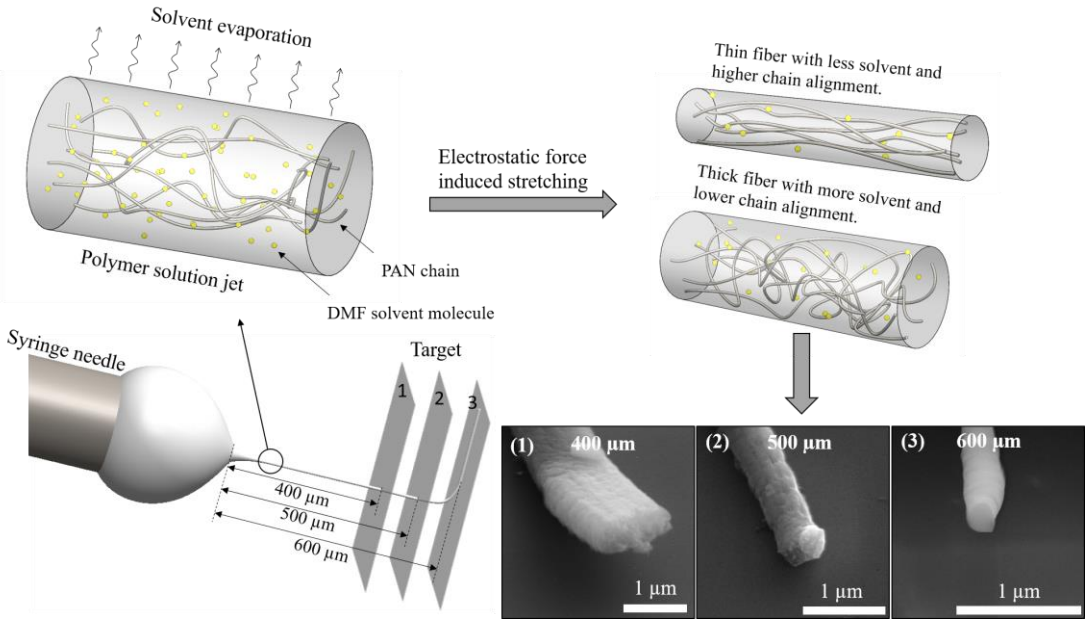

Figure 3.4. Effect of NFES distance on morphology of obtained nanofiber on target.

3.2.2 Comparison with conventional electrospinning

The NFES is considered as a modified electrospinning method to achieve orderly positioned nanofibers. Therefore, it will be illustrative to make comparisons between the

two methods. However, a meaningful comparison should be made only when some output parameters are similar in the two methods, such as average fiber diameter. This comparison will specifically be interesting when considering the fact that the bending instability is believed to be one of the main factors leading to thin fibers in conventional electrospinning, while the small electrospinning distance effectively prevents this instability in NFES (Fig.3.5).

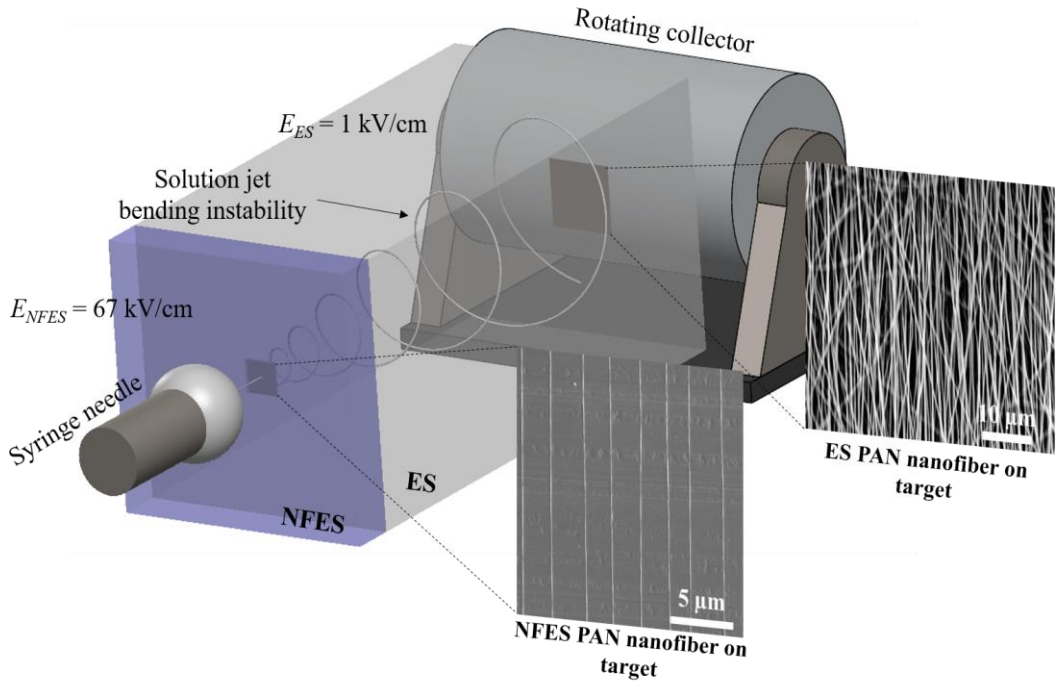

Figure 3.5. Schematic diagram of comparison between NFES and regular electrospinning (ES) with SEM images showing difference between NFES and ES obtained electrospun PAN nanofiber on target.

To make such comparison, we focused on the NFES conditions in which the average fiber diameter was 313±26 nm, which were fabricated at a solution concentration

of 8 wt.%, and electrospinning voltage and distance of respectively 400 V and 600 μm. We chose these NFES parameters, as the circular shape of their cross section (Fig.3.2) and the average fiber diameter is comparable to nanofibers that can be obtained via conventional electrospinning. An example of the latter were nanofibers electrospun in our lab from a 10 wt.% solution of PAN in DMF, at a voltage of 25 kV and distance of 20 cm, which resulted in an average diameter of 314±58 nm [50]. Admittedly, these electrospinning parameters are not the only ones to results in this average nanofiber diameter, but these are within the range commonly used in conventional electrospinning.

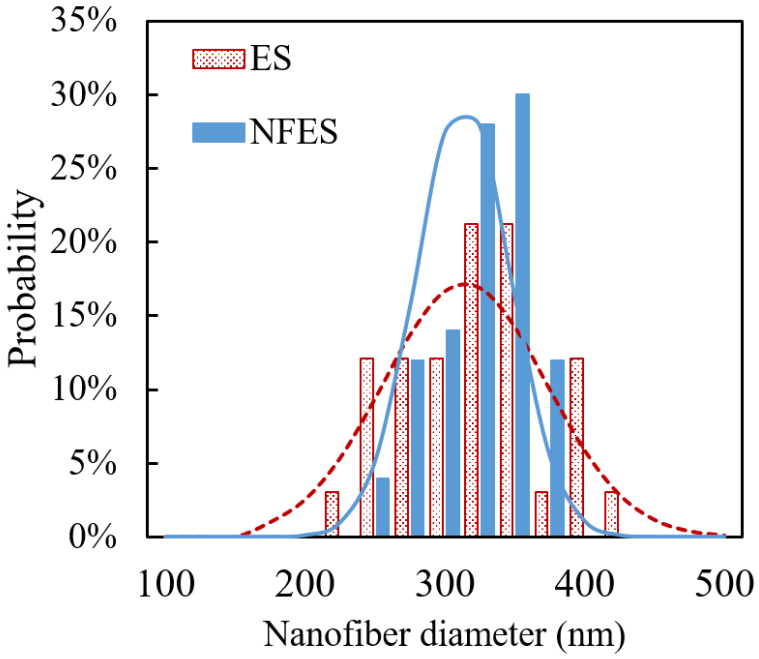

Figure 3.6. Fiber diameter distribution comparison of ES and NFES.

The similar average nanofibers diameter achieved in the two methods, despite the fact that the jet in NFES did not experience bending instability, is partly owed to the much

thinner jet in NFES and lower solution concentration and thus viscosity in NFES which enhances the drawability of the jet [55]. It is also interesting to compare the average electric fields in these two cases, a value of ~1.25 kV/cm in conventional electrospinning, which is an order of magnitude less than the average electric field employed in NFES (~67 kV/cm). In other words, a significantly larger average electric field is required to overcome the surface tension on the droplet and initiate the electrospinning when the distance between the needle and the target is reduced from ~20 cm in conventional electrospinning to below 1 mm in NFES. This is a result of the distortion of the electrostatic field around the needle by the target at small distances employed in NFES, which lowers the ratio of the local electric field on the surface of the droplet to the average electric field. To compensate for that and to initiate the electrospinning, a larger average electrostatic field needs to be employed in NFES.

Apart from that and as shown in Fig.3.6, the distribution of nanofiber diameter fabricated via NFES is much narrower than the ones fabricated via conventional electrospinning. Although the average diameter of the nanofibers fabricated with the two methods are comparable, the standard deviation of the diameter in the NFES nanofibers is ~26 nm, which is less than half the standard deviation of the diameter of nanofibers processed via conventional electrospinning (~58 nm). This lower standard deviation in NFES once again elucidates the stochastic nature of the whipping motion and bending instability, which leads to larger diameter distribution in conventional electrospinning. The ability to better control diameter distribution is crucial and can pave the path for

employing polymeric nanofibers in many applications such as precursors of CNFs as reinforcements for high performance composites.

3.2.3 Mechanical property of individual NFES nanofiber

The variation of mechanical properties of NFES nanofibers with diameter and the comparison between the mechanical properties of NFES nanofibers and those obtained from conventional electrospinning can provide us with valuable insights about the morphology of polymer chains in polymer nanofibers. In this section, we studied the mechanical properties of NFES nanofibers with circular cross sections fabricated at electrospinning voltage of 400 V and distance of 600 μm.

To this end, we used microdevices shown in Fig.3.7(a) to characterize the mechanical properties of individual NFES PAN nanofibers. The devices were designed in our lab and fabricated by a commercial processes as explained in prior publications [43, 95, 115]. The devices are composed of Silicon platforms to grip individual nanofibers at their ends. One of the grips is connected to a compliant Silicon beam with known stiffness (1.93 N/m), which serves as the loadcell, while the other one is connected to a piezoelectric actuator to load the fiber. Under the optical microscope, a tungsten probe was used to pick up single PAN nanofiber and mount it on the MEMS device. Epoxy glue was then applied to fix the nanofiber on the MEMS device beams, as shown in Fig.3.7(a-b). The MEMS device with fixed nanofiber was then placed on a picomotor piezo linear actuator platform (Newport company), which could unidirectionally displace the device on command. The moving part of the MEMS device was then fixed by another tungsten probe. Through

moving the whole MEMS device, force was applied to the single polymer nanofiber through the load cell. The testing was carried out under the optical microscope, during which continuous images were taken to perform Digital Image Correlation (DIC) by using a commercial software of VIC-2D, as shown in Fig.3.7(c-d). The relative displacements of the pads were then used to calculate the elongation of the nanofiber and the load applied to the nanofiber, from which the stress-strain curve of individual nanofibers, their strength

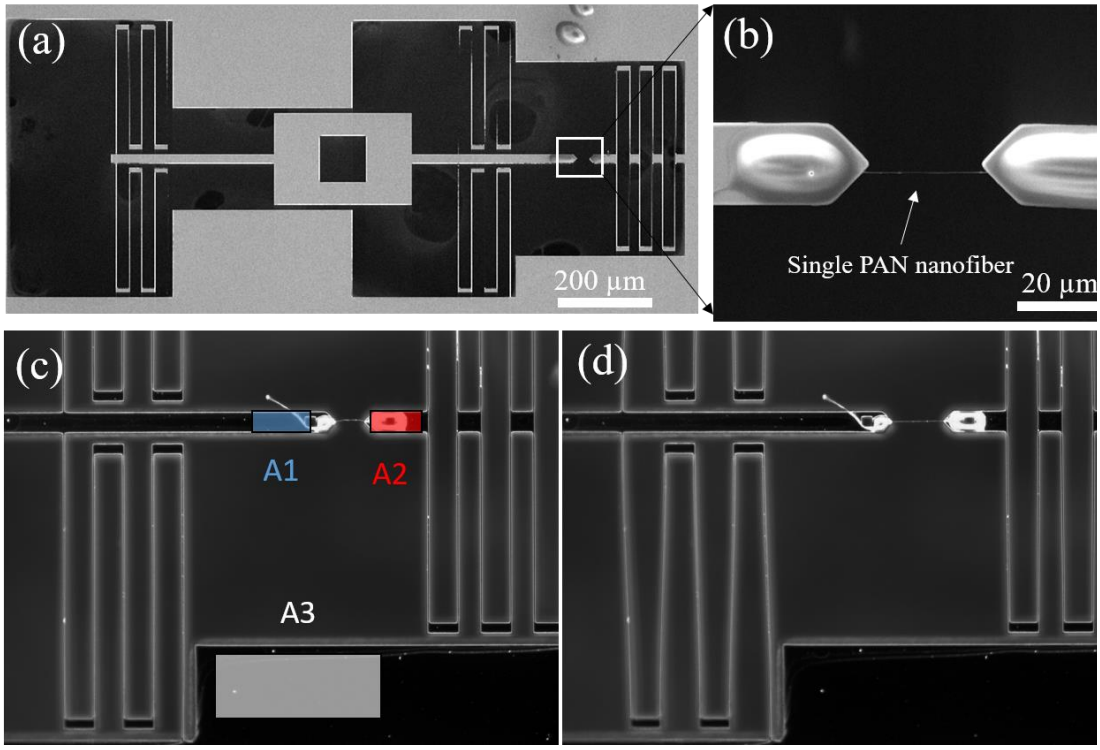

Figure 3.7. (a) MEMS device with single PAN nanofiber, **(b)** higher magnification of PAN nanofiber on MEMS, **(c)** optical microscope image for DIC of MEMS with mounted polymer nanofiber without deformation and **(d)** with deformation.

and modulus were obtained. The diameters of the nanofibers tested ranged from 200 nm to 300 nm. Details of data analysis is presented in [116].

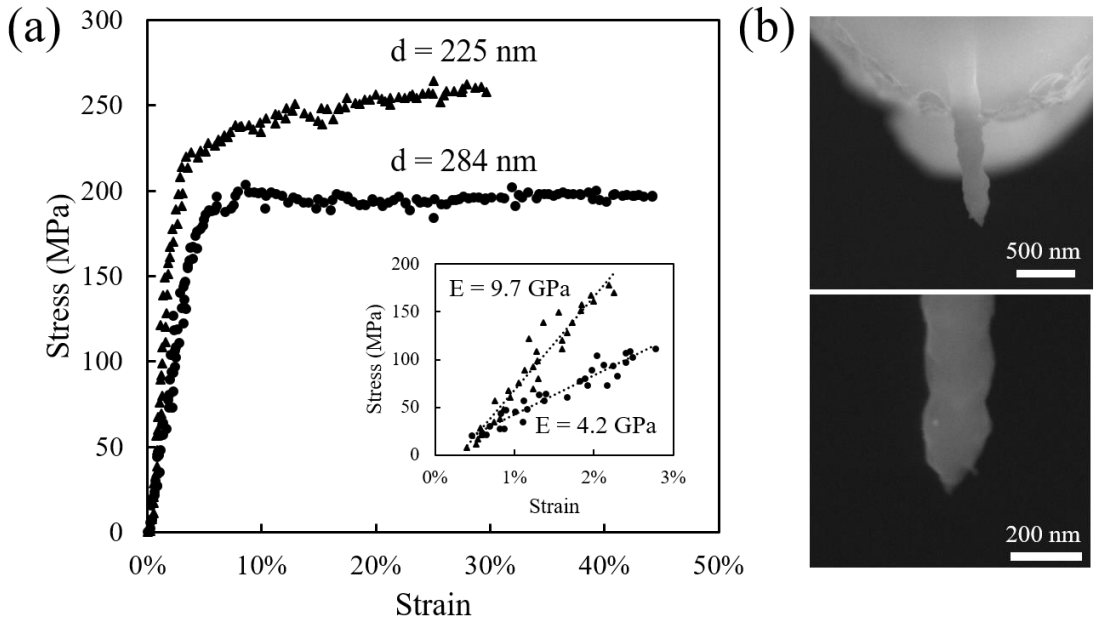

Figure 3.8. (a) Stress-strain curve of single PAN nanofiber and its modulus linear fitting with different diameters and **(b)** SEM image of failure position in PAN nanofiber after testing.

Examples of stress-strain curves of PAN nanofiber obtained by using the method described above is shown in Fig.3.8(a). The modulus of polymer nanofiber is calculated by a linear fit to the stress-strain curve at the small strain regions, as shown in the inset of the figure. The modulus of PAN nanofiber ranges from 1.8 GPa to 9.7 GPa and the strength ranges from 161 MPa to 312 MPa. The SEM image of failure zone of PAN nanofiber is

also shown in Fig.3.8(b). Evident necking happened near the failure surface. This is similar to the deformations observed in PAN nanofibers obtained from conventional electrospinning, which is likely caused by a skin-core inhomogeneity in nanofibers [117].

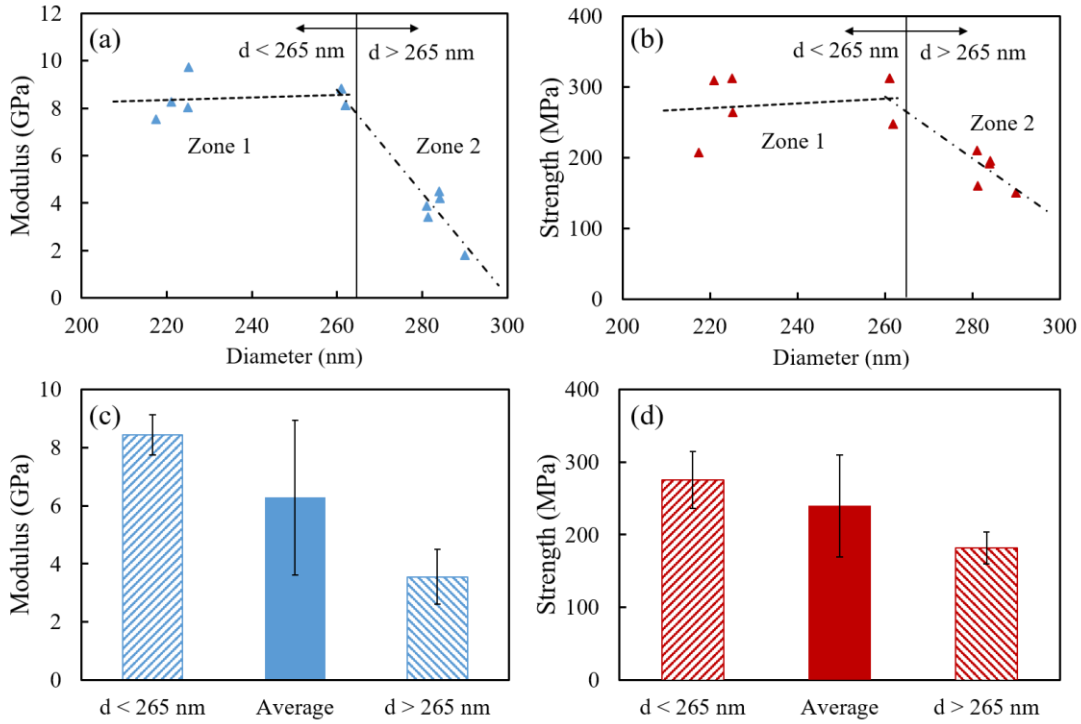

Figure 3.9. (a) Modulus and **(b)** strength of PAN nanofiber with different diameters, and average values of **(c)** modulus and **(d)** strength of CNFs in different diameter range.

The values of modulus and strength, respectively shown in Fig.3.9 (a) and (b) point to a strong mechanical size effect. For instance, the modulus of a ~200 nm thick nanofiber is ~8 GPa, which is about 4 times the modulus of a ~290 nm thick nanofiber. However, a

careful analysis of the mechanical properties as a function of diameter point to two regimes in the mechanical size effect. In zone 1 (Fig.3.9 (a) & (b)) which is identified with nanofibers thicker than ~260-270 nm, the strength and modulus decreases with diameter. This behavior is similar to the size effect observed in nanofibers obtained via conventional electrospinning, and it is an indication of lower chain alignment in thicker nanofibers. Similar to conventional electrospinning, it can be argued that the lower surface to volume ratio in thicker jets that will eventually form nanofibers can slow down the solvent evaporation in them. As a result, thicker nanofibers will have higher content of solvent residues as they reach the target. Hence, thicker nanofibers can more readily lose part of their chain alignment achieved during the electrospinning [27].

The above argument, however, cannot explain the plateau in strength and modulus of nanofibers which was observed in the diameter range of 200-260 nm (zone 2), with a plateau modulus of 8.4±0.7 GPa and strength of 275±40 MPa. This behavior is peculiar to NFES nanofibers and is not observed in conventional electrospun nanofibers [27, 61]. The plateau in material properties is an indication of similar morphologies within the range of the diameters studied, *e.g.*, chain alignment. The rather high elastic modulus of nanofibers in this range, which requires a high degree of chain alignment and packing (corresponding to Herman orientation factor of 0.5-0.8 [27, 50]), may provide some insight as to how the morphology is not changing in this range. In other words, we attribute this plateau in properties to high chain packing and interactions between chains in nanofibers, as they form on the target, which suppress chain mobility, despite different contents of solvent residues in nanofibers with various diameters.

3.3 Conclusion

The first successful effort to collect continuous single strand PAN nanofibers with aspect ratios exceeding 10^6 via continuous low-voltage near-field electrospinning (NFES) on a spool (rotating target) was presented in this work. Moreover, we studied the mechanical properties of PAN nanofibers via micromachined devices. Our studies pointed to the significant contribution of electrospinning parameters, such as distance and solution concentration, on the rate of success of electrospinning (*i.e.*, spinning continuous fibers stably) and also the shape of the spun fibers. For instance, we also realized that slight changes in the voltage from 400 V to 500 V can significantly change the shape of the cross section of the fibers, from a circular cross section to oval shaped (ribbons). We explained that in terms of the solvent residues in the jet and momentum transfer between the fibers and the target, as the fibers reach the target. We also compared the output parameters of NFES, such as fiber diameter distribution and mechanical properties, with those of nanofibers fabricated via conventional electrospinning. In comparison to conventional electrospinning, the NFES led to a significantly narrower diameter distribution, by collecting the fibers prior to the initiation of bending instability which is stochastic in nature. Moreover, the size effect observed in NFES nanofibers, unlike nanofibers fabricated via conventional electrospinning, was not monotonic. While in conventional electrospinning, the strength and modulus often increase monotonically by reducing the diameter, the increase in properties of NFES reached a plateau when the diameter of nanofibers was reduced below ~260-270 nm. The plateau in mechanical properties was explained in terms of a plateau in nanofiber morphology, and was attributed to high chain

packing and interactions between chains in this diameter range (evident in the modulus of nanofibers of as high as 9 GPa, among the highest values in PAN nanofibers) which suppressed chain mobility.

4. MICROSTRUCTURE-PROPERTIES RELATIONSHIP IN FABRICATING CNF AND CNF/F-SWNTS

Composite materials reinforced with carbon fibers (CFs) have achieved remarkable success in substituting traditional metallic based materials as a means to reduce weight for a variety of applications, such as aerospace sector, high performance racing cars and even sporting goods [1, 118-119]. CFs are fabricated through pyrolysis of polymeric precursors, including polyacrylonitrile (PAN) homopolymer and copolymer, petroleum pitch, and lignin [8]. Over 50 years of research and development on fabrication process, precursor polymer chemistry and morphology has led to considerable increase in the mechanical strength of CFs from ~2.5 GPa to ~7.0 GPa [4]. However, flaws present in the structure of traditional CFs with diameter in the range of 4-8 μm, has become a major roadblock in further improving their strength [8, 14, 17]. Thus, there has been a new push to enhance the strength of CFs by reducing their diameter from a few microns to below ~2 microns by incorporating different processing techniques, such as gel-spinning of bio-component precursors (island-in-sea method) [70] and electrospinning the precursors [18, 31]. These efforts are motivated by the strong size (i.e., diameter) effects in CFs which stems from size dependent flaws in CFs, such as inherent radial structural inhomogeneity [19, 120-121]. Among methods to generate CFs with reduced diameters, electrospinning the polymer precursors followed by carbonization the precursor stands out as the method which is capable of generating nearly continuous carbon fibers with diameters as low as 100 nm (carbon nanofibers, CNFs) [122-124]. Apart from high potential mechanical properties [11],

electrospun CNFs have also been shown to exhibit other properties which are highly sought for in developing multifunctional composites, such as high electrical conductivity [125], piezoresistivity [95] and thermal conductivity [97].

Continuum models of CNFs which treat them as composites of amorphous carbon reinforced with turbostratic particles and atomistic models of CFs in which size-dependent flaws such as skin-core inhomogeneity are absent predict that the strength of CNFs can reach values in excess of 14 GPa and conservatively may even be higher [11, 126-128]. However, due to factors such as relatively low polymer chain alignment in electrospun precursors, which leads to limited graphitic alignment, the achieved strength of CNFs is a fraction of the predicted values. Different approaches has been applied to improve the mechanical performance of CNF for instance via enhancing the chain alignment in the precursor which leads to enhanced graphic alignment in CNFs [43], controlling the concentration of graphitic domains[18], applying restricting force during carbonization [129] and adding carbon nanomaterials to restrict polymer chain shrinkage during the fabrication process and introduce templating graphitization [91, 130]. Despite all the efforts, the highest strength of CNFs measured experimentally (a value of ~4 GPa [18, 43] for gauge length 25μm or higher), compares even poorly to the highest strength of commercial CFs (~7.0 GPa for Torayca®, T1100G).

In an attempt to close the gap between the measured and theoretical strength, we studied the mechanical properties of PAN homopolymer-based electrospun CNFs in relation to their microstructure. Our efforts were in particular directed at reducing defects

in CNFs, such as poor graphitic alignment and both low degree and excessive graphitization. While compared to amorphous carbon which is achieved for instance via carbonization at ~1100 ºC, increasing the graphitization (by increasing the carbonization temperature to ~1400 ºC) can increase the strength by introducing more of the strong sp^2 C-C bonds, excessive graphitization (by employing higher carbonization temperatures) may lead to strength-compromising interactions between turbostratic domains [18]. We demonstrate that through proper engineering the microstructure of CNFs, their strength can exceed the strength of traditional CFs. This is despite the fact that the industrial CFs are fabricated from PAN copolymers which facilitate drawing-induced chain alignment compared to PAN homopolymers used in this study to fabricate CNFs. Interestingly, the remarkable strength of CNFs has come with added benefits in terms of energy to failure and ductility. That is, comparing with CF, our electrospun CNF shows evident increase in failure strain and toughness, which is discussed based on the microstructure difference between them the fracture surfaces of CFs and CNFs as observed with nearly atomic resolution. Moreover, the decreased radial dimension of precursor polymer nanofiber from electrospinning provides a lowered defect density and structural inhomogeneity, which contribute to the overall and simultaneous improvement in strength and toughness. The proposed failure mechanism of electrospun CNFs with both high strength and toughness provides new pathway for developing high-performance structural fibers in both academia and industry.

4.1 Experimental work for CNFs

4.1.1 Fabrication of hot-drawn CNFs

Polyacrylontirile (PAN) precursor nanofiber ribbon was fabricated via electrospinning. The 10 wt.% homopolymer PAN solution was obtained by dissolving PAN powder (M_w = 150,000 g/mol) in Dimethylformamide (DMF) solvent (both from Sigma–Aldrich). The flow rate of electrospinning was set to ~0.8 ml/hr to obtain stable jet. Rotating target was used to obtain aligned polymer nanofiber ribbon with ~5.7 m/s peak-up velocity and at voltage and distance of 25 kV and 20 cm, as described in our previous work [50]. Then, PAN nanofiber ribbon were drawn to different ratios, ranging from λ =1 to 3 (λ, hot-drawing ratio = final length/initial length of ribbon) by applying an engineering stress of ~19 MPa in an oven at a temperature of 135°C.

Following that, the PAN precursor nanofiber were thermally stabilized at 290 ºC for 2 hours in air. FT-IR was used to characterize the stabilization reaction extent under different conditions, such as temperature and time. Based on the calculated ring cyclization index RCI (the ratio of intensity of the C=N to the sum of the intensities of C=N and C≡N), optimum condition for stabilization was chosen, as described in elsewhere [43]. During the stabilization, 5 MPa stresses were applied to the hot-drawn ribbons to constrain the shrinkage and maintain the chain alignment during the reaction. Carbonization was carried out in tube furnace (MTI, GSL-1700x) at 1400 ºC for 2 hours under inert gas (N_2) environment, during which no stress is applied.

4.1.2 Microstructural characterization of CNFs

The surface morphology of PAN and carbon nanofiber was characterized by using FEI Quanta 600 FE-SEM. The X-ray diffraction spectrums of PAN and CNFs ribbons (XRD) (CuKα, wavelength of 0.154 nm) were obtained using GADDS BRUKER-AXS MWPC 3-thircle X-ray Diffractometer. The crystallinity of PAN precursor nanofiber was calculated based on the relative area under the deconvoluted crystalline and amorphous peaks by using Lorentzian fitting in Origin 9.0 [71]. The PAN crystallite size in PAN precursor and CNFs were calculated from PAN (110) and CNFs (002), by using Scherrer's equation (K = 0.89) [131]. The orientation of the PAN chains in the crystalline phase was determined based on the azimuthal scans of the diffraction peak at 2θ ~ 17° [106]. Orientation of CNFs crystallite was determined from the azimuthal scan at 2θ = 25° [10]. Herman's orientation factor of PAN crystal and CNFs crystal are obtained from following equations based on WAXD azimuthal curves of PAN (110) and CNFs (002) diffraction peaks.

$$\langle cos^2\psi \rangle = \frac{\int_{-\frac{\pi}{2}}^{\frac{\pi}{2}} I(\psi) cos^2(\psi) \sin(\psi) d\psi}{\int_{-\frac{\pi}{2}}^{\frac{\pi}{2}} I(\psi) \sin(\psi) d\psi}, \; f = \frac{3\langle cos^2\psi \rangle - 1}{2} \tag{4.1}$$

where ψ is off axis angel, I is diffraction intensity, and f is the Herman's orientation factor. Graphitic structure within the CNF was characterized by using Horiba Jobin-Yvon LabRam Raman Confocal Microscope with a He-Ne laser (633nm). The averaged I_D/I_G ratio and crystallite size were obtained based on three times measurements. The curve fitting was carried out in Origin 9.0 with Lorenzian fitting. FEI Tecnai G2 F20 transmission electron microscope (TEM) was used to characterize the graphitic structure of CNF, and selected area electron diffraction (SAED) was applied to measure the

alignment of turbostratic domains within CNFs. The obtained averaged full width half maximum (FWHM) of (002) arc of CNFs in SAED pattern was reported based on five times measurements.

4.1.3 Mechanical testing of individual nanofiber

The mechanical property of individual CNF was studied by using a MEMS-based nano-mechanical testing platform. After mounting individual CNFs on MEMS device with 3D-manipulator controlled sharpened tungsten tip, Tescan LYRA-3 focused ion beam (FIB) was used to deposit platinum (Pt) block on it to fix it on device. Then, the MEMS device with Pt block fixed nanofiber was mounted on stage with one-dimensional controllable motion ability. While the stage was actuated, optical images of the load cell in the device was captured via an optical microscope. Through applying Digital Image Correlation to calculate the displacement of different parts in the MEMS device and combining with the stiffness of the load cell, the stress-strain curve of individual CNF/f-SWNTs tensile test was obtained. The cross-section area of CNFs used to calculate the stress in CNFs was obtained from the diameter of the failure position. The force and strain resolution of the MEMS device was 4 MPa and 0.1%, which is suitable for characterizing the modulus and strength of individual CNF. More details of the testing apparatus can be found in our previous work [43].

4.2 Results and discussion of CNFs

4.2.1 Microstructure of CNFs and CF precursors

The microstructure and properties of CNFs are highly dependent on factors such as the degree of graphitization and graphitic alignment [18, 43, 132]. Among these parameters, alignment of turbostratic (defective graphitic) domains is strongly dependent on precursor chain alignment. Higher alignment of precursor chains can effectively enhance graphitic alignment in CNFs, and thus, lead to CNFs with improved strength and modulus [43]. The enhancement in chain alignment can be achieved to some extent via electromechanical drawing forces applied onto electrospinning jet, but more effectively via hot-drawing the as-electrospun nanofibers [43]. The chain alignment can even lead to orientation-induced crystallization, as has been demonstrate in PAN [43, 61] and other polymer nanofibers [64, 133]. On the other hand, excessive hot-drawing may induce defects in the precursor, such as chain scissor or voids, which can compromise the strength of the resulting CNFs. For instance, in a prior study, it was demonstrated that increasing the hot-drawing ratio from $\lambda = 2$ to $\lambda = 4$ increased the scatter in the strength of CNFs with no effective improvement in the average strength, suggesting defect accumulations in the precursor [43]. Therefore, in this work, $\lambda = 3$ is chosen to be the maximum hot-drawing ratio applied to as-electrospun PAN nanofibers to induce chain alignment as a means to develop high strength CNFs.

Table 4.1. Structural parameters comparison between electrospun PAN nanofibers and PAN fibers.[16,62,134]

Precursor fabrication	Polymer type	Diameter(μm)	Draw ratio	Crystallinity (%)	Crystal size	f_c (PAN)*
Hot-drawn electrospun (this work)	PAN homopolymer	0.31	1	N/A	N/A	N/A
		0.28	2	28	5.9	0.65
		0.19	3	31	6.7	0.74
Wet-spun [134]	PAN homopolymer	12	15	67	6.2	0.85
Gel-spun [62]	PAN homopolymer	10.4	13.5	50	9.2	0.89
Gel-spun [16]	PAN copolymer	20-23	38	65	11.3	0.92

* f_c is Herman's orientation factor of PAN crystallite

The microstructure of the PAN nanofibers as a function of the draw ratio, studied via X-ray diffraction method (Experimental section), is presented in Table 4.1. As shown in the table, hot-drawing of the precursor significantly increases the crystallinity, crystal size and alignment of chains within the crystalline domain. For instance, hot-drawing the PAN precursor nanofiber to $\lambda = 3$ (average diameter ~190nm) in this work led to an enhancement in crystallinity, crystal size and Herman's orientation factor of crystal phase to 31%, 6.7 nm and 0.74, respectively, from a nearly amorphous state in as-electrospun nanofibers ($\lambda = 1$). That is, hot-drawing of the precursor above the glass transition temperature of PAN enhanced the mobility of PAN chains and facilitated chain alignment. It also led to a more densely packed arrangement of polymer chains. These results are in line with our prior findings on the effect of hot-drawing on the microstructure of PAN [43, 50].

It is also illustrative to compare the morphology of PAN chains in hot-drawn electrospun nanofibers with the morphology of PAN chains obtained via other fabrication processes. For instance, PAN homopolymer microfibers made from wet-spinning exhibit higher crystallinity and crystal phase alignment [134]. This is partly due to the swelling caused by the residual solvent which weakens the interactions between chains and allows for significantly higher draw ratios in wet-spun fibers. Drawing-induced chain alignment can continue until the crystalline domains which suppress chain mobility are formed [134]. In addition, gel-spun PAN fibers can achieve larger crystal domains compared to electrospun PAN nanofibers, due to reduced entanglement of polymer chain [62]. The chain alignment can also be further enhanced by utilizing PAN copolymers such as Polyacrylonitrile-co-Methacrylic Acid (PAN-co-MAA), instead of PAN homopolymers [16]. The reduced polarity of the precursor chains by introducing MAA monomers lowers the interactions and physical entanglement between chains, thus, allowing for higher draw ratios, chain alignment and crystallinity, as shown in Table 4.1.

In addition to the processing conditions which facilitates chain alignment in gel- and wet- spun fibers, the lower degree of crystallinity of PAN chains in electrospun fibers could also be partly rooted in their sub-micron diameter (larger surface to volume ratio) which promotes solvent evaporation and lowers the residual solvent content of the fibers. As discussed earlier in the context of wet-spun fibers [134], the residual solvent can act as a plasticizer, facilitating chain reorientation in response to hot-drawing.

4.2.2 Microstructure of CNFs

The significant effect of the microstructure of CNFs on their physical properties has been alluded to in previous studies [31, 43, 95, 129, 135-140]. In this section, the microstructure of CNFs, especially their defect density and graphitic alignment, as a function of processing conditions is studied.

Raman spectroscopy was used to analyze the microstructure of CNFs obtained as a function of the carbonization temperature and precursor hot-drawing ratios, Fig.4.1. After carbonization of the precursor, two major peaks appear at ~1336 cm^{-1} and ~1580 cm^{-1} corresponding to the D- and G-peak of carbon materials. The ratio of peak intensities, I_D/I_G, can be used as a relative indicator of defect density within the materials with graphitic domains [31, 141]. By increasing the carbonization temperature from 800 °C to 1400 °C in as-electrospun CNFs (λ = 1, no precursor hot-drawing), there is a gradual decrease in the I_D/I_G ratio from 4.7 to 3.8 (~20%), indicating a reduced defect density in CNFs achieved by employing higher carbonization temperature.

The ratio of peaks in Raman spectrum also allows us to calculate the width (in plane dimension of the graphitic structures, L_a) as: [142]

$$\frac{I(D)}{I(G)} = \frac{C(\lambda_L)}{L_a} \tag{4.2}$$

where λ_L (= 633nm) is the wavelength of the He-Ne laser used to collect Raman spectrum. The value of the coefficient $C(\lambda_L)$ for the He-Ne incident laser is ~8.3 nm [143]. According to this analysis, the width of the graphitic crystallites increases from 1.75 nm to 2.05 nm by increasing the carbonization temperature, consistent with previous studies [18, 144]. The

growth of the turbostratic domains in PAN-based CNFs along the basal plane of the domains (in-plane dimensions) during the carbonization process occurs as a result of the merger of the stabilized PAN chains through dehydration and denitrogenation reactions.

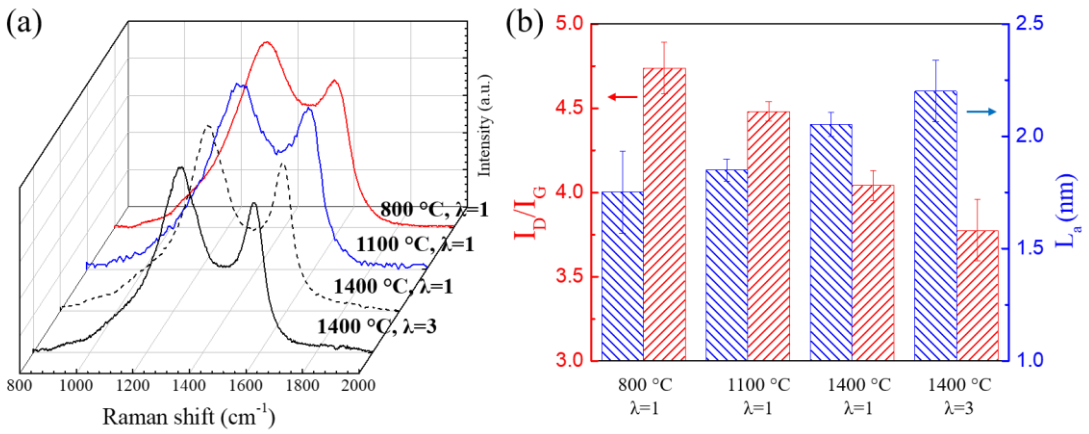

Figure 4.1. (a) Raman spectrum and **(b)** I_D/I_G ratios and L_a of CNFs with different fabrication conditions.

Increasing the carbonization temperatures, especially from relatively low carbonization temperatures can lead to stronger CNFs by promoting the graphitic content of the nanofiber [18, 145]. However, carbonization at temperatures above 1400 °C may compromise the strength of CNFs [18] and CF [34]. Hence, the highest carbonization temperature used in this study was 1400 °C. The loss of strength in CFs fabricated above 1400 °C was observed as early as 1975,[146] but even as recently as 2016 its cause is speculated [147]. A survey of literature suggests that it can be induced by stress concentration along interfaces of partially misaligned turbostratic domains [18, 34, 148], generation of atomic

scale voids due to denitrogenation,[146] or the reduction in the density of covalent crosslinks (sp^3 bonds) within turbostratic domains [147].

Apart from carbonization temperature, the Raman spectrum of the CNFs also shows that the hot-drawing of precursor nanofibers can effectively enhance the graphitic structure within CNFs, Fig.4.1 (b). For instance, as shown in the figure, the CNFs fabricated by carbonizing the hot-drawn precursor (λ = 3) have a lower I_D/I_G and thus defect density compared to the CNFs obtained from undrawn precursors (λ = 1) both fabricated at 1400 ºC. Moreover, as shown in Fig.4.1 (b), the reduction in defect density is also accompanied with a widening of the graphitic domains from ~2.05 nm to ~2.2 nm. In other words, denser packing, higher chain alignment, higher degree of crystallinity and

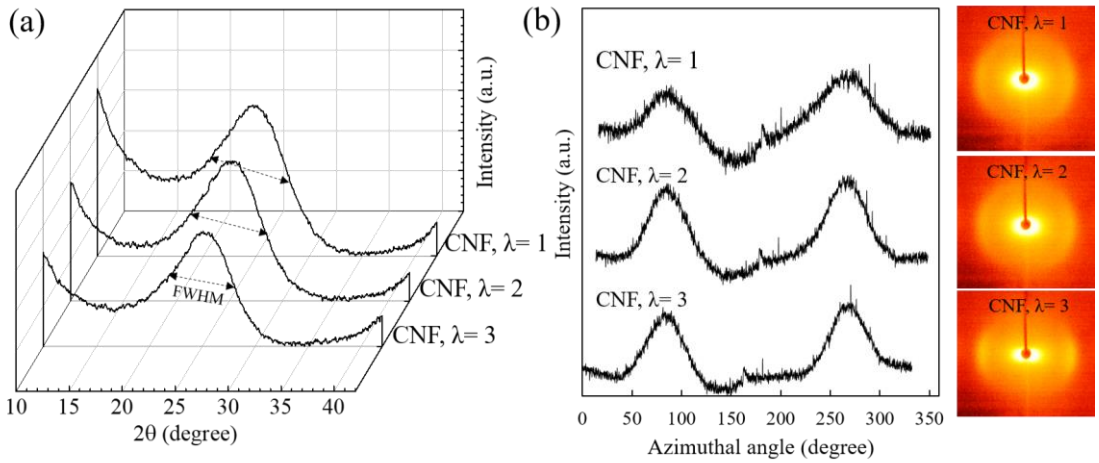

Figure 4.2. (a) WAXD curve and **(b)** 2D intensity azimuthal scan of CNFs with different hot-drawing ratios.

larger PAN crystals in hot-drawn precursors (discussed in previous section and presented in Table 4.1) which is partly preserved in the following stabilization and carbonization processes, facilitate the merger (zipping) of the cyclized PAN chains during the carbonization, leading to lower defect density of graphitic structure.

Therefore, based on the Raman spectrum of CNFs obtained at various carbonization temperatures, carbonization at 1400 ºC resulted in the lowest defect density and widest graphitic domains. The crystalline structure and mechanical properties of CNFs obtained at this temperature was further analyzed. The crystalline structure of CNFs obtained by carbonizing hot-drawn precursors to various hot-drawing ratios at 1400 ºC was characterized by WAXD. The appearance of peak at $2\theta \sim 25°\text{-}26°$, corresponding to (002) plane of the graphitic structure, indicates the formation of graphitic domains in the CNFs, Fig.4.2, in line with the emergence of the G peak in the Raman spectrum (Fig.4.1). By increasing the hot-drawing ratio of precursor nanofiber, there is a continuous increase in crystallite thickness (normal to the basal plane of graphitic domains, as measured by using Scherrer's equation with K = 0.89) from 1.15 nm in CNFs of undrawn precursors to 1.27 nm in CNFs of hot-drawn precursors with $\lambda = 3$. The increase in crystal thickness in CNFs via precursor hot-drawing is accompanied with an improvement in the alignment of the crystalline domains within the CNF as indicated by the Herman's orientation factor. For instance, increasing the precursor hot-drawing ratio from $\lambda = 1$ to $\lambda = 3$ led to an increase in the Herman's orientation factor of graphitic domains within CNFs from 0.44

to 0.52. This result reaffirms the direct correlation between chain alignment in the precursor and graphitic alignment in carbonized structures.

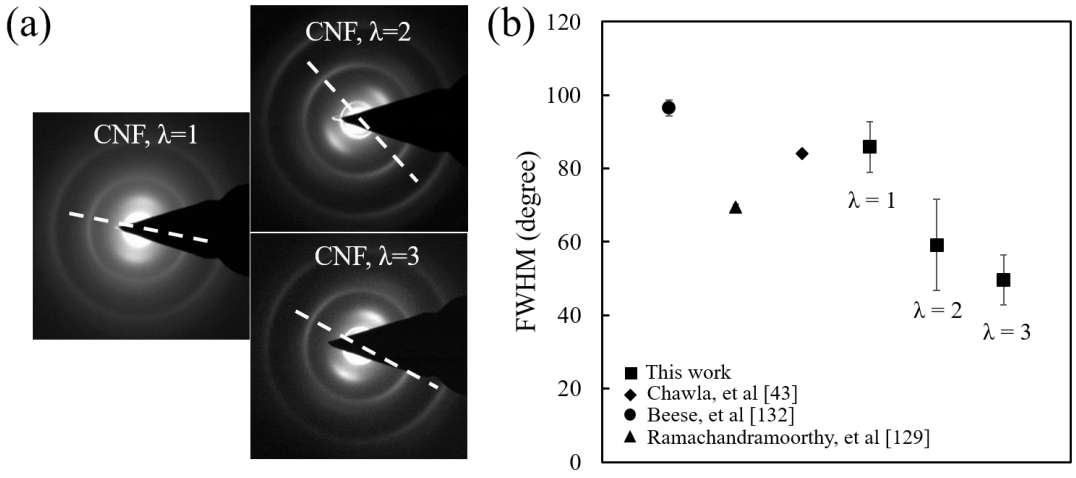

Figure 4.3. (a) SAED pattern of CNFs with different hot-drawing ratios with dash line showing direction of CNF and **(b)** FWHM of (002) arc in SAED pattern of CNFs in this work comparing with CNFs from other researches.[43,129,132]

The alignment of crystalline domains within CNFs was also studied via SAED, Fig.4.3. By increasing the hot-drawing ratio of precursors, there is a continuous increase in the alignment of crystalline domains, indicated by a reduction in the full width half maximum (FWHM) of the integrated intensity of (002) arc in SAED pattern. The FWHM of CNFs with $\lambda = 1$ decreases drastically from 86° to 50° for CNFs with $\lambda = 3$, indicating a narrower distribution of crystalline domains in CNFs with hot-drawn precursors.

The SAED is commonly used to characterize the alignment of graphitic domains in CNFs, thus, the FWHM measurements of SAED can be used to compare the graphitic

alignments in our work with existing studies. For instance, as shown in Fig.4.3(b), increasing the carbonization temperature from 1100 °C (the work by Chawla, *et al.*) [43] to 1400 °C (this work) in CNFs both obtained from undrawn precursors does not lead to any evident change in graphitic structural alignment. This is expected, as increasing the carbonization temperature can only facilitate the growth of the graphitic content, and it offers no effective mechanism to improve alignment. Compared to CNFs from another study (no precursor hot-drawing) [132] which were carbonized at 800 °C, our CNFs which were obtained from undrawn precursors have slightly higher graphitic alignment (lower FWHM) likely due to the different electrospinning parameters used which affects the microstructure of the precursor, thereby properties of CNFs, while precursor hot-drawing in this work leads to significantly narrower (002) arc, Fig.4.3(b).

Moreover, Ramachandramoorthy, *et al* [129] successfully improved the alignment of graphitic structure by applying constraining forces during carbonization at 800 °C, which effectively improved mechanical performance of CNF. However, ladder structure of stabilized cyclic PAN chains are relatively rigid. In comparison, engineering the microstructure of precursor polymer nanofibers in its rubbery state (above T_g - the present study) is likely a more convenient path to align the polymer chain due to the much higher mobility of polymer chains. As such, the FWHM of CNFs with $\lambda = 3$ in our study is ~50°, which is significantly smaller than the work of Ramachandramoorthy, *et al* [129] (~69°), demonstrating the effectiveness of aligning graphitic structure within CNFs through applying hot-drawing to the precursor prior to stabilization.

4.2.3 Mechanical properties of individual CNF

The mechanical properties of individual CNF with different hot-drawing ratios, carbonized at 1400 °C, was characterized by nano-mechanical tension tests under optical microscope. The testing method has been thoroughly discussed in a previous paper [43]. As shown in Fig.4.4(a,c), the strength and modulus of as-electrospun CNFs ($\lambda = 1$) obtained at a carbonization temperature of 1400 °C is 3.7±0.6 GPa and 138±28 GPa, respectively, which are consistent with the previous result from Arshad's work [18]. Compared with the mechanical properties of CNFs carbonized at 1100 °C [43], increasing the carbonization temperature effectively improve the mechanical properties of CNF. The increased carbonization temperature leads to about 100% and 13% improvement in strength and modulus, respectively, in as-electrospun CNFs (no precursor hot-drawing). The improved mechanical performance is due to reduced defect density and enlarged crystalline size (both width and thickness) in CNFs formed at higher carbonization temperature.

The mechanical properties of individual CNF with different hot-drawing ratios, carbonized at 1400 °C, was characterized by nano-mechanical tension tests under optical microscope. The testing method has been thoroughly discussed in a previous paper [43]. As shown in Fig.4.4(a,c), the strength and modulus of as-electrospun CNFs ($\lambda = 1$) obtained at a carbonization temperature of 1400 °C is 3.7±0.6 GPa and 138±28 GPa, respectively, which are consistent with the previous result from Arshad's work [18]. Compared with the mechanical properties of CNFs carbonized at 1100 °C [43], increasing the carbonization temperature effectively improve the mechanical properties of CNF. The increased carbonization temperature leads to about 100% and 13% improvement in strength and

modulus, respectively, in as-electrospun CNFs (no precursor hot-drawing). The improved mechanical performance is due to reduced defect density and enlarged crystalline size (both width and thickness) in CNFs formed at higher carbonization temperature.

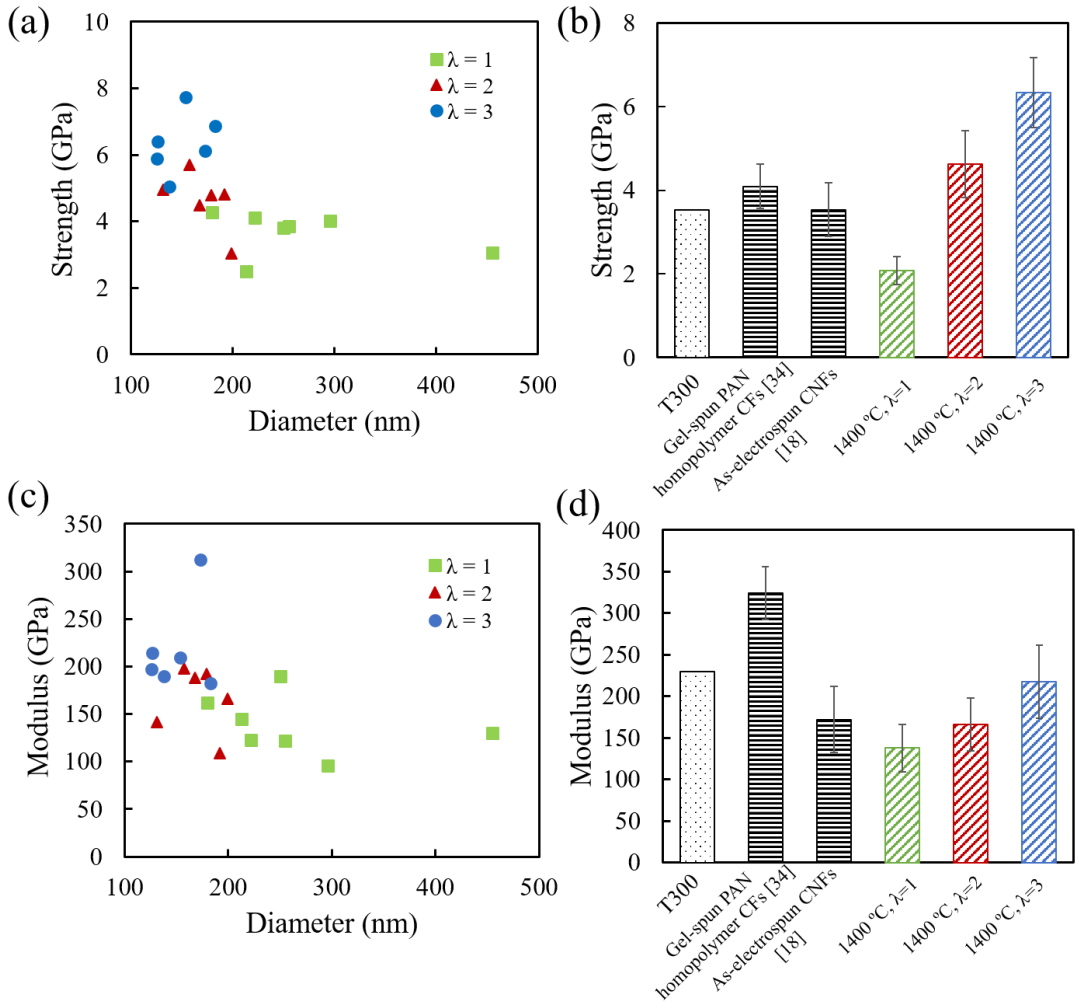

Figure 4.4. (a) Tensile strength and **(b)** modulus of CNFs with different hot-drawings with different diameters obtained in this study. The average values of strength and modulus of our CNFs is compared with **(c)** modulus and **(d)** strength of representative CNFs and CFs that are based on PAN homopolymer [18,34] and a commonly used commercial CF (T300).

We would also like to emphasize that the strongest CNF obtained in our study is ~7.7 GPa, which is even 10% larger than T1100G (strongest CF up to date from Toray Torayca®). Considering the extensive experimental works carried out to optimize the precursor chemistry of commercial CF and the utilization of PAN copolymers in CF industry, hot-drawn electrospun CNFs show great potential as the next-generation super strong reinforcement materials in nanoscale.

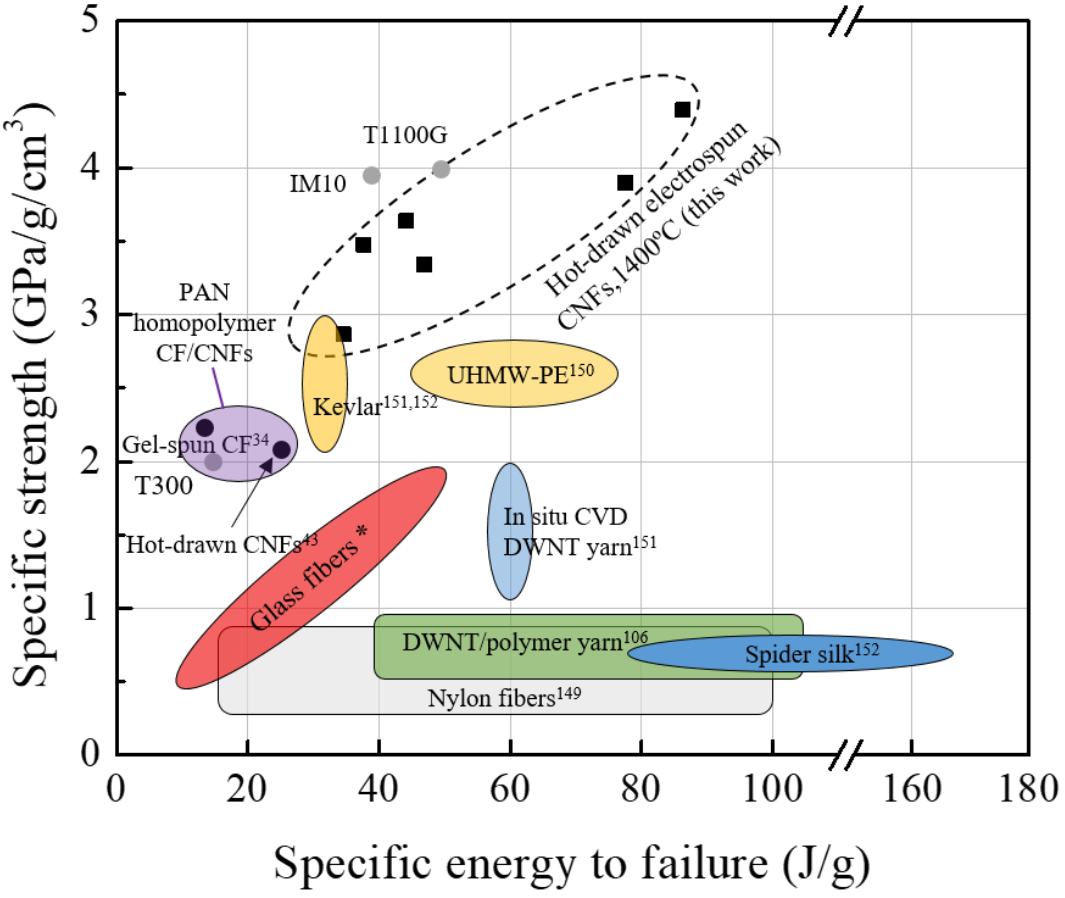

Figure 4.5. Comparison between hot-drawn CNFs (this work) and other engineering materials for their specific strength and specific energy to failure (* The data for glass fibers is obtained from www.AGY.com.)[34,43,106,149-152]

In addition to remarkable strength, the rather large ductility in our CNFs is also interesting. The averaged failure strain of hot-drawn CNF with $\lambda = 3$ is 3.0±0.7%. Compared with CFs made of PAN homopolymer (1.25±0.15%) [34], there is a 140% increase in the failure strain. This large failure strain of electrospun CNFs has also been observed by other researchers [43, 132].

The combination of high specific strength and ductility leads to remarkably high energy to failure (per unit mass), as shown in Fig.4.5. The combination of high specific strength and energy to failure is an essential requirement for advanced fibers. As shown in Fig.4.5, the combination of high specific strength and energy to failure is the highest of all CF/CNF developed up to date. Comparing with the commercial CF (T-300), there is 80% increase in the specific strength and 267% improvement in specific energy to failure. Moreover, while the obtained specific energy to failure (55±20 J/g) of CNF is comparable to some super tough fibers [149-150], such as Kevlar (36-78 J/g) [151-152], DWNTs/polymer fiber (100 J/g) [107], spider silk (165 J/g) [152], the specific strength of hot-drawn electrospun CNF is much higher than all these materials, making them a suitable candidate for applications which call for high strength and flaw-tolerance, such as aerospace fields.

4.2.4 Failure mechanism analysis of hot-drawn CNFs

Since the ductility of CNFs in the present study and a few others [24, 45] is significantly larger than that of CFs, the high toughness and ductility of CNFs is explained in this section by considering the differences in the microstructure of CFs and CNFs, as studied via TEM imaging.

A TEM image of the fracture surface of an electrospun CNF is shown in Fig.4.6 (b). As shown in the figure, the turbostratic domains are partially aligned, but more importantly they appear to be surrounded and dispersed within a *matrix* of amorphous carbon. A similar microstructure was also observed by other researcher [18]. Moreover, there is no apparent variation of the alignment or concentration of TB domains in the radial direction. While the external loading which is along the axis of the CNF favors a crack propagation in the radial direction, *i.e.*, normal to the plane of the maximum tensile stress, the locally heterogeneous microstructure of CNFs offers more energetically favorable alternative path within the weaker phase (amorphous matrix) and/or along the matrix interface with the *fillers* (turbostratic domains), as evident in the TEM images. For instance, zone I in Fig.4.6 (b) shows an instance in which the crack has propagated along the basal plane of a misoriented turbostratic domains. The graphene layers are overdrawn by white line for enhanced visibility. The TEM image of the fracture surface alone does not reveal whether the crack has propagated through the domain by exfoliating the domain in the *c*-direction ("opening" the domain), or has simply moved along the interface of the turbostratic domains with the amorphous matrix surrounding it. Another interesting fracture site is shown in zone II, which is a turbostratic domain aligned with the fiber axis. The length of this domain is comparable to the interior domains observed in the same image. Therefore, the crack has likely propagated around the domain instead of breaking it into smaller domains. The tendency of the crack to move around the rather uniformly distributed turbostratic domains, instead of breaking them, reflects the strength of the domains. As a result of that the crack is forced to follow the orientation of the turbostratic

domains. Thus, a highly tortuous crack path will form, increasing the energy required to completely fail the CNFs.

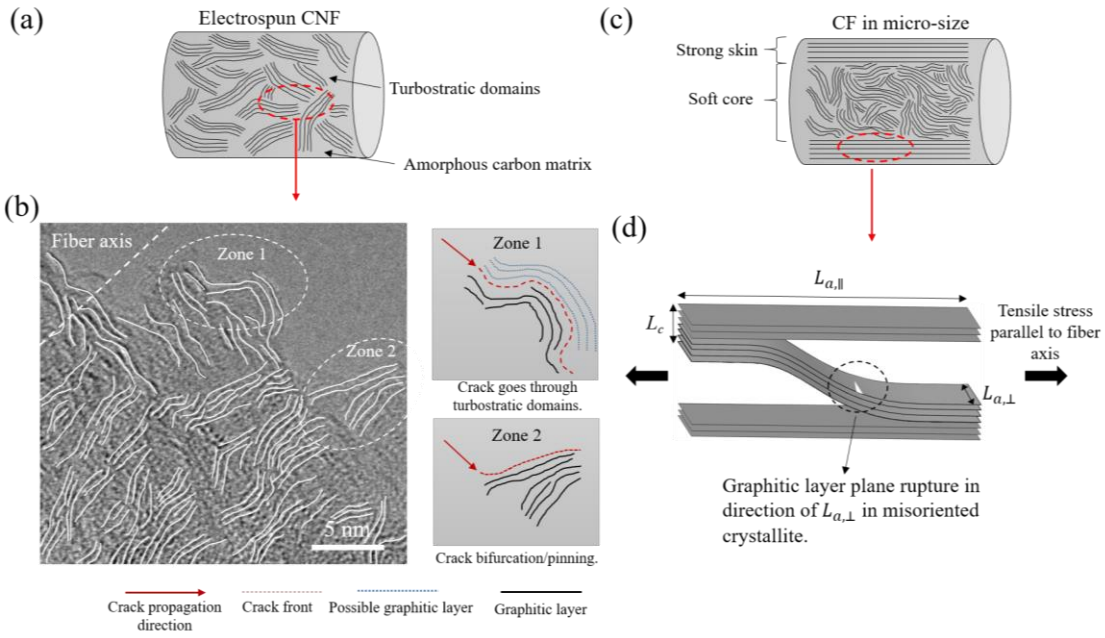

Figure 4.6. (a) Schematic diagram of microstructure in CNF showing randomly distributed graphitic domains in amorphous carbon matrix, **(b)** TEM image of CNF fracture surface and schematic diagrams describing the possible failure mechanism in electrospun CNF **(c)** schematic diagram of microstructure in CF showing skin-core inhomogeneity, and **(d)** Reynolds and Sharp mechanism of tensile failure in CFs, which shows the tensile stress initiated graphitic layer plane rupture and further exertion of stress causes the complete failure of misoriented crystallite. (The schematic diagram is not in scale).

The aforementioned mechanism of toughening in a heterogeneous structure of CNF resembles the toughening mechanisms in nanocomposites, such as graphite nano-platelets (GNP) or thermally reduced graphene oxide (TRGO) within epoxy matrix

nanocomposite [153-156]. The major toughening mechanism in all these cases are crack pinning and deflection.

The microstructure of CNFs can be contrasted with that of CFs. While the CNFs can be described as a composite of partially aligned turbostratic domains within an amorphous matrix, the microstructure of CFs is often described as an intertwined network of "interlinked layer planes" of turbostratic domains [17], Fig.4.6(c), which was demonstrated by the TEM observation of CFs, especially near the surface of CFs [89]. The classical Reynolds and Sharp mechanism of tensile failure in CFs suggests that the shear strain energy is sufficient to induce basal-plane rupture in the misorientated crystallite, and the crack will propagate through the adjacent layer planes in CFs, as shown in Fig.4.6(d) [157]. This fracture mechanism is promoted by the nearly continuous turbostratic domains, or significantly longer domains (along their basal planes) in CFs compared to CNFs. This is in contrast to the fracture mechanism observed in CNFs in which the crack will not break the turbostratic domains, but instead the crack will propagate around them. Therefore, CFs with nearly continuous turbostratic domains can absorb less energy per unit volume and will fail at lower strains compared to CNFs.

The formation of the nearly continuous, interconnected and interlinked turbostratic domains in CFs requires a considerable degree of domain alignment and packing, which is more readily achievable in CFs (compared to CNFs) due to the higher chain alignment in their precursors (for instance, see Table 4.1). As such, in CNFs with hot-drawing ratio of $\lambda = 3$, the crystallite size is about 1.3 nm, which is comparable to the commercial CFs

(T300 with 1300-1400ºC carbonization), gel-spun CFs based on PAN homopolymer (1200 ºC carbonization) [20] and copolymer (1450 ºC carbonization) [10], while the CNFs have significantly lower Herman orientation factor of the graphitic domains.

Table 4.2. Structural parameters comparison of CNFs with different hot-drawing ratios and CFs in micro-size. [10,20]

Fiber types	Diameter(μm)	f_{002}*	FWHM$_{\psi 002}$ (degree)	$L_{(002)}$ (nm)**
CNF, λ = 1 (this work)	0.27	0.44	71.5	1.15
CNF, λ = 2 (this work)	0.17	0.50	52.8	1.20
CNF, λ = 3 (this work)	0.15	0.52	47.5	1.27
CFs from gel-spun PAN homopolymer [20]	1	0.73	37.3	1.3
CFs from gel-spun PAN copolymer [10]	5	N/A	23.1	1.9
T300	7	N/A	31.9	1.5

* f_{002} is Herman's orientation factor of graphitic crystallite in CNF/CF

** L_{002} is crystal size perpendicular to (002) plane in CNF/CF

Other factors may also contribute to the lower ductility of CFs compared to CNFs. For instance, the microstructure of PAN-based CFs is typically described as a skin-core structure, originated from the insufficient stabilization reaction in core zone, as shown in Fig.4.6(c). Comparing to the more randomly orientated turbostratic domains in the core, highly aligned and less defective graphitic structure form in the skin of CF during the fabrication process [17]. This is in contrast to CNFs in which by downsizing the precursor fiber diameter to sub-micron scale, the radial inhomogeneity is effectively eliminated [11, 14]. The radial inhomogeneity in CFs can lead to the formation of microcracks along the

interface between skin and core due to thermal strains developed during processing, further lowering the ductility of the fibers. Moreover, the relatively smooth surface of electrospun CNFs is also considered as one of the reason for its high potential strength and failure strain [14].

4.3 Experimental work for CNF/f-SWNTs

Templating graphitization process, the formation of highly-ordered low defect-density graphitic structure in carbon nanofibers (CNFs), due to the existence of highly graphitic nanomaterials, such as carbon nanotubes (CNTs), was demonstrated to be an effective approach to modify the microstructure of CNFs. In this section, templating effect of functionalized single-walled CNTs (SWNTs) in CNFs facilitated by the thermo-mechanical post processing and the contribution of that to microstructure evolution and mechanical properties of CNF/f-SWNTs hybrid nanofiber are studied in details. To improve the alignment of SWNTs, polymer chain and packing density of polymer chain on surface of SWNTs, hot-drawing was applied as the post-processing treatment to as-fabricated PAN/f-SWNTs precursor nanofiber. After applying stabilization and carbonization processes, CNF/f-SWNTs was obtained. The microstructure of PAN/f-SWNTs and CNF/f-SWNTs were both characterized in a comprehensive fashion by different methods, such as Raman spectroscopy, wide-angle X-ray diffraction. The correlation between microstructure evolution in both precursor and CNFs and post-processing indicates the crucial effect of hot-drawing on microstructure improvement. The Microelectromechanical System (MEMS) based single nanofiber mechanical testing results show the templating effect of CNTs on CNFs mechanical properties would be

further exerted through applying hot-drawing. The existence and evolution of the highly order phase around the CNTs and its influence on the overall mechanical property of CNF are also discussed.

4.3.1 Fabrication of hot-drawn CNF/f-SWNTs nanofiber

To achieve better dispersion condition, functionalized single walled CNTs (P3-SWNT, from Carbon Solution) is used in this work, which contains 1-3 atomic% carboxylic acid groups on surface. Polyacrylonitrile (PAN)/f-SWNTs precursor nanofiber ribbon was fabricated through using similar electrospinning approach discussed in our previous publications [50]. The f-SWNTs were dispersed in dimethylformamide (DMF) solvent (from Sigma–Aldrich) through 4 hours ultrasonication to achieve visible homogeneous solution. Then, polyacrylonitrile powder (M_w = 150,000 g/mol, from Sigma–Aldrich) was dissolved in f-SWNTs/DMF solution to obtain 10 wt.% PAN/f-SWNTs/DMF solution. The concentration of f-SWNTs is fixed at 0.5 wt.% of PAN. Electrospinning process was performed at voltage and distance of 16 kV and 20 cm, and the flow rate of polymer solution was set to ~0.5 ml/hr to obtain stable jet with rotating target at ~5.7 m/s peak-up velocity. PAN/f-SWNTs nanofiber ribbon then was drawn to $\lambda = 3$ (λ, hot-drawing ratio = final length/initial length of ribbon) by applying an engineering stress of ~19 MPa in an oven at a temperature of 135°C. The nanofiber ribbons with different hot-drawing ratios were stabilized at 290 ºC for 2 hours in air circumstance with 5 MPa constraint stress. Carbonization of stabilized PAN/f-SWNTs was carried out in tube furnace (MTI, GSL-1700x) at 1400 ºC for 2 hours under inert gas (N_2) environment without constraint stress.

4.3.2 Microstructure characterization and mechanical testing of CNF/f-SWNTs nanofiber

The microstructure of CNF/f-SWTNs was characterized by Raman spectroscopy, wide-angle X-ray diffraction, by using the method described in section 4.1.2. The mechanical properties of individual CNF/f-SWNTs were measured by using the MEMS device, as discussed in section 4.1.3

4.4 Results and discussion of CNF/f-SWNTs

As shown in our previous experimental works [50], adding unfunctionalized (and low defect density), to electrospun PAN nanofibers especially when the nanofibers are drawn at temperatures above their glass transition temperature to draw ratios of as high as 4 leads to the formation of highly ordered (HO) polymer interphase on the surface of CNTs [136]. Prior studies also show that the carbonization of PAN with CNT inclusions can lead to the formation of highly ordered graphitic regions (HOG) around CNTs. However, the relatively low concentration of pristine SWNTs (0.1 wt.%-0.2 wt.%) that can be well-dispersed in PAN nanofiber without considerable agglomeration, significantly restricts performance improvement in PAN nanofibers and CNFs. For instance, the highest mechanical strength and modulus in PAN/CNTs (pristine CNTs) hybrid nanofibers is achieved at 0.1 wt.% SWNTs, and further increasing the concentration will introduce more CNTs agglomerations and defects, therefore lowering the mechanical properties [50]. Therefore, to overcome this problem, functionalized SWNTs with carboxylic acid groups was used in this work to fabricate the hybrid nanofiber. The carboxyl groups significantly enhanced the dispersion of CNTs in the DMF and also CNT/PAN/DMF solution, demanding significantly shorter ultrasonication times, compared to pristine CNTs, to

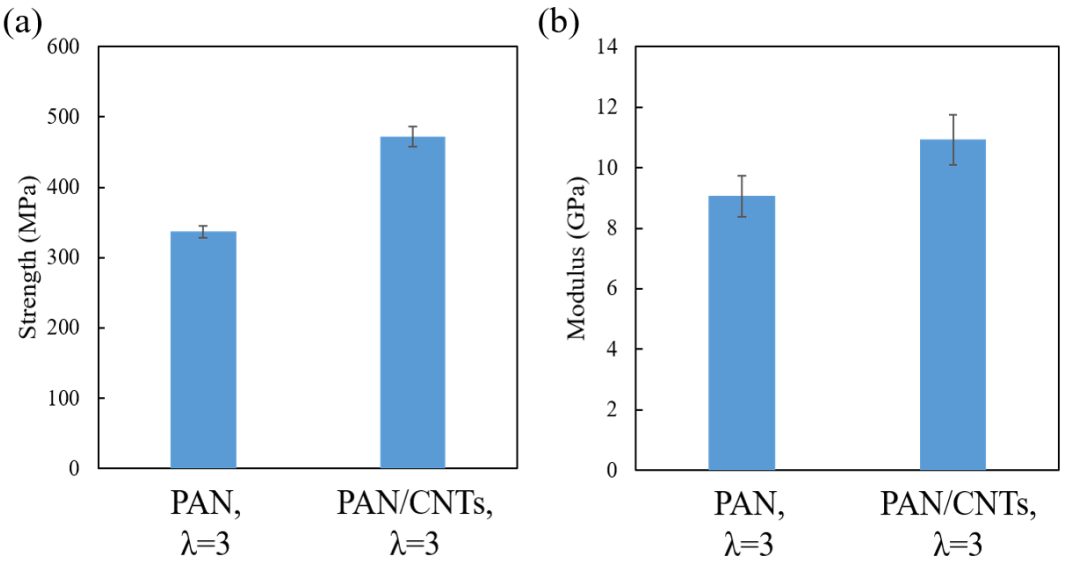

Figure 4.7. (a) Tensile strength and **(b)** modulus of PAN/CNTs nanofiber ribbon.

achieve visually homogeneous solutions. While adding 0.5 wt.% of pristine SWNTs to PAN in a previous work reduced the strength and modulus of the polymer nanofibers compared to the neat polymer nanofiber due to CNT agglomeration [50], the mechanical testing of polymer nanofiber ribbons with $\lambda = 1$ and 3, shows that adding 0.5 wt.% f-SWNTs nanofiber effectively improves the strength and modulus of the ribbons (shown in Fig.4.7). The formation of HO polymer interphase wrapping protruded f-SWNTs, likely in the form of extended chains, are also found at the broken surfaces of hot-drawn PAN/f-SWNTs nanofiber, shown in Fig.4.8. In the following sections, the microstructure of PAN/f-SWNTs with different hot-drawing ratios are analyzed by using various methods.

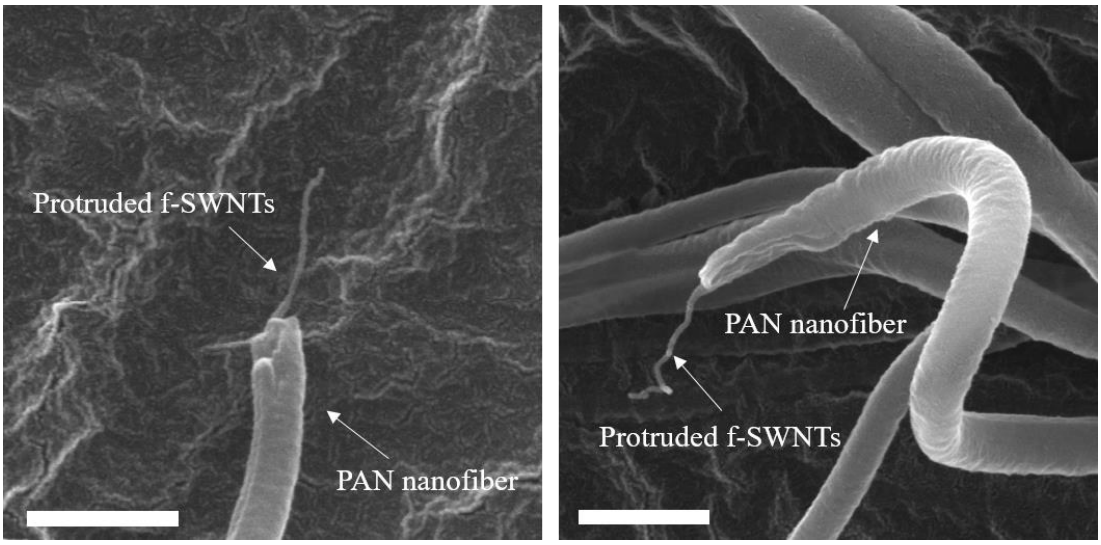

Figure 4.8. SEM images of PAN/f-SWNTs hybrid nanofiber showing protruded f-SWNTs (scale bar = 500 nm).

4.4.1 Microstructure of PAN/f-SWNTs nanofiber

The semi-crystalline structure of as-electrospun and hot-drawn PAN nanofibers was studied via X-ray powder diffraction method. In the x-ray patterns of as-electrospun PAN and PAN/f-SWNTs nanofibers (no hot-drawing), there is no evident crystalline peak (results not shown in the figure). That is due to fast evaporation of the solvent during electrospinning which "freezes" the chains prior to considerable chain alignment is achieved [50]. However, as a result of the hot-drawing to $\lambda = 3$, a crystalline peak of PAN emerges at a diffraction angle of 17º in both types of precursors, pure PAN and PAN/f-SWNTs, Fig.4.9 (a). The degree of crystallinity in pure PAN reaches ~31% (orientation-induced crystallization facilitated via hot-drawing). The degree of crystallinity of hot-

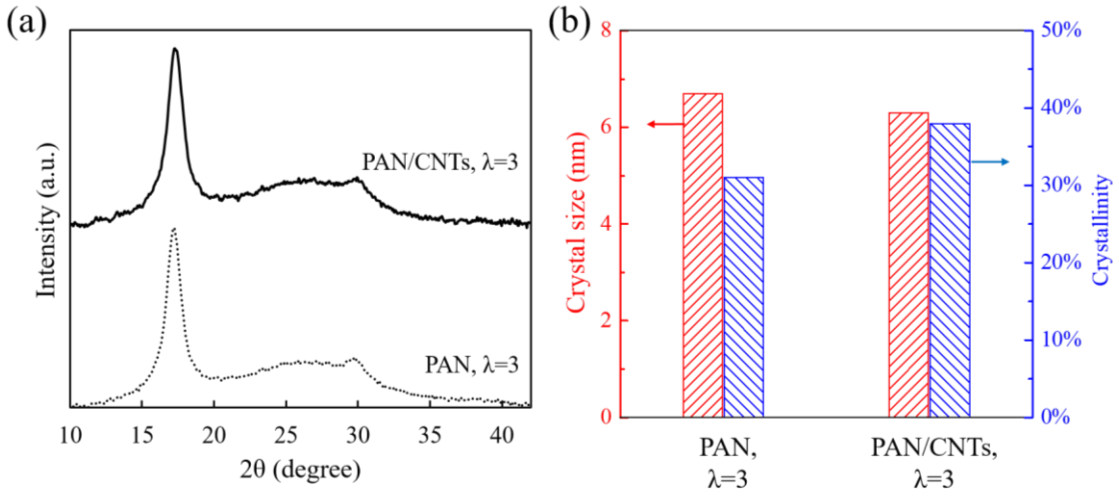

Figure 4.9. (a) WAXD patterns and **(b)** calculated crystallinity and crystal size of PAN and PAN/f-SWNTs with λ=3.

drawn PAN/f-SWNTs nanofibers is markedly higher, ~38%, indicating the role of CNTs as crystallization nucleating agent of PAN, which is consistent with previous results [50]. However, despite the higher degree of crystallinity in PAN nanofibers with CNT inclusions, the PAN crystals formed in hot-drawn PAN/f-SWNTs, measured from Scherrer's equation (K = 0.89) [131], are slightly smaller than the ones formed in pure PAN. It is likely that the growth of PAN crystals around each CNT is partly suppressed by the neighboring CNTs, thus, preventing the growth of a longer range order that can grow around an isolated CNT surrounded by PAN chains.

More information about the crystalline structure of PAN was obtained by investigating their WAXD 2D pattern, Fig.4.10. As mentioned earlier in this section, both the as-electrospun PAN and PAN/f-SWNTs nanofibers (no hot-drawing) are nearly

completely amorphous. However, the symmetric arcs that appear in the WAXD of both samples is a clear indication of not only the formation of crystals, but also the preferential alignment of the crystals, such that the backbone of the PAN chains is more or less aligned with the fiber axis. The preferential orientation of PAN crystals in both types of samples after hot-drawing is comparable, evident in the measured Herman's orientation factors, 0.70 and 0.69, for respectively pure PAN and PAN/f-SWNTs. Following this, the as-electrospun and hot-drawn hybrid nanofibers is stabilized under 5 MPa constraint stress to maintain its molecular chain alignment, which is then carbonized at 1400 ºC (The optimum temperature for obtaining high strength CNFs) to fabricate CNF/f-SWNTs nanofiber.

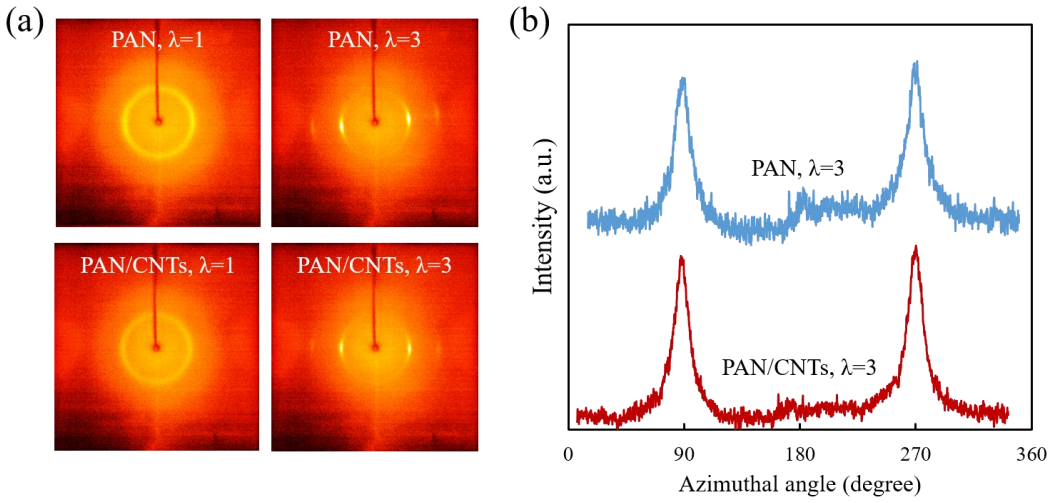

Figure 4.10. (a) WAXD 2D pattern and **(b)** azimuthal intensity scan of PAN and PAN/CNTs nanofibers with λ=3.

4.4.2 Microstructure of CNF/f-SWNTs hybrid nanofiber

The I_D/I_G ratio and the average width of the graphitic crystallites (L_a) was obtained from Raman spectrum of CNF/f-SWNTs, as shown in Fig.4.11. For comparison, the Raman spectra of pure CNFs (obtained by carbonizing pure PAN with no CNTs) are also presented in Fig.4.11. Among pure CNFs, precursor hot-drawing leads to a reduction in I_D/I_G by less than ~10%. A similar trend can also be observed among CNF/f-SWNTs. Thus, it is clear that the chains in hot-drawn precursors can more readily form graphitic domains upon carbonization. This is expected since the hot-drawing will enhance the chain packing, thus, it will facilitate the merger of the chains during thermal stabilization and carbonization. Moreover, the CNTs can as templates for the graphitic structures as they emerge out of carbonizing PAN. However, a more pronounced defect mitigation is observed in CNFs as a result of the addition of CNTs in the precursors (Fig. 4.11). In as

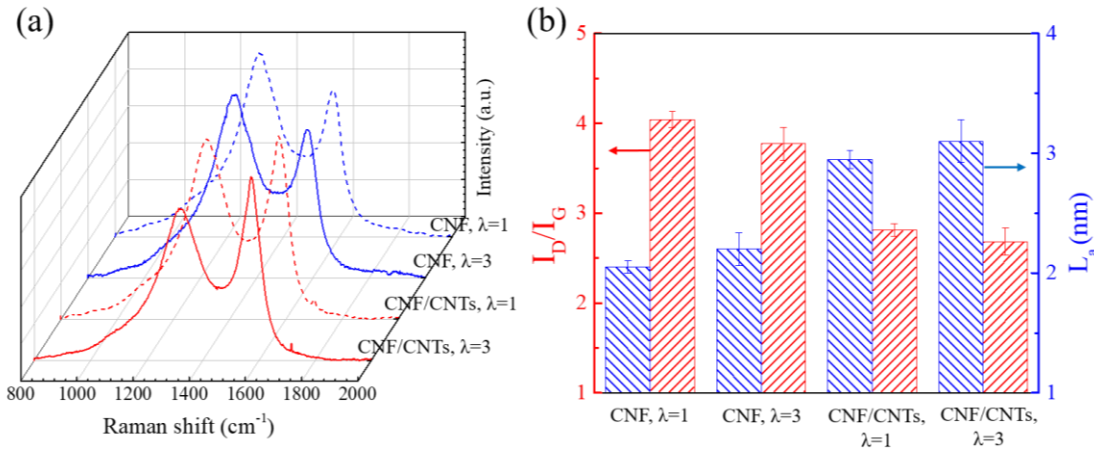

Figure 4.11. (a) Raman spectrum and **(b)** calculated I_D/I_G and crystal size (L_a) of CNF and CNF/CNTs with different hot-drawing ratios.

electrospun CNFs (no precursor hot-drawing), there is a 30% decrease in I_D/I_G ratio and 44% increase in crystallite width (L_a), respectively, in as-electrospun CNF/f-SWNTs compared to pure CNFs. Similarly, in hot-drawn CNF/f-SWNTs, precursor hot-drawing leads to a 5% decrease in I_D/I_G ratio and 5% increase in crystallite size (L_a), indicating the formation of graphitic structure with less defects and larger size, which is consistent with previous works from others [91]. It is to be noted that part of the G- and D-peak intensities in Raman spectrum of CNF/CNTs comes directly from the embedded CNTs, which has much lower I_D/I_G ratio (~0.13) than pure CNFs (~4). Therefore, the decrease in I_D/I_G ratio from as-electrospun CNFs to CNF/f-SWNTs should not exclusively be attributed to the improvement in graphitic structure from templating effect, although the low wt.% of CNTs lowers the significance of this effect.

The graphitic structure of CNF/CNTs was further analyzed by using WAXD, as shown in Fig.4.12. From the WAXD patterns, the Herman's orientation factor and crystalline thickness can be estimated as discussed in the Experimental section. These structural parameters are calculated for CNFs as a function of the precursor hot-drawing ratio and CNT content, and listed in Table 4.3. Prior to precursor hot-drawing, the graphitic crystallite thickness of as-electrospun CNF/f-SWNTs is slightly smaller than the crystallite thickness in pure CNFs (1.212 nm vs. 1.15nm). Moreover, the graphitic structure in pure CNFs has slightly more aligned graphitic structure than CNF/f-SWNTs. The Herman's orientation factor of the former is f_{002}=0.44 compared to f_{002}=0.41 for the latter. This can be traced back to the adverse effect of CNTs on chain alignment in as-electrospun PAN nanofibers. During the electrospinning process, by adding CNTs into

PAN solution, the combined effects of increased solution viscosity and lowered applied voltage leads to less electromechanical stretching on the polymer solution jet during electrospinning, therefore less molecular alignment.

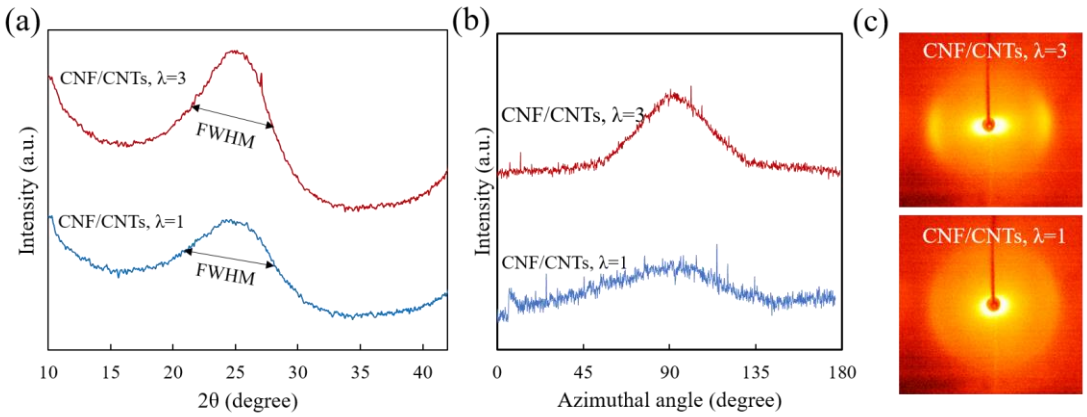

Figure 4.12. (a) WAXD pattern, (b) intensity azimuthal scan and **(c)** 2D pattern of CNF/CNTs with different hot-drawing ratios.

However, by hot-drawing the precursor, there is an evident increase in the graphitic structure of CNF/f-SWNTs, which leads to ~27% and ~19% increase in Herman's orientation factor and crystallite size, respectively, shown in Table 4.3. This improved crystal structure within hybrid CNF/f-SWNTs from WAXD results is consistent with previous Raman spectroscopy analysis result. While in CNFs that are obtained with no precursor hot-drawing, the addition of CNTs can adversely affect the graphitic structure, it is interesting to note that the hot-drawing reverses this effect, such that the hot-drawn CNF/f-SWNT have slightly higher Herman's orientation factor and thicker crystals

compared to hot-drawn pure CNFs. This is in line with the WXRD results on precursors, in which the combined effect of the hot-drawing and CNT inclusions, rather than the CNT inclusions alone, led to the enhancement in crystalline structure of PAN. Therefore, based on the microstructure analysis, it is important to apply precursor hot-drawing in fabricating CNF/f-SWNTs to better exert the templating effect of CNTs and overcome the negative effect on graphitic structural alignment of CNF.

Table 4.3. Structural parameters of CNFs and CNF/CNTs with different hot-drawing ratios.

Nanofiber types	f_{002}*	FWHM,$_{002}$ (degree)	$L_{(002)}$ (nm)**
Pure CNF, λ = 1	0.44	71.5	1.15
Pure CNF, λ = 3	0.52	47.3	1.27
CNF/CNTs, λ = 1	0.41	83.7	1.12
CNF/CNTs, λ = 3	0.52	45.9	1.33

* f_{002} is Herman's orientation factor of graphitic crystallite in CNF
** L_{002} is crystal size perpendicular to (002) plane in CNF

4.4.3 Mechanical properties of individual CNF/f-SWNTs nanofiber

The mechanical properties of individual CNF/f-SWNTs were characterized by using the MEMS-based nano-mechanical testing, Fig.4.13 (a). Two protruded f-SWNTs were observed at the broken surface of an individual CNF/f-SWNTs nanofiber after the tensile testing, which demonstrates the presence of the CNTs within the tested CNFs (Fig.4.13(b,c)). The stress-strain curves are shown in Fig.4.14(a), pointing to a linear elastic behavior of CNF/f-SWNTs with λ=1 and 3. After hot-drawing the precursor, the

mechanical performances of CNF/f-SWNTs were effectively improved. The tensile strength of CNF/f-SWNTs increases from 2.35±0.64 GPa for λ=1 to 6.92±1.39 GPa for λ=3, a 194% improvement. The precursor hot-drawing leads to a 214% increase in average elastic modulus, to 250.2±20.7 GPa.

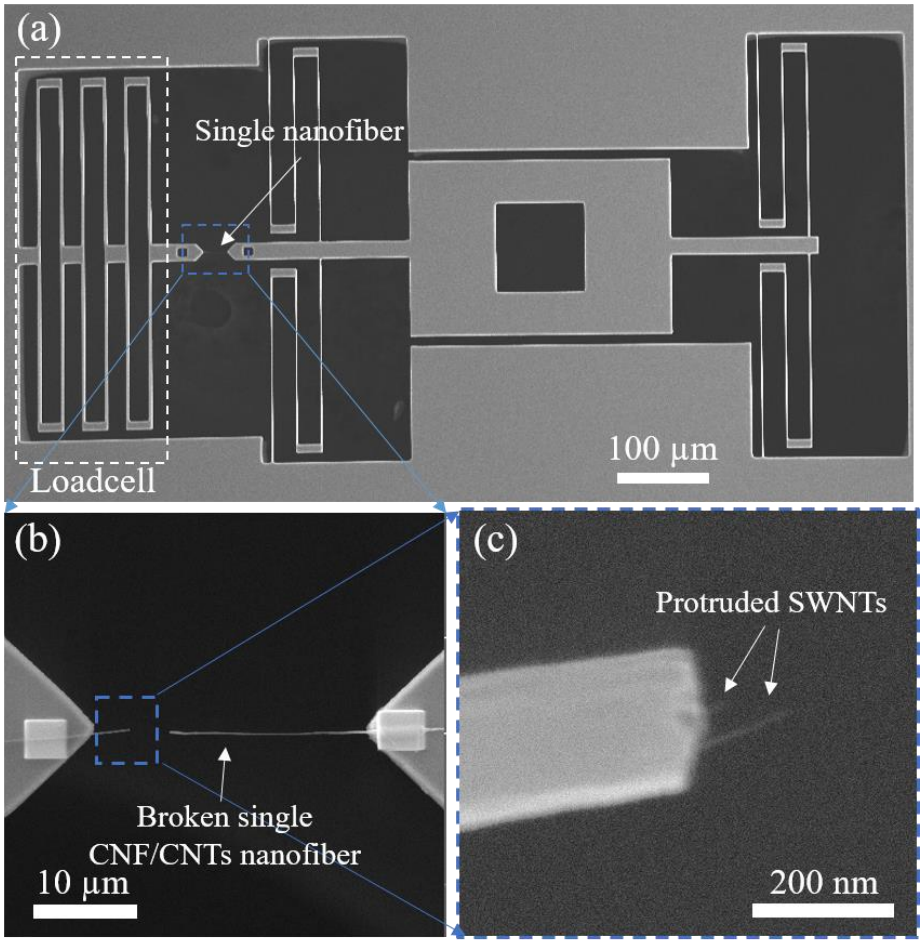

Figure 4.13. (a) MEMS device with single CNF/CNTs nanofiber and **(b,c)** broken surface of CNF/CNTs after testing showing protruded SWNTs.

While in CNFs with hot-drawn precursors, the addition of CNTs increases the strength, in as-electrospun CNFs (no precursor hot-drawing) an opposite trend is observed. For instance, the strength of pure CNFs 3.67±0.59 GPa which is significantly higher than the strength of CNF/f-SWNTs, 2.35±0.64 GPa, and the modulus of pure CNFs is 138±28 GPa which by adding CNTs drops to 80±30 GPa. The loss in mechanical properties, the strength and modulus, by adding CNTs to CNFs, which is only observed in samples with no precursor hot-drawing is consistent with the microstructure analysis in previous section. That is, in as-electrospun CNFs, adding CNTs lower the graphitic crystallite alignment and decrease its size due to the polymer solution property changes (increased viscosity) during electrospinning process. The reduced chain alignment in as-electrospun PAN/SWNT-f nanofibers will lead to a reduced graphitic domains alignment in CNFs and thus reduced strength and modulus. Although according to Raman analysis, the existence of CNTs effectively lowers the defect density within the CNFs, the property improvement due to the formation of highly-ordered graphitic structure cannot overcome the adverse effects brought about by the lowered alignment. On the other hand, after precursor hot-drawing, there is an effective improvement in chain alignment in both pure PAN and PAN/f-SWNTs, which will promote the formation of the graphitic structures as demonstrated by WAXD on CNFs.

The effect of graphitic templating of CNTs can be further alluded to by considering the mechanical properties of hot-drawn CNFs with and without CNTs. The strength of CNF increases from 6.34±0.83 GPa to 6.92±1.39 GPa and modulus increases from 217±44 GPa to 250.2±20.7 GPa, by adding SWNT-f. These are improvements of ~9% and 15%,

respectively, in strength and modulus. The lower relative improvement in strength can partly be explained by the stress concentration that can develop in CNFs around embedded CNTs due to elastic mismatch between the CNTs and its surrounding.

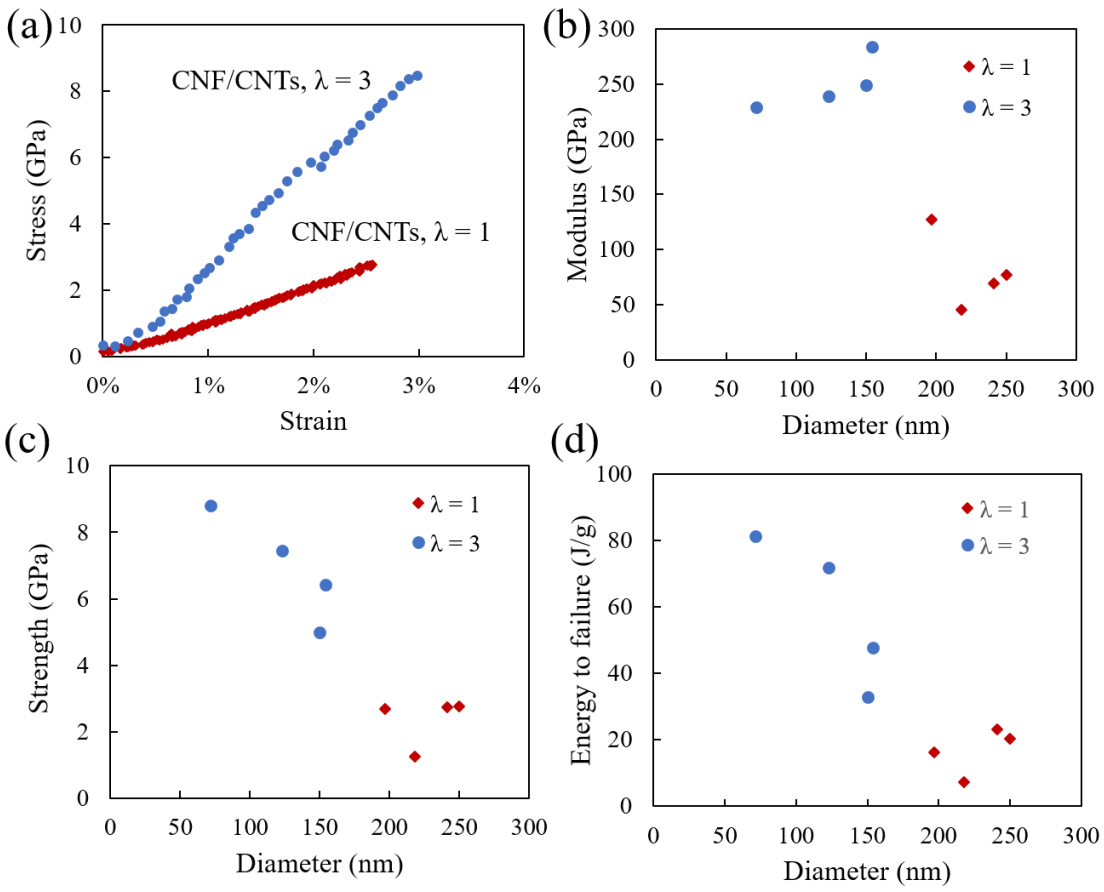

Figure 4.14. (a) Typical stress-strain curve, **(b)** modulus, **(c)** strength and **(d)** energy to failure of CNF/CNTs with different hot-drawing ratios.

The mechanical performances (gauge length > 25μm) of different CNFs and CFs are shown in Fig.4.15. For as-electrospun pure CNFs, through optimizing the carbonization temperature, the largest strength and modulus are improved to 3.5 GPa and 172 GPa, respectively [18]. In this work, by engineering the microstructure of precursor nanofiber through combining the templating effect of CNTs and hot-drawing, the averaged tensile strength and modulus of CNF/f-SWNTs has increased to 6.92±1.39 GPa and

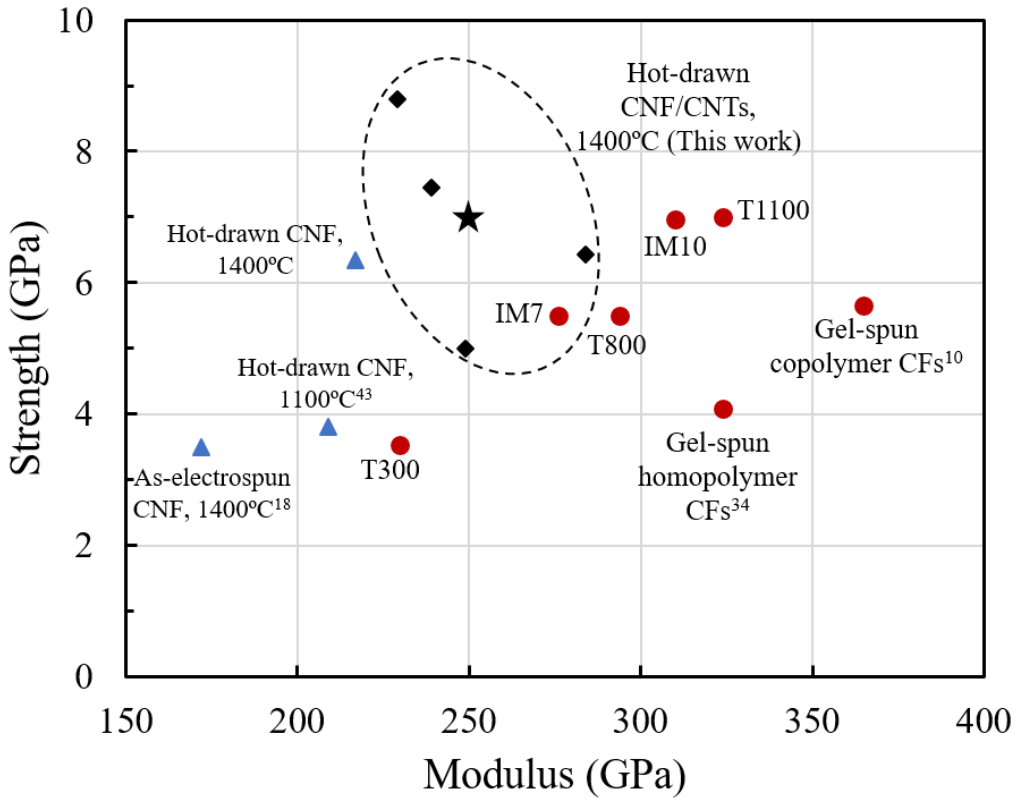

Figure 4.15. Mechanical properties comparison between CNFs and CFs (gauge length > 25μm), with the star mark indicates the average tensile strength of CNF/f-SWNTs with λ=3.[10,18,34,43]

250.2±20.7 GPa, respectively, which is the largest value achieved for CNFs. Therefore, applying hot-drawing is not only important for improving the mechanical properties of pure CNFs, but also crucial to exert the templating effect of f-SWNTs in CNF matrix.

Even comparing to the mechanical performances of CFs fabricated by various precursor polymer systems and approaches [10, 34], hot-drawn CNF/CNTs shows high tensile strength. For instance, the tensile strength of CNF/f-SWNTs is 70% larger than the gel-spun CFs based on PAN homopolymer (4.09 GPa) [34]. As shown in the previous works [43], hot-drawn CNFs shows better radial structural homogeneity and lower defect density than the CFs in micro-size, and this structural advantage has been further improved through introducing templating effect of CNTs. For modulus, considering the inherent advantage of gel-spinning process of precursor fibers, which has higher chain alignment and packing density, there is still a large gap between the achieved modulus of CNF/f-SWNTs in this work and the values from gel-spun CFs. In commercialized CFs, the tensile strength of CNF/f-SWNTs is larger than the medium strength CFs, such as IM7 and T800. The obtained average tensile strength is almost the same as the strongest CFs, which are Hexcel IM10 and Toray T1100 (~7GPa). However, due to the relatively low hot-drawing ratio induced low alignment of graphitic structure within hot-drawn CNF/CNTs, the obtained modulus is still lower than the gel-spun CFs and high performance commercial CFs.

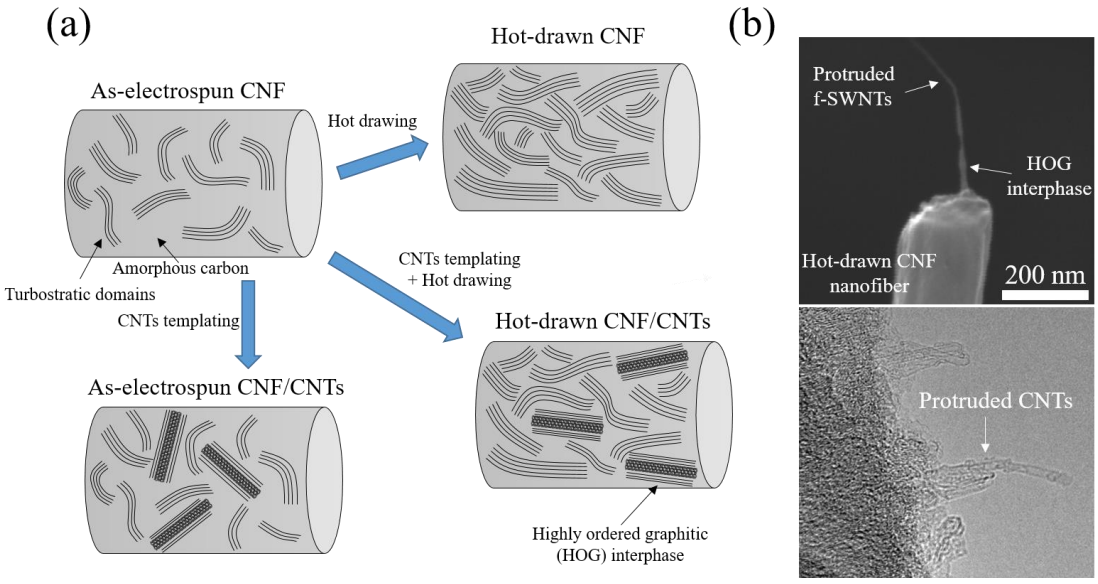

Figure 4.16. (a) Schematic diagrams of different microstructure of CNF and CNF/f-SWNTs from different fabrication methods and **(b)** SEM and TEM showing HOG interphase wrapped protruded f-SWNTs at broken surface of CNFs.

The schematic diagrams of different microstructures of CNFs are shown in Fig.4.16(a). For the as-electrospun CNFs, the randomly orientated turbostratic domains (defective graphitic structures) distribute within the amorphous carbon matrix. The relatively low graphitic alignment in it evidently limits its achievable mechanical property. For further improving its mechanical properties, two approaches were applied, which are introducing CNTs to promote the formation of HOG and applying precursor hot-drawing to increase graphitic alignment. Adding CNTs into the precursor PAN solution, due to the strong interaction between them, polymer chain tends to attach on the CNTs surface to

form highly ordered polymer interphase, which was transferred to highly ordered graphitic interphase, being observed in CF/CNTs hybrid fiber [89]. Although the templating graphitization effect of CNTs in CFs has been demonstrated to successfully improve its mechanical properties [70], for as-electrospun CNFs, due to the influence of adding CNTs on polymer solution properties, apart from templating effect, negative influence has also been brought into the CNFs, such as lowered graphitic structures. Moreover, the CNTs within the CNFs is not aligned along the fiber axis, shown in our previous results [50]. Therefore, although the templating effect of CNTs has generated some highly ordered graphitic structure around its surface, it cannot overcome the negative effect from the previous microstructure modification, which makes the mechanical properties of as-electrospun CNF/f-SWNTs to be less than the as-electrospun CNFs. Another more successful approach is applying hot-drawing process to precursor PAN nanofiber, which effectively modify hot-drawn CNFs microstructure, therefore improving its mechanical performances. To further improve the mechanical properties, f-SWNTs are added to the precursor nanofiber, then hot-drawing is applied to modify the precursor microstructure. During the hot-drawing process, the external applied stress facilitate the aligning of polymer chain, with high chain mobility along the fiber axis. In this process, the CNTs were also aligned along the fiber axis with polymer chain tightly packing around its surface. Then, after the stabilization and carbonization process, highly ordered graphitic interphase is obtained on the surface of CNTs. Due to the templating effect was promoted by the hot-drawing, the obtained interphase has larger thickness, demonstrated by the enlarged crystallite size in WAXD results. Because of the higher alignment of CNTs, the

HOG interphase is also aligned along the fiber axis. Moreover, after hot-drawing, the high alignment of turbostratic domains are maintained in the hybrid nanofiber, comparing to the hot-drawn pure CNFs. All these effects contribute to the overall mechanical property improvement of CNFs, which makes the CNF/f-SWNTs to achieve the highest combination of tensile strength and modulus. Therefore, this work provides an effect approach to further improve the mechanical properties of CNFs through engineering its microstructure.

4.5 Conclusion

We studied the mechanical properties of CNFs obtained by carbonization of electrospun polyacrylonitrile (PAN) precursors. The main microstructural parameters studied were precursor chain alignment achieved via hot-drawing and degree of graphitization controlled by adjusting the carbonization temperature. We limited the draw ratio to 3 to avoid drawing induced defects in the precursors. Moreover, the carbonization temperature was limited to 1400ºC to limit the size of the turbostratic domains and strength compromising interactions between fully grown domains. The microstructure analysis of precursor nanofiber shows the difference between electrospun nanofiber and gel-/wet-spun PAN microfibers (the latter is the precursor of the CFs). The combination of Raman spectrum, WAXD demonstrates the effective improvement of graphitic structure within CNF, including lowered the defect density, increased graphitic domains alignment along the fiber axis and crystallite size with both increased precursor chain alignment and carbonization temperature.

Based on the nano-mechanical testing of individual CNF, the strength and modulus of CNF with $\lambda = 3$ are 6.3±0.8 GPa and 217±44 GPa, respectively. The strength of the hot-drawn electrospun CNF is the largest value achieved among similar materials. Apart from the high strength, the combination of high specific strength and energy-to-failure of CNF is higher than all CNF/CF developed up to now. The energy-to-failure of the CNFs and their ductility is more than twice the corresponding value of the CFs. This was attributed to the peculiar microstructure of the CNFs (a nearly homogenous composite of partially aligned turbostratic domains within the matrix of amorphous carbon), in contrast to CFs with nearly continuous turbostratic domains. The distributed domains in CNFs allow for significant crack deflection and pinning as a means to enhance energy-to-failure.

For further improving the mechanical properties of CNFs and exploring the influence of templating graphitization of CNTs on CNF microstructure and property, functionalized single walled carbon nanotubes (f-SWNTs) were added to the CNFs. The microstructure analysis and mechanical testing of PAN/f-SWNTs indicates relatively homogeneous distribution of CNTs in PAN nanofiber has been achieved, which brings effectively precursor microstructure evolution. Then, the CNF/f-SWNTs were fabricated through applying 1400 ºC carbonization, the optimum carbonization temperature for achieving high strength CNFs identified in previous section. The mechanical properties of individual CNF/f-SWNTs were improved to 6.92 and 250 GPa for tensile strength and modulus, respectively, through effectively microstructure evolution demonstrated by various characterization methods. The strength and modulus combination of CNF/f-SWNTs is the largest value comparing to all CNFs/CFs developed based on PAN

homopolymer up to date. The experimental work in this chapter successfully developed a facile approach to develop high-strength CNFs.

5. PIEZORESISTIVE EFFECT OF INDIVIDUAL ELECTROSPUN CNF FOR STRAIN SENSING*

Extensive experimental and theoretical studies on graphitic nanomaterials, such as carbon nanotubes (CNTs), carbon nanofibers (CNFs) and graphitic nanoparticles, have pointed to their remarkable physical properties.[18, 25, 31, 74-75, 97, 158-160] For instance, the strength of individual CNTs have been measured to be as high as 100 GPa,[74] while electrospun CNFs with strength of as high as 5-8 GPa[18] have been materialized. Apart from excellent mechanical performance, CNTs and CNFs are known to have remarkable electrical conductivity,[75, 160] and thermal stability [161-162].

Inspired by their remarkable physical properties, significant research efforts in the past two decades have been focused on utilizing graphitic nanomaterials as building blocks of hybrid materials to achieve significant improvements in different aspects of physical properties of hybrid materials, such as electrical conductivity and mechanical strength.[163-166] Moreover, couplings between physical domains in graphitic nanomaterials has led to smart materials with sensing capabilities, for instance, as piezoresistive nanoscale sensors.[167] In this regard, CNTs demonstrate piezoresistive behaviors which are attributed to the strain induced opening of their band gaps. However, the theoretically predicted large gage factors[167] (75±5) of CNTs have only been realized experimentally at small strains (below 0.1%), which significantly limits their use. Moreover, the high sensitivity of the

* Part of this chapter is reprinted with permission from "Piezoresistive effect of individual electrospun carbon nanofibers for strain sensing" by J. Cai, S. Chawla, M. Naraghi. Carbon. 2014;77:738-746.

gage factor on CNT chirality will pose another challenge on developing CNT sensors with desired and controlled strain sensitivities.[168-169] Alternatively, electrospun CNFs[18, 31, 160] can be considered as potential piezoresistive materials. As stated earlier in this thesis, individual electrospun CNFs are hybrid nanomaterial, composed of sp^2 and sp^3 hybridized carbon atoms, in which sp^2 hybridized atoms may be clustered in turbostratic domains. Therefore, similar to amorphous carbon, high electrical conductivity of CNFs (~10^{4-5} [170-173]) can be approximated as a combination of electron conduction within the sp^2 hybridized carbon atom regions, followed by electron tunneling in between these regions across the sp^3 hybridized regions.[173] This mechanism of electrical conduction may lead to a piezoresistive behavior through strain induced modulation of electron tunneling distance between sp^2 hybridized regions. This potential piezoresistive mechanism in electrospun CNFs is similar to piezoresistivity in thick film resistors (TFR), which consist of metallic grains embedded in an insulating matrix.[174] While the electrical conductivities of CNFs have been investigated before, their potentials as piezoresistive nanomaterials are largely unexplored. In this chapter, we present our experimental efforts to characterize the piezoresistive behavior of individual CNFs as nanoscale strain sensors. Moreover, we will propose a model that will link the measured piezoresistivity of CNFs to their microstructure. Through the experimental results and our developed model, we will then identify microstructural parameters of CNFs that will lead to enhanced piezoresistive properties and strain sensing capabilities.

5.1 Experimental

5.1.1 Fabrication of CNF

The CNFs in this study were fabricated via thermal stabilization and carbonization of electrospun polyacrylonitrile (PAN) nanofibers. To fabricate PAN nanofiber precursors, Polyacrylonitrile (Sigma-Aldrich) powder with molecular weight of 150,000 g/mol was dissolved into Dimethylformamide (Sigma-Aldrich) to obtain a 9 wt.% solution. This solution was electrospun by using a syringe infusion system to inject the PAN/DMF solution at 1 ml/hr on the rotating disk collector at an electrospinning voltage and distance of 16 kV and 20 cm, respectively. Continuous PAN nanofiber ribbons with 1cm width were obtained on the rotating collector. The PAN nanofibers were stabilized in an oven in air 245℃ for 1h hold time. Following this, the carbonization process was

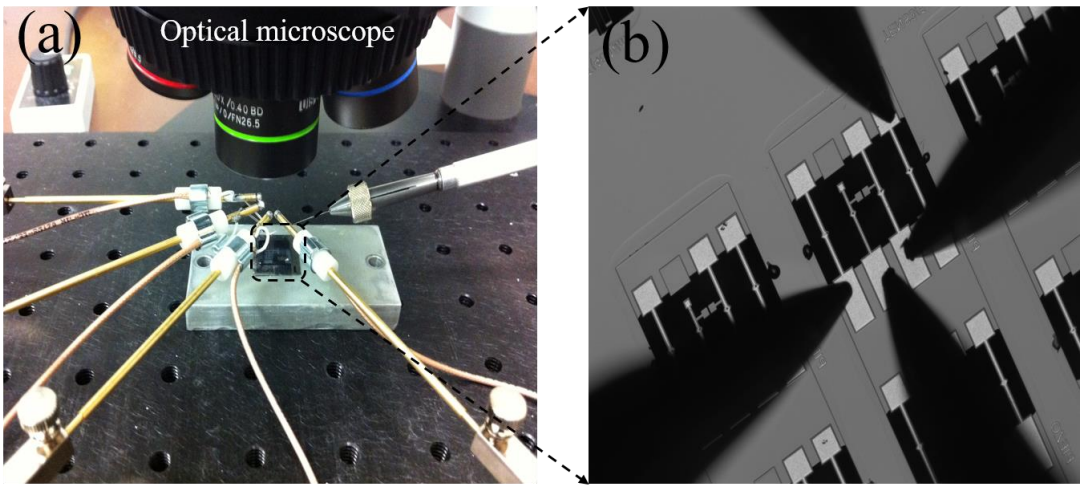

Figure 5.1. (a) Experimental setup for electrical and piezoresistivity testing and **(b)** MEMS device with four testing probes under optical microscope.

carried out in a tube furnace in N_2 atmosphere at 1100 ℃ for 1h hold time. Continuous CNFs were obtained with diameters ranging from 200-800 nm, as confirmed by SEM. The microstructure and surface morphology of CNFs was studied via Raman spectroscopy, TEM and SEM imaging. Then, the electrical and piezoresistive properties of CNF were charachterized by MEMS device, shown in Fig.5.1.

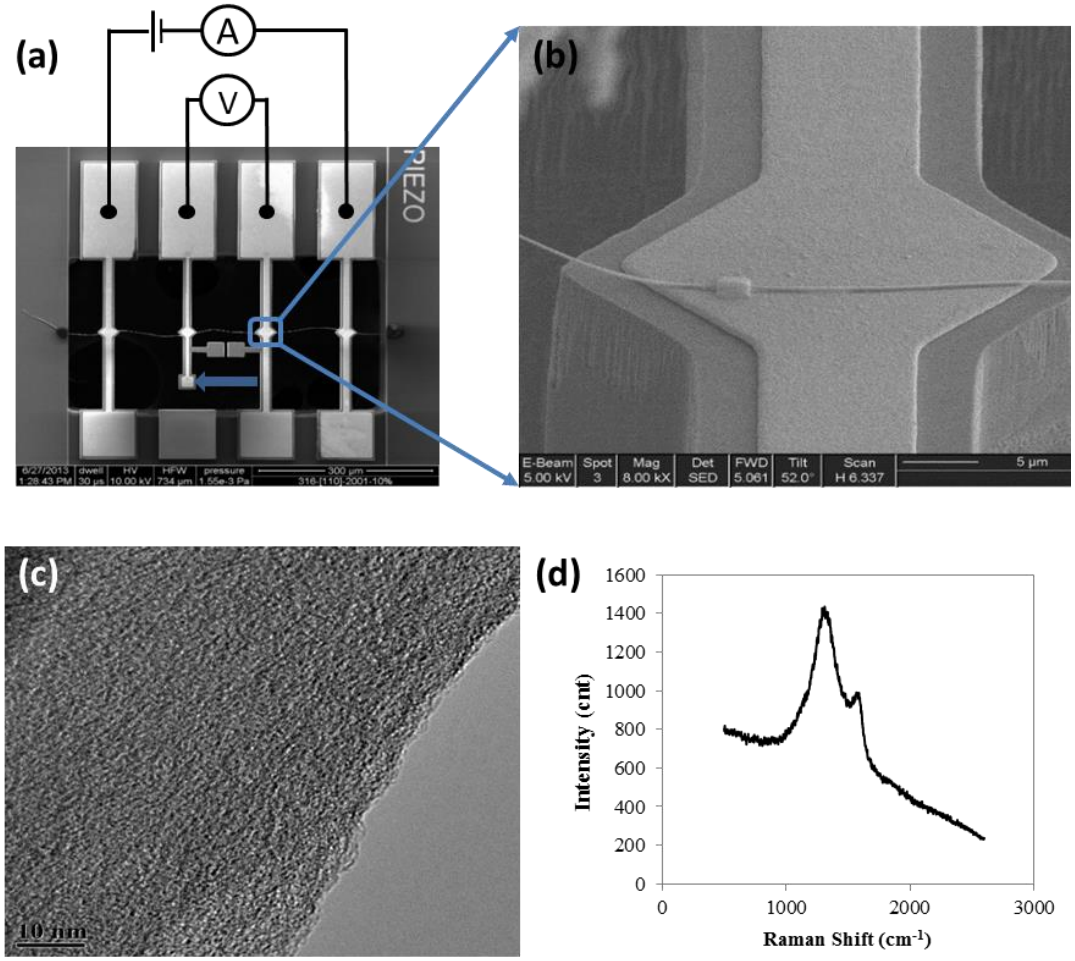

Figure 5.2. (a) SEM image of the MEMS device. **(b)** Pt block was deposited on the CNF to fix it mechanically and conductively on MEMS substrate. **(c)** TEM image of CNFs. **(d)** Raman spectrum of CNFs.

5.1.2 Piezoresisitivity testing of individual CNF

To study the piezoresistivity of individual CNFs, a microelectromechanical systems (MEMS) device with four suspended beams and proper electrical connections was designed was used under the optical microscope. The four beams with 100 µm spacing distance were used to measure the resistance of the nanofibers via 4-point resistance measurement, to eliminate the contribution of wires and contact resistance to the

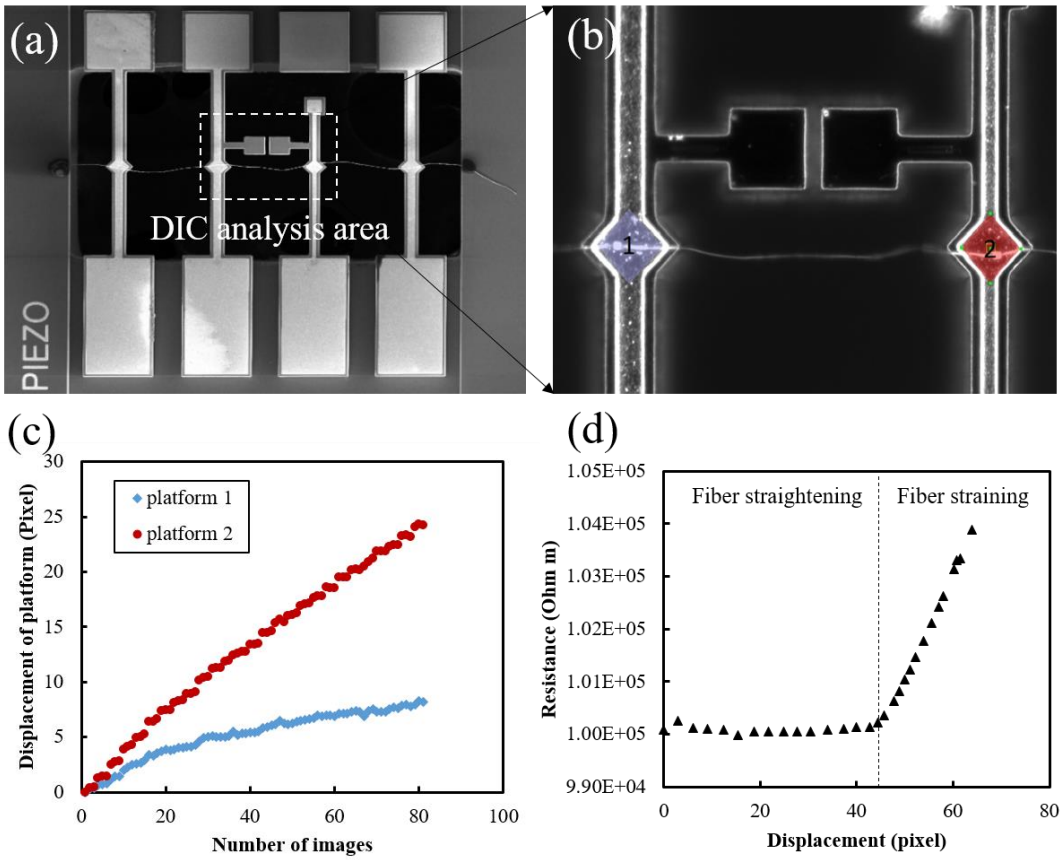

Figure 5.3. (a) DIC analysis area indicated on the MEMS device, **(b)** positions on MEMS beams for DIC analysis, **(c)** obtained displacement of two beams by DIC, **(d)** measured resistance change of individual CNF with increasing displacement.

impedance measurements, as shown in Fig.5.2 (a). The design was fabricated by MEMSCAP company, by using the Silicon-on-Insulator Micromachining Process.

The procedure to mount the CNFs on the MEMS devices was as follows. After putting epoxy glue drops on the two ends of the MEMS device, individual CNF was moved and placed at the right position by using tungsten probe controlled by a micro-manipulator under the optical microscope. To electrically and mechanically connect the CNF to the electrodes, 0.5 μm thickness Pt films with 2 μm×2 μm sizes were deposited by using Focused Ion Beam (FIB) on the CNF at the location of the electrodes, Fig.5.2(b). Four micro-manipulators were used to place tungsten tips on the four electrodes of MEMS device, which were connected to the Keithley 4200 semiconductor characterization system. Then, the electrical resistances of individual CNF were obtained, as shown in Fig.5.3(d). At the same time, another positioner was used to control a tungsten tip to push the cantilever beam in MEMS, which generated a continuous displacement to the CNF. In this process, the electrical resistances of CNF were recorded with increasing the strain of CNF. The experiment was recorded optically, under an optical microscope, and Digital Image Analysis (DIC) was used to analyze continuous optical images of the two beams connecting to CNFs (shown in Fig.5.3(b)) and the displacement information of two beams are obtained, as shown in Fig.5.3(c). Following that, the relative displacement and strain of single CNF were calculated from the difference between displacements of the two beams and the length of CNF sample obtained individually by using SEM imaging. By combining the information of electrical resistance change with time and strain change with time, the piezoresistivity of individual CNF was obtained. For researching the reliability

and repeatability of the piezoresistive effect of CNF, a 3-cycle load/unload test was performed. At first, the nanofiber was loaded continuously to 0.05% maximum strain and then unloaded to zero strain for 3 full cycles. After that, 3 full load/unload cycles with 0.1% maximum strain were applied to the CNF, and then nanofiber was loaded to fail.

5.2 Results and discussion

5.2.1 Piezoresistive effect of individual CNF

TEM images of CNFs revealed no trace of crystalline domain formation, due to the relatively low thermal stabilization temperature (below 250ºC) which was employed in this study (Fig.5.2(c)). However, the G (graphitic) and D (Defect) peaks in the Raman

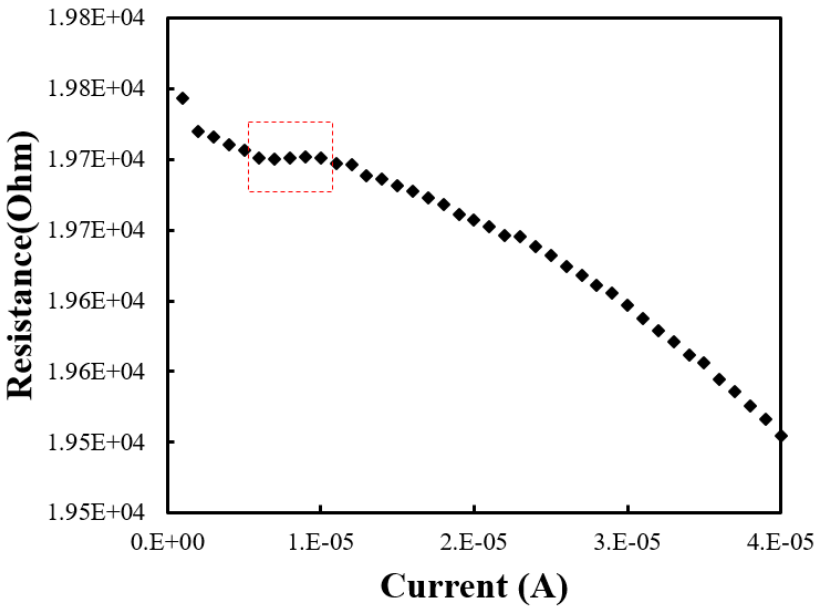

Figure 5.4. Resistance change of individual CNF with increasing testing current.

spectrum of the CNFs mats revealed the formation of sp^2 and sp^3 hybridized carbon atoms [175], respectively, Fig.5.2(d). The existences of sp^2 and sp^3 hybridized carbon atoms regions in CNF were also demonstrated by using EELS in other paper, in which the tested CNF has very similar manufacturing method to the ones we used in this work .[31]

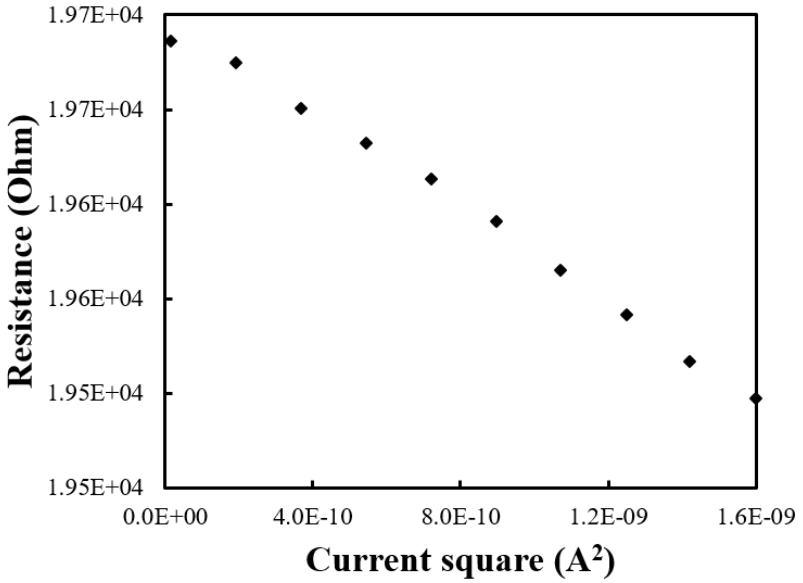

Figure 5.5. Resistance change of individual CNF with increasing testing current square.

To eliminate any uncertainty in the contact electrical resistance between the CNF, Pt films and the MEMS device, we measured the electrical resistance of the CNF using a four point electrode scheme at each step of mechanical loading, shown in Fig.5.4. For this purpose, an input current, *I*, was passed through the CNF via the two outer electrodes, and the electric potential difference between the two inner electrodes was measured. In this regard, the magnitude of the input current should be sufficiently low to avoid any

noticeable heating of the sample (Joule heating), as it will cause an undesired drop in resistance via thermal activation of electrons and releasing more electrons from the valence band to the conduction band. [176] A threshold for such low input current was realized in this study by measuring the electrical resistance of the CNF as a function of input current. As shown in Fig.5.4, within an input current range from ~5μA to ~10μA, the electrical resistance will be independent of the input current. The resistance increase below about 5 μA is believed to be from the uncertainties related to the low input current and the limitations of the instruments. However, higher input currents led to noticeably lower resistance. As shown in Fig.5.5, the change in resistance was proportional to the input electric power or the square of current. Given the fact that near room temperature, the electrical resistance of CNFs decreases linearly with temperature,[177] the linear trend in Fig.5.5 requires a linear relationship between the input electric power and the average

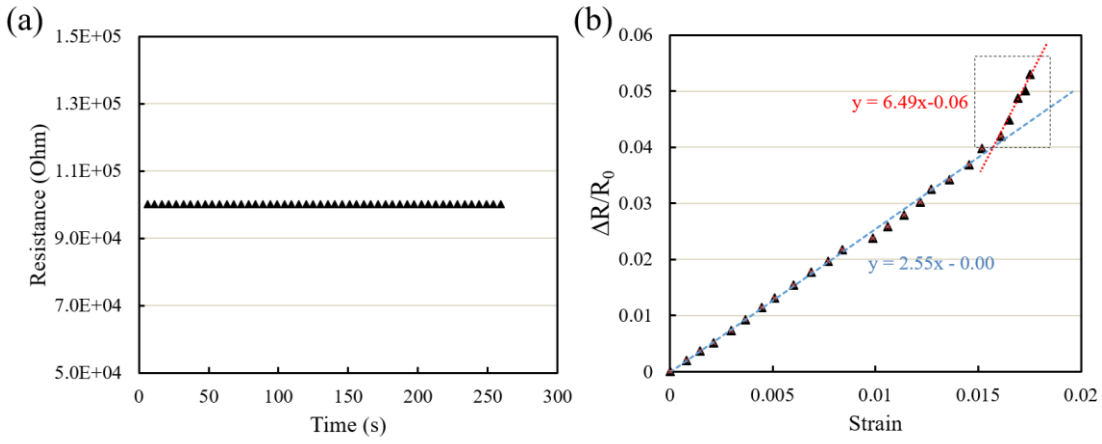

Figure 5.6. Resistance change of individual CNF with **(a)** zero and **(b)** increasing strain.

temperature of the nanofiber, in line with the our understanding that the change in resistance of the CNF in Fig.5.5 is caused by Joule heating and the change in temperature. Therefore, we used input currents of ~5μA during piezoresistive measurements.

To further establish the stability of the MEMS device in characterizing the electrical properties of CNF, several measurements of the electrical resistance of individual CNF at zero strain were made. As shown in Fig.5.6(a), the resistance of individual CNF is relatively constant as increasing the step numbers, which is the measurement of each manually movement of the testing platform for stretching the fiber, which shows beyond random variations of 0.1%, the setup can reliably measure electrical resistance of individual CNF. The piezoresistive effect of individual CNF is shown in Fig.5.6(b), in which there exists a linear response of the resistance of CNF with increasing the strain, a typical result for a piezoresistive material, such as thick film resistor and nanocomposite.[178,179] The failure strain for the CNF was found to be about 1.83%, which is similar to the values obtained by other researchers.[18] The gage factor of the linear response was measured to be ~2.55, which includes the piezoresistive effect in CNF, i.e. the relative change in resistivity per unit strain, and the geometrical changes.

To separate the two effects (piezoresistive effect and effect of geometrical changes on resistance), we considered the following relationship for the gage factor of conductive materials subjected to an applied axial strain of ε,

$$GF = \frac{\Delta R}{R}/\varepsilon = \underbrace{\frac{\Delta\rho}{\rho}/\varepsilon}_{\substack{\text{Piezoresistive}\\ \text{effect}}} + \underbrace{1 + 2\vartheta}_{\substack{\text{geometrical}\\ \text{change}}} \tag{5.1}$$

where the first term on the right hand side represents the piezoresistive effects in CNFs while the last two terms represent the contribution of geometrical changes to the nanofibers resistivity [180]. Here, $\rho \; and \; \vartheta$ are resistivity and poisson's ratio of the nanofiber, respectively. Although comparing with the equations (Eqn.6 and Eqn.39) used in other papers [181-182], Eqn.5.1 is a simplified and linearized gage factor equation, for researching the piezoresistive effect of CNF, whose failure strain is smaller than 2%, this approximated equation is still reasonable and reliable for extracting the dimensional change contribution to the gage factor and obtaining the piezoresistive coefficient.

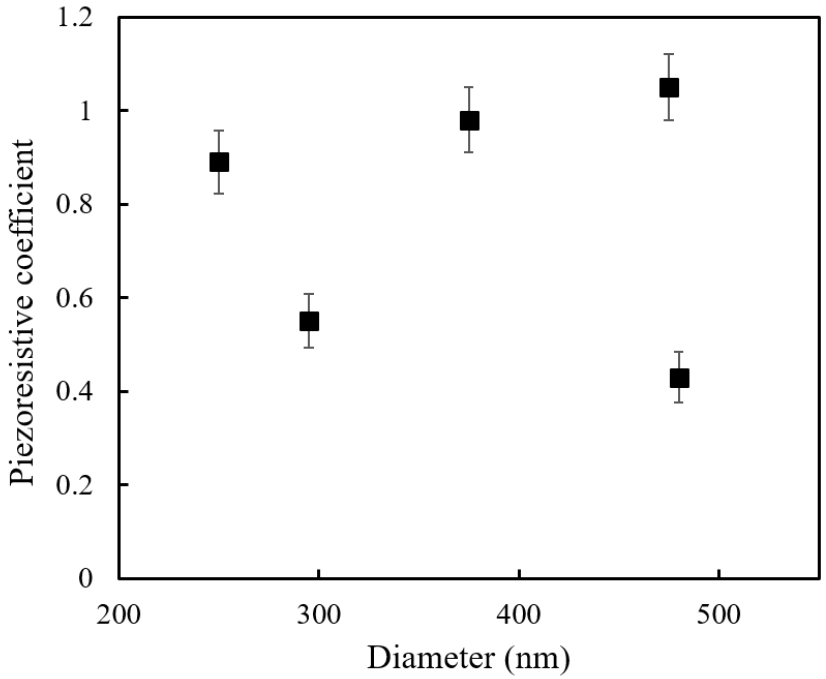

Figure 5.7. The piezoresistive coefficients for five CNFs samples with different diameters

The poisson's ratio of single PAN-derived carbon fiber is in the range of 0.22 to 0.28 [183-184]. Considering the same precursor (PAN) and similar manufacturing conditions (both containing stabilization and carbonization processes in similar temperatures), and therefore the similar structure for CF and CNF [18], the poisson's ratio of CNF is assumed to be within the poisson's ratio range (0.22-0.28) of CF. Therefore, it becomes evident that the piezoresistivity of individual CNF has a significant contribution to the gage factor ($\frac{\Delta\rho}{\rho}/\varepsilon$ constitutes up to 1.05 of 2.55 of the gage factor, which is calculated by using poisson's ratio as 0.25±0.03). Similar gage factors were also measured for four other CNFs samples, where the piezoresistivity of CNFs ($\frac{\Delta\rho}{\rho}/\varepsilon$), was measured to be in the range of 0.46-1.05, as is shown in Fig.5.7. The method for calculating the uncertainty of the measurement of piezoresistive coefficient is provided in Appendix. The initial resistivity of the CNFs is about $(11.7\pm1.8)\times10^{-5}$ ohm·m based on five testing samples. As shown in the figure, the piezoresistive coefficient does not show any dependence on nanofiber diameter, most likely due to the high sensitivity of electron tunneling resistance on average distance between conductive domains and the random nature of arrangements of these domains, as will be discussed in more details in the following paragraphs.

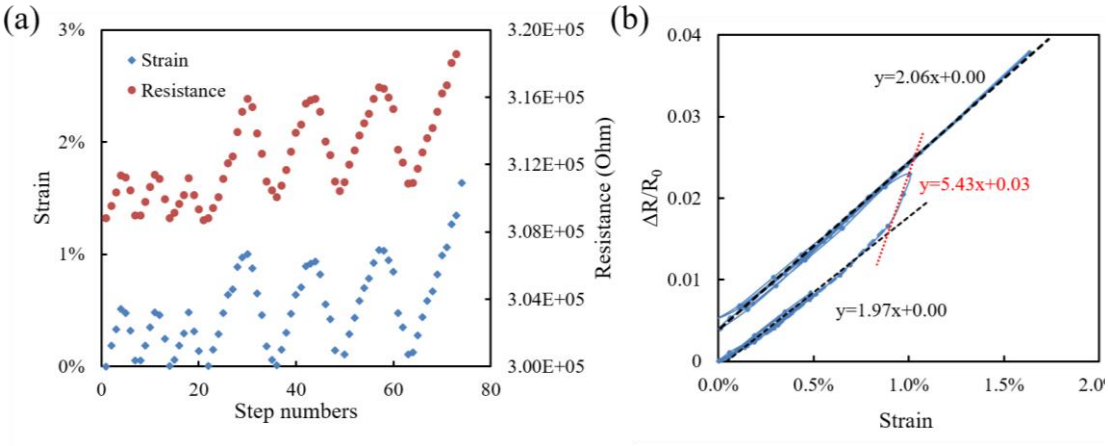

Figure 5.8. (a) The strain and resistance results of 3-cycle load/unload test with increasing step numbers and **(b)** resistance change ratio of CNFs with increasing strain.

It is also interesting to note that the piezoresistive behavior of individual CNFs starts to deviate from the initial linear response at a strain of ~1.6%. This deviation from the linear response appears to follow a linear trend with respect to strain with an apparent gage factor of ~6.49. This behavior is believed to be caused by the micro fractures and plasticity generated on the conduction path within the CNF. This increased sensitivity of electrical resistance at large strains is also found in thick film resistors, and it is typically referred to as "fictitious piezoresistive effect", [185] as it is not caused by a reversible piezoresistive effect, but from the cracks and discontinuities accumulated in conducting paths. To better illustrate this fictitious piezoresistive effect, the piezoresistive behavior of CNFs was also studied in response to cyclic loads.

The applied strain on individual CNF and the corresponding variations in the electrical resistance at each step of cyclic loading is shown in Fig.5.8(a), and the electrical resistance of CNF as a function of applied strain is shown in Fig.5.8(b). As shown in the figures, during the first 3 cycles with maximum strain of ~ 0.5%, there is no evident change in the linear response of the nanofiber, and the resistance of the undeformed CNF remains unchanged. However, by increasing the strain of the CNFs to about 1.1%, the deviation from the initial linear response ("fictitious piezoresistive effect") starts to appear and the zero strain resistance of CNFs is increased by about 0.4%, indicating the accumulation of some damage or plastic deformations in CNF. Similar to the monotonic loading case of Fig.5.6(b), the slope of the fictitious piezoresistive response (apparent gage factor) is ~5.43, which is significantly larger than the slope of the linear part. Despite this deviation from the initial linear response and the accumulation of damages in CNF during fictitious piezoresistive behavior, it is interesting to note that the slope of the strain-resistivity during reloading (cycles 4-6 in Fig.5.8(a)) follows the similar slope even beyond the 1% strain, suggesting that the flaws that caused the fictitious piezoresistive effect during the 3rd cycle at ~1% strain did not grow during reloading in the following cycles, until at least 1.5% strain, at which the nanofiber failed.

5.2.2 Analytical modeling of piezoresistivity in CNF

As demonstrated experimentally, the gage factor of electrospun CNFs is 2.29±0.24, which is higher than typical gage factors of carbon fibers (~1.8-1.9). In contrast to CNFs, the gage factor of carbon fibers (microfibers) is much closer to the values calculated based on geometrical changes of electrical resistance $(1 + 2\vartheta) = 1.44$ $(T300)$

and this obtained gage factor of single carbon fiber in such work was overestimated as including the fictitious piezoresistive behavior. After considering these factors, the author in this paper concluded that the strain induced resistance change in CF is mainly from the dimensional change.[186] Therefore, given the relatively similarities between the fabrication processes of the two types of materials, the differences between their microstructures can guide us towards the origin of piezoresistivity in CNFs. More specifically, the turbostratic domains in carbon fibers, appear to be continuous and interwoven, while in conventional electrospun CNFs, the conductive regions (sp^2 hybridized carbon atoms or the turbostratic domains) are surrounded by the amorphous carbon.[18] This difference is potentially rooted in the fact that precursors of carbon fibers prior to carbonization, unlike electrospun CNFs, are subjected to hot-drawing, which results in the molecular alignment in the precursor and graphitic alignment in carbon fibers (graphitic layers become intertwined). This step, hot-drawing of precursors, is absent from the fabrication steps of the CNFs in this study.

Therefore, it is hypothesized here that the electrical conduction in carbon fibers is dominantly through electric conductions within graphitic/trubostratic domains, while in CNFs, the electric conduction path, in addition to conduction within trubostratic domains, will contain electron tunneling between them. This proposed mechanism of conduction in CNFs is in line with electron conduction in amorphous carbon, as proposed in [173]. Moreover, given the sensitivity of the electron tunneling resistance to tunneling distance, and thus local strain, the proposed mechanism of electrical conduction may account for the enhanced piezoresistivity of CNFs compared to carbon fibers. In addition, the high sensitivity of electron tunneling to the average distance between turbostratic domains and

the random nature of their arrangements in CNFs explains the scatter observed in their pezoresistive coefficient, Fig.5.7.

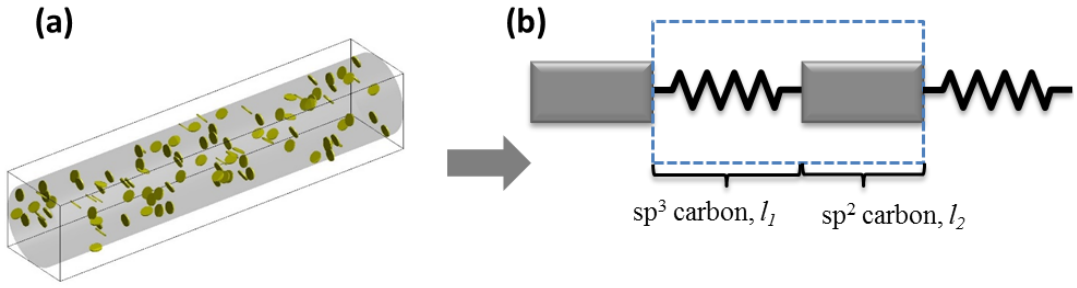

Figure 5.9. Illustration of **(a)** 3-D and **(b)** 1-D simplified microstructure of individual CNF.

To shed light on the significance of conductive domain discontinuity on piezoresistive behavior of CNFs, a simple model of CNFs was developed. Fig.5.9(a) shows a 3-D schmatic microstructure of CNFs, in which the regions of conductive (sp^2 hybridized) carbon atoms were assumed to be plates with certain diameter and thickness embedded in the regions of nonconductive (sp^3 hybridized) carbon atoms matrix in gray color. This model is in line with our Raman spectrum of CNFs, presented earlier (Fig.5.2(d)), according to which CNFs can be considered to be biphasic materials composed of sp^2 and sp^3 hybridized carbon atoms. To simply illustrate the basic mechanism in piezoresistivity of CNFs and the parameters which will influence it, a 1-D model with a periodic arrangement of N insulating parts with length l_1 (sp^3 hybridized amorphous carbon) separated from each other by N conducting parts of length l_2 (sp^2

hybridized carbon atom regions) was adopted as shown in Fig.5.9(b). In this model, the lengths l_1 and l_2 represent the averaged length of amorphous and turbostratic carbon along the axis direction of fiber, respectively. Based on this 1-D model, the total average strain applied in the whole CNF is $\varepsilon = \frac{l_1\varepsilon_1 + l_2\varepsilon_2}{l_1 + l_2}$. Moreover, considering the force equlibrium among two phases in CNF (isostress), we have $E_1\varepsilon_1 = E_2\varepsilon_2$, where E_1 and E_2 are modulii of the two phases, and ε_1 and ε_2 are local strain of each phase in CNF. From these two relationships, we can find the local strains in conductive part and insulating part of CNFs as,

$$\varepsilon_1 = \varepsilon \frac{1 + l_2/l_1}{1 + (l_2/l_1)(E_1/E_2)} \tag{5.2}$$

$$\varepsilon_2 = \varepsilon \frac{1 + l_2/l_1}{1 + (l_2/l_1)(E_1/E_2)} \frac{E_1}{E_2} \tag{5.3}$$

In addition, due to the serial arrangements of the different phases, the resistance of the whole CNF is $R = N(R_1 + R_2) = N(\rho_1 \frac{l_1}{A_1} + \rho_2 \frac{l_2}{A_2})$, where A_1 and A_2, R_1 and R_2, ρ_1 and ρ_2 are the cross sectional area, resistance, resistivity of each part. By assuming $A_1 = A_2$ and seting $V_f = \frac{l_2}{l_1 + l_2}$, as the volume fraction of sp^2 hybridized carbon atoms, we obtain the resistivity of the whole CNF as,

$$\rho = (1 - V_f)\rho_1 + V_f\rho_2 \tag{5.4}$$

Because the electrical conductivity in the sp^3 hybridized carbon phase is mainly due to electron tunneling effect, applied mechanical load will result in a resistance change due to a change of tunneling distance. In this model, the averaged length of the sp^3 hybridized carbon will be assumed to be in the range of 0.154-1 nm, beyond which the effective tunneling conductivity will effectively be negligible. The lower bound of this

range is selected based on the minium distance between Carbon atoms. The tunneling resistivity between two conductive carbon regions can be estimated as: [187]

$$\rho_1 = \rho_0 \exp(d/s) \text{ with } \rho_0 = \frac{h^2}{e^2\sqrt{2m\lambda}} \text{ and } s = \frac{h}{4\pi\sqrt{2m\lambda}} \tag{5.5}$$

where e is the quantum of electricity, m is the mass of electron, h is Planck's constant, d is the tunneling distance between adjacent turbostratic carbon and λ is height of barrier (for amourphous carbon, 0.1 – 0.5 eV [173]). In response to an applied average strain of ε, the tunneling distance will change to $(1 + \varepsilon_1)l_1$, leading to the change in total resistivity as,

$$\Delta\rho \approx \left(1 - V_f\right)\frac{\partial\rho_1}{\partial\varepsilon_1}\varepsilon_1 = \left(1 - V_f\right)\frac{\rho_0 l_1}{s}\exp\left(\frac{l_1(1+\varepsilon_1)}{s}\right)\varepsilon_1 \tag{5.6}$$

In equation (6), the resistivity of the sp^2 carbon regions is assumed to be negligible compared to the other phase, as the resistivity of the former is primarily due to free electrons, while in the latter, the electrical conductivity is controlled via electron tunneling. Therefore, the piezoresistive coefficient of CNFs can be estimated as:

$$\frac{1}{\varepsilon}\frac{\Delta\rho}{\rho} \approx \frac{l_1}{s}\frac{1}{1-V_f+V_f(E_1/E_2)} \tag{5.7}$$

The model predictions are compared with experimental results to find the average values of the electron tunneling distance in electrospun CNFs. For this purpose, the volume fraction of sp^2 hybridized carbon is assumed to be 80%, as has been measured experimentally.[31] Moreover, the ratio of the modulii of the two phases, E_2/E_1 is assumed to be approximately equal to 1. This assumption is supported by the fact that, although both sp^2 and sp^3 hybridized carbon atoms exist in CNFs (Raman spectrum of CNFs –

Fig.5.2(d)), no cyrstalline domain is discernable in TEM images (Fig.5.2(c)). The latter is potentially due to the relatively low stabilization temperatures that was used in this study. In other words, both sp^2 and sp^3 hybridized carbon atom regions are amorphous, and the modulii of their corresponding regions are expected to be about the same as modulus of amorphous carbon atom.

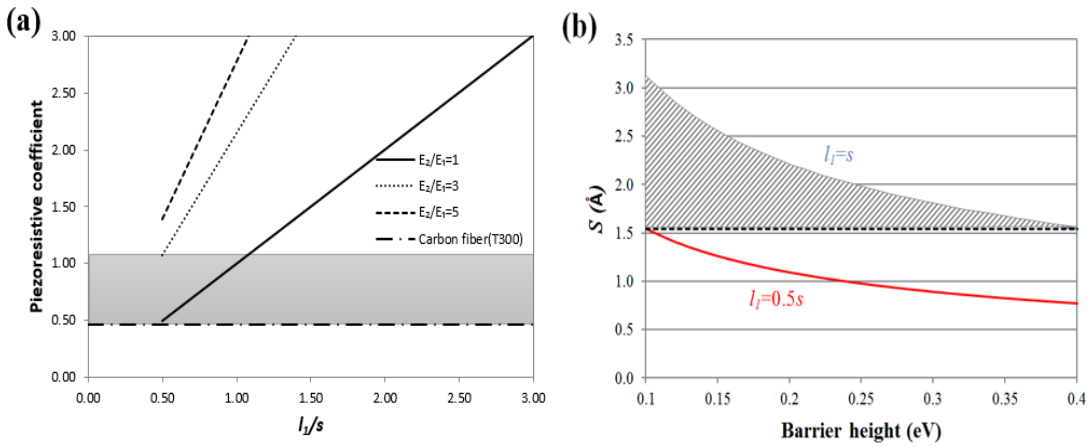

Figure 5.10. (a) The piezoresistive coefficient of CNFs as increasing l_1/s with different modulus ratios, experiment results (grey area) and piezoresistive coefficient of CF (T300). **(b)** Characteristic lengths (s) with varying barrier height and the available number for tunneling distances.

To achieve a reasonable agreement between the model predictions and the measured piezoresistive coefficient of CNFs, 0.46-1.05**,** the ratio of l_1/s should be in the range of 0.5-1 (Fig.5.10(a)). This allowable range of l_1/s was then used to estimate allowable ranges of the tunneling distance, l_1, by considering the values of characteristic length, s. Since electron tunneling occurs between two sp^2 hybridized carbon atoms, tunneling distances that are shorter than the minimum distance between carbon atoms are

not physically meaningful (l_1>0.154nm). Therefore, given the fact that the characteristic length *s* is a function of electron tunneling barrier height, λ (Equation (5.5)), the allowable ranges of the tunneling distance, l_1, can be calculated as shown in Fig.5.10(b). In other words, the predicted tunneling distance ranges from 0.154nm to 0.3nm, which is smaller than the tunneling distance (0.47nm-1nm) for CNTs in polymer matrix. [188] The sp^2 carbon clusters which exist in sp^3 amorphous carbon matrix contribute to this lowered barrier height and tunneling distance. [173]

Finally, the model can be used to devise strategies to enhance the piezoresistive properties of electrospun CNFs. As predicted by this 1-D model, the piezoresistivity of CNFs could be improved by increasing the modulus difference between two phases, for instance, through enhancing the degree of graphitization in sp^2 regions, or increasing the tunneling distance between two adjacent sp^2 carbon phases, through reducing the concentration of sp^2 regions (Fig.5.10(a)). These properties can be controlled via tunning the manufacturing parameters, such as carbonization temperature and the addition of graphitic nanoparticles to precursors of CNFs, which are the subjects of future studies.

5.3 Conclusion

In conclusion, the piezoresistivity of individual electrospun CNF was analyzed by using the newly-designed MEMS device. The resistance decrease of CNF with increasing testing current demonstrated the existence of Joule heating at relatively high current (>10μA). The results of resistance change of CNFs with increasing strain show that the piezoresistivity of CNFs could be accurately and convienently obtained by the MEMS

device, and the gage factor is 2.29±0.24. Piezoresistivity of CNFs is repeatable and stable under cyclic loading, which has been demonstrated by cyclic piezoresistivity tests. At sufficiently high strains (>0.5-1%), mechanical loading induces permanent resistance change and fictitous piezoresistive effect, caused potentially by plastic deformation and microcracks inside the CNFs. Following the experiments, a 1-D modeling work based on periodic resistor model was introduced to get a more thorough understanding of the influence of CNFs microstructures on their piezoresistivity. In this model, individual CNF were modeled as hybrid materials of conductive carbon phases in a nonconductive carbon phase (sp^2 and sp^3 hybridized carbon atoms, respectively). The results show that by increasing the barrier height of amorphous carbon and modulus anisotropy between the two phases, the piezoresistivity of individual CNF will be improved, pointing to strategies to enhance the piezoresistivity of individual CNF.

6. MODELING OF ELECTRICAL CONDUCTIVITY AND PIEZORESISITIY OF ELECTROSPUN CNF[*]

Processing parameters of CNFs provides ample opportunities to modify their microstructure, as a means to enhance certain performance metrics and properties. Given the large number of input variables and microstructural parameters, such as the volume fraction of turbostratic domains, their size and alignment, a purely experimental approach to identify the optimized microstructure for a desired material property is not feasible. To address this limitation, in this chapter, a two-dimensional numerical model based on resistor networks with inter-particle and intra-particle resistors, was developed to predict the electrical properties and piezoresistivity of CNFs. In this model, the CNFs are approximated as a hybrid materials which are composed of a network of conductive particles with electron tunneling in between them. Unlike existing modeling approaches to model the piezoresistivity of hybrid materials, our approach takes into account the impenetrable nature of the conductive particles. Moreover, our model takes into account the complicated conduction within each particle which may arise from their anisotropic electrical properties (such as graphitic particles). Our approach is in essence a multi-resolution approach, in which the electrical conductivity within each particle is calculated via finite element analysis (FEA) to be coupled with network analysis of conduction in between particles via solving Kirchhoff's circuit laws.

[*] Part of this chapter is reprinted with permission from "Computational analysis of electrical conduction in hybrid nanomaterials with embedded non-penetrating conductive particles" by J. Cai, M. Naraghi. Modelling and simulation in materials science and engineering. 2016;24:065004.

Despite the specific example of the CNFs used to elucidate the capabilities of our modeling approach, the length scale of the hybrid materials suitable for this model ranges from 100 nm to cm, representing materials from single CNF in hundreds of nanometer length scale to thick film resistor or nanocomposite materials in micrometer and millimeter length scale. In the submicron length scale, apart from analyzing electrical conductive behavior of single electrospun CNF, the developed model is also suitable to study other kind of hybrid nanomaterials which contain conductive fillers in an matrix with significantly lower conductivity, especially for the low aspect ratio nanofillers, such as hybrid structures of CNFs with CNT inclusions [89]. Moreover, the FEA based strain distribution analysis is used to study the piezoresistivity of the hybrid nanocomposite fiber.

We have used the model to study the effect of microstructure of CNFs, expressed in terms of factors such as volume fraction, alignment, and conductivity of turbostratic carbon on the macroscopic resistivity and its piezoresistivity of the carbon nanofiber. Based on the modeling results, a clear strategy for improving electrical conductivity and piezoresistivity of electrospun carbon nanofiber is proposed.

6.1 Electrical conductive model development

As briefly stated in the introduction, electrospun CNFs are fabricated via thermal stabilization and carbonization of electrospun polyacrylonitrile (PAN) nanofibers. In this process, PAN chains will first be converted to a ladder-like cyclic structure. Moreover, atoms other than carbon will gradually form volatile species such as ammonia gas which

will leave the sample[189]. During carbonization process, turbostratic domains will form in a nucleation and growth process. An example of the turbostratic domains in a CNF is shown in Fig.6.1(a). These particles will be surrounded by sp^3 carbon matrix and partially carbonized PAN. The turbostratic domains become more and more graphitic as the carbonization time and temperature is increased [18]. To estimate the electrical conductivity of CNFs, we modeled the microstructure of CNFs in 2D. Inspired by the fabrication process of CNFs, the microstructure was modeled as conductive particles (turbostratic domains) surrounded by a medium such as amorphous carbon or partially carbonized PAN which was assumed to be nonconductive. The particles were considered to be rectangular in shape, with the longer dimension representing the in-plane graphitic direction in turbostratic domains (a-axis), and the shorter direction represented the c-axis. The orientation of particles were defined as the angle between the a-axis of each particle and the CNF axis. Particles were grown in steps and in random direction from their randomly positioned nucleation sites. The relative growth rate in the a- and c-axis was controlled to achieve average aspect ratios that are consistent with experimental data. Higher and lower aspect ratio particles were also studied to provide more insight into conductivity in CNFs. The particles were grown until the percolation threshold was reached, at which a conductive path formed within the nanofiber. A comprehensive resistor network model, with both intra- and inter-particles resistance, was thus generated to analyze electrical conductivity of CNF. The conductivity of whole CNF was then calculated by solving the linear system of equations of Kirchhoff's circuit laws based on the formed resistor network. Two types of resistances are incorporated in the obtained conductive network,

intra-particle and inter-particle resistances. Complementary methods, including parallel resistor calculation and finite element analysis, were applied to calculate these two kinds of different resistances, as discussed in following parts. The microstructural generation, calculation of the equivalent resistor values and solving the Kirchhoff's circuit laws were all performed in MATLAB R2013a.

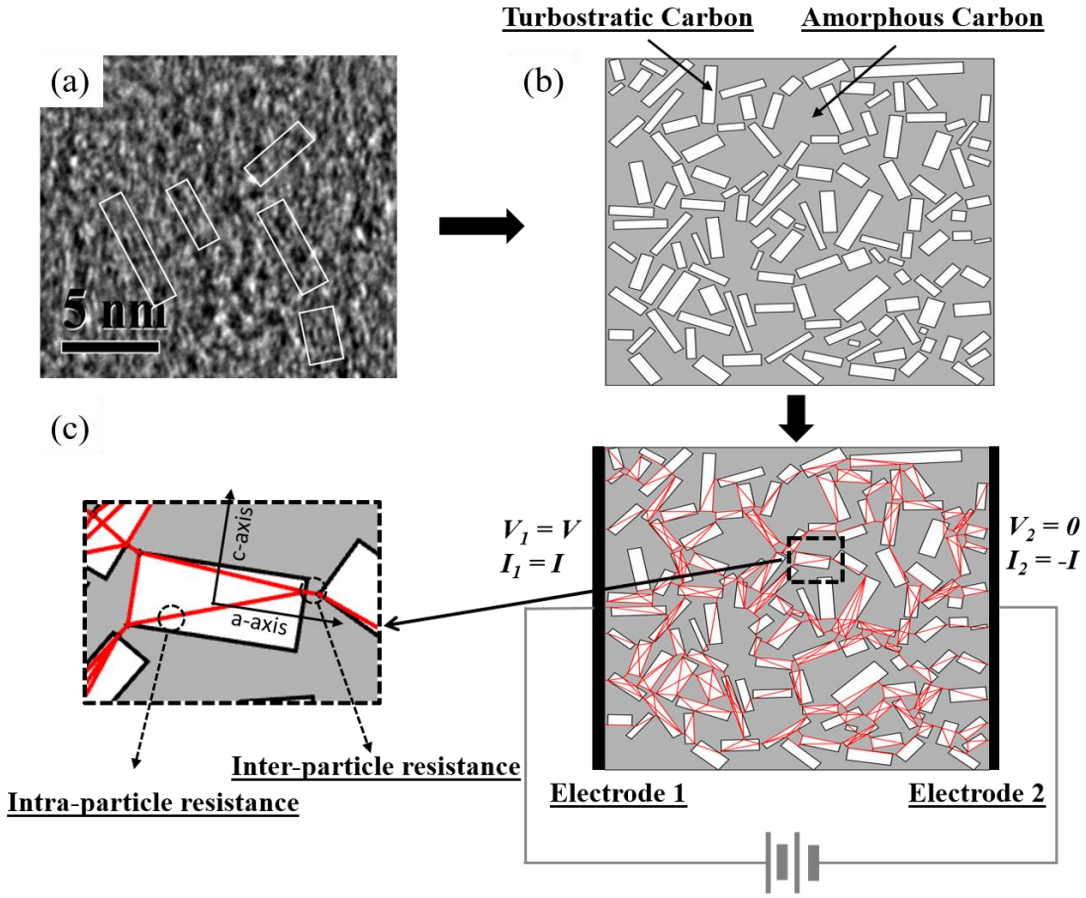

Figure 6.1. (a) TEM image of CNF with turbostratic carbon outlined in white **(b)** simulated structure of the CNF **(c)** boundary conditions for calculating CNF conductivity and obtained resistor network with inter-particle and intra-particle resistances.

6.1.1 Microstructure generation

As is shown in Fig.6.1(b), the microstructure of CNFs in 2 dimensions is approximated with a hybrid structure, in which the rectangles representing the turbostratic domain, which are randomly distributed in the amorphous carbon matrix (grey background). To generate the model, about 150 turbostratic particle nucleation sites were randomly generated within the matrix with dimension of 20 nm×20 nm. The density of the particles were chosen to represent the experimentally measured values from TEM images. The square matrix is chosen based on previous modeling works on nanocomposite, which used 2D square [190] or 3D cubic matrix [191]. Larger aspect ratios increased the scatter in the conductivity measurements.

The particles were then grown from nucleation sites in two directions, representing the a-axis and c-axis in graphitic (turbostratic) particles, as shown in Fig.6.1(c). The orientation angle of each particle, defined as the angle of the a-axis with the CNF axial direction (along which electrical conductivity was measured), was chosen randomly to be below a maximum orientation angles (θ_{max}). A value of θ_{max} of 90° corresponds to a completely randomly oriented particles (particles can have any orientation randomly selected between 0° and +90°). Reducing θ_{max} will generate a cell with particles inclined towards the CNF axis. A θ_{max} of zero corresponds to perfect alignment (not studied here). The growth rate in c-axis of turbostratic carbon is defined as 0.005nm/step, which is 0.286 times the a-axis growth rate, intended to replicate the average aspect ratio of turbostratic domains structures from experimental TEM images. The electrical conductivity of

turbostratic carbon is assumed to be the same as deposited pyrolytic graphite [192], due to its structural similarity to high defect density graphite. To avoid particle penetration, when the minimum distance between two particles became smaller than some critical distance (growth prohibition distance, GPD), the growth of particle in that direction was stopped. The minimum distance between neighboring particles was determined based on experimental electrical conductivity of CNF with different carbonization temperature, which will be explained in following section. This growth mechanism effectively simulates the random size and distribution of turbostratic carbon in practical CNF sample. As the particles grow, the volume fraction of conductive turbostratic particles will increase and reach its percolation threshold.

The electrical path within a percolated network of particles includes two types of resistances, inter- and intra-particle participate, were calculated as discussed in the following sections.

6.1.2 Inter-particle resistance

The inter-particle resistance is assumed to be generated from the electron tunneling effect between two conductive particles. The tunneling resistivity between two adjacent turbostratic particles can be estimated as [187]:

$$\rho_{tunnel} = \frac{\hbar^2}{e^2\sqrt{2m\lambda}} \exp\left(\frac{4\pi d}{h}\sqrt{2m\lambda}\right) \quad (6.1)$$

where e is electron charge, m is the mass of electron, $\hbar$ is Plank's constant, λ is the barrier height of matrix amorphous carbon and d is the tunneling distance. From experimental

results [193], two resistivity bounds are considered for the tunneling resistivity in CNF. The upper bound corresponds to the resistivity of the matrix (amorphous matrix) which is 4.56×10^{-3} Ω·m. The lower bound, 1.81×10^{-4} Ω·m, is the lowest resistivity measured in CNFs, assuming to represent the case of full growth of turbostratic domains and a completely percolated network between them, as shown in Fig.6.2 (a).

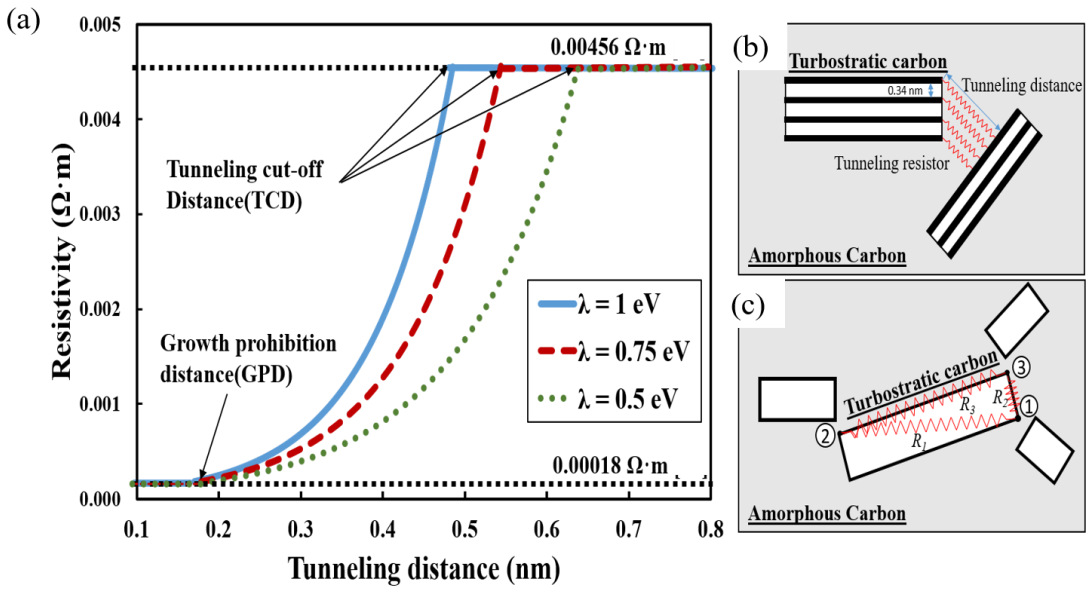

Figure 6.2. (a) Tunneling resistivity between two particles with different tunneling distances **(b)** Inter-particle conductance calculation (c) Intra-particle conductance calculation.

When the minimum distance between two particles are smaller than the tunneling cut-off distance (TCD) for certain barrier height, the tunneling resistance will be calculated. The tunneling resistance between adjacent two particles can be calculated from

the parallel tunneling resistors method, as shown in Fig.6.2(b). To this end, each turbostratic particle will be assumed to consist of parallel graphene layers (along the a-axis) spaced apart by 0.34 nm. Each graphene layer will then be connected to the neighboring particle via a tunneling resistor, which is parallel to the rest of tunneling resistors at that specific contact site (Fig.6.2(b)). To calculate the resistance of each tunneling resistor, the conducting length was considered to be the distance from end point of each graphene layer in turbostratic carbon to the edge of the other particle. Moreover, the projection of 0.34 nm, which is the interlayer distance in turbostratic carbon on the other contacting plane is used as conducting width. The tunneling resistivity is obtained from Fig.6.2(a) with different barrier height and tunneling distance.

6.1.3 Intra-particle resistance

In existing models to predict electrical conductivity of hybrid nanocomposite, such as CNTs/Polymer nanocomposite, the intra-particle conductivity is mainly assumed to be along the axis of the filler and is calculated simply by applying Ohm's law to 1D geometries [191, 194]. This is a reasonable assumption in calculating the overall electrical conductivity of the nanocomposite, mainly due to high aspect ratio (up to several hundreds) of fillers. However, the ratio of the conductivities of turbostratic domains to amorphous carbon is significantly lower, in the order of 10^2-10^4 times, and with aspect ratio to about 3.5. Therefore, proposed approaches in the literature to estimate intra-particle conductivity needs to be revisited. Given the random distribution of the size of each turbostratic carbon and location of contact points, FEA is used here to calculate the resistance within each particle.

Given the anisotropic atomic structure of turbostratic domains along the a- and c-axis in CNF, each particle is assumed to be electrically anisotropic with $\sigma_a = 4.25\times10^4$ S/m and $\sigma_c = 1.39\times10^3$ S/m [192]. Considering electrical anisotropy of particles, each particle which is in contact with n other particles (at n contact nodes), can be replaced with n(n-1)/2 equivalent internal resistors, each connecting two contact points (Appendix B). The following algorithm was then used to calculate these equivalent internal resistors of a particle. We first applied a potential of V = 1V to node 1 (here node 1 is considered to be the primary node) while all other nodes were at V = 0 V. This boundary value problem was solved via FEA (Details of FEA is in Appendix B). To this end, we meshed the rectangle particle with about 50,000 elements. The elements were triangular shaped with three nodes at the apexes. Dirichlet boundary condition was applied at all the contact points. By applying V = 1 at one contact point and V = 0 at all other points, the potential distribution for this boundary condition inside the particle is obtained by solving the steady state electrical conduction Laplace equation in orthotropic medium without internal current source as follows [195],

$$\sigma_x \frac{\partial^2 \phi}{\partial x^2} + \sigma_y \frac{\partial^2 \phi}{\partial y^2} = 0 \tag{6.2}$$

From the FEA, the input current to each node was calculated. Since all the nodes except node 1 are at zero potential, the input current from all the nodes should output from node 1. Therefore, the resistance of the equivalent internal resistor connecting any arbitrary node *i* ($i\neq1$) to node 1 is equal to the inverse of the input current at node *i* (note that the voltage difference between node *i* and 1 is 1 V). Through iteration of the primary

node (the node at V = 1V while others are at V = 0V), all the internal resistors can be calculated for each particle.

6.1.4 Calculation of electrical resistance of the network

The resistance of the conduction path composed of internal resistances of conductive particles connected via tunneling resistance within them was calculated as follows. The current for each contact node *i* within the network was calculated by using Kirchhoff's current law as follows,

$$I_i = \sum_{j=1}^{n} \frac{V_i - V_j}{R_{ij}} \quad (6.3)$$

where *j* is the node number connected to node *i*, V_i and V_j are the potential at node *i* and *j*, and R_{ij} is the resistance between node *i* and *j*. It is to be noted that R_{ij} is either the internal resistance of particles (when i and j are on the same particle) or the tunneling resistance between two particles (when a particle is connected at its contact node i to contact node j of another particle). Moreover, the left and right sides of the CNF box were considered electrodes 1 and 2, respectively, each to represent an iso-potential line. By setting the electric potential of nodes at electrode 1 to be 1V and at electrode 2 to be 0 V, the potential of all nodes within the network can be calculated by solving a system of linear equations[196]. The electrical conductivity of CNF is evaluated by using Ohm's law based on the net current flow between the two electrodes.

6.2 Results and discussion of electrical conductivity modeling

An example of the calculations of the internal resistances in a turbostratic domain with three contact nodes is shown in Fig.6.3. For a particle with 3 contacts (n = 3), the number of internal resistances is 3. The boundary conditions required to capture the internal resistance were applied at contact points[197], and the electrical potential distribution of each turbostratic particle was obtained, as shown in Fig.6.3(b). In this example, size of turbostratic particle is 1.23nm(L)×0.46nm(W), which is a typical size for turbostratic carbon in CNF from experiment, with three contact points locating on the edges of the particle, therefore three equivalent resistors within this particle. First we applied at V = 1V at node 1 while other nodes were at 0V (In B.C.1, node 1 is the primary node). Therefore, the values of R_2 and R_3 were calculated in unit of ohms as $1/i_2$ and $1/i_3$, where i_2 and i_3 were the calculated input currents based on FEA analysis of the particle (described in previous section) in units of Amps at nodes 2 and 3, respectively. Similarly, by applying V = 1V to node 2 and keeping the other two nodes at 0V (B.C.2 where node 2 is the primary node), R_1 and R_3 were calculated, and by applying V = 1V to node 3 and keeping the other two nodes at 0V (B.C.3 where node 3 is the primary node), R_1 and R_2 were calculated.

As noted in this example, each resistor can be calculated by applying V = 1V to either of its two ends, while keeping the rest of the nodes at 0V. That is, each resistor can be calculated from two sets of calculations. This redundancy is simply because of the fact that $R_{ij} = R_{ji}$ (shown in Appendix B). In our analysis, the two calculated values of each resistors were the same within a margin of 2%, believed to be caused by numerical errors.

In the example shown in Fig.6.3(b), the calculated resistance values of resistors are R_1 =8.70×10^5 Ω·m, R_2 =8.74×10^5 Ω·m and R_3 =4.86×10^5 Ω·m based on FEA calculation.

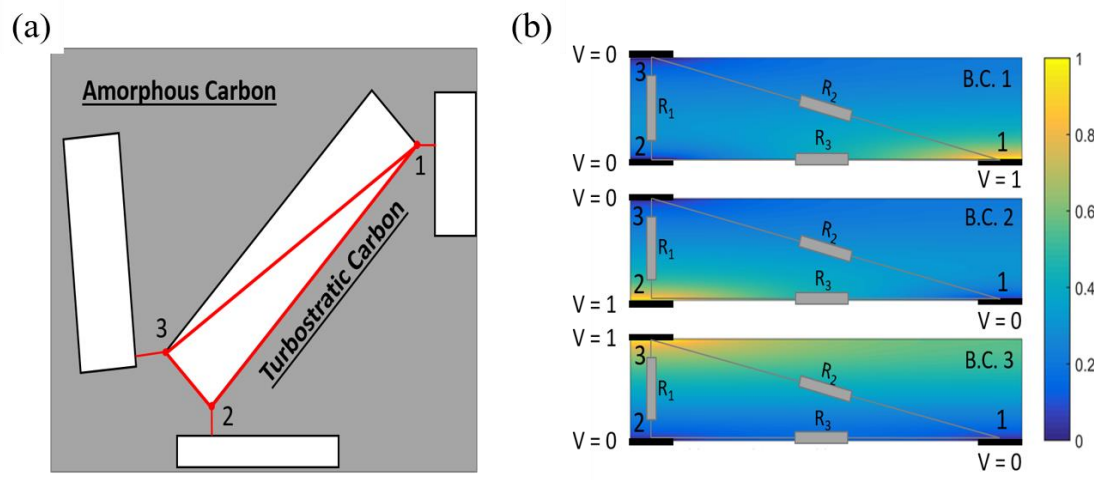

Figure 6.3. (a) Conductive particle with three contact points and **(b)** equipotential line result for a typical sized particle based on FEA.

It is to be noted that if the simplified Ohm's law method used in previous modeling work [191] for traditional nanocomposite was used, the resistance calculation results would have been $R_1 = R_2 = \rho_c \frac{L}{W*T} = 2.69 \times 10^5$ Ω·m and $R_3 = \rho_a \frac{W}{L*T} = 6.29 \times 10^4$ Ω·m which will generate a relatively large error (~ 70%) compared to the FEA results. Moreover, corresponding inter-particle resistances from these three contact points to other particles (Fig.6.3(a)) are 1.91×10^5 Ω·m, 7.98×10^4 Ω·m and 1.90×10^6 Ω·m, which are comparable to the intra-particle resistances. Therefore, for this particle, using FEA to

calculate accurate intra-resistance is critical to obtain reliable electrical conductivity of the whole CNF.

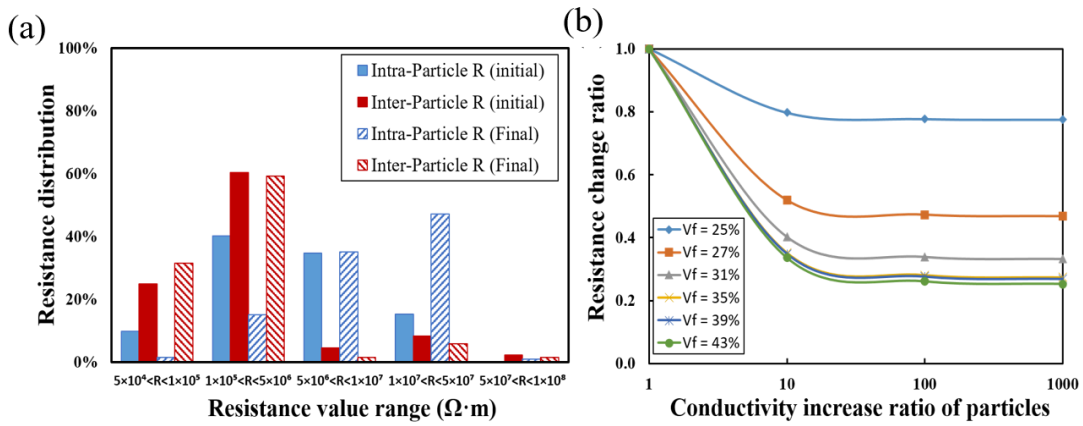

Figure 6.4. (a) Intra-particle and inter-particle resistances distribution for initial and final CNF structure and **(b)** electrical resistance change ratio of CNF with increasing particle conductivities.

The comparison between intra- and inter-particle resistances distribution in CNF on percolation (initial) and saturation (final) state is shown in Fig.6.4(a). As seen in the figure, all the inter-particle and intra-particle resistances at any volume fraction larger than percolation threshold are within the 5×10^4 Ω·m to 1×10^8 Ω·m range, indicating that both of these two types of resistances play an important role in determining the overall conductivity of the CNF. By growing the particle from the percolation state to a saturation state (where particles cannot grow any further unless the impenetrability condition for the particles is removed), the intra-particle resistance values increase and the distribution of

intra-particle resistance moves to the right (higher resistance values). This trend is expected since larger particle size is equivalent to longer conduction path within each particle. In contrast, as the particles grow, the inter-particle resistance values will decrease due to the decrease in tunneling distances between particles. Hence, by growing the turbostratic structure particles the contribution of the intra-particle resistances to the overall electrical conductivity of CNF will increase.

In order to show the significance of particle conductivity to overall conductivity of CNF, we considered hypothetical cases where the conductivity of particles was significantly above the expected values, where σ_a and σ_c were 10, 100 and 1000 times their expected value of 4.25×10^4 and 1.39×10^3 S/m, respectively. In all cases, the ratio of σ_a and σ_c remained the same (~30). The results are presented in Fig.6.4 (b). The y axis in the figure is the calculated electrical resistance of the whole CNFs for different volume fractions and electrical conductivity of particles which is normalized by the electrical resistivity of CNFs corresponding to the most expected values of particle conductivities along the a- and c-axis at percolation threshold (V_f = 25%). The normalized electrical resistance of CNFs is plotted as a function of volume fractions and electrical conductivity of particles (relative to the most expected values of electrical conductivity of particles).

As shown in Fig.6.4(b), for all volume fractions of particles studied here, by increasing electrical conductivity of turbostratic particles, the resistance of CNFs initially drops and reaches a plateau. The latter corresponds to a hypothetical case when the electrical conduction within CNF is mainly controlled by tunneling resistance simply due

to unrealistically high conductivities of particles. Hence, this analysis suggests that at low volume fractions (near the percolation threshold), the conductivity within particles may constitute only ~20% of the electrical resistance of CNFs (only a 20% drop in resistivity is observed by increasing the particle conductivity 100 and 1000 times). This ratio will increase with volume fraction. It is such that near the saturation point (V_f = 43%), the electrical resistance of CNFs is mostly (~75%) is due to conduction within particles (a nearly 75% drop in resistivity by increasing the particle conductivity 100 and 1000 times). Therefore, the consideration of both inter- and intra-particle conduction are critical in reliably predicting the electrical properties of CNFs.

To develop a better understanding of the parameters which influence overall electrical resistivity of CNF, the effect of particle alignment, anisotropic growth rate and volume fraction on the percolation threshold and conductivity is analyzed in the following parts. Moreover, the effect of the matrix tunneling barrier height on the macroscopic conductivity is also discussed.

6.2.1 Electrical conductivity of CNF vs. particle volume fraction and conductivity

Guided by the growth of turbostratic particle size with carbonization time and temperature [18], we grew the turbostratic domains in steps in the model. As is shown in Fig.6.5, the electrical conductivity of the model can be calculated after reaching the percolation threshold (81 ± 68 S/m). Moreover, by increasing the size of the particle and therefore the particle volume fraction, the electrical conductivity of CNF increases, reaching a plateau of 1303 ± 119 S/m, corresponding to the saturation volume fraction of

particles (~43%). At small volume fraction, at or near the percolation threshold, the standard deviation in the predicted electrical measurements can be a significant portion of the predicted values. However, the absolute value of the standard deviation of electrical conductivities will decrease with volume fraction, and will reach ~10% at the saturation volume fraction, which is smaller than the experimental error (~15%) [95]. The reported experimental electrical conductivity [193] of CNF with different carbonization temperature (1100 °C and 1500 °C) is shown in Fig.6.5 with dashed lines. The predicted electrical conductivity with different particle volume fraction is within the experimental conductivity range. The relatively high standard deviation near the percolation threshold

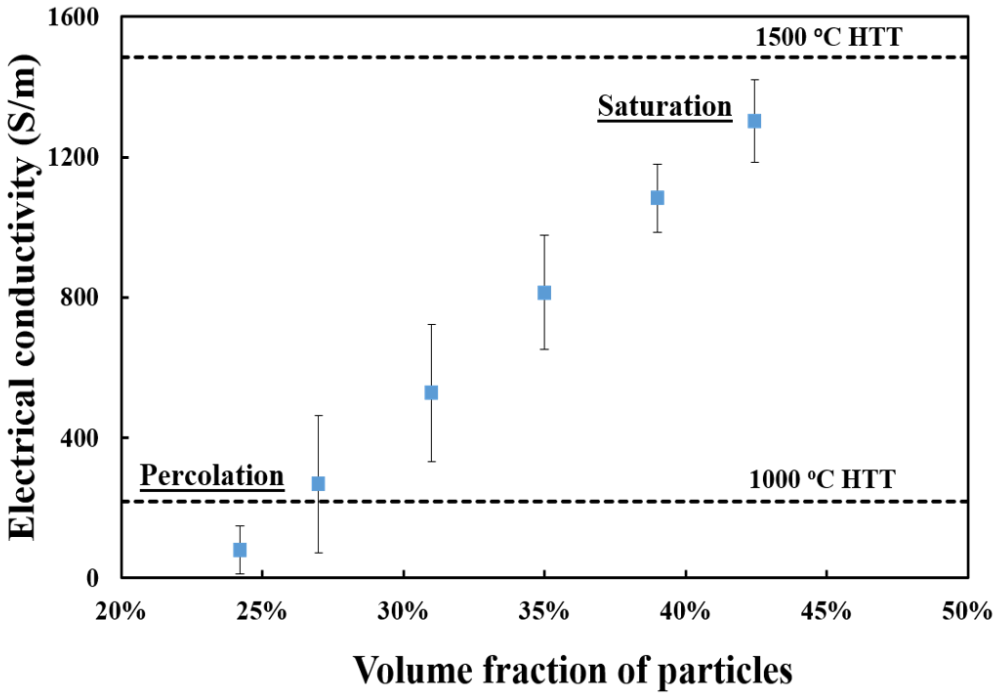

Figure 6.5. Electrical conductivity of CNF with increasing particle volume fraction.

is due to the high sensitivity of conductivity to volume fraction near the percolation threshold. While more experiments are needed to be compared with the modeling results, current 2-D model indeed effectively describes the microstructure of CNF in relation to its electrical conductivity. Moreover, the matching between experimental and modeling results is likely an indication of the proper values chosen for the particle conductivities in our analysis (σ_a and σ_c)

6.2.2 Effect of particle alignment and anisotropic growth rate on percolation probability

Apart from the physical properties of individual turbostratic particles, their geometry and alignment will also influence the formation of a conduction path within CNFs and their electrical property. The formation of the conduction path can be best described by the Percolation probability, ***P***, of turbostratic particles as a function of particle alignment and anisotropic growth rate within CNF. As shown in Fig.6.6, for very low particle volume fractions (16%), the percolation probability is very low for all alignment conditions. By increasing the volume fraction of particles, the difference in percolation probability for different alignment conditions becomes clearer. For instance, for CNF with V_f = 24%, by decreasing the maximum orientation angle of particle from 90° (corresponding to totally random orientation) to 60°, there is a slight increase in the percolation probability, indicating the contribution of particles that are more aligned with CNF axis in bridging the gap between the two ends (electrodes) of CNFs[190]. Further increase in the particle alignment by reducing θ_{max} to 30° and 10°, leads to a slight drop in ***P***.

The maximum probability is obtained between θ_{max} = 30° and 60°. The reason for generating this peak is that for CNF with highly aligned turbostratic domains, the conductive path along fiber direction is more difficult to be obtained due to less connection in transverse direction. As decreasing the content of alignment, more domains will contribute to the formation of conductive path and therefore generate a peak in percolation probability curve. The peak of percolation probability becomes broader as the particle volume fraction is increased. That is mainly because at such high volume fractions, many of the particles are grown to sufficiently large dimensions to contact with their neighboring particles.

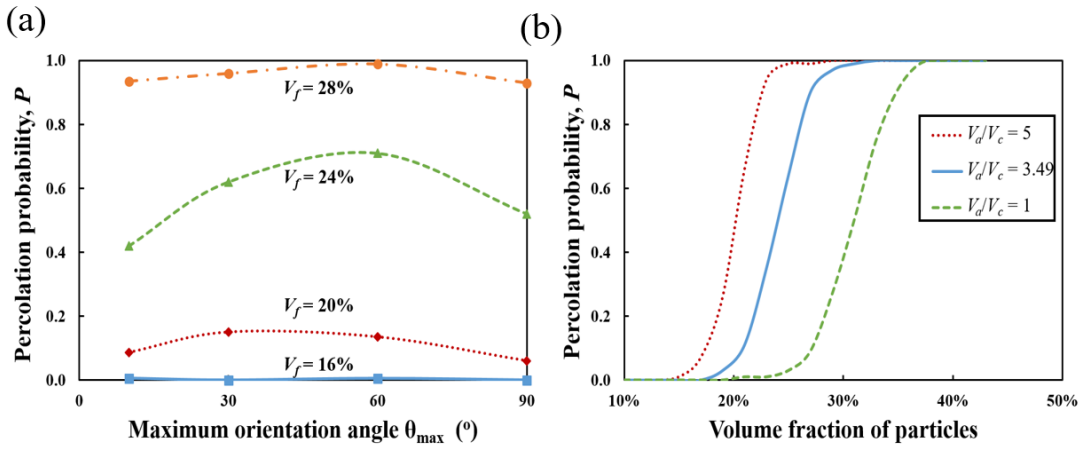

Figure 6.6. Effect of **(a)** particle alignment and **(b)** anisotropic particle growth rate on the percolation probabilities, ***P*** of CNF.

As pointed out in previous section, the growth rate of particles along the a- and c-axis in the model was taken to represent the experimentally observed aspect ratio of turbostratic domains in CNFs. However, other aspect ratios may also be reached for instance via templated carbonization or hot-drawing of precursors and consequent chain alignment[11]. In this section, we investigated the effect of particle aspect ratio on percolation threshold. As shown in Fig.6.6(b), by increasing particle anisotropic growth rate ratio from 1 to 5, there is an evident increase in percolation probability. That is simply because longer particles can reach out to other particles that are further away to form the conduction path. This increased probability indicates the effectiveness of increasing particle growth rate anisotropy in generating more conductive pathways. It is however to be noted that compared to CNTs/polymer nanocomposite, the aspect ratio of the fillers (turbostratic carbon) cannot be very large in CNF, because in practice, large particles are thermodynamically more favorable to grow in non-straight fashion.

6.2.3 Effect of particle alignment and anisotropic growth rate on conductivity

The effect of particle alignment and anisotropic growth rates on electrical conductivity of CNF was also studied. As shown in Fig.6.7(a), similar to the percolation probability corresponding to different particle alignment, there is an electrical conductivity peak at about θ_{max} = 60°, at which the electrical conductivity is 26% higher than the case of randomly oriented particles, an indication of the more conductive pathways generated due to induced particle alignment (refer to Fig.6.6(a)). The decrease in electrical conductivity by enhancing particle alignment beyond θ_{max} = 60° is mainly due to a reduction in the probability of the formation of contact points between particles in the

lateral direction (similar to the trend observed in percolation probability in Fig.6.6(a)). These contact points can generate new conduction paths, increasing the electrical conductivity. This result is consistent with previous experimental and modeling results on the effect of conductive particle alignment (CNTs) on nanocomposite electrical conductivity [190, 194]. This result provides an effective method for improving the electrical conductivity of CNF through partial particle alignment. For instance, in fabricating CNFs, the chains of the polymer precursor can be aligned through hot-drawing as a means to induce turbostratic particle alignment in the later carbonization process. Through controlling the fabrication conditions, the alignment of turbostratic particle can be controlled and based on this modeling results, an optimum alignment condition should be targeted to achieve the maximum electrical conductivity.

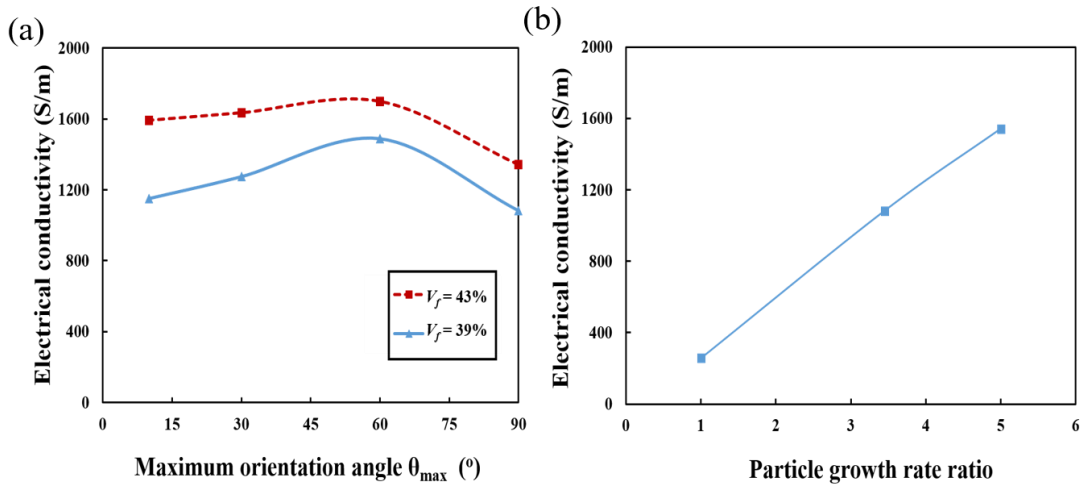

Figure 6.7. Effect of **(a)** particle alignment and **(b)** anisotropic particle growth rate on electrical conductivity of CNF.

In addition to particle alignment, particle aspect ratio can influence the CNF conductivity. As is shown in Fig.6.7(b), by increasing the particle growth rate ratio, there is an evident increase in the overall electrical conductivity. This improvement is caused by the increased percolated pathways, alluded to by the increased ***P*** for larger particle growth rate ratios.

6.2.4 The sensitivity of conduction path and conductivity to barrier height

Apart from the properties of particle, the matrix properties, mainly the energy barrier height corresponding to electron tunneling, will also have an important influence on overall conductivity of the CNF. The effect of matrix tunneling barrier height on the percolation probability and conductivity of CNF is shown in Fig.6.8(a). Because of the increased cut-off tunneling distance at lower barrier height (Fig.6.2(a)), the percolation

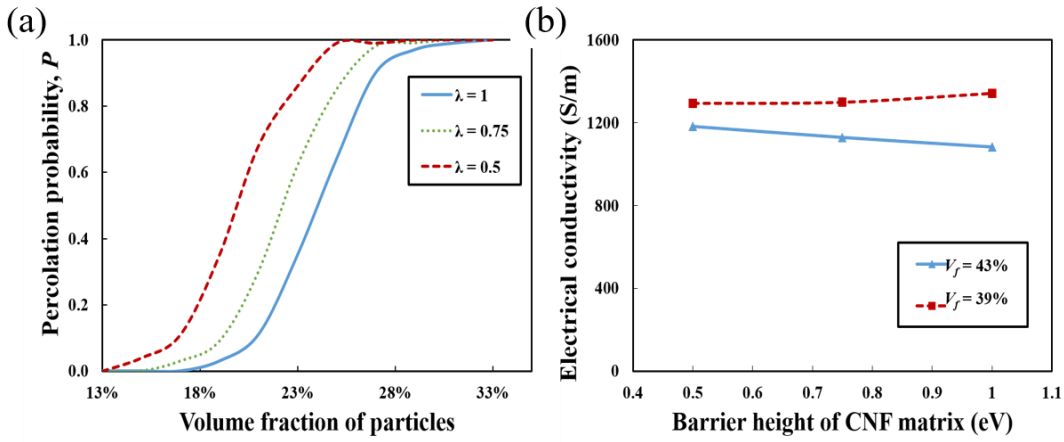

Figure 6.8. Effect of barrier height on **(a)** percolation probability, ***P*** of CNF and **(b)** electrical conductivity.

threshold will be decreased, suggesting that lower barrier height will facilitate the formation of conductive path within CNF. However, the influence of barrier height on electrical conductivity is not as evident especially at high volume fractions as the effect of other parameters discussed so far, i.e., particle conductivity and alignment (Fig.6.8(b)). The insignificant contribution of barrier height to conductivity of CNFs stems partly from the fact that at high particle volume fraction, most of the particles are in contact with other particles, thus, the tunneling distances are near the lower bound. At high particle volume fraction, the contribution of the intra-particle resistances is more important than inter-particle resistances as discussed in section 6.2.3.

6.3 Strain distribution analysis through FEA

The only problem that may restrict the application of finite element method on predicting stress distribution in CNF is the effectiveness of this method in small length scale (~1 nm). Although there is no previous published works about applying finite element method on studying CNF, the continuum elasticity method has been successfully applied to study the mechanical behavior of carbon nanotubes [198]. The researchers has shown that the laws of continuum mechanics are amazingly robust and allow one to treat even intrinsically discrete objects only a few atoms in diameter [199]. For instance, continuum approaches based on continuum mechanics have also been applied successfully for simulating the mechanical responses of individual or isolated carbon nanotubes which are treated as beams, thin shells or solids in cylindrical shapes [200-201]. Based on the previous experimental efforts of mechanical testing of individual CNF, the mechanical response of CNF is totally linear elastic and the breakage usually happens at the amorphous carbon

phase [43]. Therefore, due to the structural similarity between CNTs and turbostratic domains, both of which are composed of sp^2 hybridized carbon, and its linear elastic mechanical response under small strain (<1%), continuum linear elasticity based finite element analysis method is applicable for predicting the stress condition within the CNF matrix. Moreover, applying maximum stress concentration point in amorphous carbon phase as the failure initiation position is a reasonable assumption because of the previous experimental observation.

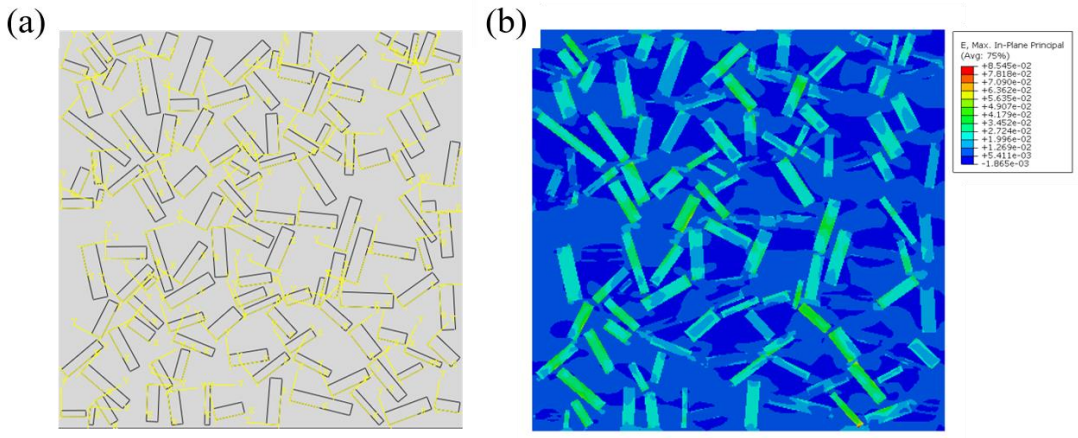

Figure.6.9. (a) Particle distribution with local coordinate system and **(b)** obtained in-plane strain distribution with 0.5 % global strain.

The generated geometries of conductive graphitic particles are input into ABAQUS 6.13, shown in Fig.6.9(a). Each particle has its own local coordinate system to represent the anisotropic mechanical performance of graphitic domains. For graphitic

domains, it's a-axis modulus (E_a=*700 GPa*) is much higher than c-axis direction (E_c=*39.5GPa*) and also the amorphous matrix (E_m = *140 GPa*), therefore considering the anisotropic nature of the graphitic domains mechanical properties is crucial for accurately obtaining local strain distribution of conductive particles. After applying 0.5 % strain to the whole hybrid structure, strain distribution of all particles is obtained, shown in Fig.6.9(b). Comparing with this FEA based strain analysis, previous rigid body rotation based model is oversimplified [202], in which the interaction between particles and particle self-deformation under global strain are not fully considered. After obtaining the strain distribution, renewed geometries of all particles are input back to MATLAB for calculating the electrical resistance of whole structure under certain global strains.

6.4 Results and discussion of piezoresistivity modeling

6.4.1 Percolation network formation

The microstructure is generated based on the particle growing model. In the growing process, the particle will grow in steps, with certain growing speeds. The growing speeds ratio between a-axis and c-axis is set as 3.5 for representing the experimental obtained aspect ratio of graphitic domains in CNF. As shown in Fig.6.10 (a), as increasing the growing steps, there is a continuous increase of the volume fraction of graphitic particles. When the V_f of conductive phases is large enough, the first percolation conduction network forms, shown in Fig. 6.10 (b), in which there are only small part of the total particles participate into the conduction. After arriving this point, most of the particles will keep growing until most of them has contacted to others and stopped

growing. The saturation point correspond to the condition, in which all particles stop growing, and therefore the V_f of graphitic domains reaches its maximum value. Comparing with the experimental data for conductive particle volume fraction in CNF obtained from 1400 ^{o}C carbonization, this simulated V_f range agrees well with it [11].

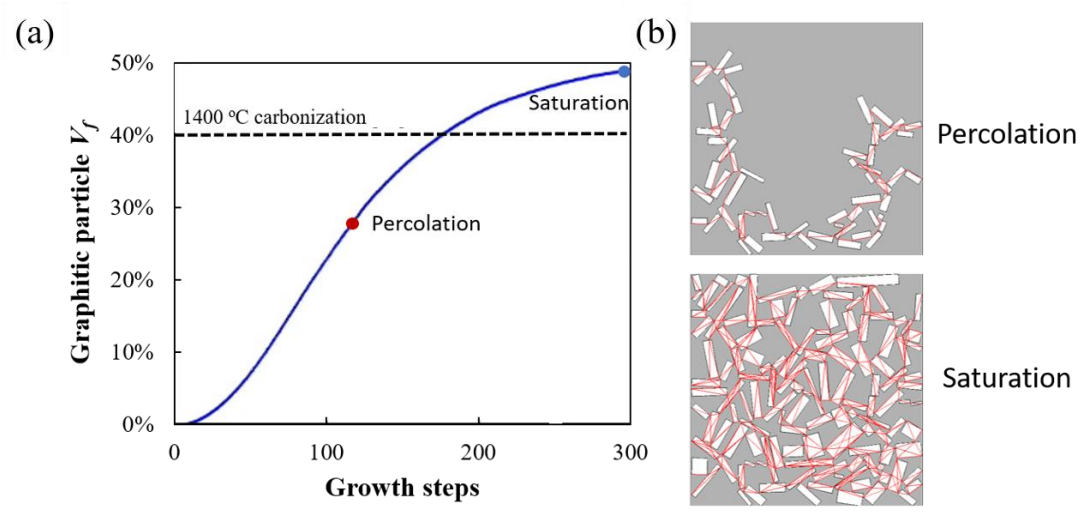

Figure 6.10. (a) Volume fraction of graphitic particle with increasing growth steps (red and blue dots indicate the corresponding V_f for percolation and saturation conditions) and **(b)** formed conduction network for percolation and saturation points.

6.4.2 Piezoresistivity of CNF with increasing turbostratic particle volume fraction

Based on electrical resistance calculations of hybrid nanofiber with increasing strains, gage factor, parameter for qualitatively characterizing piezoresistive effect, is calculated by using the equation as follows,

$$GF = \frac{\Delta R}{R_0 \varepsilon} \tag{6.4}$$

in which, ΔR is the resistance change ratio, R_0 is the initial resistance of nanofiber and ε is the applied strain. As shown in Fig.6.11(a), at percolation and saturation point, there is the volume fraction distribution due to the random generated microstructure. The gage factor of the hybrid nanofiber is about 2.3, which agrees well with the experimental obtained gage factor (2.28±0.25) for CNF with 1100 ^{o}C carbonization. As increasing the V_f of the graphitic particles, the gage factor keeps decreasing to about 0.34 for about 43% graphitic particles. The correlation between piezoresistivity and conductive particle V_f originates from the contribution of inter-particle resistance to the overall resistance of hybrid nanofibers. As shown in Fig.6.11(b), as increasing the V_f of graphitic domains through growing them, contribution of inter-particle resistance to overall resistance keeps decreasing due to the decreased inter-particle distance and increased size of particles. As

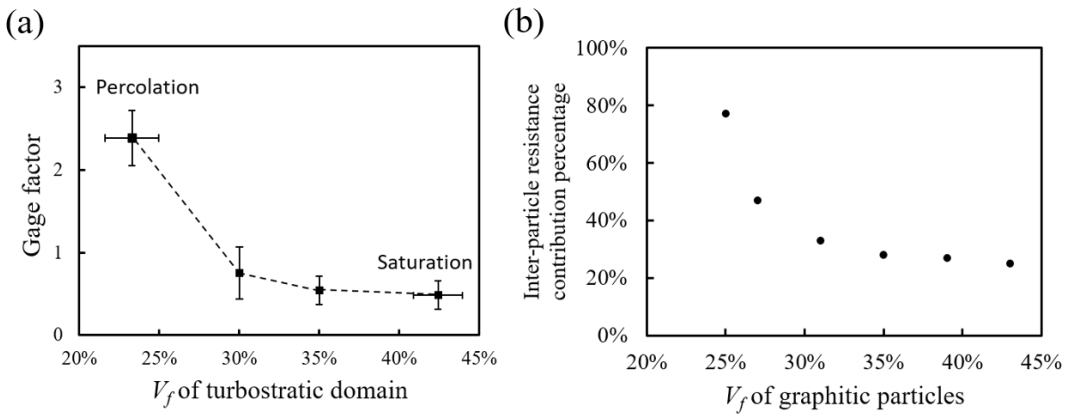

Figure 6.11. (a) Simulated gage factor of hybrid nanofiber and **(b)** contribution of inter-particles tunneling resistance to overall resistance with increasing graphitic particles V_f.

discussed previous section, inter-particle tunneling resistance increases exponentially with tunneling distance, comparing with the intra-particle resistance change depending on the geometrical change, contributes more to the overall piezoresistivity of the whole structure. The volume fraction of graphitic domains within CNF is directly related to the carbonization temperature and time. Therefore, low carbonization temperature is necessary to fabricate electrospun CNF with high piezoresistivity for strain sensing applications.

6.5 Conclusion

A multi-resolution two-dimensional (2D) resistor network model was developed and presented to analyze the electrical conductivity of hybrid nanomaterials which are composed of insulating matrix with hard-core (non-penetrating) conductive particles. The model takes into account both intra- and inter-particle resistance. The modeling results show that intra-particle resistances make an important contribution to macroscopic electrical conductivity of CNF and this contribution is higher at larger particle volume fractions. By increasing the volume fraction and conductivity of the turbostratic particle, the conductivity of whole CNF will increase, which is consistent with the experimental results. Both particle alignment and anisotropic growth rate ratio will influence the conductivity of CNFs. With respect to particle alignment, an optimum alignment is proposed to result in highest CNF conductivity. Lower or higher alignments lead to lower conductivity by reducing the possibility of the formation of a percolated conduction path within the CNFs.

Following this, combined with FEA based strain analysis, piezoresistivity of hybrid CNF/CNTs nanofiber was studied. The simulation result shows the presented method successfully characterize the mechanism of electrical conduction of the hybrid nanofiber. The simulated gage factor is decreased with increasing conductive particle volume fraction, due to the decreased inter-particle tunneling resistance contribution. Based on this simulation works, a clear method is presented to develop high piezoresistivity electrospun CNF through applying low carbonization temperature for strain sensing applications.

7. SUMMARY AND FUTURE WORKS

7.1 Summary

The overarching goal of this work was to unravel the processing-microstructure-property relationship in the fabrication of carbon nanofibers (CNFs) to realize its high potential mechanical properties, and explore its multifunctional applications through both experimental and modeling works.

The CNFs in this work were fabricated by thermal stabilization and carbonization of electrospun polyacrylonitrile (PAN) nanofibers. To further improve the properties of CNFs, CNTs were added into the PAN precursor by exerting its templated graphitization effect. The latter refers to the conversion of PAN chains into carbon in the vicinity of CNTs by removing non-carbon atoms in a thermal treatment, known as carbonization. The presence of CNTs is expected to guide the arrangement of carbon atoms into a graphite-like structure (sp^2 carbon bonds) similar to what exists in CNTs. To achieve this goal, the effect of precursor hot-drawing and CNTs inclusion on the microstructure of precursors were thoroughly researched by using different characterization methods in chapter 1. The results demonstrate applying appropriate amount of CNTs and hot-drawing ratio are crucial to exert the templating effect of CNTs. The microstructure analysis point to evident changes in the microstructure by applying hot-drawing and adding CNTs, such as enhanced alignment of PAN chains, CNTs and crystalline structure within the hybrid nanofiber. The formation of highly ordered polymer interphase around the surface of

CNTs in hot-drawn PAN/CNTs hybrid nanofiber was alluded to by both estimating CNTs reinforcement efficiency based on mechanical testing of nanofiber ribbon and directly TEM observation.

Although electrospun PAN nanofiber has been successfully used to fabricate CNFs, its inherent disadvantage, such as the poor controllability in solution jet whipping process of electrospinning, has restricted its further application in microdevices and carbon-based MEMS/NEMS device. The application of near-field electrospinning (NFES) process on fabricating PAN nanofiber on rotating target was thoroughly studied in chapter 2. The electrospinning parameters, such as solution concentration, electrospinning distance and voltage, were demonstrated to play an important role in determining the diameter and cross-section shape of the obtained fibers on target. The following individual electrospun nanofiber mechanical testing based on MEMS device shows an evident mechanical size effect, which is believed to from the high chain packing and interactions between chain in small diameter range of the obtained nanofibers. The work in this chapter provides a good starting point for developing NFES PAN nanofiber to fabricate CNFs on spool or as building materials for MEMS device.

The CNFs were then obtained through stabilizing and carbonizing the precursor nanofiber by applying the optimum precursor electrospinning and post-processing parameters identified in chapter 2. The microstructure of electrospun CNFs was characterized by applying different methods in details in chapter 4. The analysis results show that applying 1400 ºC carbonization will effectively lower the defect density of the

CNFs, which was chosen to be used to achieve high strength CNFs. The crystallite structure of CNFs carbonization at 1400 ºC was analyzed by WAXD, which shows considerable growth in crystallites and preferential orientation, obtained by precursor hot-drawing. The nano-mechanical testing of individual CNF with different hot-drawing ratio demonstrates evident improvement in both mechanical tensile strength and modulus of CNF with λ=3, which go up to 6.3±0.8 GPa and 217±44 GPa, respectively, the highest value achieved CF/CNF based on PAN homopolymer. Moreover, the high ductility and specific energy to failure of hot-drawn CNFs stem from its radial homogeneous carbonization induced peculiar microstructure (homogeneous distribution of strong turbostratic domains in amorphous carbon matrix), which results in significant crack deflection and pinning as a method to enhance toughness. To further enhance the mechanical properties of CNFs, functionalized CNFs (f-SWNTs) were added into the electrospun CNFs. The introduction of CNTs evidently modify the microstructure of the hot-drawn precursor nanofiber, such as improved crystallinity and slightly decreased crystallite size. The study of the microstructure of CNF/CNTs demonstrates hot-drawing is crucial to exert the templating effect of CNTs, through promoting polymer chain alignment and packing around CNTs. The mechanical properties of CNF/f-SWNTs were evidently improved to 6.92 GPa and 250 GPa for strength and modulus, respectively, by adding CNTs.

To explore the multifunctional applications of electrospun CNFs, the piezoresistivity of single CNF was studied in chapter 5 through using the newly-designed MEMS devices. The gauge factor of individual CNF was obtained experimentally to be

2.29±0.24. The repeatibility and stability of the pizeoresistive effect of CNF was demonstrated based on the cyclic loading/unloading test. The piezoresistive testing effectively identify the transition to fictious piezoresistive effect due to the internal plastic deformanction and microcrack formations at large strain (0.5-1%). A simplified 1-D model shows that the piezoresisitve effect of CNFs could be effectively improved through increasing the barrier height of amorphous carbon matrix or modulus anisotropy between turbostratic carbon and the matrix.

To further understand the relationship between microstructure and electrical conductivity and piezoresistivity of CNFs, a multi-resolution two-dimensional (2D) resistor network model was developed in chapter 6, which is composed of growing conductive particles that are randomly distributed in insulating matrix. The modeling results are consistent with the experimental observation in that by increasing the volume fraction and conductivity of the turbostratic particles, the electrical conductivity will increase. Moreover, the modeling results show that alignment and anisotropic growth rate of the conductive particles will influence the overall electrical conductivity. Then, combined with the FEA based localized strain analysis of particle with applied global strain, the piezoresistivity of CNF nanofiber was studied. The modeling results show that by decreasing the volume fraction of particles, there is a continuous increase in the piezoresistive effect due to increased contribution of tunneling resistance between adjacent conductive particles. The modeling works in this chapter generates an effective link between the microstructure of CNF and its electrical conductivity and piezoresistivity, which provides a solid foundation for further improving the multifunctional properties of

electrospun CNF through controlling fabrication parameters induced microstructure evolution.

Based on the combination of experimental and modeling works in this project, the processing-microstructure-properties relationship in fabricating electrospun CNFs and CNF/CNTs has been unraveled. The mechanical performance of CNF and CNF/f-SWNTs was successfully improved to the largest value among all CNFs and comparable to the strongest CFs up to date. The multifunctional properties, such as electrical conductivity and piezoresistivity of CNFs were explored and a clear path to further improve its performance through modifying its microstructure. Due to the limitation of time, there is still a great potential to further push the properties boundary of electrospun CNFs through the combination of various approaches.

7.2 Future works

7.2.1 Mechanical properties

In this work, the high potential tensile strength of CNFs has been successfully materialized to some extent by introducing precursor hot-drawing induced graphitic alignment and templating effect of f-SWNTs. However, comparing to the 14 GPa strength upper limit for CNFs, predicted based on the continuum model [11], there is still a great potential to further improve its strength through optimizing the fabrication process and precursor polymer structure.

As discussed in the precursor microstructure analysis, comparing with the gel-spun PAN, the low chain alignment and crystallinity of precursor PAN nanofiber has restricted

its further property improvement. Therefore, introducing higher hot-drawing ratio, optimizing the hot-drawing conditions, such as temperature, drawing stress and drawing medium could further improve the further improve the microstructure of precursor nanofibers. Moreover, through using PAN copolymer, such as comonomer containing carboxylic acids or vinyl ester, could effectively increase the chain alignment and packing density, due to the lowered polarity of the polymer chain. After achieving high chain alignment, the methods to maintain this alignment is crucial to transfer the high chain alignment in precursor nanofiber to graphitic alignment in CNFs. Therefore, optimizing the constraint stress during stabilization and carbonization is also important to improve the mechanical properties of CNFs. In addition to the fabrication process of CNFs, the post-processing, such as acid treatment and sizing also play an important role in determining the overall mechanical strength of CNFs. Through applying all these approaches to optimize the fabrication process and material system, there is a great potential to further push the limit for carbon fiber materials to make it to be an outstanding reinforcement materials in different fields to substitute the current CFs.

7.2.2 Multifunctional applications

The research of multifunctional properties of electrospun CNFs and their applications are still under its primary stage. For instance, although the piezoresistivity effect of individual CNFs has been obtained by the MEMS device, there is still a great space to further improve its performance. Guided by the modeling works, controlling the fabrication process could effectively improve the electrical conductivity and piezoresistivity of electrospun CNFs through controlling its microstructure. Demonstrated

by the microstructure characterization, through applying precursor hot-drawing, the size and alignment of turbostratic particles were evidently changed, which brings in significant mechanical properties improvement. Therefore, more experimental works are required to obtain the electrical conductivity and piezoresistivity of individual CNFs to generate the microstructure-properties relationship. Apart from fabrication method induced microstructure modification, adding high performance particles, such as CNTs, graphene will also effectively modify the microstructure of hybrid nanofiber, therefore its performances. Through properly controlling the fabrication process and application of post-processing, there is a great potential to further improve the multifunctional properties of CNF. The multifunctional nanocomposite materials based on electrospun CNFs with specific microstructure designing induced different properties combination, such as mechanical property, electrical conductivity, piezoresistivity and thermal conductivity, could be developed to substitute current composite in various application fields.

REFERENCES

1. Donnet J-B, W. T., Rebouillat S, Peng JCM., *Carbon fibers*. Marcel Dekker: New York, 1998.
2. LH, P., *Carbon fibers - formation, structure, and properties*. CRC Press: Boca Raton, 1995.
3. Toray Toray Data Sheet. http://www.toraycfa.com/pdfs/T300DataSheet.pdf (accessed Oct.).
4. Toray Carbon fiber composite materials. http://cs2.toray.co.jp/news/toray/en/newsrrs02.nsf/0/B126D9D8433675EE49257D11001770C5 (accessed Oct.).
5. Kiuchi, N.; Ozawa, K.; Komami, T.; Katoh, O.; Arai, Y.; Watanabe, T.; Iwai, S., Pitch-based carbon fiber with high thermal conductivity for new advanced thermal design. *Int Sampe Tech Conf* **1998,** *30*, 68-77.
6. Huang, X. S., Fabrication and Properties of Carbon Fibers. *Materials* **2009,** *2* (4), 2369-2403.
7. Tsai, J. S., Effect of Drawing Ratio during Spinning and Oxidation on the Properties of Polyacrylonitrile Precursor and Resulting Carbon-Fiber. *J Mater Sci Lett* **1992,** *11* (3), 140-142.
8. Morgan, P., *Carbon fibers and their composites*. Taylor & Francis: Boca Raton, 2005.
9. Council, N. R., *High-Performance Structural Fibers for Advanced Polymer Matrix Composites*. The National Academies Press: Washington, DC, 2005.
10. Chae, H. G.; Newcomb, B. A.; Gulgunje, P. V.; Liu, Y. D.; Gupta, K. K.; Kamath, M. G.; Lyons, K. M.; Ghoshal, S.; Pramanik, C.; Giannuzzi, L.; Sahin, K.; Chasiotis, I.; Kumar, S., High strength and high modulus carbon fibers. *Carbon* **2015,** *93*, 81-87.
11. Naraghi, M.; Chawla, S., Carbonized Micro- and Nanostructures: Can Downsizing Really Help? *Materials* **2014,** *7* (5), 3820-3833.
12. Maradur, S. P.; Kim, C. H.; Kim, S. Y.; Kim, B.-H.; Kim, W. C.; Yang, K. S., Preparation of carbon fibers from a lignin copolymer with polyacrylonitrile. *Synthetic Met* **2012,** *162* (5), 453-459.
13. Fitzer, E., Pan-Based Carbon-Fibers Present State and Trend of the Technology from the Viewpoint of Possibilities and Limits to Influence and to Control the Fiber Properties by the Process Parameters. *Carbon* **1989,** *27* (5), 621-645.

14. Liu, J.; Yue, Z.; Fong, H., Continuous Nanoscale Carbon Fibers with Superior Mechanical Strength. *Small* **2009,** *5* (5), 536-542.

15. Tagawa, T.; Miyata, T., Size effect on tensile strength of carbon fibers. *Mat Sci Eng a-Struct* **1997,** *238* (2), 336-342.

16. Chae, H. G.; Minus, M. L.; Rasheed, A.; Kumar, S., Stabilization and carbonization of gel spun polyacrylonitrile/single wall carbon nanotube composite fibers. *Polymer* **2007,** *48* (13), 3781-3789.

17. Johnson, D. J., Structure Property Relationships in Carbon-Fibers. *J Phys D Appl Phys* **1987,** *20* (3), 286-291.

18. Arshad, S. N.; Naraghi, M.; Chasiotis, I., Strong carbon nanofibers from electrospun polyacrylonitrile. *Carbon* **2011,** *49* (5), 1710-1719.

19. Wang, H. T.; Wang, Y.; Li, T.; Wu, S.; Xu, L. H., Gradient distribution of radial structure of PAN-based carbon fiber treated by high temperature. *Prog Nat Sci-Mater* **2014,** *24* (1), 31-34.

20. Chae, H. G.; Choi, Y. H.; Minus, M. L.; Kumar, S., Carbon nanotube reinforced small diameter polyacrylonitrile based carbon fiber. *Compos Sci Technol* **2009,** *69* (3), 406-413.

21. Smith, P.; Lemstra, P. J., Ultra-Drawing of High Molecular-Weight Polyethylene Cast from Solution. *Colloid Polym Sci* **1980,** *258* (7), 891-894.

22. Zhang, L. F.; Aboagye, A.; Kelkar, A.; Lai, C. L.; Fong, H., A review: carbon nanofibers from electrospun polyacrylonitrile and their applications. *J Mater Sci* **2014,** *49* (2), 463-480.

23. Al-Saleh, M. H.; Sundararaj, U., Review of the mechanical properties of carbon nanofiber/polymer composites. *Compos Part a-Appl S* **2011,** *42* (12), 2126-2142.

24. Al-Saleh, M. H.; Sundararaj, U., A review of vapor grown carbon nanofiber/polymer conductive composites. *Carbon* **2009,** *47* (1), 2-22.

25. Ozkan, T.; Naraghi, M.; Chasiotis, I., Mechanical properties of vapor grown carbon nanofibers. *Carbon* **2010,** *48* (1), 239-244.

26. Uchida, T.; Anderson, D. P.; Minus, M. L.; Kumar, S., Morphology and modulus of vapor grown carbon nano fibers. *J Mater Sci* **2006,** *41* (18), 5851-5856.

27. Naraghi, M.; Arshad, S. N.; Chasiotis, I., Molecular orientation and mechanical property size effects in electrospun polyacrylonitrile nanofibers. *Polymer* **2011,** *52* (7), 1612-1618.

28. Naebe, M.; Lin, T.; Staiger, M. P.; Dai, L. M.; Wang, X. G., Electrospun single-walled carbon nanotube/polyvinyl alcohol composite nanofibers: structure-property relationships. *Nanotechnology* **2008,** *19* (30).

29. Sundaray, B.; Subramanian, V.; Natarajan, T. S.; Krishnamurthy, K., Electrical conductivity of a single electrospun fiber of poly(methyl methacrylate) and multiwalled carbon nanotube nanocomposite. *Appl Phys Lett* **2006,** *88* (14).

30. Datsyuk, V.; Trotsenko, S.; Reich, S., Carbon-nanotube-polymer nanofibers with high thermal conductivity. *Carbon* **2013,** *52*, 605-608.

31. Zussman, E.; Chen, X.; Ding, W.; Calabri, L.; Dikin, D. A.; Quintana, J. P.; Ruoff, R. S., Mechanical and structural characterization of electrospun PAN-derived carbon nanofibers. *Carbon* **2005,** *43* (10), 2175-2185.

32. Park, S. H.; Kim, C.; Yang, K. S., Preparation of carbonized fiber web from electrospinning of isotropic pitch. *Synthetic Met* **2004,** *143* (2), 175-179.

33. Liu, Y. D.; Chae, H. G.; Kumar, S., Gel-spun carbon nanotubes/polyacrylonitrile composite fibers. Part II: Stabilization reaction kinetics and effect of gas environment. *Carbon* **2011,** *49* (13), 4477-4486.

34. Liu, Y. D.; Chae, H. G.; Kumar, S., Gel-spun carbon nanotubes/polyacrylonitrile composite fibers. Part III: Effect of stabilization conditions on carbon fiber properties. *Carbon* **2011,** *49* (13), 4487-4496.

35. Bhardwaj, N.; Kundu, S. C., Electrospinning: A fascinating fiber fabrication technique. *Biotechnology Advances* **2010,** *28* (3), 325-347.

36. He, X.-X.; Zheng, J.; Yu, G.-F.; You, M.-H.; Yu, M.; Ning, X.; Long, Y.-Z., Near-Field Electrospinning: Progress and Applications. *The Journal of Physical Chemistry C* **2017,** *121* (16), 8663-8678.

37. Li, D.; Xia, Y., Electrospinning of Nanofibers: Reinventing the Wheel? *Adv Mater* **2004,** *16* (14), 1151-1170.

38. Garg, K.; Bowlin, G. L., Electrospinning jets and nanofibrous structures. *Biomicrofluidics* **2011,** *5* (1), 013403.

39. Eda, G.; Shivkumar, S., Bead-to-fiber transition in electrospun polystyrene. *J Appl Polym Sci* **2007,** *106* (1), 475-487.

40. Ding, B.; Kim, H. Y.; Lee, S. C.; Shao, C. L.; Lee, D. R.; Park, S. J.; Kwag, G. B.; Choi, K. J., Preparation and characterization of a nanoscale poly(vinyl alcohol) fiber aggregate produced by an electrospinning method. *J Polym Sci Pol Phys* **2002,** *40* (13), 1261-1268.

41. Koski, A.; Yim, K.; Shivkumar, S., Effect of molecular weight on fibrous PVA produced by electrospinning. *Mater Lett* **2004,** *58* (3-4), 493-497.

42. Zhang, C. X.; Yuan, X. Y.; Wu, L. L.; Han, Y.; Sheng, J., Study on morphology of electrospun poly(vinyl alcohol) mats. *Eur Polym J* **2005,** *41* (3), 423-432.

43. Chawla, S.; Cai, J.; Naraghi, M., Mechanical tests on individual carbon nanofibers reveals the strong effect of graphitic alignment achieved via precursor hot-drawing. *Carbon* **2017,** *117*, 208-219.

44. Clarisse, R.; Vitor, S.; Carlos Miguel, C.; José Luís Gómez, R.; Senentxu, L.-M., Tailoring the morphology and crystallinity of poly(L-lactide acid) electrospun membranes. *Science and Technology of Advanced Materials* **2011,** *12* (1), 015001.

45. Fong, H.; Chun, I.; Reneker, D. H., Beaded nanofibers formed during electrospinning. *Polymer* **1999,** *40* (16), 4585-4592.

46. Casper, C. L.; Stephens, J. S.; Tassi, N. G.; Chase, D. B.; Rabolt, J. F., Controlling Surface Morphology of Electrospun Polystyrene Fibers: Effect of Humidity and Molecular Weight in the Electrospinning Process. *Macromolecules* **2004,** *37* (2), 573-578.

47. Yarin, A. L.; Koombhongse, S.; Reneker, D. H., Bending instability in electrospinning of nanofibers. *J. Appl. Phys.* **2001,** *89* (5), 3018-3026.

48. Guerrero, J.; Rivero, J.; Gundabala, V. R.; Perez-Saborid, M.; Fernandez-Nieves, A., Whipping of electrified liquid jets. *Proceedings of the National Academy of Sciences* **2014,** *111* (38), 13763-13767.

49. Naraghi, M.; Chasiotis, I., Mechanics of PAN Nanofibers. *Major Accomplishments in Composite Materials and Sandwich Structures: An Anthology Onr Sponsored Research* **2009**, 757-778.

50. Cai, J. Z.; Chawla, S.; Naraghi, M., Microstructural evolution and mechanics of hot-drawn CNT-reinforced polymeric nanofibers. *Carbon* **2016,** *109*, 813-822.

51. Chang, C.; Tran, V. H.; Wang, J.; Fuh, Y.-K.; Lin, L., Direct-Write Piezoelectric Polymeric Nanogenerator with High Energy Conversion Efficiency. *Nano Lett* **2010,** *10* (2), 726-731.

52. Wang, C.; Madou, M., From MEMS to NEMS with carbon. *Biosensors and Bioelectronics* **2005,** *20* (10), 2181-2187.

53. Sun, D.; Chang, C.; Li, S.; Lin, L., Near-Field Electrospinning. *Nano Lett* **2006,** *6* (4), 839-842.

54. Wang, H.; Huang, S.; Liang, F.; Wu, P.; Li, M.; Lin, S.; Chen, X., Research on Multinozzle Near-Field Electrospinning Patterned Deposition. *J Nanomater* **2015,** *2015*, 8.

55. Chang, C.; Limkrailassiri, K.; Lin, L., Continuous near-field electrospinning for large area deposition of orderly nanofiber patterns. *Appl Phys Lett* **2008,** *93* (12), 123111.

56. Bisht, G. S.; Canton, G.; Mirsepassi, A.; Kulinsky, L.; Oh, S.; Dunn-Rankin, D.; Madou, M. J., Controlled Continuous Patterning of Polymeric Nanofibers on Three-Dimensional Substrates Using Low-Voltage Near-Field Electrospinning. *Nano Lett* **2011,** *11* (4), 1831-1837.

57. Zhou, F.-L.; Hubbard, P. L.; Eichhorn, S. J.; Parker, G. J. M., Jet deposition in near-field electrospinning of patterned polycaprolactone and sugar-polycaprolactone core–shell fibres. *Polymer* **2011,** *52* (16), 3603-3610.

58. Liu, Z. H.; Pan, C. T.; Lin, L. W.; Lai, H. W., Piezoelectric properties of PVDF/MWCNT nanofiber using near-field electrospinning. *Sensors and Actuators A: Physical* **2013,** *193* (Supplement C), 13-24.

59. Pan, C.-T.; Yang, T.-L.; Chen, Y.-C.; Su, C.-Y.; Ju, S.-P.; Hung, K.-H.; Wu, I.-C.; Hsieh, C.-C.; Shen, S.-C., Fibers and Conductive Films Using Silver Nanoparticles and Nanowires by Near-Field Electrospinning Process. *J Nanomater* **2015,** *2015*, 5.

60. Liu, Z. H.; Pan, C. T.; Yen, C. K.; Lin, L. W.; Huang, J. C.; Ke, C. A., Crystallization and mechanical behavior of the ferroelectric polymer nonwoven fiber fabrics for highly durable wearable sensor applications. *Applied Surface Science* **2015,** *346* (Supplement C), 291-301.

61. Papkov, D.; Zou, Y.; Andalib, M. N.; Goponenko, A.; Cheng, S. Z. D.; Dzenis, Y. A., Simultaneously Strong and Tough Ultrafine Continuous Nanofibers. *Acs Nano* **2013,** *7* (4), 3324-3331.

62. Liu, Y. D.; Chae, H. G.; Kumar, S., Gel-spun carbon nanotubes/polyacrylonitrile composite fibers. Part I: Effect of carbon nanotubes on stabilization. *Carbon* **2011,** *49* (13), 4466-4476.

63. Ravandi, S. A. H.; Hassanabadi, E.; Tavanai, H.; Abuzade, R. A., Mechanical properties and morphology of hot drawn polyacrylonitrile nanofibrous yarn. *J Appl Polym Sci* **2012,** *124* (6), 5002-5009.

64. Deng, L. B.; Young, R. J.; van der Zwaag, S.; Picken, S., Characterization of the adhesion of single-walled carbon nanotubes in poly (p-phenylene terephthalamide) composite fibres. *Polymer* **2010,** *51* (9), 2033-2039.

65. La Mantia, F. P.; Ceraulo, M.; Mistretta, M. C.; Morreale, M., Effect of Hot Drawing on the Mechanical Properties of Biodegradable Fibers. *J Polym Environ* **2016,** *24* (1), 56-63.

66. Shin, M. K.; Lee, B.; Kim, S. H.; Lee, J. A.; Spinks, G. M.; Gambhir, S.; Wallace, G. G.; Kozlov, M. E.; Baughman, R. H.; Kim, S. J., Synergistic toughening of composite fibres by self-alignment of reduced graphene oxide and carbon nanotubes. *Nat Commun* **2012,** *3*.

67. Green, E. C.; Zhang, Y. Y.; Minus, M. L., Understanding the Effects of Nanocarbons on Flexible Polymer Chain Orientation and Crystallization: Polyethylene/Carbon Nanochip Hybrid Fibrillar Crystal Growth. *J Appl Polym Sci* **2014,** *131* (18).

68. Li, X.; Qin, A. W.; Zhao, X. Z.; Liu, D. P.; Wang, H. Y.; He, C. J., Drawing dependent structures, mechanical properties and cyclization behaviors of

polyacrylonitrile and polyacrylonitrile/carbon nanotube composite fibers prepared by plasticized spinning. *Phys Chem Chem Phys* **2015,** *17* (34), 21856-21865.

69. Lai, C. L.; Zhong, G. J.; Yue, Z. R.; Chen, G.; Zhang, L. F.; Vakili, A.; Wang, Y.; Zhu, L.; Liu, J.; Fong, H., Investigation of post-spinning stretching process on morphological, structural, and mechanical properties of electrospun polyacrylonitrile copolymer nanofibers. *Polymer* **2011,** *52* (2), 519-528.

70. Sahin, K.; Fasanella, N. A.; Chasiotis, I.; Lyons, K. M.; Newcomb, B. A.; Kamath, M. G.; Chae, H. G.; Kumar, S., High strength micron size carbon fibers from polyacrylonitrile-carbon nanotube precursors. *Carbon* **2014,** *77*, 442-453.

71. Chae, H. G.; Minus, M. L.; Kumar, S., Oriented and exfoliated single wall carbon nanotubes in polyacrylonitrile. *Polymer* **2006,** *47* (10), 3494-3504.

72. Alexander, P. D.; Mariia, O. D., Novel fluorescent carbonic nanomaterials for sensing and imaging. *Methods and Applications in Fluorescence* **2013,** *1* (4), 042001.

73. Iijima, S., Helical microtubules of graphitic carbon. *Nature* **1991,** *354*, 56.

74. Peng, B.; Locascio, M.; Zapol, P.; Li, S. Y.; Mielke, S. L.; Schatz, G. C.; Espinosa, H. D., Measurements of near-ultimate strength for multiwalled carbon nanotubes and irradiation-induced crosslinking improvements. *Nat Nanotechnol* **2008,** *3* (10), 626-631.

75. Ebbesen, T. W.; Lezec, H. J.; Hiura, H.; Bennett, J. W.; Ghaemi, H. F.; Thio, T., Electrical conductivity of individual carbon nanotubes. *Nature* **1996,** *382* (6586), 54-56.

76. Choi, T.-Y.; Poulikakos, D.; Tharian, J.; Sennhauser, U., Measurement of the Thermal Conductivity of Individual Carbon Nanotubes by the Four-Point Three-ω Method. *Nano Lett* **2006,** *6* (8), 1589-1593.

77. Hou, H. Q.; Ge, J. J.; Zeng, J.; Li, Q.; Reneker, D. H.; Greiner, A.; Cheng, S. Z. D., Electrospun polyacrylonitrile nanofibers containing a high concentration of well-aligned multiwall carbon nanotubes. *Chem Mater* **2005,** *17* (5), 967-973.

78. Haggenmueller, R.; Gommans, H. H.; Rinzler, A. G.; Fischer, J. E.; Winey, K. I., Aligned single-wall carbon nanotubes in composites by melt processing methods. *Chem Phys Lett* **2000,** *330* (3-4), 219-225.

79. Cadek, M.; Coleman, J. N.; Barron, V.; Hedicke, K.; Blau, W. J., Morphological and mechanical properties of carbon-nanotube-reinforced semicrystalline and amorphous polymer composites. *Appl Phys Lett* **2002,** *81* (27), 5123-5125.

80. Li, L. Y.; Li, C. Y.; Ni, C. Y.; Rong, L. X.; Hsiao, B., Structure and crystallization behavior of Nylon 66/multi-walled carbon nanotube nanocomposites at low carbon nanotube contents. *Polymer* **2007,** *48* (12), 3452-3460.

81. Li, L. Y.; Li, C. Y.; Ni, C. Y., Polymer crystallization-driven, periodic patterning on carbon nanotubes. *J Am Chem Soc* **2006,** *128* (5), 1692-1699.

82. Grady, B. P.; Pompeo, F.; Shambaugh, R. L.; Resasco, D. E., Nucleation of polypropylene crystallization by single-walled carbon nanotubes. *J Phys Chem B* **2002,** *106* (23), 5852-5858.

83. Zhang, Y. Y.; Song, K. N.; Meng, J. S.; Minus, M. L., Tailoring Polyacrylonitrile Interfacial Morphological Structure by Crystallization in the Presence of Single-Wall Carbon Nanotubes. *Acs Appl Mater Inter* **2013,** *5* (3), 807-814.

84. Minus, M. L.; Chae, H. G.; Kumar, S., Polyethylene Crystallization Nucleated by Carbon Nanotubes under Shear. *Acs Appl Mater Inter* **2012,** *4* (1), 326-330.

85. Zhang, Y.; Song, K.; Meng, J.; Minus, M. L., Tailoring Polyacrylonitrile Interfacial Morphological Structure by Crystallization in the Presence of Single-Wall Carbon Nanotubes. *Acs Appl Mater Inter* **2013,** *5* (3), 807-814.

86. Zhang, S.; Minus, M. L.; Zhu, L.; Wong, C.-P.; Kumar, S., Polymer transcrystallinity induced by carbon nanotubes. *Polymer* **2008,** *49* (5), 1356-1364.

87. Prilutsky, S.; Zussman, E.; Cohen, Y., The effect of embedded carbon nanotubes on the morphological evolution during the carbonization of poly(acrylonitrile) nanofibers. *Nanotechnology* **2008,** *19* (16).

88. Donnet, J. B.; Wang, T. K.; Rebouillot, S.; Peng, J. C. M., (Edited by) Carbon Fibers. *Marcel Decker Inc.* **1998**.

89. Newcomb, B. A.; Giannuzzi, L. A.; Lyons, K. M.; Gulgunje, P. V.; Gupta, K.; Liu, Y.; Kamath, M.; McDonald, K.; Moon, J.; Feng, B.; Peterson, G. P.; Chae, H. G.; Kumar, S., High resolution transmission electron microscopy study on polyacrylonitrile/carbon nanotube based carbon fibers and the effect of structure development on the thermal and electrical conductivities. *Carbon* **2015,** *93*, 502-514.

90. Guo, H.; Minus, M. L.; Jagannathan, S.; Kumar, S., Polyacrylonitrile/Carbon Nanotube Composite Films. *Acs Appl Mater Inter* **2010,** *2* (5), 1331-1342.

91. Papkov, D.; Beese, A. M.; Goponenko, A.; Zou, Y.; Naraghi, M.; Espinosa, H. D.; Saha, B.; Schatz, G. C.; Moravsky, A.; Loutfy, R.; Nguyen, S. T.; Dzenis, Y., Extraordinary Improvement of the Graphitic Structure of Continuous Carbon Nanofibers Templated with Double Wall Carbon Nanotubes. *Acs Nano* **2013,** *7* (1), 126-142.

92. Andrews, R.; Jacques, D.; Rao, A. M.; Rantell, T.; Derbyshire, F.; Chen, Y.; Chen, J.; Haddon, R. C., Nanotube composite carbon fibers. *Appl. Phys. Lett.* **1999,** *75* (9), 1329-1331.

93. Weisenberger, M. C.; Grulke, E. A.; Jacques, D.; Rantell, T.; Andrews, R., Enhanced mechanical properties of polyacrylonitrile/multiwall carbon nanotube composite fibers. *J. Nanosci. Nanotechnol.* **2003,** *3* (6), 535-539.

94. Kim, C.; Park, S. H.; Cho, J. K.; Lee, D. Y.; Park, T. J.; Lee, W. J.; Yang, K. S., Raman spectroscopic evaluation of polyacrylonitrile-based carbon nanofibers prepared by electrospinning. *J Raman Spectrosc* **2004,** *35* (11), 928-933.

95. Cai, J. Z.; Chawla, S.; Naraghi, M., Piezoresistive effect of individual electrospun carbon nanofibers for strain sensing. *Carbon* **2014,** *77*, 738-746.

96. Im, J. S.; Kim, S. J.; Kang, P. H.; Lee, Y.-S., The improved electrical conductivity of carbon nanofibers by fluorinated MWCNTs. *Journal of Industrial and Engineering Chemistry* **2009,** *15* (5), 699-702.

97. Mayhew, E.; Prakash, V., Thermal conductivity of individual carbon nanofibers. *Carbon* **2013,** *62*, 493-500.

98. Bonino, C. A.; Ji, L.; Lin, Z.; Toprakci, O.; Zhang, X.; Khan, S. A., Electrospun Carbon-Tin Oxide Composite Nanofibers for Use as Lithium Ion Battery Anodes. *Acs Appl Mater Inter* **2011,** *3* (7), 2534-2542.

99. Ji, L.; Lin, Z.; Medford, A. J.; Zhang, X., Porous carbon nanofibers from electrospun polyacrylonitrile/SiO2 composites as an energy storage material. *Carbon* **2009,** *47* (14), 3346-3354.

100. Chen, Y.; Li, X.; Park, K.; Song, J.; Hong, J.; Zhou, L.; Mai, Y.-W.; Huang, H.; Goodenough, J. B., Hollow Carbon-Nanotube/Carbon-Nanofiber Hybrid Anodes for Li-Ion Batteries. *J Am Chem Soc* **2013,** *135* (44), 16280-16283.

101. Zhu, J.; Wei, S.; Ryu, J.; Guo, Z., Strain-Sensing Elastomer/Carbon Nanofiber "Metacomposites". *The Journal of Physical Chemistry C* **2011,** *115* (27), 13215-13222.

102. Li, L.; Li, J.; Lukehart, C. M., Graphitic carbon nanofiber-poly(acrylate) polymer brushes as gas sensors. *Sensors and Actuators B: Chemical* **2008,** *130* (2), 783-788.

103. Hong, X.; Chung, D. D. L., Carbon nanofiber mats for electromagnetic interference shielding. *Carbon* **2017,** *111*, 529-537.

104. Bayat, M.; Yang, H.; Ko, F. K.; Michelson, D.; Mei, A., Electromagnetic interference shielding effectiveness of hybrid multifunctional Fe3O4/carbon nanofiber composite. *Polymer* **2014,** *55* (3), 936-943.

105. Chen, I. H.; Wang, C.-C.; Chen, C.-Y., Fabrication and Structural Characterization of Polyacrylonitrile and Carbon Nanofibers Containing Plasma-Modified Carbon Nanotubes by Electrospinning. *The Journal of Physical Chemistry C* **2010,** *114* (32), 13532-13539.

106. Sreekumar, T. V.; Liu, T.; Min, B. G.; Guo, H.; Kumar, S.; Hauge, R. H.; Smalley, R. E., Polyacrylonitrile single-walled carbon nanotube composite fibers. *Adv Mater* **2004,** *16* (1), 58-61.

107. Naraghi, M.; Filleter, T.; Moravsky, A.; Locascio, M.; Loutfy, R. O.; Espinosa, H. D., A Multiscale Study of High Performance Double-Walled Nanotube-Polymer Fibers. *Acs Nano* **2010,** *4* (11), 6463-6476.

108. Naraghi, M.; Kolluru, P. V.; Chasiotis, I., Time and strain rate dependent mechanical behavior of individual polymeric nanofibers. *Journal of the Mechanics and Physics of Solids* **2014,** *62*, 257-275.

109. Liu, Y. D.; Kumar, S., Polymer/Carbon Nanotube Nano Composite Fibers-A Review. *Acs Appl Mater Inter* **2014,** *6* (9), 6069-6087.

110. Sathyanarayana, S.; Olowojoba, G.; Weiss, P.; Caglar, B.; Pataki, B.; Mikonsaari, I.; Hubner, C.; Henning, F., Compounding of MWCNTs with PS in a Twin-Screw Extruder with Varying Process Parameters: Morphology, Interfacial Behavior, Thermal Stability, Rheology, and Volume Resistivity. *Macromol Mater Eng* **2013,** *298* (1), 89-105.

111. Ding, W.; Eitan, A.; Fisher, F. T.; Chen, X.; Dikin, D. A.; Andrews, R.; Brinson, L. C.; Schadler, L. S.; Ruoff, R. S., Direct Observation of Polymer Sheathing in Carbon Nanotube−Polycarbonate Composites. *Nano Lett.* **2003,** *3* (11), 1593-1597.

112. Tallury, S. S.; Pasquinelli, M. A., Molecular Dynamics Simulations of Flexible Polymer Chains Wrapping Single-Walled Carbon Nanotubes. *J Phys Chem B* **2010,** *114* (12), 4122-4129.

113. Deitzel, J. M.; Kleinmeyer, J.; Harris, D.; Tan, N. C. B., The effect of processing variables on the morphology of electrospun nanofibers and textiles. *Polymer* **2001,** *42* (1), 261-272.

114. Koombhongse, S.; Liu, W. X.; Reneker, D. H., Flat polymer ribbons and other shapes by electrospinning. *J Polym Sci Pol Phys* **2001,** *39* (21), 2598-2606.

115. Baniasadi, M.; Xu, Z.; Hong, S.; Naraghi, M.; Minary Jolandan, M., Thermo-electromechanical Behavior of Piezoelectric Nanofibers. *Acs Appl Mater Inter* **2016,** *8* (4), 2540-2551.

116. Naraghi, M.; Chasiotis, I.; Kahn, H.; Wen, Y.; Dzenis, Y., Novel method for mechanical characterization of polymeric nanofibers. *Rev Sci Instrum* **2007,** *78* (8).

117. Naraghi, M.; Chasiotis, I.; Kahn, H.; Wen, Y. K.; Dzenis, Y., Mechanical deformation and failure of electrospun polyacrylonitrile nanofibers as a function of strain rate. *Appl Phys Lett* **2007,** *91* (15).

118. Frank, E.; Steudle, L. M.; Ingildeev, D.; Spörl, J. M.; Buchmeiser, M. R., Carbon Fibers: Precursor Systems, Processing, Structure, and Properties. *Angewandte Chemie International Edition* **2014,** *53* (21), 5262-5298.

119. Chand, S., Review Carbon fibers for composites. *J Mater Sci* **2000,** *35* (6), 1303-1313.

120. Wicks, B. J.; Coyle, R. A., Microstructural inhomogeneity in carbon fibres. *J Mater Sci* **1976,** *11* (2), 376-383.

121. Wen, K.; Marrow, J.; Marsden, B., Microcracks in nuclear graphite and highly oriented pyrolytic graphite (HOPG). *Journal of Nuclear Materials* **2008,** *381* (1), 199-203.

122. Park, S. H.; Jung, H. R.; Lee, W. J., Hollow activated carbon nanofibers prepared by electrospinning as counter electrodes for dye-sensitized solar cells. *Electrochim Acta* **2013,** *102*, 423-428.

123. Raza, A.; Wang, J. Q.; Yang, S.; Si, Y.; Ding, B., Hierarchical porous carbon nanofibers via electrospinning. *Carbon Lett* **2014,** *15* (1), 1-14.

124. Ji, L.; Zhang, X., Electrospun carbon nanofibers containing silicon particles as an energy-storage medium. *Carbon* **2009,** *47* (14), 3219-3226.

125. Fourdrinier, L.; Le Poche, H.; Chevalier, N.; Mariolle, D.; Rouviere, E., Electrical properties measurements on individual carbon nanofibers by scanning spreading resistance microscopy. *J Appl Phys* **2008,** *104* (11).

126. Penev, E. S.; Artyukhov, V. I.; Yakobson, B. I., Basic structural units in carbon fibers: Atomistic models and tensile behavior. *Carbon* **2015,** *85*, 72-78.

127. Gupta, N.; Artyukhov, V. I.; Penev, E. S.; Yakobson, B. I., Carbonization with Misfusion: Fundamental Limits of Carbon-Fiber Strength Revisited. *Adv. Mater.* **2016,** *28* (46), 10317-10322.

128. Chae, H. G.; Kumar, S., Making Strong Fibers. *Science* **2008,** *319* (5865), 908-909.

129. Ramachandramoorthy, R.; Beese, A.; Espinosa, H., In situ electron microscopy tensile testing of constrained carbon nanofibers. *International Journal of Mechanical Sciences* **2017**.

130. Li, X.; Yang, Y.; Zhao, Y.; Lou, J.; Zhao, X.; Wang, R.; Liang, Q.; Huang, Z., Electrospinning fabrication and in situ mechanical investigation of individual graphene nanoribbon reinforced carbon nanofiber. *Carbon* **2017,** *114* (Supplement C), 717-723.

131. B.D. Cullity, S. R. S., *Elements of X-ray Diffraction, Third Edition*. Prentice-Hall: New York, 2001.

132. Beese, A. M.; Papkov, D.; Li, S. Y.; Dzenis, Y.; Espinosa, H. D., In situ transmission electron microscope tensile testing reveals structure-property relationships in carbon nanofibers. *Carbon* **2013,** *60*, 246-253.

133. Baniasadi, M.; Xu, Z.; Cai, J.; Daryadel, S.; Quevedo-Lopez, M.; Naraghi, M.; Minary-Jolandan, M., Correlation of annealing temperature, morphology, and electro-mechanical properties of electrospun piezoelectric nanofibers. *Polymer* **2017,** *127* (Supplement C), 192-202.

134. Wang, Y.-X.; Wang, C.-G.; Bai, Y.-J.; Bo, Z., Effect of the drawing process on the wet spinning of polyacrylonitrile fibers in a system of dimethyl sulfoxide and water. *J Appl Polym Sci* **2007,** *104* (2), 1026-1037.

135. Liu, C.-K.; Feng, Y.; He, H.-J.; Zhang, J.; Sun, R.-J.; Chen, M.-Y., Effect of carbonization temperature on properties of aligned electrospun polyacrylonitrile carbon nanofibers. *Materials & Design* **2015,** *85* (Supplement C), 483-486.

136. Cai, J.; Naraghi, M., Effect of Templating Graphitization on Electrical Conductivity of Electrospun Carbon nanofiber. In *58th AIAA/ASCE/AHS/ASC Structures, Structural Dynamics, and Materials Conference*, American Institute of Aeronautics and Astronautics: 2017.

137. Shilpa; Das, S. K.; Afzal, M. A. F.; Srivastava, S.; Patil, S.; Sharma, A., Enhanced electrical conductivity of suspended carbon nanofibers: Effect of hollow structure and improved graphitization. *Carbon* **2016,** *108* (Supplement C), 135-145.

138. Cai, J. Z.; Naraghi, M., Computational analysis of electrical conduction in hybrid nanomaterials with embedded non-penetrating conductive particles. *Model Simul Mater Sc* **2016,** *24* (6).

139. Askounis, A.; Yamada, Y.; Ikuta, T.; Takahashi, K.; Takata, Y.; Sefiane, K., On the linear dependence of a carbon nanofiber thermal conductivity on wall thickness. *AIP Advances* **2016,** *6* (11), 115119.

140. Cai, J.; Naraghi, M., Developing a Numerical Scheme to Capture the Piezoresistivity of CNF/CNTs Hybrid Nanofibers. In *58th AIAA/ASCE/AHS/ASC Structures, Structural Dynamics, and Materials Conference*, American Institute of Aeronautics and Astronautics: 2017.

141. Wang, Y.; Serrano, S.; Santiago-Avilés, J. J., Raman characterization of carbon nanofibers prepared using electrospinning. *Synthetic Met* **2003,** *138* (3), 423-427.

142. Ferrari, A. C., Raman spectroscopy of graphene and graphite: Disorder, electron–phonon coupling, doping and nonadiabatic effects. *Solid State Communications* **2007,** *143* (1), 47-57.

143. Matthews, M. J.; Pimenta, M. A.; Dresselhaus, G.; Dresselhaus, M. S.; Endo, M., Origin of dispersive effects of the Raman D band in carbon materials. *Phys Rev B* **1999,** *59* (10), R6585-R6588.

144. Wang, Y.; Serrano, S.; Santiago-Aviles, J. J., Raman characterization of carbon nanofibers prepared using electrospinning. *Synthetic Met* **2003,** *138* (3), 423-427.

145. Rahaman, M. S. A.; Ismail, A. F.; Mustafa, A., A review of heat treatment on polyacrylonitrile fiber. *Polym. Degrad. Stab.* **2007,** *92* (8), 1421-1432.

146. Tyson, C. N., Fracture Mechanisms in Carbon-Fibers Derived from Pan in Temperature-Range 1000-2800 Degreesc. *J. Phys. D-Appl. Phys.* **1975,** *8* (7), 749-758.

147. Kim, M. A.; Jang, D.; Tejima, S.; Cruz-Silva, R.; Joh, H. I.; Kim, H. C.; Lee, S.; Endo, M., Strengthened PAN-based carbon fibers obtained by slow heating rate carbonization. *Scientific Reports* **2016,** *6*.

148. Reynolds, W. N.; Sharp, J. V., Crystal Shear Limit to Carbon-Fiber Strength. *Carbon* **1974,** *12* (2), 103-110.

149. Rath, J. P.; Chaki, T. K.; Khastgir, D., Change in fiber properties due to the heat treatment of nylon 6 tire cords. *J Appl Polym Sci* **2008,** *108* (6), 3960-3967.

150. Kromm, F. X.; Lorriot, T.; Coutand, B.; Harry, R.; Quenisset, J. M., Tensile and creep properties of ultra high molecular weight PE fibres. *Polymer Testing* **2003,** *22* (4), 463-470.

151. Motta, M.; Moisala, A.; Kinloch, I. A.; Windle, A. H., High Performance Fibres from 'Dog Bone' Carbon Nanotubes. *Adv Mater* **2007,** *19* (21), 3721-3726.

152. Vollrath, F.; Knight, D. P., Liquid crystalline spinning of spider silk. *Nature* **2001,** *410*, 541.

153. Wetzel, B.; Rosso, P.; Haupert, F.; Friedrich, K., Epoxy nanocomposites – fracture and toughening mechanisms. *Engineering Fracture Mechanics* **2006,** *73* (16), 2375-2398.

154. Quaresimin, M.; Schulte, K.; Zappalorto, M.; Chandrasekaran, S., Toughening mechanisms in polymer nanocomposites: From experiments to modelling. *Compos Sci Technol* **2016,** *123* (Supplement C), 187-204.

155. Chatterjee, S.; Nafezarefi, F.; Tai, N. H.; Schlagenhauf, L.; Nüesch, F. A.; Chu, B. T. T., Size and synergy effects of nanofiller hybrids including graphene nanoplatelets and carbon nanotubes in mechanical properties of epoxy composites. *Carbon* **2012,** *50* (15), 5380-5386.

156. Chandrasekaran, S.; Sato, N.; Tölle, F.; Mülhaupt, R.; Fiedler, B.; Schulte, K., Fracture toughness and failure mechanism of graphene based epoxy composites. *Compos Sci Technol* **2014,** *97* (Supplement C), 90-99.

157. Reynolds, W. N.; Sharp, J. V., Crystal shear limit to carbon fibre strength. *Carbon* **1974,** *12* (2), 103-110.

158. Balandin, A. A., Thermal properties of graphene and nanostructured carbon materials. *Nat Mater* **2011,** *10* (8), 569-581.

159. Mahanta, N. K.; Abramson, A. R.; Lake, M. L.; Burton, D. J.; Chang, J. C.; Mayer, H. K.; Ravine, J. L., Thermal conductivity of carbon nanofiber mats. *Carbon* **2010,** *48* (15), 4457-4465.

160. Wang, Y.; Serrano, S.; Santiago-Aviles, J. J., Conductivity measurement of electrospun PAN-based carbon nanofiber. *J Mater Sci Lett* **2002,** *21* (13), 1055-1057.

161. Bom, D.; Andrews, R.; Jacques, D.; Anthony, J.; Chen, B. L.; Meier, M. S.; Selegue, J. P., Thermogravimetric analysis of the oxidation of multiwalled carbon nanotubes: Evidence for the role of defect sites in carbon nanotube chemistry. *Nano Lett* **2002,** *2* (6), 615-619.

162. Zhuge, J. F.; Gou, J. H.; Chen, R. H.; Gordon, A.; Kapat, J.; Hart, D.; Ibeh, C., Fire retardant evaluation of carbon nanofiber/graphite nanoplatelets nanopaper-based coating under different heat fluxes. *Composites Part B-Engineering* **2012,** *43* (8), 3293-3305.

163. Cipriano, B. H.; Kota, A. K.; Gershon, A. L.; Laskowski, C. J.; Kashiwagi, T.; Bruck, H. A.; Raghavan, S. R., Conductivity enhancement of carbon nanotube and nanofiber-based polymer nanocomposites by melt annealing. *Polymer* **2008,** *49* (22), 4846-4851.

164. Linares, A.; Canalda, J. C.; Cagiao, M. E.; Ezquerra, T. A., Conducting nanocomposites based on polyamide 6,6 and carbon nanofibers prepared by cryogenic grinding. *Compos Sci Technol* **2011,** *71* (10), 1348-1352.

165. Logakis, E.; Pollatos, E.; Pandis, C.; Peoglos, V.; Zuburtikudis, I.; Delides, C. G.; Vatalis, A.; Gjoka, M.; Syskakis, E.; Viras, K.; Pissis, P., Structure-property relationships in isotactic polypropylene/multi-walled carbon nanotubes nanocomposites. *Compos Sci Technol* **2010,** *70* (2), 328-335.

166. Rafiee, M. A.; Rafiee, J.; Wang, Z.; Song, H. H.; Yu, Z. Z.; Koratkar, N., Enhanced Mechanical Properties of Nanocomposites at Low Graphene Content. *Acs Nano* **2009,** *3* (12), 3884-3890.

167. Cullinan, M. A.; Culpepper, M. L., Carbon nanotubes as piezoresistive microelectromechanical sensors: Theory and experiment. *Phys Rev B* **2010,** *82* (115428).

168. Grow, R. J.; Wang, Q.; Cao, J.; Wang, D. W.; Dai, H. J., Piezoresistance of carbon nanotubes on deformable thin-film membranes. *Appl Phys Lett* **2005,** *86* (093104).

169. Minot, E. D.; Yaish, Y.; Sazonova, V.; Park, J. Y.; Brink, M.; McEuen, P. L., Tuning carbon nanotube band gaps with strain. *Phys Rev Lett* **2003,** *90* (15).

170. Wang, Y.; Santiago-Aviles, J. J.; Furlan, R.; Ramos, I., Pyrolysis temperature and time dependence of electrical conductivity evolution for electrostatically

generated carbon nanofibers. *Ieee Transactions on Nanotechnology* **2003,** *2* (1), 39-43.

171. Wang, Y.; Santiago-Aviles, J. J., Low-temperature electronic properties of electrospun PAN-derived carbon nanofiber. *Ieee Transactions on Nanotechnology* **2004,** *3* (2), 221-224.

172. Chawla, S.; Naraghi, M.; Davoudi, A., Effect of twist and porosity on the electrical conductivity of carbon nanofiber yarns. *Nanotechnology* **2013,** *24* (25), 255708.

173. Carey, J. D.; Silva, S. R. P., Disorder, clustering, and localization effects in amorphous carbon. *Phys Rev B* **2004,** *70* (23).

174. Grimaldi, C.; Ryser, P.; Strassler, S., Gauge factor enhancement driven by heterogeneity in thick-film resistors. *J Appl Phys* **2001,** *90* (1), 322-327.

175. Fitzer, E.; Rozploch, F., Laser Raman-Spectroscopy for Determination of the C-C Bonding Length in Carbon. *Carbon* **1988,** *26* (4), 594-595.

176. Xie, H. Q.; Chen, L. F.; Yu, W.; Wang, B. Q., Temperature dependent thermal conductivity of a free-standing graphene nanoribbon. *Appl Phys Lett* **2013,** *102* (11).

177. Yamada, T.; Yabutani, H.; Saito, T.; Yang, C. Y., Temperature dependence of carbon nanofiber resistance. *Nanotechnology* **2010,** *21* (26).

178. Tamborin, M.; Piccinini, S.; Prudenziati, M.; Morten, B., Piezoresistive properties of RuO2-based thick-film resistors: The effect of RuO2 grain size. *Sensor Actuat a-Phys* **1997,** *58* (2), 159-164.

179. Alamusi; Hu, N.; Fukunaga, H.; Atobe, S.; Liu, Y. L.; Li, J. H., Piezoresistive Strain Sensors Made from Carbon Nanotubes Based Polymer Nanocomposites. *Sensors-Basel* **2011,** *11* (11), 10691-10723.

180. Kanda, Y., Piezoresistance Effect of Silicon. *Sensor Actuat a-Phys* **1991,** *28* (2), 83-91.

181. Oliva-Aviles, A. I.; Aviles, F.; Seidel, G. D.; Sosa, V., On the contribution of carbon nanotube deformation to piezoresistivity of carbon nanotube/polymer composites. *Compos Part B-Eng* **2013,** *47*, 200-206.

182. Ren, X.; Seidel, G. D., Computational micromechanics modeling of inherent piezoresistivity in carbon nanotube-polymer nanocomposites. *J Intel Mat Syst Str* **2013,** *24* (12), 1459-1483.

183. Krucinska, I.; Stypka, T., Direct Measurement of the Axial Poisson Ratio of Single Carbon-Fibers. *Compos Sci Technol* **1991,** *41* (1), 1-12.

184. Villeneuve, J. F.; Naslain, R.; Fourmeaux, R.; Sevely, J., Longitudinal (Radial Thermal-Expansion and Poisson Ratio of Some Ceramic Fibers as Measured by Transmission Electron-Microscopy. *Compos Sci Technol* **1993,** *49* (1), 89-103.

185. Prudenziati, M.; Morten, B.; Cilloni, F.; Ruffi, G., Very High-Strain Sensitivity in Thick-Film Resistors - Real and False Super Gauge Factors. *Sensor Actuator* **1989,** *19* (4), 401-414.

186. Wang, X. J.; Fu, X. L.; Chung, D. D. L., Strain sensing using carbon fiber. *J Mater Res* **1999,** *14* (3), 790-802.

187. Simmons, J. G., Generalized Formula for Electric Tunnel Effect between Similar Electrodes Separated by a Thin Insulating Film. *J Appl Phys* **1963,** *34* (6), 1793-&.

188. Hu, N.; Karube, Y.; Yan, C.; Masuda, Z.; Fukunaga, H., Tunneling effect in a polymer/carbon nanotube nanocomposite strain sensor. *Acta Mater* **2008,** *56* (13), 2929-2936.

189. Saha, B.; Schatz, G. C., Carbonization in Polyacrylonitrile (PAN) Based Carbon Fibers Studied by ReaxFF Molecular Dynamics Simulations. *J Phys Chem B* **2012,** *116* (15), 4684-4692.

190. Du, F. M.; Fischer, J. E.; Winey, K. I., Effect of nanotube alignment on percolation conductivity in carbon nanotube/polymer composites. *Phys Rev B* **2005,** *72* (12).

191. Hu, N.; Masuda, Z.; Yan, C.; Yamamoto, G.; Fukunaga, H.; Hashida, T., The electrical properties of polymer nanocomposites with carbon nanotube fillers. *Nanotechnology* **2008,** *19* (21).

192. Klein, C. A., Pyrolytic Graphites - Their Description as Semimetallic Molecular Solids. *J Appl Phys* **1962,** *33* (11), 3338-&.

193. Kim, C.; Yang, K. S.; Kojima, M.; Yoshida, K.; Kim, Y. J.; Kim, Y. A.; Endo, M., Fabrication of electrospinning-derived carbon nanofiber webs for the anode material of lithium-ion secondary batteries. *Adv Funct Mater* **2006,** *16* (18), 2393-2397.

194. Bao, W. S.; Meguid, S. A.; Zhu, Z. H.; Meguid, M. J., Modeling electrical conductivities of nanocomposites with aligned carbon nanotubes. *Nanotechnology* **2011,** *22* (48).

195. Brebbia, C. A.; Walker, S., *Boundary Element Techniques in Engineering*. Elsevier Science: 2013.

196. Balberg, I.; Binenbaum, N., Cluster Structure and Conductivity of 3-Dimensional Continuum-Systems. *Phys Rev A* **1985,** *31* (2), 1222-1225.

197. Alberty, J.; Carstensen, C.; Funken, S. A., Remarks around 50 lines of Matlab: short finite element implementation. *Numer Algorithms* **1999,** *20* (2-3), 117-137.

198. Liu, Y. J.; Chen, X. L., Evaluations of the effective material properties of carbon nanotube-based composites using a nanoscale representative volume element. *Mech Mater* **2003,** *35* (1–2), 69-81.

199. Yakobson, B. I.; Smalley, R. E., Fullerene nanotubes: C-1000000 and beyond. *Am Sci* **1997,** *85* (4), 324-337.

200. Qian, D.; Wagner, G. J.; Liu, W. K.; Yu, M.-F.; Ruoff, R. S., Mechanics of carbon nanotubes. *Applied Mechanics Reviews* **2002,** *55* (6), 495-533.

201. Ru, C. Q., Axially compressed buckling of a doublewalled carbon nanotube embedded in an elastic medium. *J Mech Phys Solids* **2001,** *49* (6), 1265-1279.

202. Alamusi; Liu, Y. L.; Hu, N., Numerical Simulations on Piezoresistivity of CNT/Polymer Based Nanocomposites. *Cmc-Comput Mater Con* **2010,** *20* (2), 101-117.

APPENDIX A: UNCERTAINTY CALCULATION OF DR/Dε

Fig.A1 shows one example in our work of using line fitting method to calculate the uncertainty of dR/dε, in which the experimental results of resistance with measurement uncertainty, which is obtained based on 8 times testing at certain strain, in function of the strain in CNF sample with uncertainty of 0.15% of DIC method[116] was plotted and linear fitted. After drawing the best fitting line, the upper bound line and the lower bound line, the slope of the linear fitting line is obtained, which is dR/dε = 167056±3341 and the uncertainty, $\delta\left(\frac{dR}{d\varepsilon}\right) = 3341$.

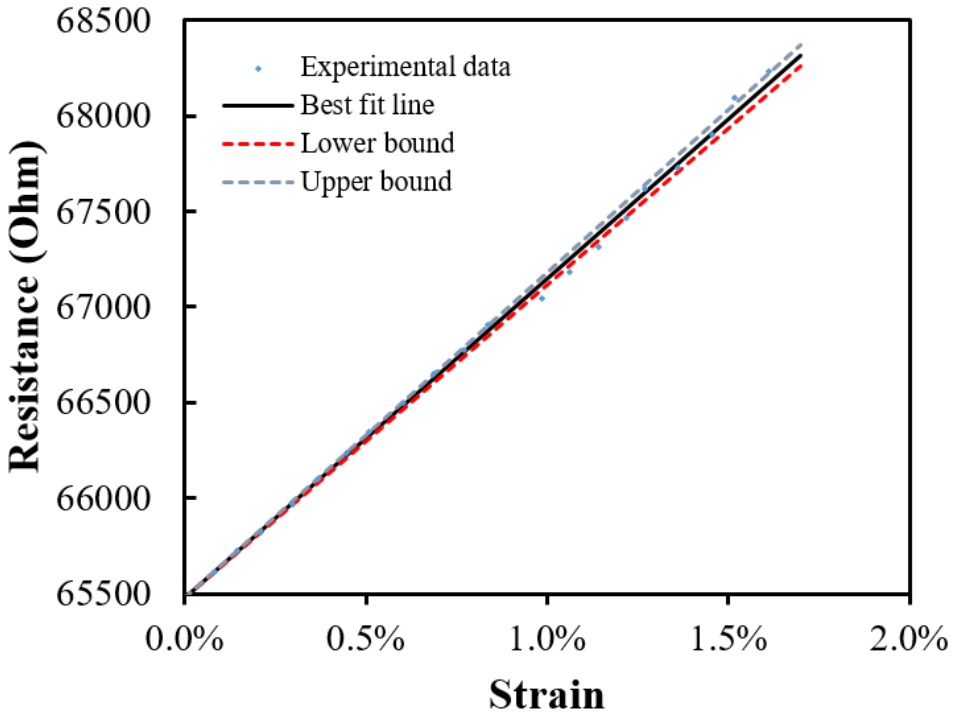

Figure A1. Calculation of the uncertainty of dR/dε by line fitting.

By using the following equations, the uncertainty of gage factor ($GF = \frac{dR/d\varepsilon}{R_0}$) and piezoresistive coefficient ($\frac{\Delta\rho}{\rho}/\varepsilon = GF - 1 - 2\vartheta$) could be obtained.

$$(\delta GF)^2 = (\delta GF)^2 = \left(\frac{dGF}{d(dR/d\varepsilon)}\right)^2 (\delta R_0)^2 + \left(\frac{dGF}{dR_0}\right)^2 \left(\delta \frac{dR}{d\varepsilon}\right)^2 = \left(\frac{\delta(dR/d\varepsilon)}{R_0}\right)^2 + \left(\frac{dR/d\varepsilon}{{R_0}^2}\delta R_0\right)^2$$

$$\left(\delta(\frac{\Delta\rho}{\rho}/\varepsilon)\right)^2 = (\delta GF)^2 + 4 \cdot (\delta\vartheta)^2$$

where $\delta(dR/d\varepsilon)$ is obtained from the previous line fitting method, which is 3341 and δR_0 is obtained from experiment based 8 times resistance measurements at the original zero strain on CNF, which is 3.48. So, the obtained uncertainty of gage factor measurement is 0.056 or 2.2%. By using 0.25±0.030 as the poisson's ratio of CNF, we could calculate the piezoresistive coefficient, which is 1.05±0.082, whose uncertainty is about 7.8%. Based on the calculation, we found that the uncertainty of piezoresistive coefficient measurement for all CNF samples is mainly from the uncertainty of piosson's ratio (0.25±0.03), which is 12% comparing with the ~2% measurement uncertainty for the gage factors. That is to say even after considering its measurement uncertainty (~2.2%), the gage factor of CNF (2.29±0.24) is still evidently larger than the CF (1.8-1.9), which also shows the different piezoresistive behavior between two materials.

APPENDIX B: EQUIVALENT RESISTOR NETWORK FOR AN INDIVIDUAL PARTICLE

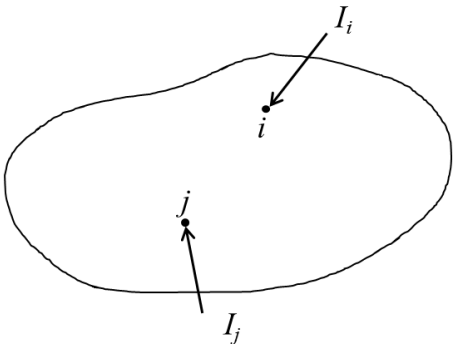

Figure B1. Static equilibrium of a body under external currents

We consider a continuous orthotropic electrical conductive medium (such as individual turbostratic domains), in which at certain points (points 1, 2, ….i, …n) on the surface, electric potential boundary conditions are prescribed. The electric currents can flow in and out of the medium only through these points, Fig.B1. In this appendix, we show that the relationships between the applied voltages and input/output currents of the points remains unchanged if the medium is replaced with a set of $n(n-1)/2$ resistors. To this end, we will first consider the PDE which governs the electric potential within the medium obtained by considering the principle of conservation of charges:

$$\frac{\partial^2 V/\partial x^2}{\rho_x} + \frac{\partial^2 V/\partial y^2}{\rho_y} = 0 \tag{B1}$$

We consider the case where node i is at V_{0i} while all the other nodes are at zero electric potential. That is:

$$V_i = V_{0i}, V_j = 0 \; for \; i \neq j \; and \; j = 1 - n \tag{B2}$$

The solution to the above PDE (Equation B1) and the set of boundary conditions (Equation A2) will be denoted as $V_{0(x,y)}$ with a current density of $J_{0(x,y)}$. If we increase $V_i = \alpha V_{0i}$, while keeping all other $V_{js} = 0$, the solution to the new boundary value problem will be $V_{(x,y)} = \alpha V_{0(x,y)}$, simply because it satisfies both the B.C.s and the PDE. For the current density of points in the continuum we have:

$$\overrightarrow{J_0} = \frac{\partial V_0/\partial x}{\rho_x}\hat{\imath} + \frac{\partial V_0/\partial y}{\rho_y}\hat{\jmath} \tag{B3}$$

Therefore, the current density of the second B.Cs will be $J_{(x,y)} = \alpha J_{0(x,y)}$.

Now let's consider point *j* ($i \neq j$). The total current passing through point *j* will be:

$$I_j = \oint_C J_0 n dA \tag{B4}$$

Therefore, if V_{0i} changes to αV_{0i}, according to Equation B4, I_{0j} will change to αI_{0j}. Hence,

$$\frac{\partial I_j}{\partial V_i} = const. = \alpha_{ij} \tag{B5}$$

Considering the principle of superposition, the above solution is applicable to most general case of B.C., in which each node is at an arbitrary potential of V_i. Moreover, by considering the energy flowing into the system in the steady state (***P***), we can also show that $\alpha_{ij} = \alpha_{ji}$, as follows. First, we consider the power input to the system at an arbitrary set of applied voltages which is,

$$P = I_2(V_2 - V_1) + I_3(V_3 - V_1) + \cdots = I_2V_2 + I_3V_3 + \cdots + (-I_2 - I_3 - \cdots I_n)V_1 \quad \text{(B6)}$$

Moreover, we have $\sum I_i = 0$ (no charge accumulation within the medium). Therefore, $P = \sum I_i V_i$. Now, let's consider the case of 2 contact points ($n = 2$). We increase the input voltages to V1 (node 1) and V2 (node 2) via two different approaches. In approach (1), first we raise $V_1 = V_1$ & $V_2 = 0$. Therefore, $I_1 = \alpha_{11}V_1 = I_2 = \alpha_{21}V_1$, as a result, $P = \sum I_i V_i = \alpha_{11}V_1^2$. We then raise $V_2 = V_2$. As a result of the latter step, an extra input current will be generated which is $\delta I_1 = \alpha_{12}V_2$ and $\delta I_2 = \alpha_{22}V_2$. Hence, the power input to the system becomes: $P = \sum I_i V_i = \alpha_{11}V_1^2 + V_1\delta I_1 + V_2\delta I_2 \quad = \alpha_{11}V_1^2 + \alpha_{12}V_1V_2 + \alpha_{22}V_2^2$

In approach (2), we first raise the voltage of node 2 toV_2 and then raise the voltage of node 1 to V_1. Hence, the power input to the system in the second approach will be:

$$P = \alpha_{22}V_2^2 + \alpha_{21}V_2V_1 + \alpha_{11}V_1^2 \quad \text{(B7)}$$

Since the powers from two approaches are expected to be the same (a linear system at similar boundary conditions), we will have $\alpha_{21} = \alpha_{12}$. Similar arguments can be made to show that $\alpha_{ij} = \alpha_{ji}$ for n>2. Therefore, the continuum system can be represented by $n(n-1)/2$ constants (α_{ij}).

Next we consider a set of *n* points ($i = 1 \ldots n$) each connected by ohmic resistors with a magnitude of R_{ij} , where the subscripts refer to the number of the points (thus R_{ij} = R_{ji}). According to the definition of the Ohmic resistors, a voltage change in the *i*th

contact point of ∂V_i will induce a current flow (input or output) of ∂I_j from contact point j such that:

$$\frac{\partial I_j}{\partial V_i} = \frac{1}{R_{ij}} = const. \tag{B8}$$

A comparison between equations A5 and A8 proves that the medium with n contact points can be replaced by a set of $n(n-1)/2$ resistors such that $\alpha_{ij} = \frac{1}{R_{ij}}$.

APPENDIX C: FINITE ELEMENT ANALYSIS TO CALCULATE INTRA-PARTICLE RESISTANCE

To calculate the macroscopic electrical conductivity of the nanocomposite, the resistance within particles need to be calculated. In appendix A, it was demonstrated that the resistance in each conductive particle with n contact points can be represented by an equivalent network of n(n-1)/2 resistors, each connecting two of the contact points. Considering the totally random size of particles and number and position of contact points, finite element analysis (FEA) is an effective method to calculate the resistance of the equivalent resistors within each particle. The conductive particle in single carbon nanofiber is turbostratic carbon which has orthotropic electrical conductivity due to its layered graphitic structure. To calculate the resistance within the turbostratic carbon particle, the electrical conduction equation in orthotropic medium was first replaced with an equivalent isotropic medium as follows. The electric flux in 2D medium can be expressed as:

$$J_x = -\sigma_{11}\frac{\partial \varphi}{\partial x} - \sigma_{12}\frac{\partial \varphi}{\partial y} \tag{C1}$$

$$J_y = -\sigma_{21}\frac{\partial \varphi}{\partial x} - \sigma_{22}\frac{\partial \varphi}{\partial y} \tag{C2}$$

where φ is the electric potential, σ_{ij} is the electric conductivity and J is the current density. Since x and y axis are lined up with the principal directions of the domains (a-

and c-axis, respectively), $\sigma_{12} = \sigma_{21} = 0$. In the steady state within the orthotropic medium, there is no current source, thus,

$$\sigma_1 \frac{\partial^2 \varphi}{\partial x^2} + \sigma_2 \frac{\partial^2 \varphi}{\partial y^2} = 0 \tag{C3}$$

The electric conduction equation for an orthotropic medium can be transformed to a standard electric conduction equation for isotropic medium, with the new independent coordinate variables, X and Y defined as,

$$X = \sqrt{\sigma/\sigma_1}x \tag{C4}$$

$$Y = \sqrt{\sigma/\sigma_2}y \tag{C5}$$

where σ is the equivalent conductivity of the isotropic medium, defined as $\sigma = \sqrt{\sigma_1\sigma_2}$,

In the new coordinate system, equation (B1) becomes,

$$\sigma\left(\frac{\partial^2 \varphi}{\partial X^2} + \frac{\partial^2 \varphi}{\partial Y^2}\right) = 0 \tag{C6}$$

The electric current leaving/entering the particle along the x (or y) edge between y_1 and y_2 (or x_1 and x_2) can be calculated in the new coordinates as,

$$I_x = \int_{y_1}^{y_2} J_x dy = \int_{y_1}^{y_2} \sqrt{\sigma\sigma_1}\frac{\partial \varphi}{\partial X}\frac{dY}{\sqrt{\frac{\sigma}{\sigma_2}}} = \sigma \int_{\sqrt{\frac{\sigma}{\sigma_2}}y_1}^{\sqrt{\frac{\sigma}{\sigma_2}}y_2} \frac{\partial \varphi}{\partial X} dY \tag{C7}$$

$$I_y = \int_{x_1}^{x_2} J_y dx = \int_{x_1}^{x_2} \sqrt{\sigma\sigma_2}\frac{\partial \varphi}{\partial Y}\frac{dX}{\sqrt{\frac{\sigma}{\sigma_1}}} = \sigma \int_{\sqrt{\frac{\sigma}{\sigma_1}}x_1}^{\sqrt{\frac{\sigma}{\sigma_1}}x_2} \frac{\partial \varphi}{\partial Y} dX \tag{C8}$$

To calculate the current flux in new coordinates, the regular finite element analysis method can be applied. In this work, each particle has several contact points. Considering the size of hexagonal carbon structure in turbostratic carbon, the minimum length for the

contact point is set to be 0.14 nm (minimum distance between carbon atoms). At first, the rectangle shape with arbitrary size with contact points representing individual turbostratic particle was meshed using triangular elements. An example for a meshed particle with three contact points is shown in Fig.C1

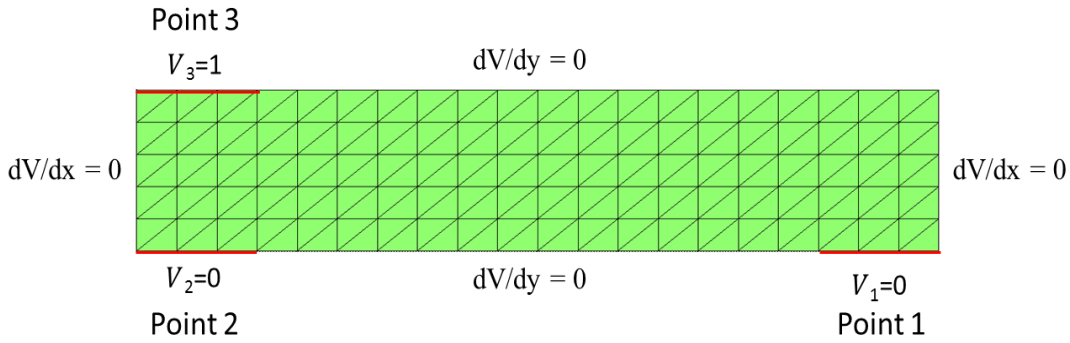

Figure C1. Regular meshing in FEA and applied Dirichlet boundary conditions

Mesh convergence analysis was carried out and the number of elements was set to 50,000 to achieve mesh independent results. After meshing each particle, the Dirichlet boundary condition was applied to the particle. That is, at each contact point, V=1 or V=0 was applied depending on the calculation sequence which was specified in the text, and all other portions of the edges of the particle were subjected to boundary conditions of dV/dx = 0 or dV/dy = 0 to make sure that there is not current flow except out of / into the sample other than from the contact points.

As shown in Equation C2, the calculation of input/output currents needed to estimate particle internal resistance values requires the calculation of potential gradients,

which are typically very large right at the contact points. The calculation of large gradients can introduce large numerical errors to the resistance calculations. To overcome this problem and to calculate the input/output flows from each contact point, we considered a small box around each contact point, such that the contact point lies on one of its edges (Fig.C2). Along that edge, due to the specified boundary conditions, the current can only enter/exit the box only through the contact point. Therefore, due to conservation of charge principle (in the steady state) the current exiting/entering the box on three other edges is equal to the current entering/exiting the box through the contact point. Hence, the former was calculated directly as a measure of the latter. The potential gradient is significantly lower in the former compared to the latter, considerably reducing the computational errors.

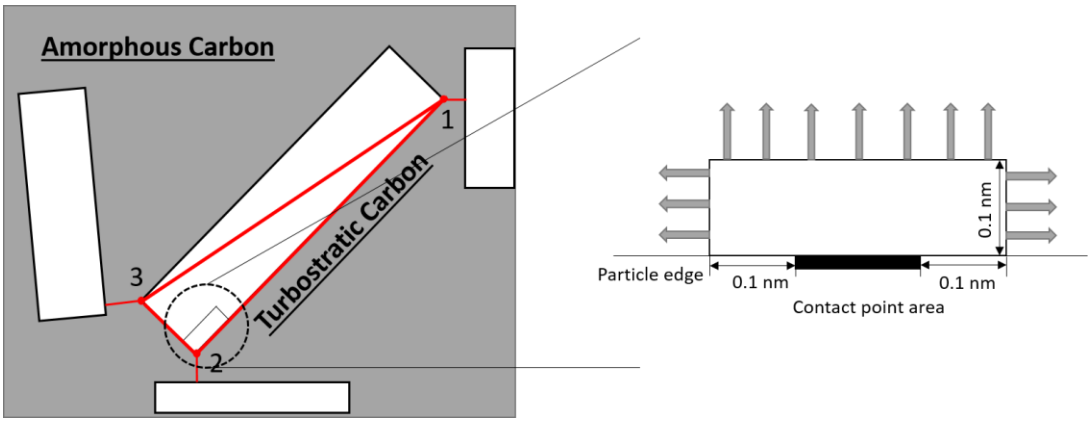

Figure C2. Turbostratic particle with three contact points and contact point current flow calculation